Instabilities and emergence of coherent structures in the turbulent channel flow

Department of Mechanics, Mathematics and Management
MECHANICAL AND MANAGEMENT ENGINEERING
Ph.D. Program
SSD: ING-IND/08–FLUID MACHINERY

Final Dissertation

Instabilities and emergence of coherent structures in the turbulent channel flow

---

by
Nicola Ciola

Supervisors:

Prof. Stefania Cherubini

Prof. Pietro De Palma

Prof. Jean-Christophe Robinet

Coordinator of Ph.D. Program:
Prof. Giuseppe Casalino

Course n°38, 01/11/2022-31/10/2025

Politecnico di Bari

LIBERATORIA PER L'ARCHIVIAZIONE DELLA TESI DI DOTTORATO

Al Magnifico Rettore
del Politecnico di Bari

Il/la sottoscritto/a Ciola Nicola nato/a a Chiaromonte il 14/05/1998

residente a Genzano di Lucania in via Pascoli, 4 e-mail nicolaciola98@gmail.com

iscritto al 3° anno di Corso di Dottorato di Ricerca in Ingegneria Meccanica e Gestionale ciclo 38°

ed essendo stato ammesso a sostenere l'esame finale con la prevista discussione della tesi dal titolo:

Instabilities and emergence of coherent structures in the turbulent channel flow

DICHIARA

1) di essere consapevole che, ai sensi del D.P.R. n. 445 del 28.12.2000, le dichiarazioni mendaci, la falsità negli atti e l'uso di atti falsi sono puniti ai sensi del codice penale e delle Leggi speciali in materia, e che nel caso ricorressero dette ipotesi, decade fin dall'inizio e senza necessità di nessuna formalità dai benefici conseguenti al provvedimento emanato sulla base di tali dichiarazioni;
2) di essere iscritto al Corso di Dottorato di ricerca in Ingegneria Meccanica e Gestionale ciclo 38°, corso attivato ai sensi del "*Regolamento dei Corsi di Dottorato di ricerca del Politecnico di Bari"*, emanato con D.R. n.286 del 01.07.2013;
3) di essere pienamente a conoscenza delle disposizioni contenute nel predetto Regolamento in merito alla procedura di deposito, pubblicazione e autoarchiviazione della tesi di dottorato nell'Archivio Istituzionale ad accesso aperto alla letteratura scientifica;
4) di essere consapevole che attraverso l'autoarchiviazione delle tesi nell'Archivio Istituzionale ad accesso aperto alla letteratura scientifica del Politecnico di Bari (IRIS-POLIBA), l'Ateneo archivierà e renderà consultabile in rete (nel rispetto della Policy di Ateneo di cui al D.R. 642 del 13.11.2015) il testo completo della tesi di dottorato, fatta salva la possibilità di sottoscrizione di apposite licenze per le relative condizioni di utilizzo (di cui al sito http://www.creativecommons.it/Licenze), e fatte salve, altresì, le eventuali esigenze di "embargo", legate a strette considerazioni sulla tutelabilità e sfruttamento industriale/commerciale dei contenuti della tesi, da rappresentarsi mediante compilazione e sottoscrizione del modulo in calce (Richiesta di embargo);
5) che la tesi da depositare in IRIS-POLIBA, in formato digitale (PDF/A) sarà del tutto identica a quelle **consegnate**/inviate/da inviarsi ai componenti della commissione per l'esame finale e a qualsiasi altra copia depositata presso gli Uffici del Politecnico di Bari in forma cartacea o digitale, ovvero a quella da discutere in sede di esame finale, a quella da depositare, a cura dell'Ateneo, presso le Biblioteche Nazionali Centrali di Roma e Firenze e presso tutti gli Uffici competenti per legge al momento del deposito stesso, e che di conseguenza va esclusa qualsiasi responsabilità del Politecnico di Bari per quanto riguarda eventuali errori, imprecisioni o omissioni nei contenuti della tesi;
6) che il contenuto e l'organizzazione della tesi è opera originale realizzata dal sottoscritto e non compromette in alcun modo i diritti di terzi, ivi compresi quelli relativi alla sicurezza dei dati personali; che pertanto il Politecnico di Bari ed i suoi funzionari sono in ogni caso esenti da responsabilità di qualsivoglia natura: civile, amministrativa e penale e saranno dal sottoscritto tenuti indenni da qualsiasi richiesta o rivendicazione da parte di terzi;
7) che il contenuto della tesi non infrange in alcun modo il diritto d'Autore né gli obblighi connessi alla salvaguardia di diritti morali od economici di altri autori o di altri aventi diritto, sia per testi, immagini, foto, tabelle, o altre parti di cui la tesi è composta.

Luogo e data Bari, 04/02/2026 Firma Nicola Ciola

Il/La sottoscritto, con l'autoarchiviazione della propria tesi di dottorato nell'Archivio Istituzionale ad accesso aperto del Politecnico di Bari (POLIBA-IRIS), pur mantenendo su di essa tutti i diritti d'autore, morali ed economici, ai sensi della normativa vigente (Legge 633/1941 e ss.mm.ii.),

CONCEDE

- al Politecnico di Bari il permesso di trasferire l'opera su qualsiasi supporto e di convertirla in qualsiasi formato al fine di una corretta conservazione nel tempo. Il Politecnico di Bari garantisce che non verrà effettuata alcuna modifica al contenuto e alla struttura dell'opera.
- al Politecnico di Bari la possibilità di riprodurre l'opera in più di una copia per fini di sicurezza, back-up e conservazione.

Luogo e data Bari, 04/02/2026 Firma Nicola Ciola

Politecnico di Bari

Department of Mechanics, Mathematics and Management
MECHANICAL AND MANAGEMENT ENGINEERING
Ph.D. Program
SSD: ING-IND/08–FLUID MACHINERY

Final Dissertation

Instabilities and emergence of coherent structures in the turbulent channel flow

by
Nicola Ciola:

Referees:

Prof. Carlo Cossu

Prof. Dwight Barkley

Supervisors:

Prof. Stefania Cherubini

Prof. Pietro De Palma

Prof. Jean-Christophe Robinet

Coordinator of Ph.D Program:

Prof. Giuseppe Casalino

Course n°38, 01/11/2022-31/10/2025

Acknowledgments

The preparation of this work was a challenging journey that I could not have completed without the support, guidance, and valuable input of the people around me.

First of all, I thank my supervisors, who introduced me to the world of scientific research and contributed to this work with their ideas. I was lucky enough to have, in practice, four supervisors, each of them adding a different flavour to my experience as a PhD student. To Stefania, for your dynamism and your pragmatic approach to problems. To Pietro, for our stimulating discussions and all the interest you have invested in my work since the beginning. To Jean-Christophe, for your broad scientific expertise, your spiritual guidance and the great time we spent together at various conferences around Europe. To Yohann, for our long brainstorming sessions during which I learnt a lot about subcritical transition, but also and foremost about the process of producing high-quality research.

Then, I thank Carlo Cossu and Dwight Barkley, who accepted to review the manuscript, and Javier Jiménez and Innocent Mutabazi, who completed the jury, bringing in their long experience as researchers. It was a huge honour to defend my thesis in front of you. Your exceptional careers and your innovative contributions to your respective fields are an important source of inspiration for me. I also thank you for the interesting discussions that we had before the defence at various conferences and meetings.

I am also indebted to Laurette Tuckerman, Juan Cruz Gonzalez Sembla, Benoit Semin, Eduardo Wesfreid, Olivier Dauchot, Arnaud Prigent, Grégoire Lemoult and Arthur Viallefont, who attended two ad hoc meetings at which I presented part of this work (and thank you, Yohann, for organising these meetings). With your sharp observations, you have given me an incredible opportunity to enrich my understanding of the subject and of my own work. I also thank Lukasz Klotz for interesting discussions on various occasions.

Next, I have to thank my fellow adventurers at DynFluid. To Alessandro F. for our deep intellectual connection which, working like gravity in a two-body problem, resulted in beautiful discussions, to Donato for your ironic and *Senecanian* attitude, to Simon for your efforts to create a cohesive group and for sharing with me the fear of non-divergence-free flow fields, to Ricardo for your passion, to Chloé for your broad cultural interests, to Erwan for enjoying the card games and to all the other young researchers whom I had the pleasure to meet, Gabriel H., Ziming, Yu, Thomas, Léo, Paul, Aurélien, Camille and Mateus. I also thank the permanent staff of the lab for the stimulating discussions during

lunch breaks, and I wish good luck to the new recruits, Gabriel D. and Baptiste.

I also thank Alessandro T., who, in some sense, will go down in history as my first student. Thank you for enduring my obsessive-compulsive control over your code and for illuminating my days with your wonderful, expansive personality.

When I left the south of Italy to go to Paris, I left behind some close friends who nevertheless managed to overcome the distance with their moral support. To Vito P., Vito B., Marco I., Marco B., Fabio T., Fabio B., Maurizio and Nicolas, for your historical and unwavering friendship and for all the unforgettable moments that we have lived together around our common hometown, Genzano. To Alessandro C. and Terry, for all the respect and affection you have always shown me, which I am happy to return. To Simone, for your calls at random times and for suggesting *scrip*.

Last but not least, I thank my family. Thank you for the support you provided during my studies, for the strong ethical values you instilled in me, and for all the questions you continue to ask about my work, even if my answers too often begin with "You will never understand...".

I also want to acknowledge the institutions. First of all, the Italian Ministry of University and Research, which funded my work and my stay in Paris with a Doctoral Scholarship. Then, I thank the two universities, Politecnico di Bari and Arts et Métiers Paris, for hosting me during my PhD studies and also before. Lastly, I thank the Grand Equipement National de Calcul Intensif (GENCI) in France for allowing me to burn a few million computational hours during these years.

Sincerely, thank you all.

Abstract

Turbulent flows are characterised by a marvellous phenomenology combining chaos and order, fluctuations on multiple scales and recurrent patterns named *coherent structures*. This thesis aims to elucidate certain physical processes involving coherent structures in the turbulent channel flow. Different numerical techniques are implemented towards this aim, with a common ground: investigate how coherent structures become unstable and, eventually, generate new coherent structures on different scales. This investigation is divided into three parts.

In the first part, the generation of extreme dissipation events is considered. Nonlinear optimal perturbations are computed with respect to a fully turbulent snapshot, and the dynamics induced by these perturbations are analysed and compared to the dynamics of naturally occurring extreme events, establishing a connection between the two. Interestingly, the nonlinear optimal perturbation works towards a destabilisation of near-wall *streaks*, suggesting that an instability of streaks is a possible cause of extreme events.

In the second part, the instability of streaks is addressed more directly but in a different direction. A linear stability analysis is performed on an array of periodic streaks to show that these structures undergo sub-harmonic or detuned instabilities with unstable modes characterised by large wavelengths (several times larger than the streak's wavelength). These instabilities are related to the large-scale motions (LSMs) observed in experiments and direct numerical simulations of high-Reynolds number flows.

In the third part, the large-scale linear instability of streaks is revisited at low Reynolds number in order to capture the wavelengths and the critical Reynolds number of the instability leading to laminar-turbulent patterns. The thesis concludes with the development of a nonlinear model for laminar-turbulent pattern formation. Ideas, limitations and possible directions to improve this model are tested and discussed.

Keywords: Instabilities, coherent structures, pattern formation, wall-bounded turbulence.

Contents

Chapter 1

Introduction

1.1 General Context

Most environmental processes and industrial applications involve turbulent flows. Some intrinsic characteristics of turbulent flows have important practical implications. On the one hand, enhanced diffusivity due to turbulent fluctuations can be desirable in certain situations. On the other hand, it is the main cause of aerodynamic drag on aeroplanes, of wall friction in channels and pipes and of power losses in turbomachinery. Consequently, scientists and engineers need to deal with the complex dynamics that turbulence entails and try to control it. However, the rich multiscale nature of these flows makes this task one of the toughest endeavours of current scientific research.

Turbulence is an open problem in many ways. A general mathematical theory based on the governing equations is lacking (Gallavotti, 2013). Physical theories encompass only a limited part of the phenomenology (Landau and Lifshitz, 1987; Frisch, 1995). The direct numerical simulation (DNS) approach is not viable in most applications. Turbulence research is an effort towards the solution of these problems with the idea that an improved general understanding of the phenomenon will point the way towards better reduced models and more effective control strategies.

This thesis is concerned with the particularly difficult case of wall-bounded turbulent flows. These flows are highly anisotropic and intrinsically multiscale (Jiménez, 2012). For this reason, scale interactions need to be studied carefully to improve the current understanding of the physical processes involved. In this thesis, we offer a new perspective on such scale interactions, modelling them as instabilities of coherent structures which engender new coherent structures on a different scale. While instabilities are often thought to produce smaller scales with respect to the base flow, in this work, it is shown that they can also produce larger scales, contributing to the production of large-scale coherent structures.

The subject of the thesis is the study of coherent structures and their multiscale dynamics in the turbulent channel flow. These mechanisms will be investigated first at moderately high Reynolds numbers (Re). Then, we will focus on the low Re regimes in which laminar and turbulent flow coexist. Different phenomena will be analysed with an innovative use of techniques which stem from the realm

of hydrodynamic stability theory. Before we start, however, a short review of the current state of the art on wall-bounded turbulent flows is required.

1.2 State of the Art

1.2.1 Wall-bounded turbulence

1.2.1.1 The self-sustaining process

Since the first experimental observations, wall-bounded turbulence has been characterised by the coherent structures that populate the flow. In particular, Kline et al. (1967) observed elongated low-momentum zones in turbulent boundary layers and introduced the term *streaks* to denote them (figure 1.1 (a)). These structures are localised near the wall and display a spanwise spacing of ≈ 100 wall units. One wall unit is the length scale obtained from the kinematic viscosity of the fluid and the mean wall shear stress. It is the characteristic scale of near-wall processes at all Re and in every turbulent wall-bounded flow.

Similar structures were also observed in the first direct numerical simulations of turbulent channel flow by Kim et al. (1987). Many other experimental and numerical studies reported observations about these structures (Robinson, 1991). Jiménez and Moin (1991) were able to isolate them using the concept of *minimal flow unit*, namely the smallest computational domain in which turbulence can be sustained. These authors performed several simulations of turbulent channel flow, gradually reducing the streamwise and spanwise size of the domain until the turbulent flow relaminarised. Interestingly, they noted that the minimal spanwise size is almost constant when expressed in wall units and corresponds to the spanwise size of the streaks (≈ 100 wall units). In contrast, the minimal streamwise size is between 300 and 600 wall units depending on Re. The concept of the minimal flow unit proved extremely useful to study the detailed dynamics of near-wall structures. Jiménez and Moin (1991) describe an intermittent bursting cycle in which the shear layer formed by the streak rolls up and generates streamwise vorticity, which in turn leads to the formation of a new streak.

This quasi-periodic dynamics was further examined in another seminal paper by Hamilton et al. (1995), who considered minimal flow units of turbulent Couette flow. These authors conjectured the existence of a *self-sustaining process* (SSP) involving three stages and analysed each of these stages separately. In the first stage, streaks are generated by streamwise vortices[1] through the lift-up effect. Through this mechanism, a strong streamwise perturbation is produced by a small wall-normal perturbation thanks to the amplification provided by the mean shear. The lift-up effect was first described by Ellingsen and Palm (1975) and Landahl (1980) and further studied in numerous other contexts, especially transition to turbulence (Brandt, 2014). Hamilton et al. (1995) demonstrated the importance of this mechanism in wall-bounded turbulence, showing that streamwise elongated streaks were produced in a simulation with frozen streamwise vortices. Streaks are amplified up to a saturation amplitude. Then, the second stage of the process consists of the breakdown of saturated

[1] Also termed *rolls* by some authors.

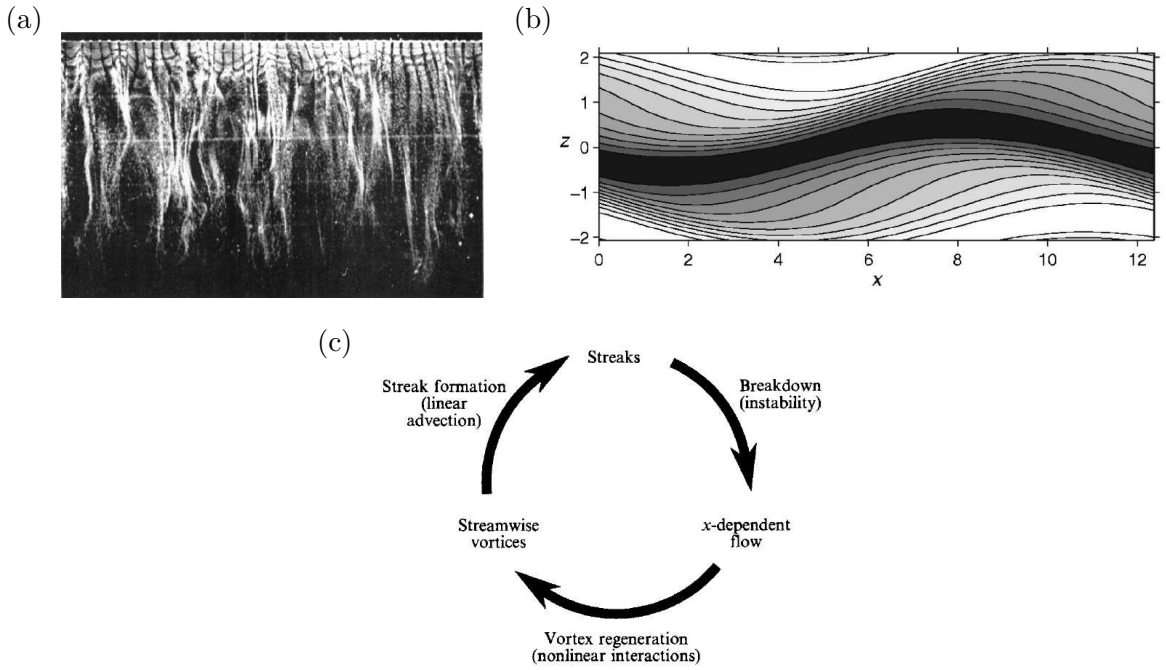

Figure 1.1: (a) Velocity streaks visualised in a turbulent flat plate boundary layer at ≈ 3 wall units from the wall (adapted from Kline et al. (1967)). (b) Contour of the streamwise velocity component of an exact travelling wave solution in plane Couette flow at $Re = 163.4$ (adapted from Waleffe (2003)). (c) Schematic illustration of the SSP (adapted from Hamilton et al. (1995)).

streaks through a modal instability. Hamilton et al. (1995) test this idea by perturbing a frozen streak field and showing that the perturbation increases exponentially. Finally, in the last stage, streamwise vortices are regenerated thanks to nonlinear interactions between the streak instability modes. Note that streak instability modes are characterised by a finite streamwise wavelength. The streamwise dependence of these modes makes the streak *wavy* (figure 1.1 (b)), making the SSP an inherently three-dimensional process. A schematic representation of the three-stage SSP is displayed in figure 1.1 (c). Certain aspects of this cycle were anticipated by Hall and Smith (1991) in their vortex-wave interaction theory.

Soon after, Waleffe (1997) used the physical insights provided in Hamilton et al. (1995) to formulate a reduced model of the SSP. In this study, the author introduces a free-slip wall-bounded flow driven by a sinusoidal forcing, the *Waleffe flow*. This flow is an idealised wall-bounded flow: it does not feature proper walls, but it has both the confinement effect due to the non-penetration condition at the vertical boundaries and the shear induced by the forcing. Importantly, the boundary conditions and the sinusoidal shape of the forcing allow a Galerkin decomposition of the flow based on Fourier modes. In this way, it is possible to retain only the modes which are essential to the existence of a non-laminar solution. At the end, Waleffe (1997) arrives at a four-equation model exhibiting a stable limit cycle. In the model, consistently with the SSP, the variable representing the streak instability produces a feedback on the variable representing the streamwise vortices (rolls).

Another corroboration of the SSP theory came from exact invariant solutions of the Navier-Stokes

(NS) equations: steady state equilibria, travelling waves and periodic orbits. The first non-trivial steady state solution was found by Nagata (1990) in Couette flow using continuation from steady solutions of Taylor-Couette flow. Other solutions were reported by Clever and Busse (1992, 1997). In a series of articles (Waleffe, 1998, 2001, 2003), Waleffe used different continuation strategies to find equilibria and travelling waves in Couette and channel flow, both with free-slip and no-slip wall conditions in minimal domains. The term *exact coherent structures* (ECS) was introduced in Waleffe (2003) to denote such solutions. Indeed, these solutions are always made up of a wavy streak combined with shorter streamwise vortices (figure 1.1 (b)). Therefore, they can be seen as "frozen" proxies of the SSP: the vortices sustain the streak, and the waviness of the streak feeds energy back to the vortices. Again, it is important to highlight that these solutions are inherently three-dimensional. Indeed, a purely two-dimensional (streamwise uniform) streak-roll system can not be sustained because no feedback is possible from transverse to streamwise velocity components. This is argued and demonstrated by Moffatt (1989).

In the following years, other ECS have been found in pipe flow, Couette flow and channel flow (Kawahara and Kida, 2001; Toh and Itano, 2003; Wedin and Kerswell, 2004; Faisst and Eckhardt, 2003; Gibson et al., 2008, 2009; Duguet et al., 2008). In general, they all feature wavy streaks and short-length streamwise vortices. Localised ECS have also been found (Schneider et al., 2010; Brand and Gibson, 2014; Zammert and Eckhardt, 2014, 2016; Paranjape et al., 2020), proving that the SSP can act as a local mechanism. This is relevant for transitional regimes, in which localised turbulence is observed (see Subsection 1.2.2). Related ECS have been found by Doohan et al. (2019) in a shear stress-driven flow. This model flow has been introduced by these authors as a minimal model of near-wall turbulence which does not depend on the Reynolds number.

Other numerical studies of the SSP corroborated its main features (*e.g.* Jiménez and Pinelli (1999)). However, the regeneration of streamwise vortices through streak instability and subsequent nonlinear interaction proved a little controversial. Schoppa and Hussain (2002) investigated in detail this aspect by performing DNS of turbulent channel flow. They performed linearised simulations of the perturbation around a streamwise-uniform streak, both with frozen and freely evolving base flow. With the frozen base flow, an exponential instability is observed if the streak is strong enough. However, in agreement with the argument of Moffatt (1989), the streak is rapidly dissipated when it is left free to evolve. Consequently, the perturbation is amplified only transiently in the linearised simulation with the freely evolving base flow. Moreover, these authors report that $\approx 80\%$ of near-wall streaks detected in their DNS have an insufficient amplitude to be unstable. Therefore, they conjecture that linear transient growth rather than modal instability is responsible for the regeneration of streamwise vortices (for an introduction to the concepts of modal instability and transient growth, see Schmid and Henningson (2012)). Moreover, they point out that purely nonlinear mechanisms may also be responsible for the feedback of energy from the streak to the vortices. All these mechanisms involve the interaction of a sinuous streamwise-dependent perturbation with the spanwise shear-layer produced by the streak. This point of view has been supported by Cossu et al. (2011), who found different streak breakdown scenarios for different amplitudes of the streak and different amplitudes of the sinuous perturbation. More recently, Lozano-Durán et al. (2021) and Oxley and Kerswell (2025) supported the transient growth scenario based on the push-over mechanism, *i.e.* the transient amplification of a

spanwise velocity perturbation induced by the spanwise gradient of the streak field.

Furthermore, Cassinelli et al. (2017) and de Giovanetti et al. (2017) have retrieved the perturbations inducing streak breakdown in the channel flow using Dynamic Mode Decomposition (DMD). They have found that the leading DMD modes have a sinuous structure and other characteristics reminiscent of the streak modal instability. Moreover, Liu et al. (2024) have recently supported the relation between streak waviness and vortex regeneration using PIV measurements of Couette-Poiseuille flow.

1.2.1.2 High$-Re$ effects

The most relevant definition of Re in wall-bounded flows is the friction Reynolds number, based on the channel half-gap h^* (or, equivalently, the pipe radius, the boundary layer thickness, etc...) and the friction velocity $u_\tau^* = \sqrt{\tau_w^*/\rho^*}$: $Re_\tau = u_\tau^* h^*/\nu^*$, where ν^* is the kinematic viscosity of the fluid, ρ^* the density and τ_w^* the mean wall shear stress[2]. The importance of this adimensional ratio stems from the fact that it represents the ratio between two length scales: the channel half-gap h^*, which is the maximum size turbulent eddies can achieve in these flows, and the viscous length (or wall unit) $\delta_\nu^* = \nu^*/u_\tau^*$. Near-wall structures (like the streaks observed by Kline et al. (1967)) have a size proportional to this length, whereas the largest eddies of the flow have a size proportional to the macrosopic length (channel half-gap, pipe radius, etc...). Classical studies on the SSP and ECS are performed at $Re_\tau \lessapprox 300$. At these Reynolds numbers, the separation between the two length scales is moderate. Moreover, the limited size of minimal flow units further constrains the size achievable by turbulent eddies. Therefore, the classical SSP represents a one-scale process.

As Re is increased, the shear becomes more localised near the wall, and the two characteristic length scales of the flow differ by several orders of magnitude. As a consequence, the flow becomes populated by self-similar eddies developing on a wide range of scales (Townsend, 1976). These self-similar eddies form the logarithmic layer of wall-bounded turbulent flows. For increasing Reynolds number, the contribution of the logarithmic layer to the total turbulence production becomes increasingly important (Smits et al., 2011). For this reason, most of the literature on high$-Re$ wall-bounded flows focuses on these self-similar structures.

By the end of the nineties, several experimental studies had described structures characterised by larger scales with respect to the streaks involved in the near-wall SSP. Kim and Adrian (1999) performed experiments on the turbulent pipe flow and reported the presence of structures having streamwise length between 12 and 14 times the pipe radius. The taxonomy of such structures in the pipe was improved by the work of Guala et al. (2006), who made a distinction between very-large-scale motions (VLSMs), having streamwise size between 8 and 16 pipe radii, and large-scale motions (LSMs), having streamwise length of 2-3 pipe radii. Balakumar and Adrian (2007) extended these results to turbulent channels and zero-pressure-gradient boundary layers. Balakumar and Adrian (2007) observed that boundary layer flows typically have shorter VLSMs with respect to channels and pipes. Similar remarks on the structural differences between LSMs and VLSMs in turbulent pipe, channel and boundary layer flows were made by Monty et al. (2007, 2009). Both Guala et al. (2006)

[2]Here, for consistency with the rest of the manuscript, an asterisk is used to denote dimensional quantities.

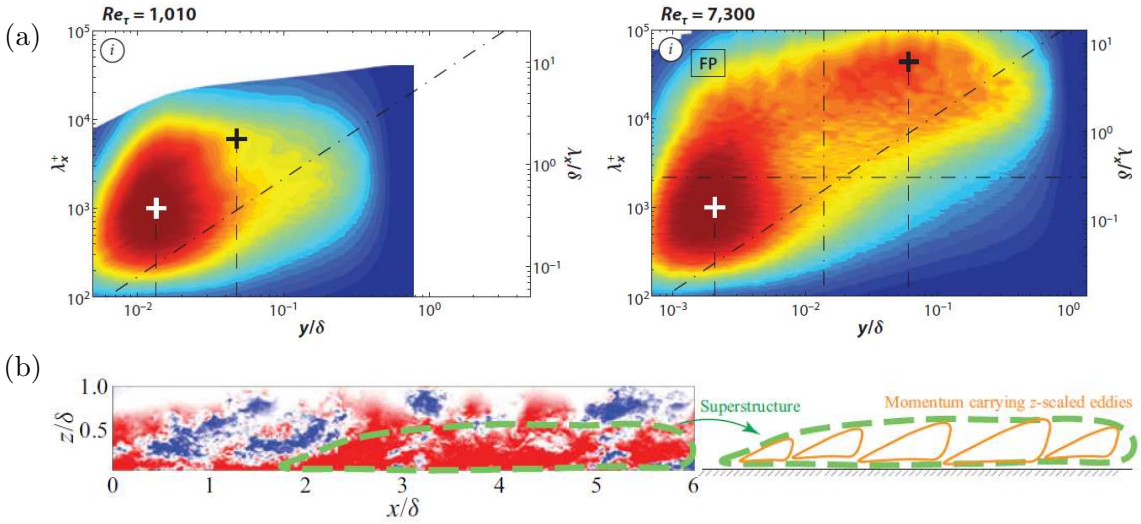

Figure 1.2: (a) Contours of one-dimensional premultiplied spectra as a function of streamwise wavenumber and wall-normal position for a turbulent boundary layer at two Reynolds numbers (adapted from Smits et al. (2011)). An inner and an outer peak are noted at the higher Reynolds number. (b) Contours of instantaneous streamwise velocity fluctuations in a turbulent boundary layer at $Re_\tau \approx 2000$ and conceptual representation of a superstructure (adapted from Deshpande et al. (2023)).

and Balakumar and Adrian (2007) show that LSMs and VLSMs carry a large fraction of the turbulent kinetic energy (TKE) and most of the turbulent shear stress. As a consequence, they are the main responsible for wall friction drag (Abe et al., 2004; de Giovanetti et al., 2016).

Simultaneously, the experimental work of Hutchins and Marusic (2007) on turbulent boundary layers showed that, at large Re ($Re_\tau \gtrsim 5000$), there are two well-separated peaks in the pre-multiplied streamwise fluctuation spectrum (figure 1.2 (a)). The *inner* peak is localised near the wall and associated with the near-wall SSP and an *outer* peak which appears only at high Re. These authors introduce the term *superstructures* to denote the motions associated with the outer peak. Figure 1.2 (b) shows a superstructure in a recent experiment on turbulent boundary layers (Deshpande et al., 2023). In principle, superstructures should correspond to VLSMs. We note that the double-peaked spectrum was observed only recently in numerical simulations of turbulent channel (Lee and Moser, 2015; Hoyas et al., 2022), due to the high computational cost of DNS at such high Re.

Furthermore, consistently with the attached eddy theory of Townsend (1976), LSMs extend to the wall and influence the near-wall region. Hutchins and Marusic (2007) report the existence of a footprint of the large-scale structure near the wall. Moreover, Hutchins and Marusic (2007) and Mathis et al. (2009) describe a modulation effect that large-scale structures exert on near-wall fluctuations. This effect is the result of nonlinear interactions (Andreolli et al., 2023).

Large-scale structures are affected by the presence of the walls. Experiments in zero-pressure-gradient boundary layers (Vincenti et al., 2013) and turbulent pipes (Vallikivi et al., 2015) showed that the wall-normal location of the peak at large wavelength of the pre-multiplied streamwise fluctuation spectrum scales with the square root of the friction Reynolds number. As argued by Hwang (2016),

this means that viscous effects are non-negligible even at large wavelengths.

1.2.1.3 Multiscale dynamics

Given their important role in high$-Re$ wall turbulence, it is important to understand the origin of large-scale structures. In the first experimental studies (Kim and Adrian, 1999; Adrian et al., 2000; Adrian, 2007), it was conjectured that such structures are the result of the concatenation of smaller structures and subsequent vortex reconnection. The concatenation hypothesis has been further underpinned by Lee and Sung (2011) and Dennis and Nickels (2011) in boundary layers and by Baltzer et al. (2013) in turbulent pipes. More recently, it was supported by Lee et al. (2019) and Deshpande et al. (2023), who analysed, respectively, DNS data of pipe flow and experimental measurements of turbulent boundary layers. The conceptual representation of a VLSM as a concatenation of smaller structures proposed by Deshpande et al. (2023) is reproduced in figure 1.2 (b). This hypothesis, however, was questioned by Mizuno and Jiménez (2013), who showed that LSMs exist even without a wall, and Zhou et al. (2022), who showed that the merging of near-wall streaks is weakly correlated with LSMs.

An important development was the contribution of Hwang and Cossu (2010c). These authors performed large eddy simulations (LES) of turbulent channel flow at $Re_\tau = 550$ using a Smagorinsky eddy viscosity model for the subgrid scale fluctuations. They progressively increased the Smagorinsky constant, thereby augmenting the dissipation provided by the model. In this way, all the small-scale fluctuations were progressively filtered out, and the dynamics of the large-scale motions were isolated. The remarkable result is that, even if all the small scales are heavily damped, the dynamics of the LSMs are almost unaffected and, in particular, LSMs are always sustained in the over-damped flow. In conclusion, LSMs do not need smaller-scale fluctuations to "survive", as they can be directly amplified by the mean shear. Hwang and Cossu (2010c) remark that the isolated LSMs seem to undergo a self-sustaining cycle similar to the SSP of near-wall structures.

These results have been extended to higher Re ($Re_\tau = 1000$) and different domain sizes in Hwang and Cossu (2011), where the same authors were able to isolate different LSMs and their SSP at different scales. It was shown in this paper that these motions correspond to the self-similar eddies constituting the logarithmic layer of the turbulent channel flow. In light of these results, the authors postulate a hierarchy of self-similar SSP which act independently of each other at different scales. This hypothesis represents a multiscale extension of the SSP classic theory.

In subsequent studies, Hwang (2013, 2015) and Hwang and Bengana (2016) have investigated the dynamics of isolated attached eddies (still using overdamped LES) stressing the self-similarity of these structures near the wall (figure 1.3 (a)), their contribution to the wall shear stress and the various elements that consitute the SSP. In particular, Hwang (2015) compares the isolated attached eddies to the theoretical predictions of Townsend (1976). Figure 1.3 (b) shows the streamwise velocity streak of one of the isolated attached eddies. The author also comments on the role of the lift-up mechanisms in generating the streaks, pointing out how, in linear theories, vortices and streaks do not coexist (the vortices generate the streaks transiently and then die out), whereas, in the nonlinear dynamics, both vortices and streaks seem to coexist, such that streaks are continuously forced by the vortices.

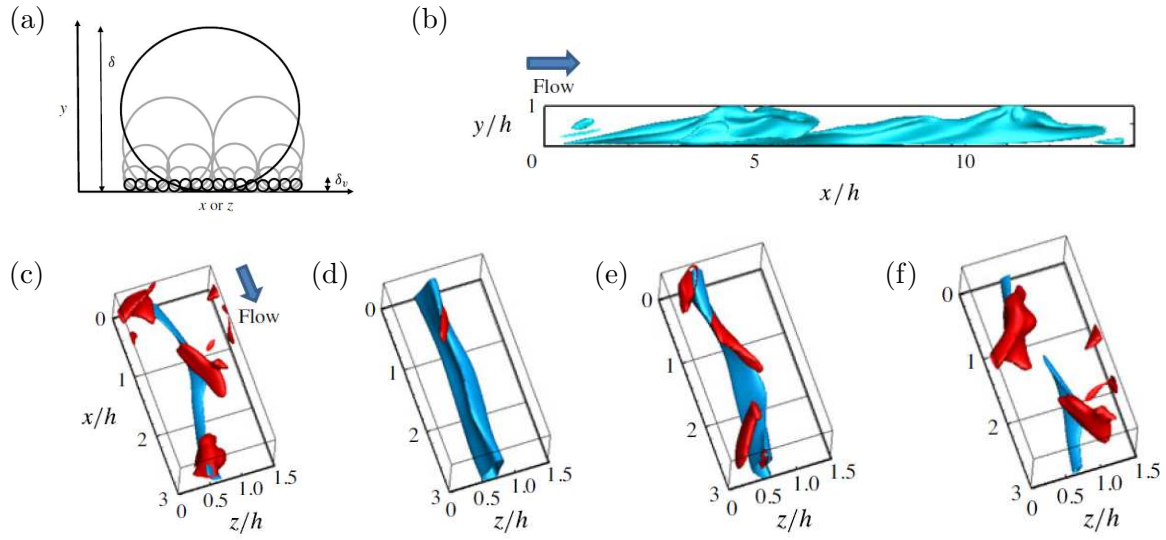

Figure 1.3: (a) Conceptual representation of self-similar attached eddies (Hwang, 2015). (b) Isosurface of negative streamwise velocity fluctuation of a self-sustained large-scale attached eddy at $Re_\tau = 950$ (adapted from Hwang (2015)). (c-f) Visualisations of the various SSP steps of an isolated attached eddy at $Re_\tau = 950$. The blue and red isosurfaces denote, respectively, a negative streamwise velocity fluctuation and a positive wall-normal velocity fluctuation (adapted from Hwang and Bengana (2016)).

As we will see in the following chapters, this fact implies that, in linear models of wall turbulence, the vortices must be modelled as a steady "external" forcing (external because the nonlinearity does not belong to a linear model). Hwang and Bengana (2016) measured the characteristic time scales of the process using temporal auto- and cross-correlations of the velocity components. Importantly, the temporal correlation curves are superposed when the time is scaled with the spanwise size of the isolated structure and the friction velocity. This supports the theory of self-similar SSP at all scales (figure 1.3 (c)).

As for the near-wall SSP, further evidence for the multiscale SSP came from invariant solutions of the NS (and LES) equations (multiscale ECS). Rawat et al. (2015) and Hwang et al. (2016) compute such solutions (equilibria and travelling waves) in, respectively, Couette and channel flow using the overdamped LES system. Then, they perform continuation with respect to the damping parameter and, in some cases, they find exact solutions of the NS equations. These ECS feature wavy streaks and short vortices as the isolated attached eddies of the previously mentioned studies. Additional self-similar travelling waves are reported by Yang et al. (2019). Doohan et al. (2022) employed their shear-stress-driven flow model to search for two-scale ECS. The presence of only two scales in their model flow is imposed by the choice of the computational box lengths. However, the travelling waves that they have identified are characterised only by one prominent wavelength. The authors argue that a purely two-scale solution would be characterised by two different time scales and, therefore, should be a periodic orbit or a quasi-periodic solution. Nevertheless, they find an interesting small-scale travelling wave solution that consistently feeds energy to the larger scale through a sub-harmonic streak instability.

Another group of numerical studies have tried to elucidate inter-scale interactions. Jiménez and Simens (2001) performed DNS of turbulent channel flow both in minimal domains and in longer domains, damping the fluctuations at the channel centre. When the domains are minimal and the damping acts on a large part of the channel bulk, they observe travelling waves. As the domain size is increased and the damping region reduced, the dynamics become more complex (two-frequency torus, intermittent bursting and finally chaotic dynamics). This behaviour is explained by suggesting that the streaks emit vorticity towards the channel centre, which then comes back to perturb the streaks. This inner-outer interaction is probably the first example of *bottom-up* interaction in the literature. A similar mechanism is described in Jiménez et al. (2005), who speculate that *bursts*[3] in the buffer layer can generate LSMs in the logarithmic layer. The study of Toh and Itano (2005) investigates this bottom-up mechanism more explicitly with DNS of turbulent channel flow at moderate Re ($Re_\tau = 137$ and $Re_\tau = 349$) in a domain wider than minimal flow units. They find that conglomerations of near-wall streaks correspond to large-scale structures farther from the wall. Therefore, they conjecture the existence of a co-supporting cycle that involves LSMs and near-wall streaks. However, the evidence brought forward in this study is limited in several aspects: (i) the considered Re are quite low with respect to other observations of LSMs and, as a consequence, the computational domains are only slightly larger than minimal flow units; (ii) no causal relation is established between the formation of LSMs and the observed conglomerations of near-wall streaks. The fact that LSMs and conglomerations of near-wall streaks are correlated may simply be due to the modulation effect that LSMs exert on the wall (Mathis et al., 2009) and, therefore, does not automatically imply that LSMs are generated by near-wall streaks. In this thesis, we will try to establish this lacking causal relation, showing that near-wall streaks can lead to an amplification of LSMs through an instability.

Instabilities of large-scale streaks have been investigated by Park et al. (2011). Large-scale streaks are computed using the two-dimensional Reynolds-Averaged Navier-Stokes equations (RANS) containing the Cess (1958) eddy viscosity. Streamwise uniform streaks are computed using an optimal initial condition[4]. The modal linear stability of *frozen* saturated streaks is investigated. Park et al. (2011) find that the streaks become unstable if their amplitude is sufficiently high, with the unstable mode having a streamwise wavelength compatible with LSMs. These results have been extended to higher Re by Alizard (2015). Interestingly, he found self-similar unstable modes varying the spanwise wavelength of the base flow streaks. Both Park et al. (2011) and Alizard (2015) focus only on fundamental instabilities, *i.e.* they consider only perturbations which have the same fundamental wavelength as the base flow. Therefore, their eigenmodes have the same spanwise wavelength as the base flow streaks and a smaller streamwise wavelength (which is infinite for their streaks and finite for the eigenmode). This type of instability can be seen as a step of the multiscale SSP (Hwang and Cossu, 2010c, 2011). Indeed, the self-similar attached eddies isolated by Hwang (2013, 2015) and Hwang and Bengana (2016) feature vortices that are shorter than the streak. Therefore, an instability that breaks the streak in smaller vortices is coherent with the SSP of these structures.

[3] See the next subsection for an explication of this term.

[4] It is known from the studies on transient growth and nonmodal transition to turbulence that streaks are generated by initial conditions that maximise the perturbation kinetic energy at a given finite time. Therefore, streaks can be computed by formulating a variational problem, see *e.g.* Butler and Farrell (1992).

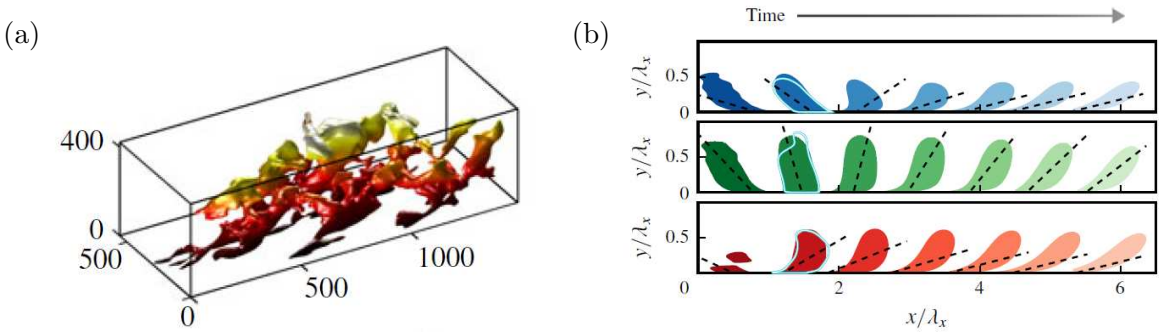

Figure 1.4: (a) Instantaneous visualisation of an attached ejection event (axes are scaled in wall units, and the colour denotes the distance from the wall, adapted from Lozano-Durán et al. (2012)). (b) Conceptual evolution of an Orr's burst for the streamwise, wall-normal and spanwise velocity components (from top to bottom). Adapted from Encinar and Jiménez (2020).

The recent works of Doohan et al. (2021, 2022) in the shear-stress-driven flow model suggest a different mechanism (*feeding*) that resembles the bottom-up scenario. As mentioned before, this model flow is characterised by two scales imposed by the computational box size. It is found that energy is driven from the smaller to the larger scale through a sub-harmonic streak instability. This finding suggests that an extension of the results of Park et al. (2011) and Alizard (2015) to sub-harmonic instabilities is needed.

Other recent works have used fully nonlinear analyses to investigate multiscale interactions. For example, Cho et al. (2018) have performed a spectral energy transfer analysis of LES data at $Re_\tau = 1672$ using spanwise wavelengths to distinguish between small scales and large scales. Among the several important findings of this study, the authors discuss the importance of the pressure strain term to close the SSP and report a consistent transfer of energy from small scales to large scales in the wall region. Lee and Moser (2019), performed a more comprehensive spectral analysis involving both streamwise and spanwise wavelengths, using their DNS data at $Re_\tau = 5200$. They also stress the importance of the pressure strain term in transferring energy from the streamwise to the transverse velocity components and confirm, in part, the transfer of energy from small to large scales near the wall.

1.2.1.4 Bursts and optimal perturbations

Kim et al. (1971) have introduced the term *bursts* to denote the intermittent events associated with an instantaneous high production of Reynolds shear stress. If u' is the streamwise velocity fluctuation and v' the wall-normal velocity fluctuation, the Reynolds shear stress in typical wall-bounded flows is given by the long-time average $\overline{u'v'}$. Wallace et al. (1972) introduced the *quadrant analysis* to investigate the production of Reynolds shear stress, which consists of plotting the joint probability density function of u' and v'. Using this analysis, they were able to identify two types of events that contribute to $\overline{u'v'}$: the *sweeps* characterized by $u' > 0$ and $v' < 0$ and the *ejections* characterized by $u' < 0$ and $v' > 0$. Further experimental evidence of the intermittent nature of the Reynolds shear stress has been provided by Willmarth and Lu (1972) and Lu and Willmarth (1973). There has been

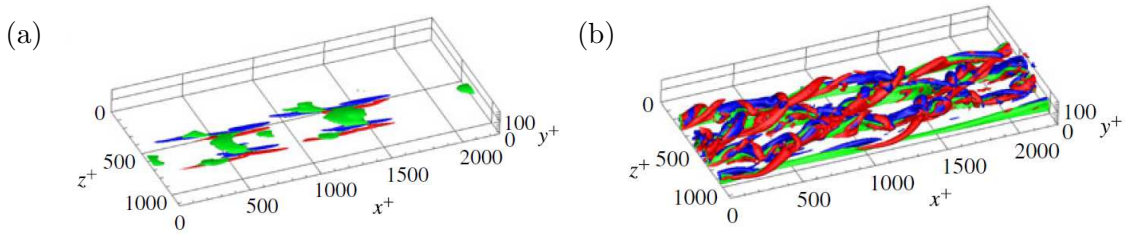

Figure 1.5: Nonlinear optimal perturbation of the turbulent channel flow (with respect to the mean flow) at $Re_\tau = 180$ at (a) initial and (b) target time $T^+ = 305$. Isosurfaces of negative streamwise velocity (green) and of the Q criterion (blue/red for positive/negative streamwise vorticity). Adapted from Farano et al. (2017).

some controversy about the meaning of the term bursts, as the one-point measurements of these early experiments are consistent with permanently advecting objects which are not intermittent in time. Recent advances in numerical simulations have lifted this ambiguity and, nowadays, the term denotes intermittent events that are localised both in time and in space (Jiménez, 2013).

Bursts have been investigated in DNS of turbulent channel flow by Flores and Jiménez (2010) and Lozano-Durán et al. (2012). In particular, Lozano-Durán et al. (2012) have used a percolation analysis to isolate eddies that are associated with intense production of the Reynolds shear stress. They have found that self-similar attached eddies carry a significant part of the Reynolds stress (figure 1.4 (a)). Detached eddies are also identified at the channel centre, but their global contribution to the Reynolds shear stress is negligible. These detached eddies form a background turbulence which could be interpreted as a byproduct of other dynamical processes. More recently, shear stress bursts in the turbulent channel flow have been the object of causal analyses. Jiménez (2023) used the Perron-Frobenius operator to isolate the conditionally averaged dynamics of these events and investigate their regeneration cycle. He finds that the bursts are generated after a phase of low wall shear. Osawa and Jiménez (2024) have performed interventional experiments by realising a huge amount of slightly perturbed simulations. They find that the perturbation is causally *significant* if it is localised over a sweep, whereas perturbations of ejections are classified as causally *irrelevant*.
A different type of intermittent events was investigated by Hack and Schmidt (2021), who focused on instantaneous dissipation. They have isolated the structures correlated with highly dissipative events using a Conditional Space-Time POD (Schmidt and Schmid, 2019) on a DNS dataset of turbulent channel flow at $Re_\tau = 2000$. They report that these events are associated with strong gradients forming at the interface between two opposite-sign velocity structures.

The dynamics of bursts have been linked both to linear and nonlinear optimal perturbations. Jiménez (2013, 2015) have associated the bursts with the transient dynamics of the linear Orr's mechanism (Orr, 1907). Encinar and Jiménez (2020) have substantiated this theory by looking for Orr-like bursts in turbulent channel flow DNS data using wavelet-based filters (figure 1.4 (b)). Bursts have also been linked to nonlinear optimal perturbations (NLOPs). These perturbations have been introduced in the context of subcritical transition to turbulence (Pringle and Kerswell, 2010; Cherubini et al., 2010, 2011; Monokrousos et al., 2011; Pringle et al., 2012; Duguet et al., 2013; Cherubini and De Palma, 2015; Cherubini et al., 2015) and are computed using a direct-adjoint looping technique

(see section 2.4). For a given initial energy, these perturbations lead to the maximisation of an integral observable (global kinetic energy or dissipation) in a given target time. Cherubini and De Palma (2013) have computed NLOPs in laminar Couette flow and, varying the target time and the initial energy, they have found that some perturbations lead to highly dissipative paths and resemble the bursts observed in turbulent flows. These results have been extended to the channel flow by Farano et al. (2015, 2016). Moreover, to link more explicitly NLOPs to turbulent bursts, Farano et al. (2017, 2018) have computed NLOPs with respect to the turbulent channel mean profile (figure 1.5). They have compared the Reynolds stress statistics of the NLOPs with those of DNS using quadrant analysis and pre-multiplied spectra, and they concluded that the dynamics of the NLOPs are representative of typical bursting events in turbulent channel flow DNS. One of the objectives of this thesis is to extend the results of Farano et al. (2017), aiming at a more direct comparison with the structures extracted from DNS (see section 1.3).

1.2.2 Laminar-turbulent pattern formation

This section is an introduction to the phenomenology and related theories of wall-bounded plane shear flows in transitional regimes. This is the topic of the last part of the thesis (Chapters 5 and 6). Fundamental concepts of subcritical transition are introduced with a short description of transitional pipe flow (Eckhardt et al., 2007; Avila et al., 2023). Then, the phenomenology of transitional plane shear flows is presented (Tuckerman et al., 2020). Lastly, the theoretical efforts to explain these phenomena are summarised. Currently, these theoretical efforts follow two main directions: directed percolation theory and linear instability theory. These theories stem from two different points of view. Directed percolation theory considers that localised turbulence arises from fully laminar flow (the critical point is between laminar and laminar-turbulent flow). Linear instability theory considers that the laminar-turbulent patterns arise from fully turbulent flow (the critical point is between turbulent and laminar-turbulent flow). The two are not necessarily in contrast.

1.2.2.1 Subcritical transition - the case of pipe flow

Since the seminal experiments of Reynolds (1883), the transition to turbulence of the parabolic flow in a circular pipe has been an open problem for fluid dynamics. As it is well known, Reynolds (1883) observed the dispersion of a scalar tracer injected in the flow. He understood that the behaviour of the flow was uniquely determined by an adimensional control parameter formed with the bulk velocity of the pipe, the pipe diameter and the viscosity of the fluid. This parameter was termed in his honour the *Reynolds number* Re, which we have introduced before. Varying this parameter, Reynolds identified a regime of stable laminar motion at low Re, a regime of chaotic fully turbulent motion at high Re and, for intermediate values of Re, a *transitional* regime characterised by intermittent turbulent regions surrounded by laminar flow that he called *flashes*. The transitional regime was further studied experimentally in the 20th century by Lindgren (1969), Wygnanski and Champagne (1973) and Wygnanski et al. (1975) who classified intermittent turbulent regions in two categories: the *puffs* are short arrow-like turbulent structures which are triggered at some point in the flow and then

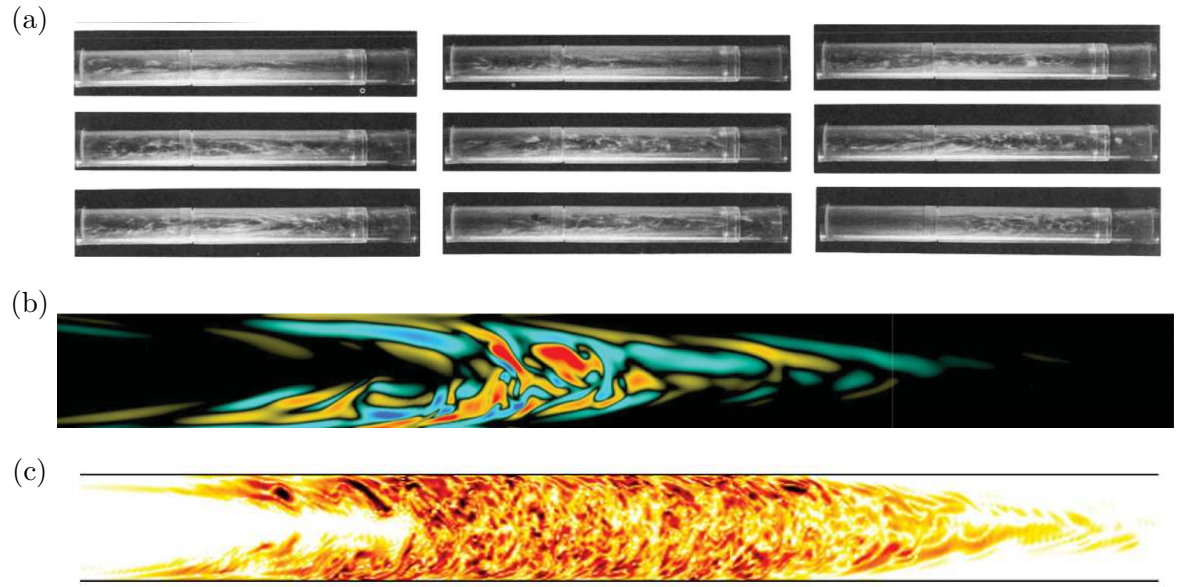

Figure 1.6: (a) Experimental visualisations of an equilibrium puff at $Re = 2200$ from Darbyshire and Mullin (1995). (b) Contours of the axial vorticity field of a puff computed using an edge-tracking algorithm at $Re = 2000$ (adapted from Duguet et al. (2010b)). (c) Contours of the axial vorticity field of a slug at $Re = 3000$ (DNS, adapted from Duguet et al. (2010b)).

advected downstream (figure 1.6 (a) and (b)); the *slugs* are longer turbulent regions which feature a sharp upstream end and a smooth or sharp downstream end according to the regime (figure 1.6 (c)). The puffs were described as equilibrium structures in these early experiments, but, as we will see, they can actually split or decay. Slugs are expanding structures that tend to fill the pipe with turbulent flow while they are advected downstream. Since these early experiments, it was clear that the shear near the upstream edge of a puff or slug is instrumental for the turbulence production that sustains the structure. For example, Bandyopadhyay (1986) describes the roll-up of vortices near the upstream edge of puffs and how these *entrain* laminar flow, feeding energy to the turbulent dissipation inside the puff.

The major theoretical problem with these observations was that the laminar flow in a circular pipe is linearly stable at all Re (Salwen et al., 1980; Meseguer and Trefethen, 2003). Therefore, the transition to turbulence is due to the amplification of finite amplitude disturbances. This type of transition is termed *subcritical* because the flow becomes turbulent for values of Re lower than the critical one. In the case of the pipe, the critical value is infinite, so the transition is always subcritical. Other shear flows, such as the channel flow or boundary layer flows, have a finite critical Re at which the laminar flow becomes linearly unstable, but they can still undergo a subcritical transition at Re lower than the critical values. Darbyshire and Mullin (1995) and Hof et al. (2003) investigated this problem, performing experiments in which the laminar flow was impulsively perturbed. Looking for critical disturbance amplitudes beyond which turbulence is triggered and sustained, Darbyshire and Mullin (1995) tried to plot a critical curve in the amplitude$-Re$ plane, but the data showed a significant scatter. The idea of a critical disturbance amplitude was undermined by Faisst and Eckhardt (2004).

These authors performed simulations of periodic pipe flow for $Re < 2300$ using a synthetic disturbance as a trigger. They found that eventually all perturbations decay. Some decay almost immediately, others after a long turbulent transient. Importantly, they found that the turbulence lifetime does not increase monotonically with the disturbance amplitude but, rather, oscillates abruptly with this parameter. These findings led them to conjecture that the turbulent attractor is a chaotic saddle at the considered values of Re (Eckhardt et al., 2007) and that the edge between rapidly decaying initial conditions and long-lived turbulent transients has a fractal nature, which prevents any definition of a critical amplitude. After these developments, research focused on turbulence lifetimes and the critical Re beyond which the turbulent flow is indefinitely sustained. It was shown that turbulence lifetimes are exponentially distributed and that the characteristic time-scale extracted from the distribution fit increases with Re. Peixinho and Mullin (2006) and Willis and Kerswell (2007) measured these characteristic lifetimes using, respectively, experiments and DNS data and conjectured the existence of a finite value of Re at which the turbulence lifetime diverges. This would represent a critical Re for the onset of turbulence in pipe flow. In contrast, Hof et al. (2006, 2008) showed that the turbulence characteristic lifetime increases super-exponentially with Re but never diverges at finite Re. Therefore, they argued that there is no critical Re for transition in pipe flow. This super-exponential scaling of turbulence lifetime was confirmed with DNS by Avila et al. (2010) and theoretically corroborated by Goldenfeld et al. (2010). All these investigations concern the decay of a single puff.

In the meantime, a new series of phenomenological studies was performed by several groups. Nishi et al. (2008) have performed experiments of puffs and observed that they eventually split, forming new puffs. Shimizu and Kida (2009) and Duguet et al. (2010b) have investigated the dynamics of puffs and slugs using numerical simulations and edge state computations (Skufca et al., 2006; Schneider et al., 2007) and van Doorne and Westerweel (2009) and Hof et al. (2010) performed further experiments. All these authors stressed the importance of the instabilities which are generated at the upstream end of puffs.

Moxey and Barkley (2010) were the first to identify a regime in which several puffs randomly split and decay, but turbulence is globally sustained. This key idea was developed by Avila et al. (2011), who showed that the characteristic time scale of puff splitting decreases with Re, while the characteristic lifetime of puff decay increases with Re (as was already known). Therefore, the two time scales will cross over at a well-defined Re, which can be considered the critical Re for sustained turbulence in pipe flow. This solved a long-standing problem of fluid mechanics.

Another important idea about the dynamics of puffs and slugs was introduced by Barkley (2011a), who linked these phenomena to *excitable media* (Winfree, 1991; Barkley, 1991) through a phenomenological analogy. The author proposes a stochastic two-equation model that is able to reproduce the formation of puffs and slugs, their decay and splitting statistics and their interaction dynamics (Samanta et al., 2011; Barkley et al., 2015). Barkley (2016) discussed in more detail the principles underlying the model and the dynamics of fronts. Comparisons with DNS measurements of front advection speeds reported by Holzner et al. (2013) and Song et al. (2017) are also made. Interestingly, this pipe flow model has prompted new statistical analyses of transitional pipe flow (Nemoto and Alexakis, 2018; Rolland, 2018).

There are important lessons to be learned from these developments in the case of pipe flow. The first one is that the transition in shear flows is a complex mix of nonlinear phenomena. The second one is that localised patches of turbulence at very low Re can split or decay, and that the time scales of these two mechanisms determine whether turbulence is sustained or not. We will see that similar arguments have been used for plane shear flows. The last one is that a phenomenological model, which can reproduce the fundamental behaviour of the system, can be useful to improve the theoretical understanding of the problem and test new ideas.

1.2.2.2 Phenomenology of patterns in shear flows

Coexistence of laminar and turbulent regions characterises the transition of other wall-bounded shear flows as well. The first observations of this phenomenon were made by Coles and Van Atta (1966) in Taylor-Couette flow (the flow between two rotating cylinders). They found a regime of counter-rotating cylinders featuring a spiral of turbulent flow (*spiral turbulence*). The visualisation of their turbulent spiral is reproduced in figure 1.7 (a). Already in this early experimental study, the presence of a large-scale flow at the interface between laminar and turbulent regions was highlighted. The existence of this spiral turbulence regime was confirmed at different radius ratios (the ratio between the inner and the outer radius) and aspect ratios (the ratio between the cylinders' length and gap) by later experimental studies (Andereck et al., 1986; Hegseth et al., 1989; Goharzadeh and Mutabazi, 2001), which also investigated the transition between adjacent regimes.

In the meantime, a series of experiments on the transition to turbulence in plane Couette flow were performed by the CEA Saclay group (Daviaud et al., 1992; Bottin et al., 1997, 1998; Bottin and Chaté, 1998). In these experiments, turbulent spots are triggered by using finite-amplitude localised perturbations. It is observed that if Re is beyond a certain threshold, the spot spreads and a heterogeneous mix of turbulent and laminar flow fills the experimental domain. This coexistence of laminar and turbulent flow is related in these studies to a similar phenomenology observed in numerical simulation of map-lattice models (Kaneko, 1985) and Kuramoto-Sivashinsky equation (Chaté and Manneville, 1987), and is termed *spatio-temporal intermittency*.

Plane Couette flow can be obtained from Taylor-Couette flow in the limit of the radius ratio approaching one. As such, it can be expected that the turbulent spiral in Taylor-Couette flow and spatio-temporal intermittency in plane Couette flow are related phenomena, with differences arising from curvature effects. Prigent et al. (2002, 2003) studied the two flows experimentally and showed that the same oblique pattern of turbulent bands characterises the transitional regimes of both (see figure 1.7 (b) for a visualisation of the pattern in plane Couette flow). To investigate how the patterned regime arises from uniform turbulence, they employed experimental observations to tune the parameters of a Ginzburg-Landau model with noise. Accordingly, they postulate that the pattern arises through a linear instability of the uniform turbulent flow.

Up to this point, patterns were numerically simulated only using simple models like the Ginzburg-Landau equation or map-lattice models. The first Navier-Stokes DNS of laminar-turbulent patterns appeared in the early 2000s. One of the reasons is that most of the DNS of shear flows at the time focused on minimal flow units, as we have seen in previous sections, whereas large domains are required

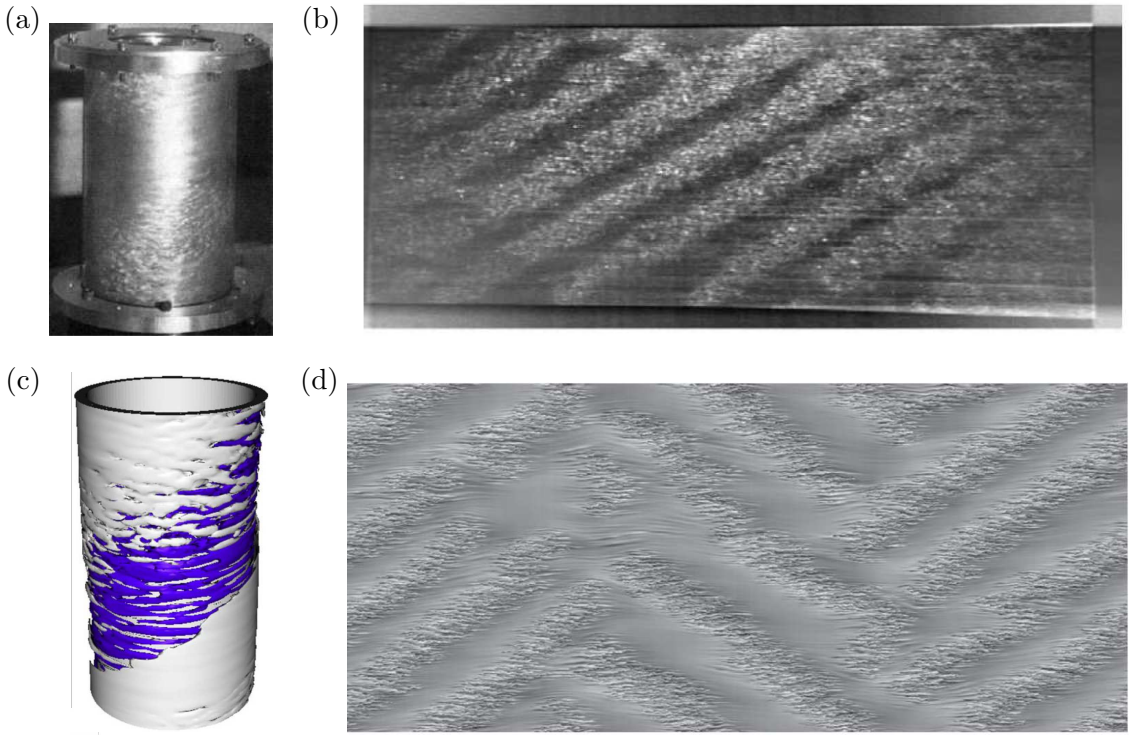

Figure 1.7: Laminar-turbulent patterns in shear flows. (a) Early experimental visualisation in Taylor-Couette flow of spiral turbulence by Coles and Van Atta (1966). (b) Experimental visualisation of patterns in plane Couette flow by Prigent et al. (2002). (c) DNS of spiral turbulence by Meseguer et al. (2009). (d) DNS of oblique patterns in plane Couette flow by Duguet et al. (2010a).

to observe the patterns. Barkley and Tuckerman (2005) performed the first DNS of laminar-turbulent patterns in plane Couette flow, introducing the concept of *minimal band unit*. They consider a domain which is inclined with respect to the streamwise direction of an angle θ which is chosen to match the angle of inclination of the turbulent bands. In this way, the spanwise direction of the *tilted* domain corresponds to the direction perpendicular to the turbulent band (figure 1.8). They consider a domain which is wide in the spanwise direction (to accommodate the pattern wavelength) and relatively short in the (tilted) streamwise direction (to accommodate the size of turbulent streaks and vortices). Varying Re, three different regimes were identified between the laminar and fully turbulent regimes: isolated band, periodic pattern and an intermittent regime which features laminar holes without a clear periodicity. The analysis of the patterned regime was further developed in Barkley and Tuckerman (2007) with the computation of the mean flow surrounding the pattern, which revealed a large-scale flow structure similar to the one reported by Coles and Van Atta (1966). At the same time, the first DNS of laminar-turbulent patterns in the channel flow was reported by Tsukahara et al. (2005). In contrast to Couette flow, in which the pattern is approximately steady, the pattern in the channel flow is advected with a group velocity approximately equal to the bulk velocity of the channel. In fact, the pattern advection velocity decreases with Re, as reported more precisely by Tuckerman et al. (2014).

DNS of turbulent spirals in Taylor-Couette flow were performed by Dong (2009), Meseguer et al.

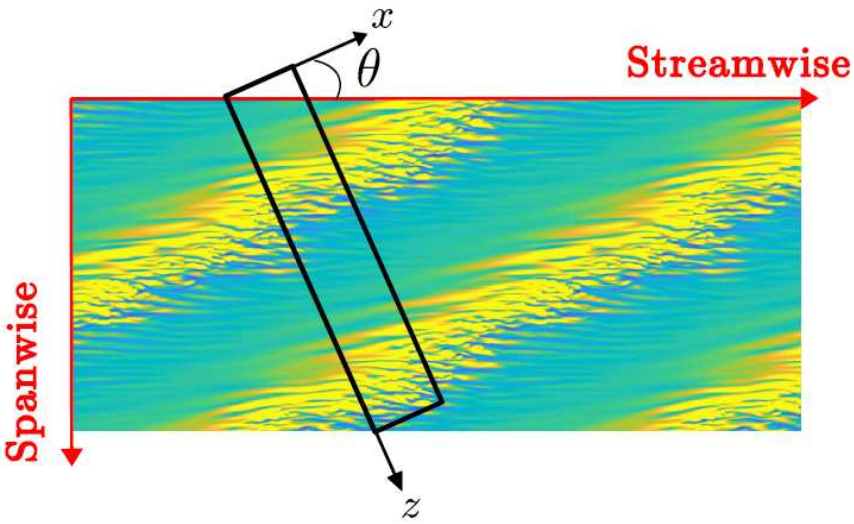

Figure 1.8: Schematic representation of a minimal band unit containing two wavelengths of the pattern (adapted from Gomé et al. (2020)).

(2009) and, more recently, by Berghout et al. (2020). Duguet et al. (2010a) performed DNS of transitional plane Couette flow in extended domains, studying the transition from localised spots to oblique self-sustained laminar-turbulent patterns. Some visualisations of the patterns from these numerical simulations are displayed in figure 1.7 (c) and (d). It can be seen that they match well the early experimental observations by Coles and Van Atta (1966) and Prigent et al. (2002) (panels (a) and (b) of the same figure). Duguet and Schlatter (2013) explained the oblique character of the pattern with the advection of small-scale fluctuations exerted by the large-scale flow (figure 1.9), which is itself oblique due to the continuity constraint. The presence of the large-scale flow was also documented by the experimental PIV measurements of Lemoult et al. (2013, 2014) in transitional channel flow.

Other simulation campaigns of laminar-turbulent patterns in Couette flow were conducted by Manneville (2011) and Manneville and Rolland (2011), who performed under-resolved simulations and found that the pattern is relatively robust with respect to a coarse graining of the numerical grid in the three spatial directions. Rolland and Manneville (2011a,b) also compared the under-resolved simulations to the Ginzburg-Landau model with noise. Rolland and Manneville (2011b) also noted that the double-well potential of the Ginzburg-Landau system is relevant to model the change of orientation that the turbulent bands experience. Finally, Philip and Manneville (2011) investigated through DNS the effect of the computational domain size on the bifurcation diagram of plane Couette flow.

More recently, the increasing power of supercomputers has allowed researchers to perform simulations in bigger domains and for longer simulation times, leading to a thorough statistical characterisation of the patterned regime. Shimizu and Manneville (2019) performed DNS of transitional channel flow, characterising the various regimes that are observed for Re spanning the entire transitional range (from stable laminar flow to uniform *featureless* turbulence). A "catalogue" of their results is shown in figure 1.10. Kashyap et al. (2020) have performed similar simulations, reporting various statistics of

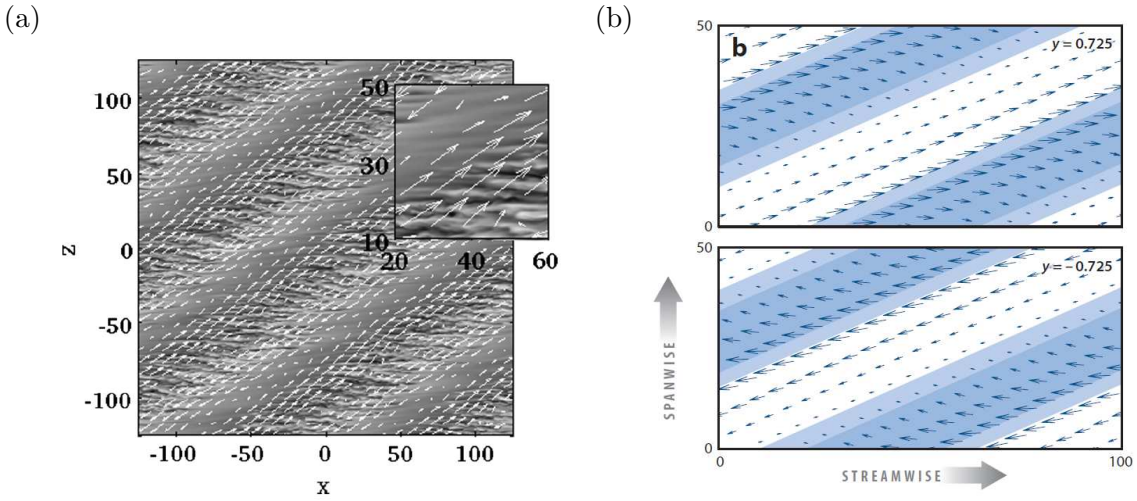

Figure 1.9: Illustrations of the large-scale flow in plane Couette flow. Panels adapted from (a) Duguet and Schlatter (2013) and (b) Tuckerman et al. (2020).

the flow in these regimes. Both Shimizu and Manneville (2019) and Kashyap et al. (2020) note that the friction factor $c_f = 2\tau_w^*/\rho^* U_b^{*2}$ (τ_w^* is the mean wall shear stress and U_b^* the channel bulk velocity) is almost constant and approximately equal to 0.01 in the transitional regime. An explication for this behaviour is currently unknown. Kashyap et al. (2020) also noted that the probability distribution of the wall shear stress is not bimodal even at very low Re, when the laminar and turbulent flows are visually distinct. Moreover, they showed that there is an almost perfect correlation between the kurtosis and the squared skewness of the local Re_τ distributions, which works all across the transitional regime and even beyond (Jovanović et al., 1993). Gomé et al. (2023a,b) have statistically characterised the emergence of the patterns in plane Couette flow using tilted domains. In the first paper, they analysed the energy transfer between small and large scales and the mean flow. In the second one, they reported several statistics on laminar gap nucleation and wavelength selection, and also a friction factor near 0.01 (which makes it an interesting universal constant for plane shear flows).

Other studies focused specifically on very low-Re cases, which feature individual bands rather than patterns (figure 1.11). Xiong et al. (2015) used DNS of channel flow to show that isolated bands (at the low Re end of the transitional regime) are decaying, whereas, when the bands start to interact and split, turbulence is sustained. This calls for an immediate analogy with puffs in pipe flow. Indeed, analogously to puffs in pipe flow, the cross-over between the characteristic splitting time and the characteristic decay time of isolated bands has been used to define a critical Re for self-sustained turbulence in plane Couette flow (Shi et al., 2013) and plane channel flow (Gomé et al., 2020). Lu et al. (2019) have shown in Couette flow that during the decay, the band orientation and thickness remain constant while its length decreases. Liu et al. (2020) and Xiao and Song (2020) demonstrated, by using PIV measurements, DNS and local stability analysis of plane channel flow, that fluctuations are generated at the downstream end of the band by a local destabilisation of the velocity profile. Parente et al. (2022a,b) investigated how a single band grows from a localised nonlinear optimal

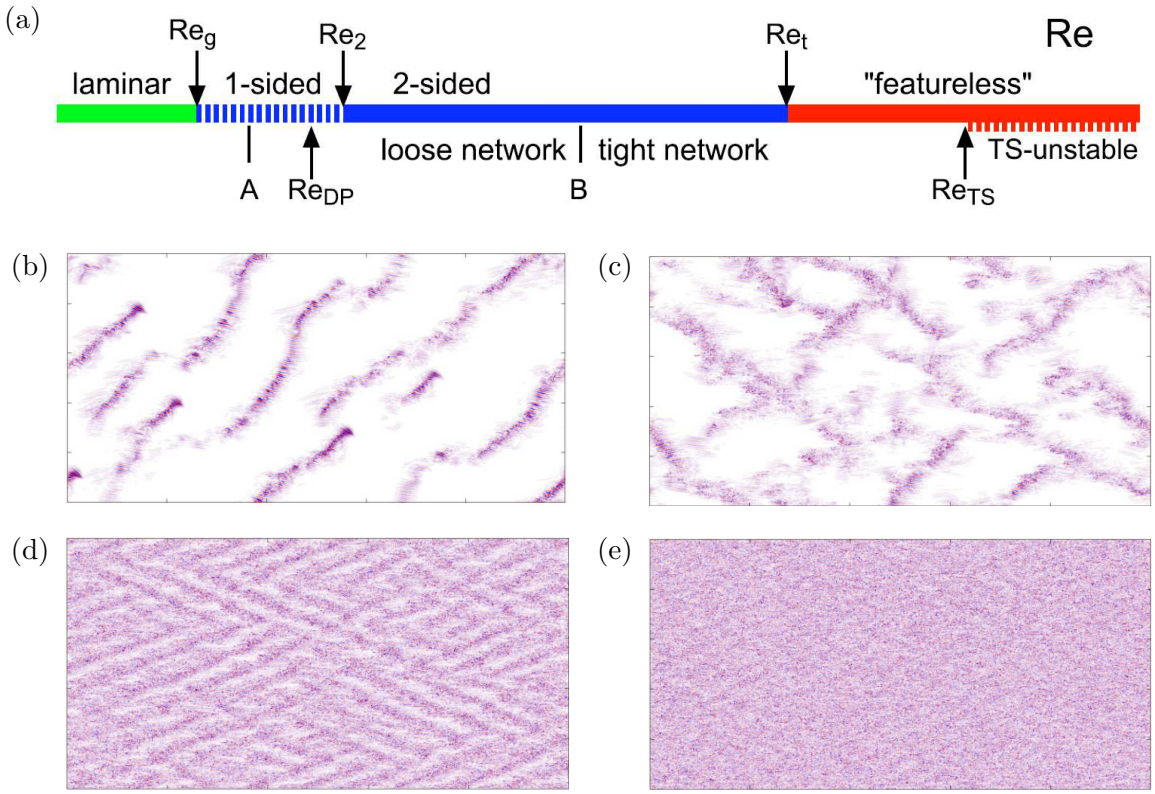

Figure 1.10: (a) Bifurcation diagram for the transitional range of plane channel flow. (b-e) Contours of the wall-normal velocity fluctuation at the channel centre for (b) one-sided stripes, (c) two-sided stripes, (d) tight pattern and (e) *featureless* turbulence. Panels adapted from Shimizu and Manneville (2019).

perturbation and how the large-scale flow is formed and stretches the band in one direction. Still in channel flow, Mukund et al. (2025) have shown that the band decay process is not memoryless (lifetime distributions are not exponentials) because there is an ageing process associated with the decay of the large-scale flow, which means that long survival times are less probable with respect to a memoryless process. Nevertheless, Wu and Song (2025) argue that the decay of a single band becomes a memoryless process beyond a certain threshold in Re. Recently, Marensi et al. (2023) investigated through DNS the differences between isolated bands in Couette and channel flow. They showed that, while in channel flow, streaks are created at the downstream end consistently with Liu et al. (2020) and Xiao and Song (2020), in Couette flow, streaks nucleate randomly inside the band.
Due to their different peculiarities, isolated bands and patterns can be seen as different regimes even if there is no sharp transition between the two (Shimizu and Manneville, 2019; Kashyap et al., 2025).

To conclude this section, it must be mentioned that laminar-turbulent patterns have also been observed in less-canonical shear flows. For example, Chantry et al. (2016, 2017) have shown that they also exist in Waleffe flow and that they are very similar to the patterns of plane Couette and channel flow. Thanks to the absence of boundary layers near the free-slip boundaries, this flow is simpler to simulate and can be seen as a model of other plane shear flows. Laminar-turbulent patterns have also been shown to exist in the presence of rotation, stratification or magnetic fields (Tsukahara

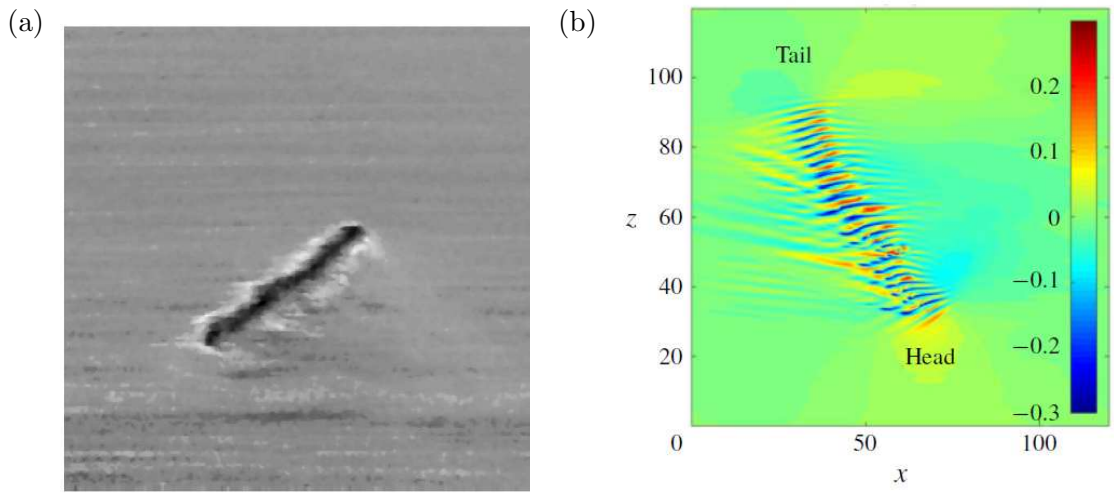

Figure 1.11: (a) Flow visualisation of an isolated turbulent band in channel flow at $Re = 750$ from the experiments of Mukund et al. (2025). (b) Streamwise velocity contours of an isolated turbulent band in channel flow at $Re = 750$ from the DNS of Xiao and Song (2020). Re based on the laminar centreline velocity.

et al., 2010; Brethouwer et al., 2012; Deusebio et al., 2015). In these cases, there are body forces that stabilise the laminar flow to higher Re. Therefore, the patterns appear later and feature a more pronounced separation of scales with respect to turbulence fluctuations. Interestingly, Brethouwer et al. (2012) and Deusebio et al. (2015) have also found that patterns can be localised only near the walls while the bulk of the flow is turbulent. Takeishi et al. (2015) and Kohyama et al. (2022) have investigated the transition in duct flows with various aspect ratios. This flow is similar to pipe flow for low aspect ratios and similar to channel flow for high aspect ratios. For intermediate aspect ratios, they find a *snake-like* regime induced by the turbulent band reflections on the side walls (figure 1.12 (a)). Similarly, Ishida et al. (2016, 2017a) have considered annular Poiseuille flow and have found regimes characterised by helical patterns and helical puffs (figure 1.12 (b)). On the other hand, Ishida et al. (2017b) have considered plane Couette flow with wall roughness and found that patterns are not observed for large values of the roughness parameter. Finally, Khapko et al. (2016) have searched for a patterned regime in the asymptotic suction boundary layer (ASBL) without finding it (they only found a transient pattern). They argue that the absence of an upper boundary affects the development of the large-scale flow.

1.2.2.3 Directed percolation theory

In a highly influential paper, Pomeau (1986) drew an analogy between subcritical transition to turbulence and propagating fronts in reaction-diffusion systems. Therefore, he speculated that the subcritical transition process could belong to the *directed percolation* (DP) universality class. DP is a stochastic process in which two states (or phases) are possible: an inactive state and an active state. This process is defined on $n + 1$-dimensional lattices, where the $+1$ denotes the temporal dimension. The active nodes can contaminate neighbouring nodes with a finite probability. They

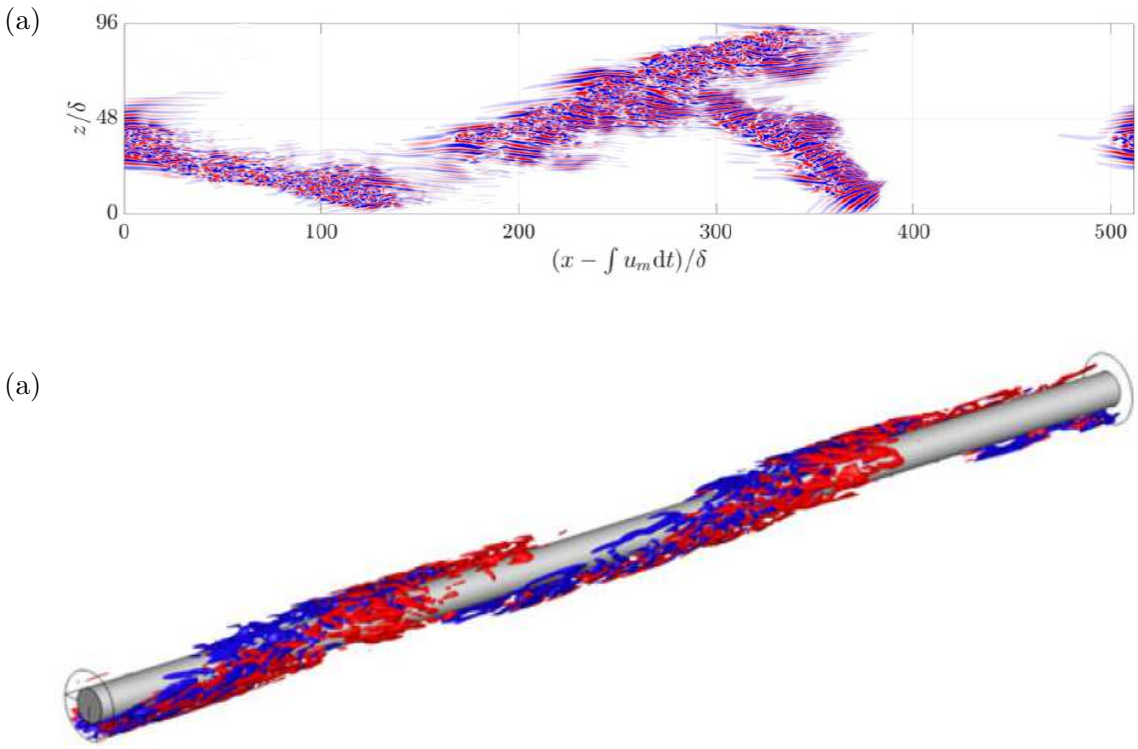

Figure 1.12: Laminar-turbulent patterns in less-canonical shear flows. (a) Turbulent band reflecting on the sidewalls in rectangular duct flow with aspect ratio 48 and $Re_\tau = 46.5$ (contours of the wall-normal velocity fluctuation at the channel centre, adapted from Kohyama et al. (2022)). (b) Spiral turbulence in annular Poiseuille flow at $Re_\tau = 56$ (isosurfaces of azimuthal velocity fluctuations, adapted from Ishida et al. (2016)).

can also spontaneously decay to the inactive state. The contamination is unidirectional in time (the contamination takes place at the next time-step), hence the adjective *directed*. Inactive nodes can not contaminate neighbouring nodes. These rules imply that an inactive node surrounded only by other inactive nodes will not become active at the next time-step (the inactive state is an *absorbing phase*). Therefore, the active phase spreads through propagating fronts. The interesting feature of this class of models is that they undergo a continuous (second-order) phase transition at a critical value of the contamination probability. The critical value depends on the details of the lattice, but the scaling exponent of the active state fraction near the critical point depends only on the number of dimensions of the lattice (and other scaling exponents as well). For a given number of dimensions, the scaling exponents do not depend on the physical details of the system. Hence, DP constitutes an *universality class*. Pomeau (1986) suggested that these scaling exponents could be used to experimentally assess whether the subcritical transition to turbulence belongs to this universality class.

However, it was only after almost thirty years that Pomeau's project was put into practice. The first experimental validation of the theory (for shear flows) is due to Lemoult et al. (2016). They performed experiments and DNS of plane Couette flow and showed that the turbulent fraction increases continuously from zero with the same power-law predicted by DP theory. The distributions of spatial and temporal laminar gaps match the theoretical prediction as well. An analogous experi-

mental endeavour was undertaken by Sano and Tamai (2016) in channel flow. Their data corroborate a continuous phase transition of the DP class. However, turbulence was continuously forced at their channel inlet, and they considered small domains and short observation times. Therefore, their evidence was questioned in later publications. Chantry et al. (2017) considered the Waleffe flow and were able to perform very long simulations in very large domains thanks to a severe truncation of the number of Fourier modes in the wall-normal direction. They also reported good agreement with DP scalings of turbulent fraction and laminar gaps. Lastly, Klotz et al. (2022) performed experiments in a Taylor-Couette system with a very large aspect-ratio and also found good agreement with DP critical exponents.

To understand the challenge involved in the experimental validation of DP theory, it is important to note that, near the critical point, a very long time is needed to converge the statistical results. This timescale has been estimated to be of the order of $4 \cdot 10^4$ advective time units for Couette flow, $2 \cdot 10^6$ advective time units for channel flow (Klotz et al., 2022) and 10^7 advective time units for pipe flow (Mukund and Hof, 2018). Likewise, spatial scales must be very large to avoid finite-size effects, which may alter the nature of the transition. This fact explains why controversies easily arise in the literature around the subject of phase transitions, with different studies claiming different types of transition for a given system. Demonstrating DP scaling laws in pipe flow experimentally is still a challenge today. However, Barkley (2011a, 2016) found DP scalings with his pipe flow model.

The applicability of DP theory to wall-bounded shear flow has been questioned by Pomeau himself (Pomeau, 2016), Tao et al. (2018) and Shimizu and Manneville (2019) due to the presence of coherent structures even at very low Re. Indeed, a second-order phase transition implies scale-invariance near the critical point, which, according to these authors, would not be compatible with the presence of spots and oblique bands near the critical point. However, Gomé et al. (2024) show that plane Couette flow transitions via expanding fronts when the large-scale flow is filtered out. The transition, however, is not necessarily continuous.

Recently, new stochastic models, belonging to the DP universality class, have been proposed in order to explain the apparent regularity of puff and band spacings. Manneville and Shimizu (2020) developed a stochastic model designed to mimic the splitting dynamics of isolated bands in channel flow. Lemoult et al. (2024) proposed a model for pipe flow based on puff interaction and *jamming* and compared the resulting phase transition of the model to DP theory. Lastly, Ayats et al. (2025) constructed a similar model for plane shear flows based on the interaction between different turbulent bands. An important difference with respect to Manneville and Shimizu (2020) is that they consider as an active phase a pattern element (*i.e.* a mix of turbulent and laminar flow) because, according to their argument, isolated turbulent flow is not a stable state and can not constitute an active phase on its own. However, these models remain purely phenomenological and, as such, do not involve any link to first principle physics, *i.e.* the Navier-Stokes equations (Duguet, 2024).

1.2.2.4 Linear instability of turbulent channel flow

Most of the DP theory is concerned with the critical point at which the turbulent fraction grows from zero. However, the work of Prigent et al. (2002) suggested that pattern formation may be

explained by looking at the other critical point: the one at which the *laminar* fraction grows from zero, *i.e.*, how the pattern emerges from uniform turbulence. By definition, a pattern is characterised by well-defined wavelengths. This contrasts with the divergence of spatial correlations near the critical point of a continuous phase transition. For this reason, Prigent et al. (2002) suggest that pattern formation may be better explained with a linear instability, which is usually characterised by critical wavelengths. They demonstrate the idea using the Ginzburg-Landau model, which features pattern-forming instabilities, as is well-known (Tuckerman and Barkley, 1990).

Similar to the DP theory, the instability hypothesis has been revisited over the years by several authors. Tuckerman et al. (2010) performed a stability analysis of plane Couette turbulent mean flow using the $k-\omega$ RANS model, but did not find any instability, and the wavelengths of the least stable mode were not consistent with the wavelengths and angles of the patterns observed in DNS. Manneville (2012) derived a reaction-diffusion model starting from the Waleffe model (Waleffe, 1997) to demonstrate the existence of a pattern-forming Turing instability. Reetz et al. (2019) have shown that an exact invariant solution of plane Couette flow featuring a pattern very similar to those observed in DNS bifurcates from the Nagata (1990) solution. This means that a pattern can emerge from a linear instability of another invariant solution.

However, only recently, the linear instability hypothesis was addressed using DNS by Kashyap et al. (2022). In this study, the authors propose a protocol to compute a statistical dispersion relation for the turbulent channel flow. They perturb the turbulent flow with white noise and trace the temporal evolution of the energy at large scales. They repeat the numerical experiment and ensemble average the evolution curve over 40 realisations. Interestingly, they find that the averaged curve has an exponential section that can be used to compute a decay rate. Tracing the evolution of the decay rate with respect to Re, they conclude that the decay rate crosses zero at $Re_\tau = 95$, which they define as the critical Re for the emergence of the pattern. The authors were also able to identify a critical wavenumber couple corresponding to $\{k_x, k_z\} = \{0.18, 0.42\}$[5] in units of one over the channel half-gap.

Importantly, linear instability is advocated by Kashyap et al. (2022) to explain the emergence of the modulations that anticipate the pattern in a top-down approach (descending Re). Such precursive modulations do not seem to exist in Couette flow (Gomé et al., 2023b; Manneville and Shimizu, 2025). Therefore, the linear instability hypothesis may not apply to this flow.

Anyway, the finding of Kashyap et al. (2022) revived the quest for models featuring a linear instability. Kashyap et al. (2024) tried to retrieve the instability by linearising the equations around the mean profile of the turbulent channel. They tested several closures for the Reynolds stresses, but they did not find any instability. In particular, using this model, it was not possible to define any critical Re, because the growth rates were approximately independent of this parameter, and it was not possible to infer anything about wavelength selection, because the most unstable wavenumber couple was always the $\{0, 0\}$ one. So these authors validated, extending the computations to low Re, the claim of Reynolds and Hussain (1972) that the turbulent mean profile of the channel flow is linearly stable.

Better results have been achieved using a simpler model based on Waleffe flow by Benavides and

[5] k_x and k_z are, respectively, the streamwise and the spanwise wavenumber.

Barkley (2025). In this study, a heavily truncated Galerkin expansion in the wall-normal direction and a closure for the Reynolds stresses were combined to derive a six-equation model with variables depending on time and wall-parallel directions. The model has a "turbulent" fixed point which, lowering Re, becomes unstable. The instability leads to steady patterns. Meanwhile, Kashyap et al. (2025) revisited the work of Manneville (2012) on the Waleffe model undergoing a Turing instability. With this model, they studied the pattern wavelength selection throughout the whole transitional range, from the linear instability of the turbulent flow to the emergence of solitary solutions (isolated bands).

1.2.3 Linear and quasi-linear models of wall-bounded flows

In the previous sections, we have presented phenomenological and theoretical works on turbulent wall-bounded flows, relevant to the subject of this thesis. We now present a short review of studies which are relevant to the methodological aspects of this thesis. As we will see, one of the major difficulties in our work is the formulation of a linear stability problem in a turbulent environment. Here, we review a number of (mostly recent) studies that cope with this problem in one way or another.

Turbulence is inherently nonlinear. Nonlinearity transfers energy to the small scales where it is dissipated (Symon et al., 2021; Ding et al., 2025). Moreover, in wall-bounded turbulence, nonlinearity is needed to close the SSP (Waleffe, 1997). However, individual energy growth mechanisms can be linear. Since the original problem is nonlinear, linear mechanisms are defined by introducing a flow decomposition which partitions the flow into two (or more) parts. A linear mechanism can be seen as the interaction between the two parts, while the self-interaction of the parts with themselves is neglected. For example, the lift-up effect (Ellingsen and Palm, 1975; Landahl, 1980) is the interaction of streamwise vortices on a given scale with the mean flow. Linear mechanisms can be analysed and modelled using the linearised Navier-Stokes equations (LNS). LNS benefit of a greater range of properties with respect to the nonlinear equations and lead to simpler theories. For this reason, they have been the object of increasing interest from the turbulence research community.

Butler and Farrell (1993) conducted the first linear study of a turbulent channel flow. Extending their previous result on laminar flow (Butler and Farrell, 1992), they found that streaks with a spanwise wavelength of 100 wall units result from an optimal perturbation of the mean profile when the optimisation time is constrained by the typical eddy turnover time at ≈ 30 wall units from the wall (buffer layer). Butler and Farrell (1993) used the Cess (1958) eddy viscosity (as reported by Reynolds and Tiederman (1967)) for the computation of the mean profile, but they used only the molecular viscosity in the linear operator applied to the perturbation (we will call this approach a *quasi-laminar* approximation). Del Alamo and Jimenez (2006) extended their results by including the eddy viscosity in the perturbation equation as well. The results of Del Alamo and Jimenez (2006) were revised shortly later by Pujals et al. (2009) to amend an inconsistency present in their equations. Moreover, a similar computation is presented for the zero-pressure-gradient turbulent boundary layer by Cossu et al. (2009). All these studies show that optimal perturbations of the mean flow in a turbulent environment lead to streaks and that, at sufficiently high Re, there are two peaks in the amplification curve with respect to the spanwise wavelength. One peak scales in inner units and corresponds to the ≈ 100 wall

units spacing, whereas the other scales with the channel half-gap (or boundary layer thickness). This feature is consistent with the presence of LSM at high Re and has led to the formulation of the multiscale SSP (see sections 1.2.1.2 and 1.2.1.3 above). Equivalent results are obtained if, instead of the initial value problem, the forced LNS are considered. This was shown by Hwang and Cossu (2010a,b) in channel flow and plane Couette flow. They considered both optimal and stochastic forcing.
Streak breakdown has been interpreted as a linear mechanism as well. Both modal instabilities (Hamilton et al., 1995; Park et al., 2011; Alizard, 2015) and transient growth over the streaks (Schoppa and Hussain, 2002; Cossu et al., 2007) have been advocated to explain this step of the SSP. In this case, the linear mechanism is an interaction between the mean flow plus streaks base flow and a streamwise-dependent mode.
We have already mentioned the connection between Orr's mechanism and near-wall bursts, which was investigated using a linear model by Jiménez (2013). The different role of all these linear mechanisms was recently reviewed by Lozano-Durán et al. (2021) using an interventional causality analysis.

This prominent role of linear mechanisms in wall-bounded flows and the desirable properties of linear systems have led McKeon and Sharma (2010) to perform a systematic study on the response to forcing of the NS operator linearised around the mean flow (resolvent operator). They found, considering turbulent pipe flow, that highly amplified modes are either localised near the wall or near the critical layer, *i.e.* near the point at which the mode phase velocity equals the mean flow velocity. These modes have been used in a later study (Sharma and McKeon, 2013) as a basis to build coherent packets of hairpin vortices. Moarref et al. (2013) performed the analysis of the resolvent operator for the turbulent channel flow. They found that for a wide range of streamwise and spanwise wavelengths, the resolvent is of low rank. Therefore, they used the leading resolvent response modes to build an approximation of the streamwise turbulence intensity profile. Modes with different phase velocities are weighted in the model, optimising the weights to fit DNS data at low Re. Resolvent modes proved to be a good basis to build low-rank models of wall-bounded flows. Sharma et al. (2016) consider invariant solutions of pipe and channel flow, compute the resolvent modes linearising the NS equations around the mean profile of these solutions and demonstrate that a good approximation of the invariant solutions can be obtained with a minimal number of modes. Other applications of these ideas can be found in McKeon (2017).

The resolvent operator has also been considered, in different ways, to address the problem of spectral estimation of turbulent flows. This task consists of predicting the pre-multiplied energy spectra of a turbulent flow with no or partial prior information from experiments or DNS. The forerunners have been Farrell and Ioannou (1998), who used the linearised NS equations forced by stochastic delta-correlated white noise to estimate the spatio-temporal power spectrum of turbulent channel flow. More recently, Zare et al. (2017) have considered coloured in time stochastic forcing, optimising the forcing to match one-point statistics of DNS data and then used the model to predict spectra and wall-normal two-point correlations. Still, for the channel flow, Illingworth et al. (2018) and Madhusudanan et al. (2019) have formulated an input-output operator based on the resolvent operator, which takes as input the streamwise velocity at a given wall-parallel plane and estimates the streamwise velocity at other planes. They showed that the inclusion of the eddy viscosity in the LNS operator ameliorates the estimation sensibly. Similar conclusions are reached by Morra et al. (2019), who used

the resolvent operator and both delta-correlated and coloured in time stochastic forcing to estimate the space-time power spectral density of the turbulent channel flow. Towne et al. (2020) considered the same estimation problem and used a few leading modes of the resolvent operator to build low-rank approximations of the estimator. Moreover, they optimised the model using one-point probe measurements. At this point, it was realised that elements like the forcing and the eddy viscosity compensate for the neglected nonlinearities. For example, the eddy viscosity introduces an additional dissipation which plays the role of the nonlinear energy transfer towards the small scales (Gupta et al., 2021; Symon et al., 2021). Consequently, linear models have been sophisticated, optimising the eddy viscosity profile or introducing a scale-dependent eddy viscosity to target this role explicitly (Gupta et al., 2021; Symon et al., 2023; Abootorabi and Zare, 2023; Ying et al., 2025).

To conclude this section, we mention a slightly different approach: the *quasi-linear* approximation (QLA). In this approach, the flow is still partitioned into mean flow plus fluctuation, but the nonlinear feedback of the fluctuations to the mean flow is retained. Therefore, the two parts are solved simultaneously with two different equations. Early quasi-linear models of wall-bounded flows were formulated to study the SSP. Gayme et al. (2010, 2011), Farrell and Ioannou (2012), Thomas et al. (2014) and Bretheim et al. (2015) all consider the channel or plane Couette flow and study the feedback of streamwise dependent modes (which represent streak instabilities) on the streamwise averaged flow (which is made of the mean profile plus streaks and rolls). Gayme et al. (2010, 2011) replaced streamwise dependent modes with stochastic forcing, whereas Bretheim et al. (2015) showed that even a single streamwise dependent mode is sufficient to sustain turbulence (without forcing) and, interestingly, to obtain a fairly correct mean profile. Pausch et al. (2019) used a quasi-linear model to approximate invariant solutions of channel and plane Couette flow. Hwang and Eckhardt (2020) and Skouloudis and Hwang (2021) implemented the eddy viscosity in the equation for the fluctuations to improve the QLA predictions. A thorough analysis of the quasi-linear models augmented with eddy viscosity and an optimisation of these models using DNS data is treated in the recent works of Holford et al. (2023, 2024a,b). Lastly, the concept of quasi-linearity can be pushed further with the *generalised quasi-linear* approximation (GQL) proposed by Marston et al. (2016). In this approach, the fluctuations are partitioned into two parts (usually, using a cutoff wavelength). One part behaves fully nonlinearly, while in the equations for the second part, nonlinear interactions are truncated according to some rules that preserve the energy conservation property of the nonlinearity. Tobias and Marston (2017) apply the GQL approach to the turbulent rotating plane Couette flow and find that even the addition of a small number of large-wavelength modes in the fully nonlinear part improves the predictions with respect to the standard QLA. GQL is useful to study the role of multiscale interactions in turbulence dynamics. A recent work in this direction on the turbulent channel flow is the one of Hernández et al. (2022a,b).

In this section, we have given a short review of recent developments in linear models of wall-bounded turbulent flows. We have seen that the lack of nonlinearity in the models is compensated by introducing closure terms, such as the eddy viscosity term and harmonic or stochastic forcings. This short review is useful since, in the course of the thesis, we will use linear stability models and we will introduce the same elements in our equations.

1.3 Objectives of this work

This thesis addresses three main research themes in the channel flow:

1. Bursts and extreme events. The objective of our work is to artificially generate such highly dissipative events with a nonlinear optimal perturbation (Farano et al., 2017), prove that the resulting dynamics are similar to those of *natural* ones and investigate the features of the perturbation. The aim is to provide a link between intermittent dissipation and the instability of coherent structures towards small scales (Hack and Schmidt, 2021).

2. Large-scale motions. In principle, these motions have an autonomous self-sustaining process (SSP) (Hwang and Cossu, 2010c) and can be generated by the transient amplification of streamwise perturbations due to the mean shear (Hwang and Cossu, 2010a). However, SSP at different scales can interact when structures become unstable (Doohan et al., 2021). Our study will aim to assess the bottom-up generation of large-scale motions (Toh and Itano, 2005) through a detuned linear stability analysis (Schmid et al., 2017; Jouin et al., 2024). In this way, we will describe an alternative process for the generation of large-scale motions in wall-bounded turbulent flows.

3. Modulations and pattern formation. We have seen that, in the channel flow, the precursors of laminar-turbulent patterns are modulations and that these modulations arise from an instability of the turbulent flow (Kashyap et al., 2022). We aim to model this instability with an eigenvalue problem, similarly to classic laminar flow instabilities. This will provide eigenmodes that can be analysed to give further physical insights. After the work of Kashyap et al. (2024), the pending question is whether linear stability analysis can be applied to predict the modulation, and if yes, starting from which simple enough base flow. Once the linear instability is found, we will address whether the problem of the nonlinear development of the instability can be addressed with an ad-hoc model.

In general, the thesis aims to model scale interaction phenomena as instabilities of coherent structures. Coherent structures characterised by a certain spatial scale become unstable and generate other coherent structures on different scales. This idea is the common ground on which our numerical investigations are based.

1.4 Organisation of the Manuscript

Chapter 2 sets the mathematical framework of our work: it describes the channel flow, the equations of motion, stability theory and introduces the notation used throughout the thesis. Part of this information is repeated at the beginning of each chapter for clarity. In Chapter 2, we also describe the numerical methods employed and their validation.

Chapter 3 deals with the study of extreme events in the channel flow. The nonlinear optimal perturbation and its related temporal evolution are described. It is demonstrated that it generates

extreme dissipation events and that these artificial events have the same local structure as *natural* ones. The mechanisms activated by the perturbation are investigated and discussed.

In Chapter 4 we present our investigation on large-scale motions at high Re. We describe a strategy to compute the base flow using Proper Orthogonal Decomposition (POD) and formulate the secondary stability problem for the detuned instability. We present the results of the instability and compare them with DNS and experimental observations.

In Chapter 5 we present a similar investigation at lower Re in order to retrieve turbulence modulations (Kashyap et al., 2022) with a modal stability analysis. We discuss two different strategies to compute the base flow (both different from the POD of Chapter 4) and several possible closures for incoherent fluctuations. Results of the stability analysis are presented and analysed with an energy budget equation. Moreover, it is argued that this model is not adequate to represent nonlinearly saturated laminar-turbulent patterns, which motivates the next chapter.

In Chapter 6 we present some ideas on a nonlinear model of pattern formation. The model is analysed at different levels: uniform nullclines and fixed points, linear instability of the turbulent fixed point, and nonlinear development of the unstable wave towards a pattern.

At the end of each of these chapters limitations of the approach and key takeaways are critically discussed. Overall conclusions are drawn in Chapter 7. This chapter concludes with perspectives and outlooks according to the author's point of view.

Chapter 2

Mathematical Framework and Numerical Methods

2.1 The channel flow

In Chapter 1, we have given an overview of past and recent works on wall-bounded shear flows. Most studies focus on canonical flows: plane channel flow, plane Couette flow, Taylor-Couette flow, flat plate boundary layers, etc... We have seen that there may be some differences between the phenomenologies of these flows. However, many of the fundamental questions are common to all of them. In this thesis, we choose to focus solely on the channel flow, which is probably the most studied one. This Chapter aims to introduce the problem under consideration, its mathematical formalisation and the numerical methods that we have employed throughout the thesis. Part of the information reported here is partially repeated at the beginning of each of the following chapters to make them self-contained.

We consider a "theoretical" channel flow characterised by periodic boundary conditions in the streamwise and spanwise directions. This theoretical channel is an idealisation of real channels, which have finite streamwise and spanwise size and, therefore, feature an inlet, an outlet and spanwise end walls. No-slip boundary conditions are imposed in the wall-normal direction to model the presence of walls.

We now introduce some general notation. The streamwise, wall-normal and spanwise directions are denoted, respectively, by x, y and z or x_1, x_2 and x_3 when using index notation. Similarly, the streamwise, wall-normal and spanwise velocity components are denoted, respectively, by u, v and w or u_1, u_2 and u_3. We will consider a periodic domain with dimensions $[L_x, L_y, L_z]$ (L_x and L_z representing the streamwise and the spanwise periods of the flow). Dimensional quantities are denoted by an asterisk. Quantities without any superscript are made dimensionless with the channel half-gap h^* (such that $L_y = 2$ and $0 \leqslant y \leqslant 2$) and the bulk velocity $U_b^* = \int_0^2 \int_0^{L_z} u^* \, dydz/2L_z$ (outer units). Quantities with a + superscript are made dimensionless with the viscous length $\delta_\nu^* = \nu^*/u_\tau^*$ and the friction velocity $u_\tau^* = \sqrt{\tau_w^*/\rho^*}$ (inner or wall units), where ρ^* is the fluid density, ν^* the kinematic viscosity and τ_w^* the measured mean wall shear stress.

2.2 The Navier-Stokes equations

The instantaneous flow is governed by the Navier-Stokes (NS) equations for incompressible flows

$$\begin{cases} \dfrac{\partial \boldsymbol{u}}{\partial t} + \boldsymbol{u} \cdot \boldsymbol{\nabla} \boldsymbol{u} = -\boldsymbol{\nabla} p + \dfrac{1}{Re} \nabla^2 \boldsymbol{u} + \boldsymbol{f}_b, \\ \boldsymbol{\nabla} \cdot \boldsymbol{u} = 0, \end{cases} \tag{2.1}$$

where $\boldsymbol{u}$ is the velocity vector field, p is the hydrodynamic pressure field and $Re = U_b^* h^*/\nu^*$ is the Reynolds number. The flow in the channel is pressure-driven, which, in the real world, means that there is a pressure head between the inlet and the outlet of the channel. In our theoretical channel flow, we can replace the pressure head by a uniform volume forcing in the streamwise direction ($\boldsymbol{f}_b$ in (2.1)). Moreover, we consider a time-varying forcing which adapts to the flow to keep the flow rate constant. This is implemented by adding the constraint $\int_0^2 \int_0^{L_z} u \, dydz/2L_z = 1$ to (2.1) and using the value of the forcing as an additional unknown that enforces the constraint (*i.e.* a Lagrange multiplier).

Direct numerical simulations (DNS) of (2.1), which resolve all the scales of motion and their interactions, will be considered as the reference physics. Throughout the thesis, we will introduce stability analyses and other models which rely on linearised and/or modified versions of (2.1). They do not resolve all the scales of motion and their interactions and, therefore, need stronger assumptions. The results of these analyses will usually be compared to DNS results for *a posteriori* validation of the assumptions involved.

2.3 Direct Numerical Simulations

DNS is performed throughout the thesis using the channelflow 2.0 code by Gibson et al. (2021). Here, we give a short description of the numerical method used in the solver and a quick validation of our DNS data with previous studies.

2.3.1 The channelflow DNS code

The most efficient approach to solving flows in simple geometries, like the plane channel flow, is spectral methods. Spectral methods represent the numerical solution of the problem relying on particular functional bases which have desirable properties like orthogonality of the basis elements (Quarteroni et al., 2006). The choice of the basis depends on the geometry and the boundary conditions. The code channelflow 2.0 has been conceived to solve the flows in plane periodic channels (like Couette flow and pressure-driven channel flow). To comply with the periodic boundary conditions in the streamwise and spanwise directions, Fourier modes are used in these directions. Chebyshev polynomials are used in the wall-normal direction to comply with the no-slip boundary conditions. The advantage of these bases is that the Fourier and Chebyshev coefficients can be efficiently computed using a Fast Fourier Transform (FFT) library (Peyret, 2002), which is what channelflow does.

The velocity field is represented in spectral space as[1]

$$\begin{aligned}\boldsymbol{u}(\boldsymbol{x},t) &= \sum_{m_x=-\frac{N_x}{2}+1}^{Nx/2}\sum_{m_z=-\frac{N_z}{2}+1}^{Nz/2} \hat{\boldsymbol{u}}_{m_x,m_z}(y,t)e^{2\pi\iota\left(\frac{m_x x}{L_x}+\frac{m_z z}{L_z}\right)} \\ &= \sum_{m_x=-\frac{N_x}{2}+1}^{Nx/2}\sum_{m_y=0}^{Ny-1}\sum_{m_z=-\frac{N_z}{2}+1}^{Nz/2} \tilde{\boldsymbol{u}}_{m_x,m_y,m_z}(t)T_{m_y}(y)e^{2\pi\iota\left(\frac{m_x x}{L_x}+\frac{m_z z}{L_z}\right)},\end{aligned} \tag{2.2}$$

where T_{m_y} is the m_y-th order Chebyshev polynomial. A similar expression applies to the pressure field and any other field. The $N_x \times N_y \times N_z/2$ complex Fourier-Chebyshev coefficients needed to represent a real scalar field correspond to $N_x \times N_y \times N_z$ collocation points on which the field is sampled. Fourier collocation points are equispaced along the periodic directions, whereas Chebyshev collocation points in the wall-normal direction correspond to the Chebyshev-Gauss-Lobatto points $y_i = \cos(\pi i/(N_y-1))$ for $i = 0, 1, \ldots, N_y - 1$. We denote by t_n the $n-$th time step and by $\boldsymbol{u}(\boldsymbol{x}_i, t_n)$ the velocity field on the $i-$th collocation point at the $n-$th time step. The FFTW3 library (Frigo and Johnson, 2005) provides the routines to pass from $\boldsymbol{u}(\boldsymbol{x}_i, t_n)$ to $\hat{\boldsymbol{u}}(y_i, t_n)$ and $\tilde{\boldsymbol{u}}(t_n)$ and vice versa.

The numerical method consists of the formulation of a linear algebraic system for the coefficients $\hat{\boldsymbol{u}}_{m_x,m_z}(y_i, t_n)$ for each m_x and m_z. Inserting (2.2) in (2.1) and simplifying the common terms, the following system is obtained:

$$\begin{cases} \dfrac{\partial}{\partial t}\hat{\boldsymbol{u}}_{m_x,m_z} = -\hat{\boldsymbol{N}}_{m_x,m_z} - \hat{\boldsymbol{\nabla}}\hat{p}_{m_x,m_z} + \dfrac{1}{Re}\left(-k^2 + \dfrac{\partial^2}{\partial y^2}\right)\hat{\boldsymbol{u}}_{m_x,m_z} + \boldsymbol{f}_b\delta_{m_x,0}\delta_{m_z,0}, \\ \hat{\boldsymbol{\nabla}}\cdot\hat{\boldsymbol{u}}_{m_x,m_z} = 0, \end{cases} \tag{2.3}$$

where $\hat{\boldsymbol{\nabla}}$ and $\hat{\boldsymbol{\nabla}}\cdot$ are the gradient and divergence operators in Fourier space, $k^2 = (2\pi m_x/L_x)^2 + (2\pi m_z/L_z)^2$ and $\delta_{i,j}$ the Kronecker delta. The nonlinear term gives the coefficient $\hat{\boldsymbol{N}}_{m_z,m_z}$ whose direct evaluation involves a costly convolution sum. Therefore, the direct evaluation in spectral space is avoided, as we will see. The bulk forcing $\boldsymbol{f}_b$ acts only on the $\hat{\boldsymbol{u}}_{0,0}$ coefficient and is determined from the bulk velocity constraint. This implies a slight modification of the algebraic system for the $\{0, 0\}$ wavenumber couple. Otherwise, we can forget about this term in the following.

The problem is discretised in time using a third-order Semi-Implicit Backwards Differentiation scheme (SBDF3). The nonlinear term is treated explicitly, *i.e.*, it is computed using the velocity fields of previous time steps. The pressure, the continuity constraint and the diffusion term are treated implicitly, *i.e.* they are evaluated at the current time step. The scheme reads:

$$\begin{cases} \dfrac{1}{Re}\dfrac{d^2}{dy^2}\hat{\boldsymbol{u}}^{n+1}_{m_x,m_z} - \lambda\hat{\boldsymbol{u}}^{n+1}_{m_x,m_z} - \hat{\boldsymbol{\nabla}}\hat{p}^{n+1}_{m_x,m_z} = -\displaystyle\sum_{j=0}^{2}\frac{\alpha_j}{\Delta t}\hat{\boldsymbol{u}}^{n-j}_{m_x,m_z} - \sum_{j=0}^{2}\beta_j\hat{\boldsymbol{N}}^{n-j}_{m_z,m_z} \\ \hat{\boldsymbol{\nabla}}\cdot\hat{\boldsymbol{u}}^{n+1}_{m_x,m_z} = 0, \end{cases} \tag{2.4}$$

where Δt is the time step. The scheme coefficients are $\lambda = 11/6\Delta t + k^2/Re$, $\alpha_0 = -3$, $\alpha_1 = 3/2$, $\alpha_2 = -1/3$, $\beta_0 = 3$, $\beta_1 = -3$ and $\beta_2 = 1$.

[1]Here and throughout the thesis, ι denotes the imaginary unit.

Since $\hat{\boldsymbol{N}}_{m_z,m_z}$ is treated explicitly, this term can be computed with the following strategy: the gradient of the velocity field is computed in the spectral space, then the velocity and its gradient are transformed to physical space and their product is computed, finally the result is transformed back to the spectral space to obtain $\hat{\boldsymbol{N}}_{m_z,m_z}$. This procedure is convenient because it allows the use of the FFT, whose cost scales as $N \log N$, instead of the convolution sum, whose cost scales as N^2 (N being the number of collocation points). However, the direct transform from physical to spectral space introduces an aliasing error (Peyret, 2002). To avoid this error, the Orzasag's two-thirds rule is used, which consists of discarding the last one-third of the high-wavenumber Fourier coefficients in x and z.

With this expedient, the right-hand side of the first equation in (2.4) is known at the time step n. We will denote this term by $\hat{\boldsymbol{R}}^n_{m_x,m_z}$. The pressure can be decoupled from the velocity by taking the divergence of the first equation and using continuity:

$$\frac{d^2}{dy^2}\hat{p}^{n+1}_{m_x,m_z} - k^2\hat{p}^{n+1}_{m_x,m_z} = -\hat{\boldsymbol{\nabla}}\cdot\hat{\boldsymbol{R}}^n_{m_x,m_z}. \tag{2.5}$$

This equation, however, is not equipped with boundary conditions. Therefore, the pressure equation needs to be solved together with the wall-normal velocity equation using the *influence matrix* method. For the details of this method, we refer to specialised texts (Canuto et al., 1988). Once pressure is computed, each velocity component can be retrieved by solving equations having the same form as (2.5) (which is called *Helmholtz* equation). Using a Chebyshev transform in the wall-normal direction, the Helmholtz equation can be reworked in a tridiagonal linear system for the Chebyshev coefficients $\tilde{\boldsymbol{u}}_{m_x,m_y,m_z}$ (*Chebyshev-tau* method, see Canuto et al. (1988) for the details). At the end, the numerical integration of (2.1) is reduced to the solution of $\propto N_x N_z/2$ complex-valued tridiagonal systems.

Of course, this numerical method was already implemented in the original code, which is available online (Gibson et al., 2021). However, the code was customised during the thesis to include, *e.g.*, the eddy viscosity (which is implemented as an explicit term similarly to treatment of the nonlinear term) or an additional scalar equation coupled to the velocity-pressure system for the models of Chapter 6 (again, the coupling term was treated explicitly).

2.3.2 DNS validation

The channelflow code has been employed on a number of previous studies by several groups. The code itself does not need to be validated. Here, we validate the reliability of our data. For $Re_\tau = 180$, we compare in figure 2.1 our profiles of mean flow, Reynolds shear stress, velocity fluctuations root mean square (r.m.s.) and vorticity fluctuations r.m.s. to those reported by Kim et al. (1987). We used the same number of collocation points as the reference. The agreement is excellent for all the variables.
Moreover, in figure 2.2, we compare with previous literature our mean flow and streamwise velocity fluctuation r.m.s. profiles obtained from the minimal flow unit data of the DNS computed for Chapter 4 at $Re_\tau = [590, 1000, 2000]$ in domains of size $L_x \times L_z = \pi/2 \times \pi/4$. The numerical resolution of these simulations is comparable to the reference studies (see also table 4.1). It can be seen that the two profiles are well computed near the wall, whereas minor differences arise towards the channel

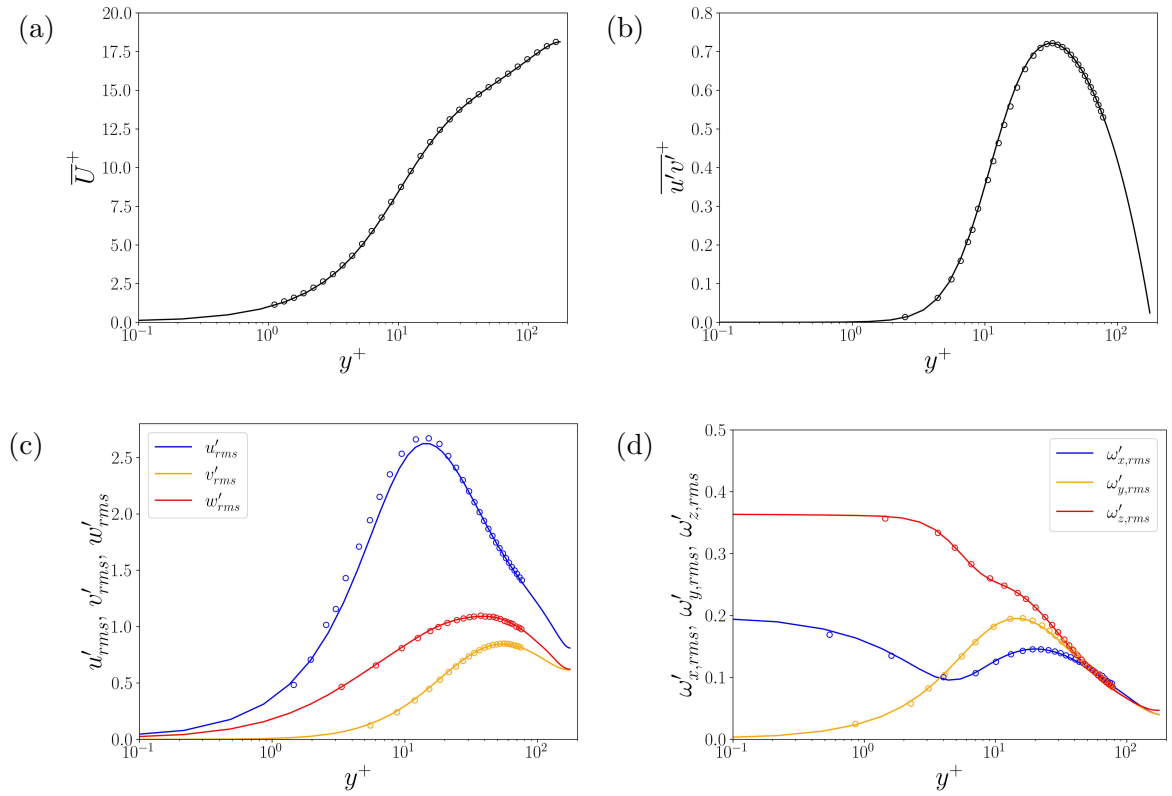

Figure 2.1: Validation of DNS data at $Re_\tau = 180$. (a) Mean flow, (b) Reynolds shear stress, (c) r.m.s. of the three velocity components fluctuations and (d) r.m.s. of the three vorticity components fluctuations. Open circles are reference data by Kim et al. (1987).

centre due to the use of very small domains. We note that these small-size effects influence the flow only for $y \gtrsim L_z/3 \approx 0.25h$ (Flores and Jiménez, 2010), so that the considered minimal flow units are appropriate to extract near-wall coherent structures for the purposes of Chapter 4.

2.4 Nonlinear Optimal Perturbations

In this section, the procedure to compute nonlinear optimal perturbations (NLOP) is outlined. We consider a baseline flow $\boldsymbol{u}_u(\boldsymbol{x}, t)$ which is perturbed at time t_0 with a perturbation $\tilde{\boldsymbol{u}}(\boldsymbol{x}, t_0) \equiv \tilde{\boldsymbol{u}}_0$. For $t \geqslant t_0$, the flow can be decomposed such that

$$\boldsymbol{u}_p(\boldsymbol{x}, t) = \boldsymbol{u}_u(\boldsymbol{x}, t) + \tilde{\boldsymbol{u}}(\boldsymbol{x}, t), \tag{2.6a}$$

$$p_p(\boldsymbol{x}, t) = p_u(\boldsymbol{x}, t) + \tilde{p}(\boldsymbol{x}, t). \tag{2.6b}$$

$\boldsymbol{u}_p$ is obtained solving (2.1) from the initial condition $\boldsymbol{u}_u(\boldsymbol{x}, t_0) + \tilde{\boldsymbol{u}}_0$ and the perturbation $\tilde{\boldsymbol{u}}(\boldsymbol{x}, t)$ can be obtained by subtracting $\boldsymbol{u}_u(\boldsymbol{x}, t)$ from $\boldsymbol{u}_p(\boldsymbol{x}, t)$ for every $t > t_0$. Therefore, the only undetermined variable is $\tilde{\boldsymbol{u}}_0$. In principle, the flow can be perturbed arbitrarily under the constraints imposed by continuity ($\boldsymbol{\nabla} \cdot \tilde{\boldsymbol{u}}_0 = 0$) and boundary conditions.

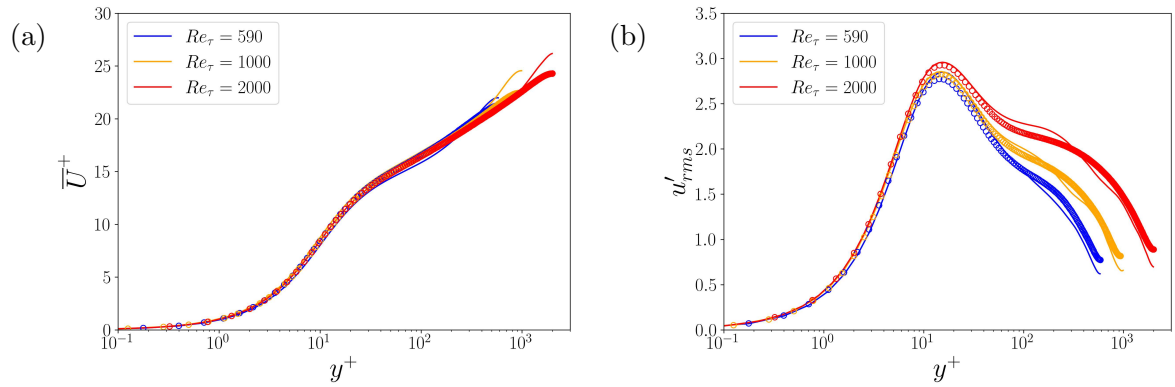

Figure 2.2: Validation of DNS data at $Re_\tau = [590, 1000, 2000]$. (a) Mean flow and (b) r.m.s. of the streamwise velocity fluctuation. Open circles are reference data: respectively Moser et al. (1999), Del Alamo et al. (2004) and Hoyas and Jiménez (2006) for $Re_\tau = 590$, $Re_\tau = 1000$ and $Re_\tau = 2000$.

The NLOP problem is

$$\text{find } \tilde{\boldsymbol{u}}_0 \text{ such that } \mathcal{J}[\tilde{\boldsymbol{u}}_0] = \max_{\boldsymbol{u}_0} \mathcal{J}[\boldsymbol{u}_0] \text{ under constraints.} \tag{2.7}$$

$\mathcal{J}$ is an objective functional which depends on the perturbed solution $\boldsymbol{u}_p(\boldsymbol{x}, t)$. Hence, it depends on $\tilde{\boldsymbol{u}}_0$ through the NS equations, which must be included in the problem as constraints. Another constraint which is usually employed is the initial energy of the perturbation (E_0).

2.4.1 Numerical method

To specify further the problem and the method, we introduce some additional notation. We consider the NS equations in index notation:

$$\begin{cases} \dfrac{\partial u_i}{\partial t} + u_j \dfrac{\partial u_i}{\partial x_j} + \dfrac{\partial p}{\partial x_i} - \dfrac{1}{Re} \dfrac{\partial^2 u_i}{\partial x_j \partial x_j} = 0, \\ \dfrac{\partial u_i}{\partial x_i} = 0, \end{cases} \tag{2.8}$$

where summation is implied over the repeated indices. Both $\boldsymbol{u}_u(\boldsymbol{x}, t)$ and $\boldsymbol{u}_p(\boldsymbol{x}, t)$ are subject to these equations by definition. To ease the notation, hereafter, we will denote $\boldsymbol{u}_p$ by $\boldsymbol{u}$, and it will be implicitly assumed that it depends on the perturbation $\tilde{\boldsymbol{u}}$ according to (2.6). We consider a rectangular three-dimensional domain $\mathcal{V}$ having dimensions L_j for each direction $j = 1, 2, 3$. Its frontier surface will be denoted by $\mathcal{S}$, while $\mathcal{S}_j^0$ will denote the surface at $x_j = 0$ and $\mathcal{S}_j^1$ the surface at $x_j = L_j$.

In this section, we consider a general objective functional of the form:

$$\mathcal{J} = \int_{t_0}^{t_0+T} \int_{\mathcal{V}} f\left(\frac{\partial u_i}{\partial x_j}, \frac{\partial u_i}{\partial t}, u_i, x_j, t\right) d\mathcal{V} dt. \tag{2.9}$$

The problem (2.7) can be solved using the calculus of variations. The constraints are introduced in the problem using the Lagrange multiplier method (Kochenderfer and Wheeler, 2019). Therefore, the

following augmented functional is considered:

$$\begin{aligned}\mathcal{L} =& \mathcal{J} + \int_{t_0}^{t_0+T} \int_{\mathcal{V}} u_i^\dagger \left[\frac{\partial u_i}{\partial t} + u_j \frac{\partial u_i}{\partial x_j} + \frac{\partial p}{\partial x_i} - \frac{1}{Re} \frac{\partial^2 u_i}{\partial x_j \partial x_j} \right] \, d\mathcal{V} dt \\ &+ \int_{t_0}^{t_0+T} \int_{\mathcal{V}} p^\dagger \frac{\partial u_i}{\partial x_i} \, d\mathcal{V} dt + \lambda \left(\int_{\mathcal{V}} \frac{1}{2} \tilde{u}_i \tilde{u}_i \, d\mathcal{V} - E_0 \right),\end{aligned} \tag{2.10}$$

where $u_i^\dagger$, $p^\dagger$ and λ are the Lagrange multipliers or adjoint variables. The augmented functional depends on u_i, p, $u_i^\dagger$ and $p^\dagger$. To make the functional stationary, the first variation of $\mathcal{L}$ with respect to these variables must be zero for every δu_i, δp, $\delta u_i^\dagger$ and $\delta p^\dagger$. The derivative of $\mathcal{L}$ with respect to λ is simply set to zero by imposing the energy constraint with a projection method (Foures et al., 2013). Note that the bulk flow rate constraint is not introduced in this functional for conciseness, but its treatment is straightforward. It will also be used to nullify certain surface terms in the derivation below.

The variation of $\mathcal{L}$ with respect to $p^\dagger$ and $u_i^\dagger$ is:

$$\delta_{p^\dagger} \mathcal{L} = \frac{\partial}{\partial \epsilon} \mathcal{L} \left[p^\dagger + \epsilon \delta p^\dagger \right] \Big|_{\epsilon=0} = \int_{t_0}^{t_0+T} \int_{\mathcal{V}} \frac{\partial u_i}{\partial x_i} \delta p^\dagger \, d\mathcal{V} dt, \tag{2.11}$$

$$\begin{aligned}\delta_{u_i^\dagger} \mathcal{L} = & \frac{\partial}{\partial \epsilon} \mathcal{L} \left[u^\dagger + \epsilon \delta u_i^\dagger \right] \Big|_{\epsilon=0} = \\ & \int_{t_0}^{t_0+T} \int_{\mathcal{V}} \left[\frac{\partial u_i}{\partial t} + u_j \frac{\partial u_i}{\partial x_j} + \frac{\partial p}{\partial x_i} - \frac{1}{Re} \frac{\partial^2 u_i}{\partial x_j \partial x_j} \right] \delta u_i^\dagger \, d\mathcal{V} dt,\end{aligned} \tag{2.12}$$

which, on posing the integrands equal to zero, gives the direct equations (2.8) as desired.

The variation with respect to p is:

$$\delta_p \mathcal{L} = \frac{\partial}{\partial \epsilon} \mathcal{L} \left[p^\dagger + \epsilon \delta p \right] \Big|_{\epsilon=0} = \int_{t_0}^{t_0+T} \int_{\mathcal{V}} u_i^\dagger \frac{\partial \delta p}{\partial x_i} \, d\mathcal{V} dt. \tag{2.13}$$

Using integration by parts, it can be recast as:

$$\delta_p \mathcal{L} = \int_{t_0}^{t_0+T} \int_{\mathcal{S}_i^1} u_i^\dagger \delta p \, d\mathcal{S}_i^1 dt - \int_{t_0}^{t_0+T} \int_{\mathcal{S}_i^0} u_i^\dagger \delta p \, d\mathcal{S}_i^0 dt - \int_{t_0}^{t_0+T} \int_{\mathcal{V}} \frac{\partial u_i^\dagger}{\partial x_i} \delta p \, d\mathcal{V} dt. \tag{2.14}$$

Zeroing the last term for every δp, the incompressibility constraint for the adjoint velocity is obtained. The surface terms are zero if the adjoint velocity verifies homogeneous boundary conditions, *e.g.* at walls, or periodic boundary conditions. In addition, when a flow is forced with a constant flow rate in the direction i, the adjoint velocity must have zero net flux in that direction (Kerswell, 2018). Indeed, in that case, $\delta p \left(\mathcal{S}_i^{0,1} \right)$ will have a periodic and a constant contribution: $\delta p \left(\mathcal{S}_i^{0,1} \right) = \delta p_p + \delta p_c^{0,1}$. Therefore, assuming $u_i^\dagger$ periodic along the i direction, $u_i^\dagger \delta p_p$ will also be periodic, and its surface integrals will cancel out. The constant contribution will give:

$$\int_{t_0}^{t_0+T} \left[\int_{\mathcal{S}_i^1} u_i^\dagger \delta p_c^1 \, d\mathcal{S}_i^1 - \int_{\mathcal{S}_i^0} u_i^\dagger \delta p_c^0 d\mathcal{S}_i^0 \right] dt = \int_{t_0}^{t_0+T} \left[\left(\delta p_c^1 - \delta p_c^0 \right) \int_{\mathcal{S}_i^1} u_i^\dagger \, d\mathcal{S}_i^1 \right] dt.$$

Then, it is clear that this contribution vanishes if the surface integral of $u_i^\dagger$ vanishes for every t.

Lastly, the variation of $\mathcal{L}$ with respect to u_i is:

$$\delta_{u_i}\mathcal{L} = \frac{\partial}{\partial\epsilon}\mathcal{L}\left[u_i+\epsilon\delta u_i\right]\Big|_{\epsilon=0} = \delta_{u_i}\mathcal{J} + \int_{t_0}^{t_0+T}\int_{\mathcal{V}}\left[u_i^\dagger\left(\frac{\partial\delta u_i}{\partial t}+u_j\frac{\partial\delta u_i}{\partial x_j}+\delta u_j\frac{\partial u_i}{\partial x_j}-\frac{1}{Re}\frac{\partial^2\delta u_i}{\partial x_j\partial x_j}\right)+p^\dagger\frac{\partial\delta u_i}{\partial x_i}\right]d\mathcal{V}dt + \lambda\int_{\mathcal{V}}\tilde{u}_i\delta u_i\,d\mathcal{V}\Big|_{t_0} \tag{2.15}$$

Again, some integration by parts is needed:

$$\int_{t_0}^{t_0+T}\int_{\mathcal{V}}u_i^\dagger\frac{\partial\delta u_i}{\partial t}\,d\mathcal{V}dt = \int_{\mathcal{V}}u_i^\dagger\delta u_i\,d\mathcal{V}\Big|_{t_0+T} - \int_{\mathcal{V}}u_i^\dagger\delta u_i\,d\mathcal{V}\Big|_{t_0} - \int_{t_0}^{t_0+T}\int_{\mathcal{V}}\frac{\partial u_i^\dagger}{\partial t}\delta u_i\,d\mathcal{V}dt; \tag{2.16}$$

$$\int_{t_0}^{t_0+T}\int_{\mathcal{V}}u_i^\dagger u_j\frac{\partial\delta u_i}{\partial x_j}\,d\mathcal{V}dt = \int_{t_0}^{t_0+T}\int_{\mathcal{S}_j^1}u_i^\dagger u_j\delta u_i\,d\mathcal{S}_j^1dt - \int_{t_0}^{t_0+T}\int_{\mathcal{S}_j^0}u_i^\dagger u_j\delta u_i\,d\mathcal{S}_j^0dt - \int_{t_0}^{t_0+T}\int_{\mathcal{V}}u_j\frac{\partial u_i^\dagger}{\partial x_j}\delta u_i\,d\mathcal{V}dt; \tag{2.17}$$

$$\begin{aligned}\int_{t_0}^{t_0+T}\int_{\mathcal{V}}u_i^\dagger\frac{\partial^2u_i}{\partial x_j\partial x_j}\,d\mathcal{V}dt &= \int_{t_0}^{t_0+T}\int_{\mathcal{S}_j^1}u_i^\dagger\frac{\partial\delta u_i}{\partial x_j}\,d\mathcal{S}_j^1dt - \int_{t_0}^{t_0+T}\int_{\mathcal{S}_j^0}u_i^\dagger\frac{\partial\delta u_i}{\partial x_j}\,d\mathcal{S}_j^0dt - \int_{t_0}^{t_0+T}\int_{\mathcal{V}}\frac{\partial u_i^\dagger}{\partial x_j}\frac{\partial\delta u_i}{\partial x_j}\,d\mathcal{V}dt\\ &= \int_{t_0}^{t_0+T}\int_{\mathcal{S}_j^1}u_i^\dagger\frac{\partial\delta u_i}{\partial x_j}\,d\mathcal{S}_j^1dt - \int_{t_0}^{t_0+T}\int_{\mathcal{S}_j^0}u_i^\dagger\frac{\partial\delta u_i}{\partial x_j}\,d\mathcal{S}_j^0dt - \int_{t_0}^{t_0+T}\int_{\mathcal{S}_j^1}\frac{\partial u_i^\dagger}{\partial x_j}\delta u_i\,d\mathcal{S}_j^1dt + \int_{t_0}^{t_0+T}\int_{\mathcal{S}_j^0}\frac{\partial u_i^\dagger}{\partial x_j}\delta u_i\,d\mathcal{S}_j^0dt + \int_{t_0}^{t_0+T}\int_{\mathcal{V}}\frac{\partial^2u_i^\dagger}{\partial x_j\partial x_j}\delta u_i\,d\mathcal{V}dt;\end{aligned} \tag{2.18}$$

$$\int_{t_0}^{t_0+T}\int_{\mathcal{V}}p^\dagger\frac{\partial\delta u_i}{\partial x_i}\,d\mathcal{V}dt = \int_{t_0}^{t_0+T}\int_{\mathcal{S}_i^1}p^\dagger\delta u_i\,d\mathcal{S}_i^1dt - \int_{t_0}^{t_0+T}\int_{\mathcal{S}_i^0}p^\dagger\delta u_i\,d\mathcal{S}_i^0dt - \int_{t_0}^{t_0+T}\int_{\mathcal{V}}\frac{\partial p^\dagger}{\partial x_i}\delta u_i\,d\mathcal{V}dt. \tag{2.19}$$

The surface terms cancel out if $u_i^\dagger$ verifies the same periodicity or homogeneity boundary conditions as u_i. Concerning the pressure terms, the surface integrals are zero where δu_i is identically zero (at

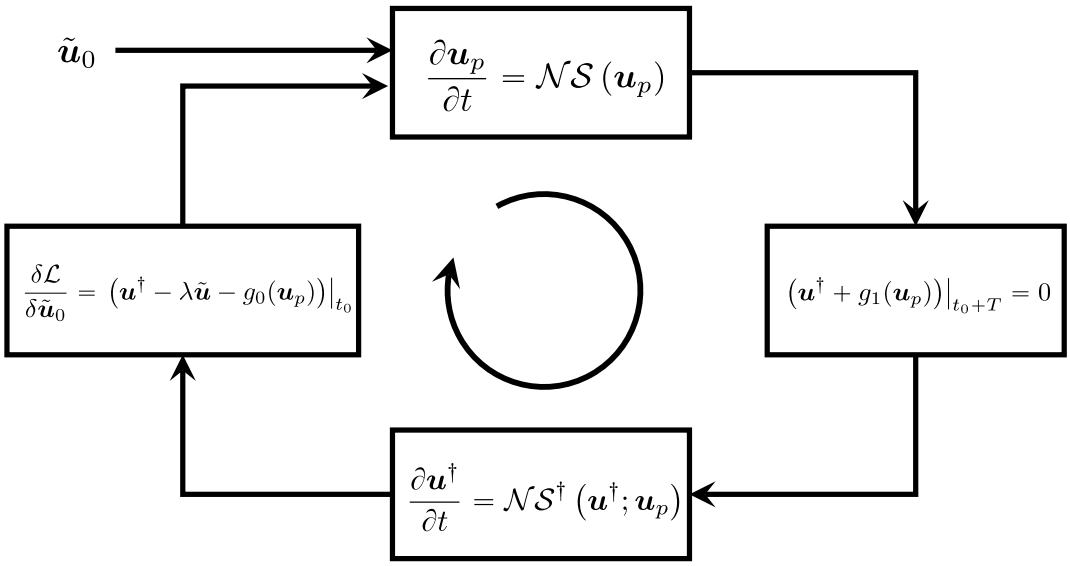

Figure 2.3: Schematic visualisation of the direct-adjoint loop.

walls) and at boundaries where $p^\dagger$ and δu_i are both periodic. When the pressure $p^\dagger$ can be decomposed into periodic and constant contributions, the surface terms are zero if the integral of δu_i is zero, which is verified because the flow rate of the direct velocity is fixed.

Therefore, the first variation of $\mathcal{L}$ with respect to u_i is:

$$\begin{aligned}\delta_{u_i}\mathcal{L} = \delta_{u_i}\mathcal{J} + \int_{\mathcal{V}} u_i^\dagger \delta u_i \, d\mathcal{V}\Big|_{t_0+T} - \int_{\mathcal{V}} \left(u_i^\dagger - \lambda\tilde{u}_i\right)\delta u_i \, d\mathcal{V}\Big|_{t_0} - \\ \int_{t_0}^{t_0+T}\int_{\mathcal{V}} \left[\frac{\partial u_i^\dagger}{\partial t} - u_j^\dagger\frac{\partial u_j}{\partial x_i} + u_j\frac{\partial u_i^\dagger}{\partial x_j} + \frac{\partial p^\dagger}{\partial x_i} + \frac{1}{Re}\frac{\partial^2 u_i^\dagger}{\partial x_j \partial x_j}\right]\delta u_i \, d\mathcal{V}dt.\end{aligned} \tag{2.20}$$

The variation $\delta_{u_i}\mathcal{J}$ is, in general, the sum of three terms:

$$\delta_{u_i}\mathcal{J} = \int_{\mathcal{V}} g_1(u_i)\delta u_i \, d\mathcal{V}\Big|_{t_0+T} + \int_{\mathcal{V}} g_0(u_i)\delta u_i \, d\mathcal{V}\Big|_{t_0} + \int_{t_0}^{t_0+T}\int_{\mathcal{V}} h(u_i)\delta u_i \, d\mathcal{V}dt. \tag{2.21}$$

Hence, to have $\delta_{u_i}\mathcal{L}$ be zero for every δu_i, the following equations must be satisfied in addition to the direct equations:

i. the adjoint equation:

$$\frac{\partial u_i^\dagger}{\partial t} - u_j^\dagger\frac{\partial u_j}{\partial x_i} + u_j\frac{\partial u_i^\dagger}{\partial x_j} + \frac{\partial p^\dagger}{\partial x_i} + \frac{1}{Re}\frac{\partial^2 u_i^\dagger}{\partial x_j \partial x_j} - h(u_i) = 0; \tag{2.22}$$

ii. the compatibility condition:

$$\left(u_i^\dagger + g_1(u_i)\right)\Big|_{t_0+T} = 0; \tag{2.23}$$

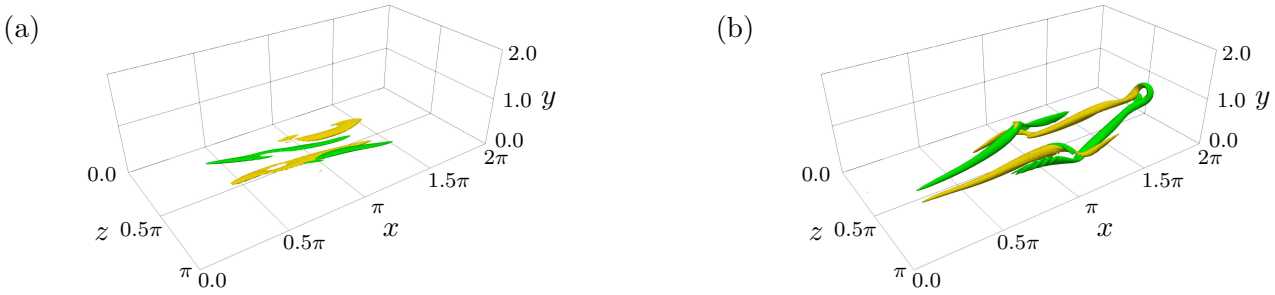

Figure 2.4: Visualisation of the hairpin-like optimal perturbation found by Farano et al. (2015). Q criterion coloured with streamwise vorticity (yellow/green for positive/negative) at (a) initial time t_0 ($Q = 0.03$) and (b) target time $t_0 + T$ ($Q = 2.0$).

iii. the optimality condition:

$$\left(u_i^\dagger - \lambda \tilde{u}_i - g_0(u_i)\right)\Big|_{t_0} = 0. \tag{2.24}$$

The standard numerical approach for this problem is direct-adjoint looping: the direct equations are solved starting from an initial guess for $\tilde{\boldsymbol{u}}_0$, the compatibility condition is used to initialise $u_i^\dagger$, the adjoint equations are solved backwards in time to give $u_i^\dagger(t_0)$. At this point, the optimality condition will not be satisfied, but the expression $G_i = u_i^\dagger - \lambda \tilde{u}_i - g_0(u_i)$ will give the direction of the gradient along which $\tilde{\boldsymbol{u}}_0$ must be updated. The unknown λ, due to the energy constraint, is handled with the gradient rotation method (Foures et al., 2013). This method consists of rescaling the perturbation to the desired energy after the update. The direct-adjoint loop is outlined in figure 2.3. The iteration is stopped when the norm of the solution update is below a given tolerance.

An important detail which impacts the implementation of the method is the presence of the direct solution in the adjoint equation. This implies that the solution needs to be stored in memory for every time step during the direct integration. Especially for large T, a checkpointing strategy can be used to relax the memory requirements.

The adjoint equations and the direct-adjoint looping were implemented in channelflow in previous PhD works (Parente, 2021; Farano, 2018). In this thesis, the code was modified to work with unsteady turbulent baseline flows.

2.4.2 NLOP validation

The nonlinear optimisation procedure was validated at the very beginning of the thesis, reproducing previously known NLOPs in the channel flow. For example, figure 2.4 shows the hairpin-like NLOP found by Farano et al. (2015) perturbing the limanar solution at $Re_c = 4000$ (based on the laminar flow centreline velocity) in a domain of size $[L_x \times L_y \times L_z] = [2\pi \times 2 \times \pi]$ with target time $T = 10$ and initial energy $E_0 = 2.0 \cdot 10^{-6}$.

2.5 Proper Orthogonal Decomposition

This section aims to introduce various Proper Orthogonal Decomposition (POD) methods. The classical approach, introduced in turbulence research by Lumley (1967), is described first. Then, we briefly describe the variant that is used in Chapter 3. The idea behind these techniques is to search for a set of modes (eigenvectors) which can optimally represent physical data. Usually, the aim is to approximate well enough the important dynamics of the system under consideration with a limited number of modes (dimensionality reduction). In the most widely used version, spatial POD, the orthogonal modes take into account the spatial structure of the flow, while the temporal dynamics are retained in the amplitude coefficients.

2.5.1 Standard formulation

The following description is adapted from Holmes et al. (2012). For simplicity, the method is presented on a scalar field $q(\boldsymbol{x}, t)$. Let us assume that the field can be written as a Galerkin expansion:

$$q(\boldsymbol{x}, t) = \sum_{j=1}^{\infty} a_j(t)\phi_j(\boldsymbol{x}) \approx \sum_{j=1}^{N} a_j(t)\phi_j(\boldsymbol{x}). \tag{2.25}$$

The functions $\boldsymbol{\phi}_j$ constitute a functional basis for the spatial variation of $q(\boldsymbol{x}, t)$. They are referred to as the spatial modes.
An approximation is done when the sum is truncated. This approximation is useful if the discarded modes play a negligible role in the dynamics of q. POD aims to find a set of orthogonal modes such that the relevant information is contained in the least possible number of modes.

The orthogonality property can be expressed by $\langle \phi_i, \phi_j \rangle = \delta_{ij}$ if the functional inner product

$$\langle f, g \rangle (t) = \int_{\mathcal{V}} g(\boldsymbol{x}, t) f(\boldsymbol{x}, t)\, d\boldsymbol{x} \tag{2.26}$$

is introduced ($\mathcal{V}$ is the spatial domain). The induced functional norm is $\|f\|^2 = \langle f, f \rangle$.

Owing to the orthogonality property, the expansion coefficients are given by the projection of q on the modes:

$$a_j(t) = \langle q(\boldsymbol{x}, t), \phi_j(\boldsymbol{x}) \rangle . \tag{2.27}$$

The POD mode is defined by

$$\text{find } \phi_j(\boldsymbol{x}) \quad \text{such that} \quad \frac{E\left[|\langle q, \phi_j \rangle|^2\right]}{\|\phi_j\|^2} = \max_f \frac{E\left[|\langle q, f \rangle|^2\right]}{\|f\|^2}, \tag{2.28}$$

where $E[\cdot]$ is the expected value operator. If the system is ergodic in time, the expected value operator can be taken as the temporal average.

Again, this is a variational problem. The POD mode can be found as the field that maximises the following augmented functional:

$$\mathcal{L} = E\left[\left(\int_{\mathcal{V}} q(\boldsymbol{x}) \phi(\boldsymbol{x})\, d\boldsymbol{x} \right)^2 \right] - \lambda \left(\|\phi\|^2 - 1 \right). \tag{2.29}$$

The first variation of the functional is

$$\begin{aligned}\delta\mathcal{L} &= \frac{\partial}{\partial\epsilon}\mathcal{L}\left[\phi+\epsilon\delta\phi\right]\Big|_{\epsilon=0} \\ &= E\left[2\int_{\mathcal{V}} q(\boldsymbol{x})\delta\phi(\boldsymbol{x})\,d\boldsymbol{x}\int_{\mathcal{V}} q(\boldsymbol{x}')\phi(\boldsymbol{x}')\,d\boldsymbol{x}'\right]-2\lambda\int_{\mathcal{V}}\phi(\boldsymbol{x})\delta\phi(\boldsymbol{x})\,d\boldsymbol{x} \\ &= 2\int_{\mathcal{V}}\left(E\left[q(\boldsymbol{x})\int_{\mathcal{V}} q\left(\boldsymbol{x}'\right)\phi\left(\boldsymbol{x}'\right)\,d\boldsymbol{x}'\right]-\lambda\phi(\boldsymbol{x})\right)\delta\phi(\boldsymbol{x})\,d\boldsymbol{x} \\ &= 2\int_{\mathcal{V}}\left(\int_{\mathcal{V}} E\left[q(\boldsymbol{x})q\left(\boldsymbol{x}'\right)\right]\phi\left(\boldsymbol{x}'\right)\,d\boldsymbol{x}'-\lambda\phi(\boldsymbol{x})\right)\delta\phi(\boldsymbol{x})\,d\boldsymbol{x}.\end{aligned} \tag{2.30}$$

Therefore, in order to make $\delta\mathcal{L}$ zero for every $\delta\phi$,

$$\int_{\mathcal{V}} C\left(\boldsymbol{x},\boldsymbol{x}'\right)\phi\left(\boldsymbol{x}'\right)\,d\boldsymbol{x}'=\lambda\phi(\boldsymbol{x}), \tag{2.31}$$

where $C\left(\boldsymbol{x},\boldsymbol{x}'\right)=E\left[q(\boldsymbol{x})q\left(\boldsymbol{x}'\right)\right]$ is the two-point correlation function of q. This gives an integral equation for ϕ called *Fredholm eigenvalue problem*. Note that ϕ is defined up to an arbitrary norm. The Hilbert-Schmidt theorem, a theorem on integral equations (Riley et al. (2006)), states that there are infinite solutions $(\lambda_j,\phi_j(\boldsymbol{x}))$ to (2.31) and the positive-semi-definiteness of $C\left(\boldsymbol{x},\boldsymbol{x}'\right)$ ensures that λ_j is always non-negative. The theory is valid for vector fields as well as for complex-valued fields.

POD has the following important property:

$$E\left[a_i(t)a_j(t)\right]=\delta_{ij}\lambda_j, \tag{2.32}$$

i.e. the temporal coefficients corresponding to different modes are uncorrelated. If $i=j$, it turns out that $\lambda_j^2=E\left[a_j^2\right]$. Hence, the $j-th$ eigenvalue is a measure of the energy contained in the $j-th$ mode. Therefore, a hierarchy of modes is obtained from (2.31): the most energetic modes are statistically important for the dynamics of the system, while the less energetic ones can be neglected in a reduced order model. Note, however, that this empirical argument may fail.

2.5.2 POD variants

Despite some shortcomings, POD is still used to investigate the dynamics of coherent structures, with different variants that have been proposed. Among these variants, the Conditional Space-Time POD, proposed by Schmidt and Schmid (2019) for the analysis of short transient events, is employed in Chapter 3.

In this variant, an ensemble of short transient events $\mathcal{E}=\{q_1(\boldsymbol{x},t),q_2(\boldsymbol{x},t),\dots\}$ is considered. The expected value operator is the average over the ensemble $\mathcal{E}$. A space-time inner product is considered:

$$\langle f,g\rangle=\int_T\int_{\mathcal{V}} g(\boldsymbol{x},t)f(\boldsymbol{x},t)d\boldsymbol{x}dt, \tag{2.33}$$

where $\mathcal{V}$ is the spatial domain and T the temporal duration of the event.

With these definitions, the eigenvalue problem that solves (2.28) is:

$$\int_T \int_{\mathcal{V}} C\left(\boldsymbol{x}, t, \boldsymbol{x}', t'\right) \phi\left(\boldsymbol{x}', t'\right) d\boldsymbol{x}' dt' = \lambda \phi\left(\boldsymbol{x}, t\right), \tag{2.34}$$

where $\boldsymbol{C}\left(\boldsymbol{x}, t, \boldsymbol{x}', t'\right) = E\left[q(\boldsymbol{x}, t) q(\boldsymbol{x}', t')\right]$ is the spatio-temporal two-point correlation function.

2.5.3 Numerical implementation

In principle, the integral eigenvalue problems (2.31,2.34) can be discretised to give matrix-based eigenvalue problems:

$$\mathbf{Q}\mathbf{Q}^T\mathbf{W}\boldsymbol{\phi} = \lambda\boldsymbol{\phi}. \tag{2.35}$$

The matrix $\mathbf{Q}$ contains M columns of dimension N and its arrangement depends on the variant considered, while the matrix $\mathbf{W}$ is a diagonal matrix containing the (positive) quadrature weights. In spatial POD, a column is a snapshot of the flow at a certain instant of time, N is the number of spatial points, and M is the number of temporal snapshots. In CST-POD, M is the number of events, and N is the number of spatial points times the number of time steps considered for each event. Usually, $N \gg M$. The matrix in (2.35) is of size $N \times N$. Therefore, it is inconvenient to compute the modes through (2.35).

Luckily, (2.35) is equivalent to the Singular Value Decomposition (SVD) of $\mathbf{W}^{1/2}\mathbf{Q}$. This decomposition can be written as:

$$\mathbf{W}^{1/2}\mathbf{Q} = \mathbf{U}\mathbf{\Sigma}\mathbf{V}^T, \tag{2.36}$$

where $\mathbf{U}$ and $\mathbf{V}$ are the unitary matrices and $\mathbf{\Sigma}$ is a rectangular matrix containing the non zero $\sqrt{\lambda_j}$ on its diagonal. Moreover, $\mathbf{U}$ contains the eigenvectors $\boldsymbol{\phi}$ as its columns. Numerically, the SVD-based method is the best conditioned one (Taira et al., 2017). Therefore, we choose this approach, which is implemented in some *in-house* python codes using the scipy linalg library.

2.5.4 POD validation

The POD code is validated with the results of Moin and Moser (1989) on the turbulent channel flow at $Re_\tau = 180$. In the first part of their paper, Moin and Moser (1989) cosidered the POD decomposition of the 1D two-point correlation matrix $\boldsymbol{C}(y, y')$ defined by $C_{i,j}(y, y') = \langle u_i(y) u_j(y') \rangle$ with $\langle\rangle$ denoting the average in x, z and t. Therefore, the POD is perfomed tiling the wall-normal profiles of the instantaneous velocity components as columns of the matrix $\mathbf{Q}$ for each x, z and t. Only half of the channel is considered. Due to the channel symmetries, the fields reflected in the wall-normal direction (changing the sign of the wall-normal velocity component) are added to the statistical ensemble. The computation was performed using 400 and 800 DNS snapshots with minimal changes in the results. We obtain as energy fraction of the first three leading modes $(\lambda_i / \sum_i \lambda_i)$ $31.4 \pm 0.1\%$, $15.4 \pm 0.1\%$ and $8.4 \pm 0.1\%$, in good agreement with the reference, which reports, respectively, 32%, 16% and 8%. The first four leading modes $\boldsymbol{\phi}^{(i)}$ are compared to the reference data in figure 2.5. It can be seen that the modes agree very well, validating our POD code.

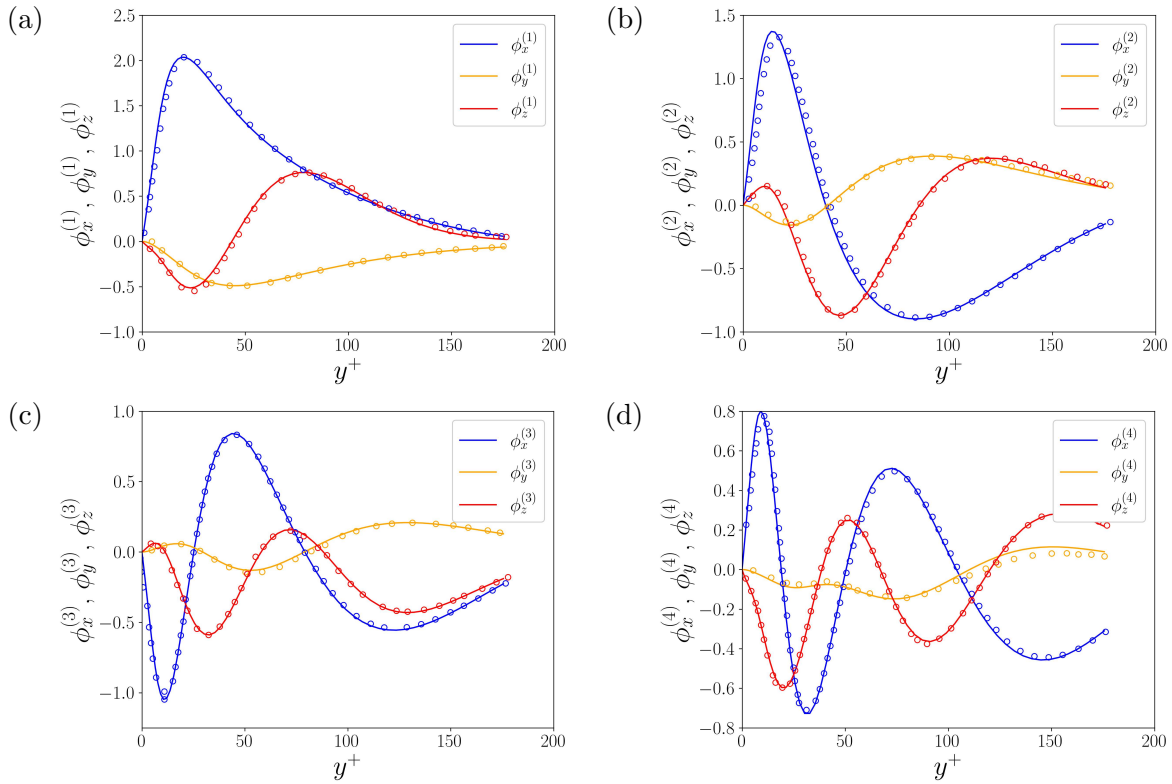

Figure 2.5: Validation of the POD code on the turbulent channel flow at $Re_\tau = 180$. The leading four POD modes of the 1D two-point correlation matrix $\boldsymbol{C}(y, y')$ are shown from (a) to (d) for decreasing contribution to the total energy. Open circles are reference data by Moin and Moser (1989).

2.6 Linear Stability Analysis

2.6.1 Generalities

Linear stability analysis (LSA) is concerned with the behaviour of small perturbations added to invariant solutions of (2.1). The unperturbed solution is called the *base flow* and will be denoted by $\{\boldsymbol{U}, P\}$ in this section and, generally, throughout the thesis.
We consider the most usual case where the base flow is a steady state. This means that the base flow verifies the following equations:

$$\begin{cases} \boldsymbol{U} \cdot \boldsymbol{\nabla} \boldsymbol{U} + \boldsymbol{\nabla} P - \dfrac{1}{Re} \nabla^2 \boldsymbol{U} = 0, \\ \boldsymbol{\nabla} \cdot \boldsymbol{U} = 0. \end{cases} \tag{2.37}$$

The perturbation, denoted by $\{\boldsymbol{u}', p'\}$ in this section, is assumed to have a vanishing amplitude. Since the total flow verifies (2.1), the perturbation equations can be obtained by subtracting (2.37) from (2.1). Moreover, the quadratic term $\boldsymbol{u}' \boldsymbol{\nabla} \boldsymbol{u}'$, being a second-order term in perturbation amplitude,

can be neglected. As a result, the following system is obtained:

$$\begin{cases} \dfrac{\partial \boldsymbol{u}'}{\partial t} + \boldsymbol{U}\cdot\boldsymbol{\nabla}\boldsymbol{u}' + \boldsymbol{u}'\cdot\boldsymbol{\nabla}\boldsymbol{U} = -\boldsymbol{\nabla}p' + \dfrac{1}{Re}\nabla^2\boldsymbol{u}', \\ \boldsymbol{\nabla}\cdot\boldsymbol{u}' = 0. \end{cases} \tag{2.38}$$

Clearly, the equations are linear with respect to $\boldsymbol{u}'$.

This thesis is concerned with LSA of coherent structures in turbulent flows. Therefore, the question arises of how to model the effect of incoherent fluctuations on the base flow plus perturbation system. Following Reynolds and Hussain (1972), an eddy viscosity term is included in the system:

$$\begin{cases} \dfrac{\partial \boldsymbol{u}}{\partial t} + \boldsymbol{u}\cdot\boldsymbol{\nabla}\boldsymbol{u} = -\boldsymbol{\nabla}p + \dfrac{1}{Re}\nabla^2\boldsymbol{u} + \boldsymbol{\nabla}\cdot\left[\nu_t\left(\boldsymbol{\nabla}\boldsymbol{u} + (\boldsymbol{\nabla}\boldsymbol{u})^T\right)\right], \\ \boldsymbol{\nabla}\cdot\boldsymbol{u}' = 0. \end{cases} \tag{2.39}$$

which can be linearised around the base flow to give:

$$\begin{cases} \dfrac{\partial \boldsymbol{u}'}{\partial t} + \boldsymbol{U}\cdot\boldsymbol{\nabla}\boldsymbol{u}' + \boldsymbol{u}'\cdot\boldsymbol{\nabla}\boldsymbol{U} = -\boldsymbol{\nabla}p' + \dfrac{1}{Re}\nabla^2\boldsymbol{u}' + \boldsymbol{\nabla}\cdot\left[\nu_t\left(\boldsymbol{\nabla}\boldsymbol{u}' + (\boldsymbol{\nabla}\boldsymbol{u}')^T\right)\right], \\ \boldsymbol{\nabla}\cdot\boldsymbol{u}' = 0. \end{cases} \tag{2.40}$$

Other possible models will be considered in Sections 5.3 and 6.4.1. We note that, in our models, $\boldsymbol{U}$ is not a steady state solution of (2.39), as explained in 2.6.2.

It is also important to note that the system with the eddy viscosity, or any other modelling term, is not derived from the Navier-Stokes equations (2.1). More precisely, it is not possible to define a mathematical relation between the solutions of (2.1) and (2.39). Therefore, system (2.39) is conceived as an empirical model representing a coarse-grained version of the physics of turbulent flows.

At this point, owing to the linearity and the equivariance in x and t of the system, the analysis is carried out by introducing a normal mode *ansatz* (modal analysis). The case considered in Chapters 4 and 5 of a two-dimensional baseflow, $[U(y,z), V(y,z), W(y,z)]^T$, will be specified. We assume that the eddy viscosity depends only on y, as in most of the cases considered in this thesis. Then, a normal mode with a complex frequency σ and a real streamwise wavenumber k_x, namely,

$$\boldsymbol{q}'(x,y,z,t) = e^{\sigma_r t}\hat{\boldsymbol{q}}(y,z)e^{\imath(k_x x+\sigma_i t)} + \text{ c.c. }, \tag{2.41}$$

can be injected in the linearised equations (2.40) for the perturbation $\boldsymbol{q}' = [\boldsymbol{u}', p']^T$ and the following generalized eigenvalue problem is obtained:

$$\sigma\mathscr{B}\hat{\boldsymbol{q}} = \mathscr{A}\hat{\boldsymbol{q}}. \tag{2.42}$$

with:

$$\mathscr{B} = \begin{bmatrix} 1 & 0 & 0 & 0 \\ 0 & 1 & 0 & 0 \\ 0 & 0 & 1 & 0 \\ 0 & 0 & 0 & 0 \end{bmatrix}; \qquad \mathscr{A} = \begin{bmatrix} \mathscr{L} & -\frac{\partial U}{\partial y} + \imath k_x \frac{d\nu_t}{dy} & -\frac{\partial U}{\partial \overline{z}} & -\imath k_x \\ 0 & \mathscr{L} - \frac{\partial V}{\partial y} + \frac{d\nu_t}{dy}\frac{\partial}{\partial y} & -\frac{\partial V}{\partial z} & -\frac{\partial}{\partial y} \\ 0 & -\frac{\partial W}{\partial y} + \frac{d\nu_t}{dy}\frac{\partial}{\partial z} & \mathscr{L} - \frac{\partial W}{\partial \overline{z}} & -\frac{\partial}{\partial \overline{z}} \\ \imath k_x & \frac{\partial}{\partial y} & \frac{\partial}{\partial z} & 0 \end{bmatrix};$$

$$\mathscr{L} = -\imath k_x U - V\frac{\partial}{\partial y} - W\frac{\partial}{\partial z} + \left(\frac{1}{Re} + \nu_t\right)\nabla^2 + \frac{d\nu_t}{dy}\frac{\partial}{\partial y},$$

where $\nabla^2 = -k_x^2 + \frac{\partial^2}{\partial y^2} + \frac{\partial^2}{\partial \overline{z}^2}$ is the laplacian operator.

After discretization, (2.42) becomes an algebraic generalised eigenvalue problem $\sigma \mathbf{B}\tilde{\mathbf{q}} = \mathbf{A}\tilde{\mathbf{q}}$. The matrix $\mathbf{B}$ is present because we consider the formulation with primitive variables (velocity and pressure). In the literature, it is called *prolongation matrix* (Cerqueira and Sipp, 2014). In all the cases considered in the thesis, differential operators are discretised using a pseudospectral collocation method implemented in an in-house python code. Fourier collocation is used along the spanwise direction z and Chebyshev collocation along the wall-normal direction y. The expression of the differentiation matrices in physical space can be found in standard textbooks on spectral methods (Trefethen, 2000; Peyret, 2002). The matrices $\mathbf{A}$ and $\mathbf{B}$ are implemented as sparse matrices to reduce the memory requirements. Boundary conditions at the walls consist of homogeneous Dirichlet conditions for the perturbation velocity components and are implemented by modifying the matrices accordingly. The eigenvalue problem is solved using the scipy linalg library.

2.6.2 Stability of frozen base flows

Coherent structures persistently characterise turbulent flows, but usually, they are not invariant solutions of the Navier-Stokes equations. Exact coherent structures (ECS) as equilibria, travelling waves and periodic orbits are reported in the literature (see Section 1.2), but they are far from the turbulent attractor (Doohan et al., 2019). Instead, we will consider the stability of structures which are statistically representative of the turbulent flow. They will be computed using different methods, but they will not be invariant solutions. Therefore, their LSA relies on the frozen base flow assumption, which means that they will be treated *as if* they were steady solutions.

To illustrate this assumption, we recall the work of Barkley (2006), who performed the LSA of the mean flow around a circular cylinder to predict the frequency of the vortex shedding far from the Hopf bifurcation critical point. Its result is interesting since the LSA of the laminar solution can predict the frequency of the vortex shedding only at the critical point. However, contrary to the laminar flow, the mean flow is not a steady solution of the NS equations. Barkley (2006) argues that the mean flow

verifies the time-averaged NS equations:

$$\overline{\boldsymbol{U}} \cdot \boldsymbol{\nabla}\overline{\boldsymbol{U}} + \boldsymbol{\nabla}\overline{P} - \frac{1}{Re}\nabla^2\overline{\boldsymbol{U}} = -\boldsymbol{\nabla} \cdot (\overline{\boldsymbol{u}'\boldsymbol{u}'}). \tag{2.43}$$

Therefore, it can be seen as a steady solution of the forced system

$$\frac{\partial \boldsymbol{u}}{\partial t} + \boldsymbol{u} \cdot \boldsymbol{\nabla}\boldsymbol{u} = -\boldsymbol{\nabla}p + \frac{1}{Re}\nabla^2\boldsymbol{u} + \boldsymbol{f}, \tag{2.44}$$

with $\boldsymbol{f} = -\boldsymbol{\nabla} \cdot (\overline{\boldsymbol{u}'\boldsymbol{u}'})$. If $\boldsymbol{f}$ is constant, *i.e.* is not altered by the perturbation, it cancels out in the equations for the perturbations. Therefore, the linear equations for the perturbation are identical to those that would be obtained by perturbing a steady state.

Now, we note that this argument works for any base flow. Indeed, given an arbitrary base flow $\boldsymbol{U}$, which verifies the continuity constraint and the appropriate boundary conditions, one can always find a forcing $\boldsymbol{f}$ which, by definition, makes $\boldsymbol{U}$ verify the equation:

$$\boldsymbol{U} \cdot \boldsymbol{\nabla}\boldsymbol{U} + \boldsymbol{\nabla}P - \frac{1}{Re}\nabla^2\boldsymbol{U} = \boldsymbol{f}. \tag{2.45}$$

It can be assumed, as in the case considered by Barkley (2006), that the perturbation of $\boldsymbol{f}$ is negligible with respect to the perturbation of $\boldsymbol{U}$. In a turbulent environment, this hypothesis can be partially relaxed if an eddy viscosity model is introduced such that $\boldsymbol{U}$ verifies the equation

$$\boldsymbol{U} \cdot \boldsymbol{\nabla}\boldsymbol{U} + \boldsymbol{\nabla}P - \frac{1}{Re}\nabla^2\boldsymbol{U} - \boldsymbol{\nabla} \cdot \left[\nu_t \left(\boldsymbol{\nabla}\boldsymbol{U} + (\boldsymbol{\nabla}\boldsymbol{U})^T\right)\right] = \boldsymbol{f}, \tag{2.46}$$

and is a steady state of the system

$$\frac{\partial \boldsymbol{u}}{\partial t} + \boldsymbol{u} \cdot \boldsymbol{\nabla}\boldsymbol{u} = -\boldsymbol{\nabla}p + \frac{1}{Re}\nabla^2\boldsymbol{u} + \boldsymbol{\nabla} \cdot \left[\nu_t \left(\boldsymbol{\nabla}\boldsymbol{u} + (\boldsymbol{\nabla}\boldsymbol{u})^T\right)\right] + \boldsymbol{f}, \tag{2.47}$$

In this way, the effects of unresolved fluctuations are modelled by two terms: the ν_t term depends on $\boldsymbol{u}$ and is perturbed, while $\boldsymbol{f}$ is a constant term that models implicitly those effects that sustain the base flow. Now, if $\boldsymbol{U}$ is perturbed in (2.47), (2.46) is subtracted, and the quadratic perturbation terms are neglected, equation (2.40) is obtained for the perturbation. Note that in more sophisticated models, also ν_t is perturbed. This is not the case here, but will be studied in Chapter 6.

Of course, the introduction of the forcing $\boldsymbol{f}$ is *ad hoc* and does not change the fact that our LSA relies on the frozen base flow assumption. However, $\boldsymbol{f}$ helps to justify the assumption because it can be seen as an additional modelling term. In Section 1.2.3, we have seen that many linear studies employ a forcing in their model and that this forcing can be seen as a lumped nonlinear term. Specifically to our case, the forcing is needed to sustain two-dimensional streaks, which are not self-sustained (Moffatt, 1989). Therefore, it can be seen as a simplified model of the nonlinear interactions which are involved in the SSP.

2.6.3 Stability analysis of periodic systems

In this section, we assume that the baseflow $\boldsymbol{U}(y, z)$ is periodic along the direction z with wavelength ℓ_z. Floquet theory applied to the variable z, allows us to write the perturbation *ansatz* as

(Schmid and Henningson, 2012)

$$\boldsymbol{q}'(x,y,z,t) = e^{\sigma_r t}\hat{\boldsymbol{q}}(y,z)e^{\iota k_z z}e^{\iota(k_x x+\sigma_i t)} + \text{ c.c. }, \tag{2.48}$$

where $\hat{\boldsymbol{q}}(y,z)$ is periodic along z with wavelength ℓ_z and k_z is a spanwise wavenumber. In certain contexts, $\hat{\boldsymbol{q}}(y,z)e^{\iota k_z z}$ is called a *Bloch wave*. Taking the Fourier series of $\hat{\boldsymbol{q}}(y,z)$ with respect to z, the above expression can be rewritten as

$$\boldsymbol{q}'(x,y,z,t) = e^{\sigma_r t}e^{\iota(k_x x+\sigma_i t)}\sum_{m=-\infty}^{\infty}\tilde{\boldsymbol{q}}(y)e^{\iota\frac{2\pi}{\ell_x}(m+\epsilon)z} + \text{ c.c. }, \tag{2.49}$$

where $\epsilon = k_z\ell_z/2\pi$ is termed *Floquet parameter* and is a free parameter of the problem. In principle, ϵ can be any real number. However, the sum over m is invariant under the transformation $m+\epsilon \mapsto m+\epsilon+k \quad \forall k \in \mathbb{Z}$. Therefore, without loss of generality, ϵ can be taken in $[0,1)$. For $\epsilon = 0$, the term $e^{\iota k_z z}$ of the Bloch wave is 1, and the eigenmode reduces to $\hat{\boldsymbol{q}}(y,z)$, which has the same periodicity as the base flow (wavelength ℓ_z). This particular class of eigenmodes are called *harmonic modes*. On the other hand, choosing $\epsilon > 0$ is equivalent to choosing $k_z > 0$ and gives the fundamental[2] wavelength of the instability $\lambda_z^f = 2\pi/k_z = \ell_z/\epsilon$. From the expression of λ_z^f, we see that $\epsilon = 1/n$ with $n \in \mathbb{N}^+$ implies $\lambda_z^f = n\ell_z$. Therefore, in this case, the fundamental wavelength is an integer multiple of the base flow wavelength. The eigenmodes with this feature are called *sub-harmonic modes*. Lastly, the remaining modes, *i.e.* those which have a fundamental wavelength which is not an integer multiple of the base flow wavelength, are called *detuned modes* (Herbert, 1988).

Floquet theory is useful to classify the instabilities which arise on periodic base flows, and it has also been used to ease the numerical solutions of the LSA eigenvalue problem. Our numerical method, however, does not implement the Floquet *ansatz*. In principle, one can consider the simpler *ansatz* (2.41) and discretise the problem for $\hat{\boldsymbol{q}}(y,z)$ in a large domain of spanwise size L_z which contains N_u periods of the base flow, such that $L_z = N_u\ell_z$. If λ_z^f is contained in L_z, the corresponding detuned or sub-harmonic mode will be retrieved. However, a large L_z may be needed to capture a certain λ_z^f, and the computation would become very expensive. This problem can be avoided with the method proposed by Schmid et al. (2017), which is the one that we implement.

This method stems from the fact that, when the problem is discretised for N_u repetitions of the base flow (sub-units), the matrix $\mathbf{A}$ in $\sigma\mathbf{B}\tilde{\mathbf{q}} = \mathbf{A}\tilde{\mathbf{q}}$ has a block-circulant structure

$$\mathbf{A} = \begin{bmatrix} \mathbf{A}_0 & \mathbf{A}_1 & \cdots & \mathbf{A}_{N_u-1} \\ \mathbf{A}_{N_u-1} & \mathbf{A}_0 & \cdots & \mathbf{A}_{N_u-2} \\ \cdots & \cdots & \cdots & \cdots \\ \mathbf{A}_1 & \mathbf{A}_2 & \cdots & \mathbf{A}_0 \end{bmatrix}, \tag{2.50}$$

where N_u is the number of periodic units of the system. We assume that each block $\mathbf{A}_j$ has size $M \times M$ and, therefore, the matrix $\mathbf{A}$ has size $N_u M \times N_u M$.

[2]Certain authors call *fundamental instability* the harmonic instability ($\epsilon = 0$). This is not to be confused with our use of the adjective "fundamental", which denotes the longest wavelength of any eigenmode.

The matrix $\mathbf{A}$ can be transformed into block-diagonal form using the unitary transformation[3]

$$\hat{\mathbf{A}} = \mathbf{P}^H \mathbf{A} \mathbf{P} = \begin{bmatrix} \hat{\mathbf{A}}_0 & & & \\ & \hat{\mathbf{A}}_1 & & \\ & & \ddots & \\ & & & \hat{\mathbf{A}}_{N_u-1} \end{bmatrix}, \tag{2.51}$$

where the H superscript denotes the conjugate-transpose. The matrix $\mathbf{P}$ which maps $\mathbf{A}$ to $\hat{\mathbf{A}}$ involves N_u roots of unity $\rho_j = \exp(2\pi\imath\gamma_j)$ parametrised by the factor $\gamma_j = j/N_u$ for $j = 0, 1, \ldots, N_u - 1$. In particular, $\mathbf{P}$ is constructed as

$$\mathbf{P} = \mathbf{J} \otimes \mathbf{I}_{M\times M}, \tag{2.52}$$

where $\otimes$ is the Kronecker product, $\mathbf{I}_{M\times M}$ is the identity matrix of size M and $\mathbf{J} \in \mathbb{C}^{N_u \times N_u}$ is the matrix with elements $\mathbf{J}_{j+1,k+1} = \rho_j^k/\sqrt{N_u}$.

After some algebra, the following relation is established:

$$\hat{\mathbf{A}}_j = \sum_{k=0}^{N_u-1} \rho_j^k \mathbf{A}_k. \tag{2.53}$$

Note that $\hat{\mathbf{A}}_j$ has size $M \times M$.

The following important properties can be proven. The union of the eigenspectra of the matrices $\hat{\mathbf{A}}_j$ for $j = 0, 1, \ldots, N_u - 1$ gives the eigenspectrum of the original matrix $\mathbf{A}$. Moreover, let $\{\sigma_j, \mathbf{v}_j\}$ be a given eigenvalue-eigenvector couple of $\hat{\mathbf{A}}_j$. Then, $\{\sigma_j, \mathbf{q}_j\}$ is an eigenvalue-eigenvector couple of $\mathbf{A}$ with the eigenvector given by

$$\mathbf{q}_j = \begin{bmatrix} \mathbf{v}_j \\ \rho_j \mathbf{v}_j \\ \rho_j^2 \mathbf{v}_j \\ \vdots \\ \rho_j^{N_u-1} \mathbf{v}_j \end{bmatrix}. \tag{2.54}$$

The above expression means that an eigenmode of the original problem is obtained by *tiling* an eigenmode $\mathbf{v}_j$ along the sub-units. At each sub-unit, $\mathbf{v}_j$ is phase-shifted by the powers of ρ_j. Therefore, $\mathbf{v}_j$ will be repeated after the condition $\rho_j^{N_p} = 1$ is met and N_p, defined by this condition, gives the number of sub-units over which $\mathbf{q}_j$ is periodic. This allows to find the fundamental wavelength of $\mathbf{q}_j$ with the expression $\lambda_z^f = N_p \ell_z = \ell_z/\gamma_j$. Therefore, γ_j can be used to fix the fundamental wavelength of the eigenmode and plays the same role as the Floquet parameter ϵ, the only difference being that ϵ can take any real value while γ_j takes N_u discrete rational values.

In conclusion, the LSA of a large system containing N_u repetitions of the base flow is performed with the following procedure:

1. A large domain of spanwise size $L_z = N_u \ell_z$ is discretised and the blocks $\mathbf{A}_j$ are obtained;

[3] Concerning $\mathbf{B}$, note that it is a diagonal matrix invariant under this transformation.

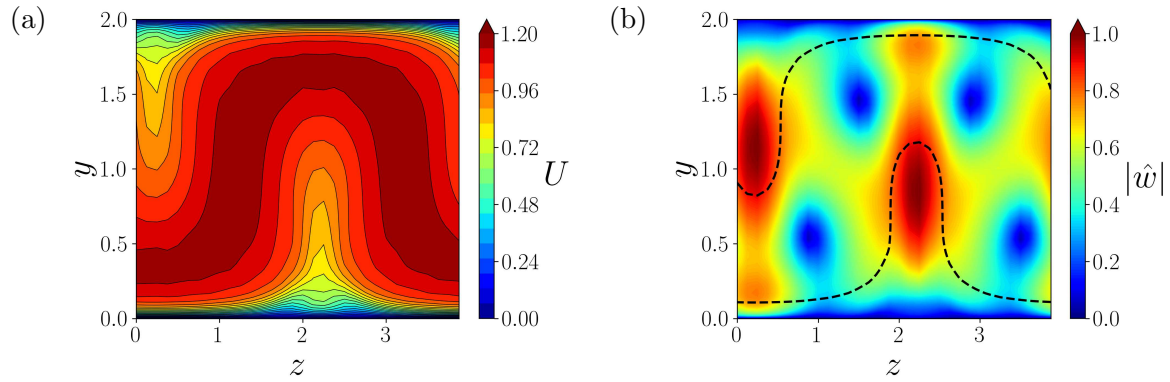

Figure 2.6: Validation of the LSA code with the case of Park et al. (2011) (see text). $Re_\tau = 300$, $A_s = 0.23$ and $k_x = 1.3$. (a) Base flow obtained from the saturation of a linear optimal perturbation. (b) Absolute value of the spanwise velocity component of the unstable eigenmode. The dashed line is the critical layer.

2. For each $j = 0, 1, \ldots, N_u - 1$, $\rho_j = \exp(2\pi\iota\gamma_j)$ is used to compute the $M \times M$ matrix $\hat{\mathbf{A}}_j$ using (2.53) and the problem $\sigma_j \mathbf{B}_0 \mathbf{v}_j = \hat{\mathbf{A}}_j \mathbf{v}_j$[4] is solved resulting in an ensemble of $\{\sigma_j, \mathbf{v}_j\}$ eigenvalue-eigenvector couples (for each j).

3. The eigenspectrum of $\mathbf{A}$, $\{\sigma\}$ is obtained by the union of the eigenspectra of $\hat{\mathbf{A}}_j$, $\{\sigma_j\}$;

4. The eigenvectors are stored as the ensemble $\bigcup_{j=0}^{N_u-1}\{\mathbf{v}_j\}$. A given eigenvector of the original problem belonging to the ensemble $\{\mathbf{q}_j\}$ is retrieved when needed using (2.54).

It is apparent from the above procedure that, with this method, the analysis of a system of size $N_u M \times N_u M$ has been reduced to N_u computations on a system of size $M \times M$. This is equivalent to N_u computations with the Floquet *ansatz* for N_u different values of ϵ.

The block-circulant matrix method and Floquet theory give identical results. This is shown in the next subsection as part of the validation of the numerical code. The block-circulant matrix method is slightly more flexible, since it can be easily extended to perform nonmodal analyses (Schmid et al., 2017). The code has been adapted from the code used by Jouin (2023), from which the method is inherited.

2.6.4 LSA validation

The LSA code for two-dimensional base flows is validated against the results of Park et al. (2011) at $Re_\tau = 300$. Their procedure is followed: a linear optimal perturbation is computed linearising the equations around the mean flow, like in Pujals et al. (2009); the optimal initial vortices are rescaled with an amplitude $A_v = 0.1$ and evolved nonlinearly using, in our case, the channelflow code; then, the resulting streaks with amplitude $A_s = 0.23$ are added to the mean flow to form the base flow (figure 2.6 (a)). LSA of this base flow with streamwise wavenumber $k_x = 1.3$ gives an unstable mode, which is shown in figure 2.6 (b). The absolute value of the spanwise velocity component is shown along with

[4] $\mathbf{B}_0$ is a $\mathbf{B}$ with size $M \times M$.

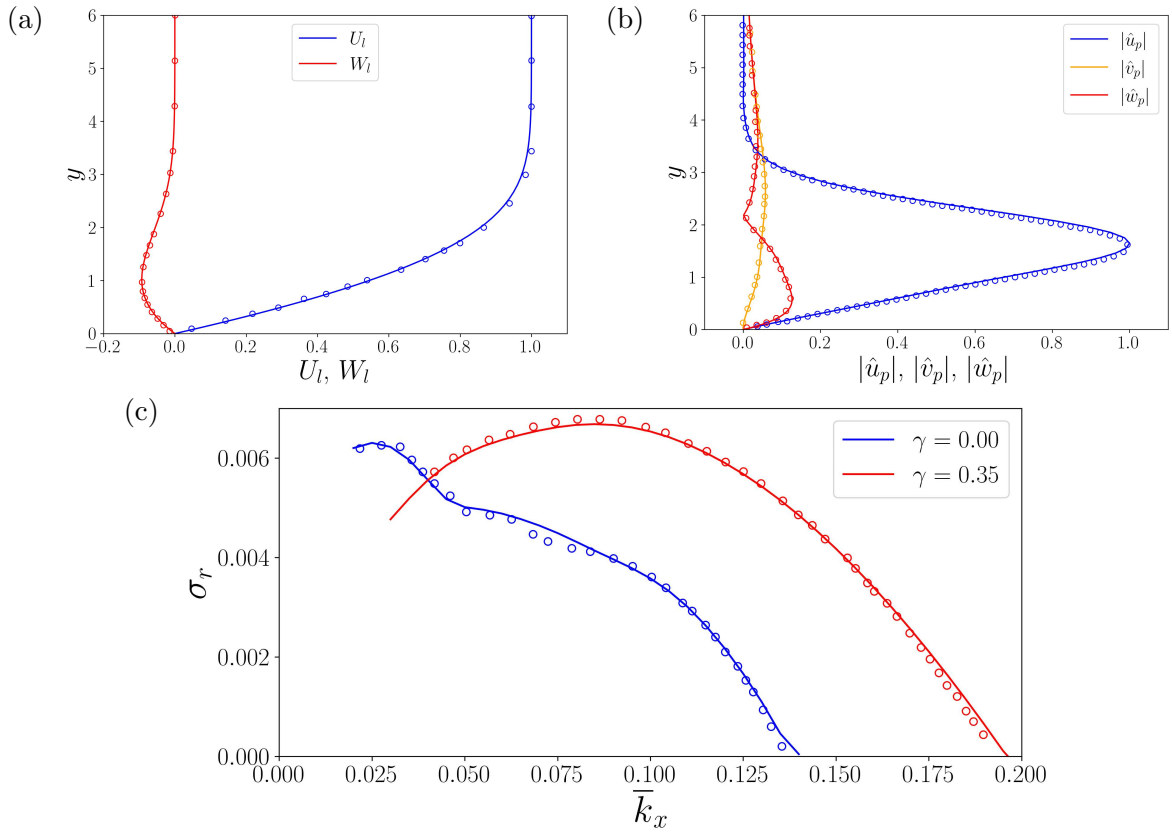

Figure 2.7: Validation of the LSA code with the secondary instability of crossflow vortices. (a) Laminar solution (Falkner-Skan-Cook profiles) for $\beta_H = 0.630$ and $\theta = 46.9°$. (b) Absolute value profiles of primary unstable eigenmode velocity components at $Re = 826$ for $k_x^p = 0.0361$ and $k_z^p = 0.4774$. (c) Growth rate of the secondary disturbance as a function of $\overline{k}_x$ for $A_p = 0.0789$ for the harmonic and a detuned case. In all panels, the circles are reference data from Fischer and Dallmann (1991).

the critical layer (the locus of points where the phase velocity of the mode is equal to the streamwise velocity of the base flow). This figure is identical to figure 4 (b) of Park et al. (2011) and figure 15 (d) of Alizard (2015). The growth rate and the phase velocity of the unstable mode are respectively $\sigma_r = 0.021$ and $c/U_c = 0.86$, which are in excellent agreement with Park et al. (2011) and Alizard (2015).

The above case validates the code for 2D LSA with eddy viscosity. However, only one period of the base flow was considered. To validate the block-circulant matrix method, we consider the study of Fischer and Dallmann (1991). This case was revisited in Jouin et al. (2024) and concerns the transition to turbulence on a swept boundary layer. The laminar profile is given by the Falkner-Skan-Cook profiles, which depend on two parameters: the sweep angle θ and the Hartree pressure gradient parameter β_H. Consistently with Fischer and Dallmann (1991) we consider $\theta = 46.9°$ and $\beta_H = 0.630$ (figure 2.7 (a)). This laminar solution is subject to an instability leading to *crossflow vortices*. The vortices saturate and undergo a secondary instability before the breakdown to turbulence. Fischer and Dallmann (1991) computed the secondary instability using spatial Floquet theory and showed that a

detuned mode is dominant for the secondary instability. Following Fischer and Dallmann (1991), figure 2.7 (b) shows the eigenmode of the primary instability at $Re = 826$ for the most amplified stationary disturbance, which is obtained with wavenumbers $k_x^p = 0.0361$ and $k_z^p = 0.4774$ (the p superscript stands for primary mode). The secondary instability of laminar flow plus this stationary disturbance rescaled to the amplitude 0.0789 can be studied in a rotated frame (similarly to what is done in Chapter 4 for inclined streaks). In this rotated frame, the base flow is uniform along a direction $\overline{x}$ and periodic along the rotated spanwise direction $\overline{z}$. The secondary disturbance will have the form (2.41) with $\overline{k}_x$ instead of k_x to denote the wavenumber in the $\overline{x}$ direction. We solve the secondary stability problem with the block-circulant matrix method, considering $N_u = 20$ periods of the base flow. The problem is solved only for the roots of unity which correspond to $\gamma = 0$ (harmonic disturbances) and $\gamma = 0.35$ (detuned disturbances). The curves of the leading growth rate as a function of $\overline{k}_x$ are shown in figure 2.7 (c) and compared to the results that Fischer and Dallmann (1991) obtained using the Floquet *ansatz* with $\epsilon = 0.00$ and $\epsilon = 0.35$ (ϵ is σ in the original paper). The excellent agreement between the two curves validates our implementation and demonstrates that Floquet theory and the block-circulant matrix method give identical results.

2.7 Resolvent Analysis

2.7.1 Optimal Harmonic Forcing

In Section 2.6.2, a forcing was introduced in the NS equations to sustain a certain base flow and make it a steady state. It was argued that this forcing models turbulent processes which are not resolved in the LSA model. In the introduction (see Section 1.2.3), it was discussed that the analysis of the linearised forced equations was introduced in the context of turbulent flows by Hwang and Cossu (2010a) and McKeon and Sharma (2010), who studied the structures, induced by a harmonic forcing, that are most amplified by the mean flow. The optimal harmonic forcing (OHF) problem was already studied in laminar-turbulent transition to explain subcritical transition (Jovanović and Bamieh, 2005) and convective instabilities (Alizard et al., 2009). Since Hwang and Cossu (2010a) showed that streaks are the optimal response of the mean flow to harmonic forcing, we will use OHF as a tool to compute the streaks for the stability analysis of Chapter 5.

In turbulent flows, OHF is studied with the system linearised around the mean profile:

$$\begin{cases} \dfrac{\partial \boldsymbol{u}'}{\partial t} = -\overline{\boldsymbol{U}} \cdot \boldsymbol{\nabla} \boldsymbol{u}' - \boldsymbol{u}' \cdot \boldsymbol{\nabla} \overline{\boldsymbol{U}} - \boldsymbol{\nabla} p' + \dfrac{1}{Re} \nabla^2 \boldsymbol{u}' + \boldsymbol{\nabla} \cdot \nu_t \left(\boldsymbol{\nabla} \boldsymbol{u}' + (\boldsymbol{\nabla} \boldsymbol{u}')^T \right) + \boldsymbol{f}, \\ \boldsymbol{\nabla} \cdot \boldsymbol{u}' = 0. \end{cases} \tag{2.55}$$

The eddy viscosity term is included in some models (Hwang and Cossu, 2010a) but not in others (McKeon and Sharma, 2010). Recent works, however, suggest that its inclusion ameliorates the model predictions (Illingworth et al., 2018; Morra et al., 2019; Symon et al., 2023). In the particular case of

the channel flow, the fields can be Fourier transformed in x, z and t:

$$\begin{aligned}
\hat{\boldsymbol{u}}(k_x, y, k_z, \omega) &= \int_{-\infty}^{\infty}\int_{-\infty}^{\infty}\int_{-\infty}^{\infty} \boldsymbol{u}'(x, y, z, t) e^{-\iota(k_x x + k_z z - \omega t)}\, dx dz dt, \\
\hat{p}(k_x, y, k_z, \omega) &= \int_{-\infty}^{\infty}\int_{-\infty}^{\infty}\int_{-\infty}^{\infty} p'(x, y, z, t) e^{-\iota(k_x x + k_z z - \omega t)}\, dx dz dt, \\
\hat{\boldsymbol{f}}(k_x, y, k_z, \omega) &= \int_{-\infty}^{\infty}\int_{-\infty}^{\infty}\int_{-\infty}^{\infty} \boldsymbol{f}(x, y, z, t) e^{-\iota(k_x x + k_z z - \omega t)}\, dx dz dt,
\end{aligned} \tag{2.56}$$

where k_x, k_z and ω are the (real) streamwise and spanwise wavenumbers and the (real) temporal frequency. Substituting (2.56) in (2.55) a linear equation is obtained for each $\{k_x, k_z, \omega\}$ triplet: $\iota\omega\mathscr{B}\hat{\boldsymbol{q}} = \mathscr{L}\hat{\boldsymbol{q}} + \mathscr{B}\hat{\boldsymbol{f}}$, where $\hat{\boldsymbol{q}}$ contains the primitive variables $\{\hat{\boldsymbol{u}}, \hat{p}\}$. For a known forcing, this equation can be formally inverted to give

$$\hat{\boldsymbol{q}} = (\iota\omega\mathscr{B} - \mathscr{L})^{-1}\mathscr{B}\hat{\boldsymbol{f}} = \mathcal{H}\hat{\boldsymbol{f}}, \tag{2.57}$$

where $\mathcal{H}(y; k_x, k_z, \omega) = (\iota\omega\mathscr{B} - \mathscr{L})^{-1}\mathscr{B}$ is the *Resolvent Operator*.

OHF is defined as the forcing that gives

$$R(k_x, k_z, \omega) = \max_{\hat{\boldsymbol{f}}\neq\boldsymbol{0}} \frac{\|\hat{\boldsymbol{u}}\|^2}{\left\|\hat{\boldsymbol{f}}\right\|^2} = \|\mathcal{H}\|^2, \tag{2.58}$$

where the standard functional L^2 norm has been used. The second equality follows from the definition of the induced norm of an operator. As a consequence of the definition, the response to OHF is the fluctuation that is optimally amplified by the system (in this case, by the mean flow).

2.7.2 Numerical method

The linear operators stemming from (2.55) for a one component 1D mean profile are:

$$\mathscr{B} = \begin{bmatrix} 1 & 0 & 0 & 0 \\ 0 & 1 & 0 & 0 \\ 0 & 0 & 1 & 0 \\ 0 & 0 & 0 & 0 \end{bmatrix}; \qquad \mathscr{L} = \begin{bmatrix} \mathcal{L} & -\frac{d\overline{U}}{dy} + \iota k_x \frac{d\nu_t}{dy} & 0 & -\iota k_x \\ 0 & \mathcal{L} + \frac{d\nu_t}{dy}\frac{d}{dy} & 0 & -\frac{d}{dy} \\ 0 & \iota k_z \frac{d\nu_t}{dy} & \mathcal{L} & -\iota k_z \\ \iota k_x & \frac{d}{dy} & \iota k_z & 0 \end{bmatrix};$$

$$\mathcal{L} = -\iota k_x \overline{U} + \left(\frac{1}{Re} + \nu_t\right)\nabla^2 + \frac{d\nu_t}{dy}\frac{d}{dy},$$

where $\nabla^2 = -k_x^2 - k_z^2 + \frac{d^2}{dy^2}$ is the laplacian operator. Similarly to LSA, these operators are discretised using a pseudospectral Chebyshev collocation method. Then, the discretised resolvent operator is

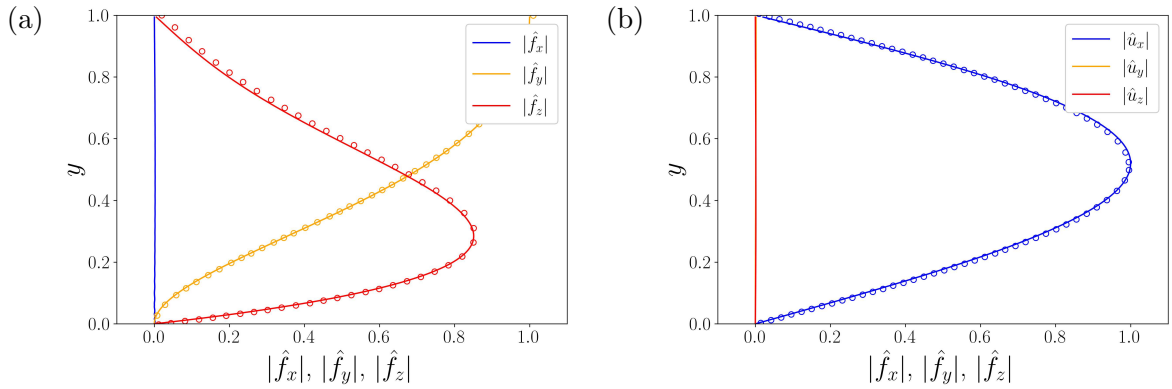

Figure 2.8: Validation of the resolvent code on the turbulent channel flow mean profile at $Re_\tau = 2000$ for $k_x = 0$, $k_z = 2\pi/3$ and $\omega = 0$. The figure shows the profiles of the three components of (a) the forcing and (b) the velocity response. Open circles are reference data by Symon et al. (2018).

obtained by matrix inversion $\mathbf{H} = (\imath\omega\mathbf{B} - \mathbf{L})^{-1}\mathbf{B}$. The optimal gain (2.58) is the algebraic L_2 norm of the matrix $\mathbf{W}^{1/2}\mathbf{H}\mathbf{W}^{-1/2}$, where $\mathbf{W}$ is a diagonal matrix containing the quadrature weights. This norm is computed by the SVD $\mathbf{W}^{1/2}\mathbf{H}\mathbf{W}^{-1/2} = \mathbf{U}\mathbf{\Sigma}\mathbf{V}^T$. The most amplified harmonic forcing is given by the first column of $\mathbf{V}$, the corresponding response mode by the first column of $\mathbf{U}$ and the energy amplification factor R by the square of the leading singular value of $\mathbf{H}$, which is the first diagonal element of $\mathbf{\Sigma}$. The method is implemented in an in-house python code which employs the scipy linalg library for matrix inversions and SVD.

2.7.3 OHF validation

The numerical code for the resolvent analysis was validated by some computations on the turbulent channel flow mean profile at high Re. The computations in this subsection are performed with 513 Chebyshev collocation points.

Figure 2.8 shows the optimal forcing and response at $Re_\tau = 2000$ for $\{k_x, k_z, \omega\} = \{0, 2\pi/3, 0\}$. Following the reference (Symon et al., 2018), this computation is performed without the eddy viscosity. It can be seen that the forcing and response modes perfectly agree with the reference. As in Symon et al. (2018), the streamwise component of the forcing and the wall-normal and spanwise components of the response are zero. This indicates that all the energy contained in the wall-normal and spanwise components is transferred to the streamwise component, a well-known effect of nonnormality of the NS operator induced by the shear. With the eddy viscosity and at lower Re, this energy transfer is not perfect, such that, for example, the response will contain some energy also in the transverse velocity components.

The above case does not validate the implementation of the eddy viscosity in the resolvent operator. For this reason, we also reproduce some results from Hwang and Cossu (2010a), which are shown in figure 2.9. In this figure, we have defined $R_{max} = \max_\omega R(k_x, k_z, \omega)$. We show the curve for $k_x = 0$, and we note that the optimal ω for this case is always zero. The figure shows that our results match

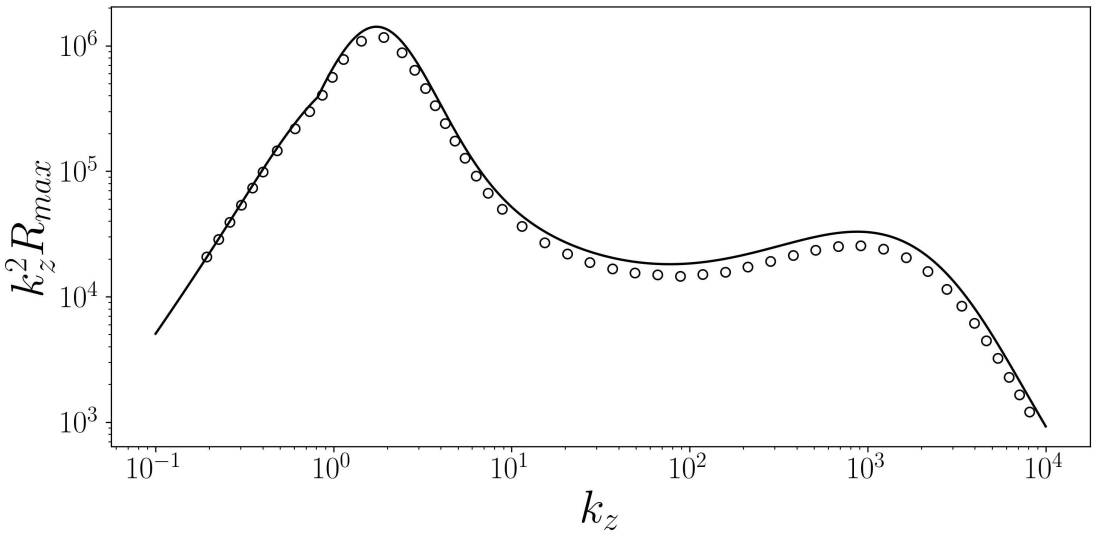

Figure 2.9: Validation of the resolvent code on the turbulent channel flow mean profile with eddy viscosity. Pre-multiplied resolvent norm as a function of spanwise wavenumber at $Re_\tau = 10000$ for $k_x = 0$. Open circles are reference data by Hwang and Cossu (2010a).

well with the reference, reproducing the double peak of the amplification factor.

Chapter 3

Nonlinear Optimal Perturbations and Extreme Events

3.1 Introduction to the chapter

Turbulent flows are characterised by intermittent dynamics. Highly energetic events known as *bursts* (Kim et al., 1971; Lozano-Durán et al., 2012) occur randomly in the flow alternated by periods of relatively quiescent dynamics. This intermittent behaviour is evident in minimal flow units (Jiménez and Moin, 1991; Blonigan et al., 2019) and is typical of the self-sustaining process in these domains (Hamilton et al., 1995). In larger domains, the multiscale nature of the flow makes the occurrence of the bursts more unpredictable. Therefore, they can be qualified as *extreme events* (EEs), *i.e.* essentially stochastic events in which a given observable reaches a large deviation from its mean value. These events are associated with the tail of the probability density function (PDF) of the observable (Sapsis, 2021).

Hack and Schmidt (2021) have recently investigated this subject using a Conditional Space-Time Proper Orthogonal Decomposition (CST-POD). They focused on highly dissipative events by sampling the flow field around intense local peaks of the turbulent dissipation. In this way, they have been able to identify the flow structure that is more correlated to these events. They have separated symmetric and antisymmetric structures, and they have found that the symmetric ones are slightly prevalent. Finally, they have related these structures to the hairpin vortices (Adrian, 2007) and the varicose streak instability (Andersson et al., 2001; Hack and Moin, 2018). The objective of this chapter is to link the structures found by Hack and Schmidt (2021) with those found by Farano et al. (2017) in nonlinear optimal perturbations (NLOPs). However, Farano et al. (2017) computed the optimal perturbations on the turbulent mean flow, whereas, to highlight the relation between EEs and streak instability, we extend the method to three-dimensional turbulent instantaneous fields. It will be shown that the resulting perturbations trigger a large number of EEs locally. Then, the question of whether these *artificial* EEs and the natural ones observed in direct numerical simulations (DNS) are equivalent is addressed using the CST-POD algorithm. Due to the high computational cost of the NLOP, the present work is limited to one Reynolds number, $Re_\tau = 180$.

The chapter is organised as follows. Governing equations and the procedure to compute NLOPs are recalled in Section 3.2. The resulting NLOPs are described in Section 3.3, while their temporal evolution is analysed in Section 3.4. The CST-POD analysis is presented in Section 3.5 followed by a brief discussion of the results in Section 3.6. The exposition in this chapter is adapted from the published paper Ciola et al. (2023).

3.2 Problem Formulation

The incompressible flow in a channel is considered. Periodic boundary conditions are imposed in the streamwise (x or x_1) and spanwise (z or x_3) directions. No-slip conditions are imposed in the wall-normal direction (y or x_2). The periodic domain has dimensions $[L_x, L_y, L_z]$. Quantities without any superscript are made dimensionless with the channel half-gap h^* (such that $L_y = 2$ and $0 \leqslant y \leqslant 2$) and the bulk velocity $U_b^* = \int_0^2 \int_0^{L_z} u^* \, dydz/2L_z$ (outer units). Quantities with a + superscript are made dimensionless with the viscous length $\delta_\nu^* = \nu^*/u_\tau^*$ and the friction velocity $u_\tau^* = \sqrt{\tau_w^*/\rho^*}$ (inner or wall units), where ρ^* is the fluid density, ν^* the kinematic viscosity and τ_w^* the measured mean wall shear stress. The streamwise, wall-normal and spanwise velocity components are denoted, respectively, by u, v and w or u_1, u_2 and u_3 when using index notation.

The instantaneous flow is governed by the Navier-Stokes equations for incompressible flows

$$\begin{cases} \dfrac{\partial \boldsymbol{u}}{\partial t} + \boldsymbol{u} \cdot \boldsymbol{\nabla} \boldsymbol{u} = -\boldsymbol{\nabla} p + \dfrac{1}{Re} \nabla^2 \boldsymbol{u} + \boldsymbol{f}_b, \\ \boldsymbol{\nabla} \cdot \boldsymbol{u} = 0, \end{cases} \tag{3.1}$$

where $Re = U_b^* h^*/\nu^*$ is the Reynolds number and $\boldsymbol{f}_b$ is a time-varying forcing that keeps the flow rate constant. The flow can be decomposed in long-time average $\overline{\boldsymbol{U}} = \overline{U}(y)\boldsymbol{e}_x$ plus instantaneous fluctuation $\boldsymbol{u}'$. By integrating the above equations in time from a given initial condition, a DNS of the turbulent flow is performed.

We can choose an instant t_0 and denote the flow field at t_0 as $\boldsymbol{u}_u(t_0)$. This flow field is perturbed, adding another field $\tilde{\boldsymbol{u}}(\boldsymbol{x}, t_0) \equiv \tilde{\boldsymbol{u}}_0$, which only needs to verify the boundary conditions and the continuity equation. The perturbed flow field at t_0 gives a new initial condition which can be integrated in time to give a new DNS trajectory $\boldsymbol{u}_p(\boldsymbol{x}, t)$. Extending the notation, the original DNS trajectory is denoted by $\boldsymbol{u}_u(\boldsymbol{x}, t)$ for $t \geqslant t_0$. Then, the instantaneous perturbation of the turbulent field is defined for $t \geqslant t_0$ by:

$$\tilde{\boldsymbol{u}}(\boldsymbol{x}, t) = \boldsymbol{u}_p(\boldsymbol{x}, t) - \boldsymbol{u}_u(\boldsymbol{x}, t), \tag{3.2}$$

and similarly for the pressure fields $\tilde{p}(\boldsymbol{x}, t) = p_p(\boldsymbol{x}, t) - p_u(\boldsymbol{x}, t)$. Note that $\tilde{\boldsymbol{u}}$ is different from the turbulent fluctuation $\boldsymbol{u}'$.

We look for the perturbation $\tilde{\boldsymbol{u}}_0$ that maximises the volume-averaged turbulent dissipation in a given time interval $[t_0, t_0 + T]$, namely

$$\mathcal{J} = \frac{1}{TV} \int_{t_0}^{t_0+T} \int_V \left(\frac{1}{Re} \boldsymbol{\nabla} \boldsymbol{u}' : \boldsymbol{\nabla} \boldsymbol{u}' \right) \, d\boldsymbol{x} dt, \tag{3.3}$$

subject to the constraint:

$$\frac{1}{V}\int_V \frac{\tilde{\boldsymbol{u}}\cdot\tilde{\boldsymbol{u}}}{2}\,dV = E_0. \tag{3.4}$$

A similar objective function was already considered by Monokrousos et al. (2011) and Eaves and Caulfield (2015) to compute NLOPs of the laminar flow.

The optimisation problem must include as constraints the governing equations for $\boldsymbol{u}_p(\boldsymbol{x},t)$. Therefore, the objective function must be augmented with the Lagrange multiplier method. The details of the method can be found in Section 2.4. As explained there, an adjoint equation and a compatibility condition are obtained by nullifying the first variation of the objective functional. With the chosen objective function (3.3), the adjoint equation reads[1]:

$$\frac{\partial u_i^\dagger}{\partial t} - u_j^\dagger\frac{\partial u_{p,j}}{\partial x_i} + u_{p,j}\frac{\partial u_i^\dagger}{\partial x_j} + \frac{\partial p^\dagger}{\partial x_i} + \frac{1}{Re}\frac{\partial^2 u_i^\dagger}{\partial x_j\partial x_j} + \frac{1}{ReT}\frac{\partial^2 u_i'}{\partial x_j\partial x_j} = 0. \tag{3.5}$$

The compatibility condition is simply $u_i^\dagger(t_0+T)=0$. Note that the adjoint equations (3.5) are forced by the fluctuations due to the form chosen for the objective function (3.3).

The direct and adjoint equations are solved simultaneously with the technique of the direct-adjoint looping (see also figure 2.3):

i. starting from an initial guess for $\tilde{\boldsymbol{u}}_0$, the direct equations (3.1) are advanced in time up to t_0+T;

ii. the compatibility condition $u_i^\dagger(t_0+T)=0$ is used to initialize the adjoint equations;

iii. the adjoint equations (3.5) are solved backward in time from t_0+T to t_0;

iv. the gradient

$$\frac{\delta\mathcal{L}}{\delta\tilde{\boldsymbol{u}}(t_0)} = u^\dagger(t_0) - \lambda\tilde{\boldsymbol{u}}(t_0) \tag{3.6}$$

is used to update the initial guess towards the optimal. The Lagrange multiplier λ is computed from the energy constraint (3.4) using the gradient rotation method (Foures et al., 2013). The new initial guess is used to restart from (i.) until convergence.

For a given initial energy E_0 and optimisation time T, the algorithm returns a perturbation field $\tilde{\boldsymbol{u}}_0$. This, in turn, brings to a certain perturbed flow evolution $\boldsymbol{u}_p(\boldsymbol{x},t)$. The first nontrivial question is how to fix E_0 and T.

3.3 Nonlinear optimal perturbations

3.3.1 Choice of parameters

The direct and adjoint equations are solved using the channelflow code by Gibson et al. (2021). For this study, we consider a domain having dimensions $[L_x, L_y, L_z] = [4\pi, 2, 2\pi]$ discretised with 288,

[1] Summation is implied on the repeated indices.

129 and 240 collocation points, respectively, in the streamwise, wall-normal and spanwise directions. After dealiasing, this choice provides the same resolution as Kim et al. (1987). The time step was fixed to $0.0025h^*/U_b^*$. For a validation of the DNS and of the optimisation procedure, see Sections 2.3.2 and 2.4.2.

The nonlinear optimisation depends on two free parameters: the target time interval T and the initial perturbation energy E_0. While in the study of laminar-turbulent flow transition, their role is well understood (Cherubini et al. (2010), Pringle et al. (2012)), when computing perturbations to a turbulent flow, the choice of these parameters is less clear and must be related to the objectives of the study. For example, Butler and Farrell (1993) matched the target time with the eddy turnover time at a given wall-normal distance. Farano et al. (2017) made a similar choice, discussing the influence of the target time on the resulting optimals thoroughly. Recalling the aim of the present work, here we should choose a time interval typical of extreme events.

Analysing the results of the DNS, we have found that a typical lifetime for the dissipation peaks is $T = 2$ ($T^+ \approx 23.1$), which will be chosen as the target time interval. Note that such a timescale is not very different from the observation time used by Hack and Schmidt (2021) for their CST-POD analysis. Moderately changing such a value does not affect the conclusions of this work. Considerably increasing it leads to very different results, which go beyond our scope.

The fact that we are interested in short target times is also a key aspect for the feasibility of the optimisation. Indeed, the presence of positive Lyapunov exponents, linked to the chaotic nature of the turbulent flow, may undermine the convergence of the algorithm (Jahanbakhshi and Zaki, 2019). Nikitin (2018) reports for the flow under consideration ($Re_\tau = 180$) a leading Lyapunov exponent of $\lambda_1^+ \approx 0.021$ ($\lambda_1 \approx 0.243$), from which we can estimate the characteristic Lyapunov time. The most restrictive predictability time is given by (Boffetta et al., 1998):

$$T_L \sim \frac{1}{\lambda_1} \log\left(\frac{\Delta}{\delta}\right) \approx \frac{1}{\lambda_1} \log\left(\sqrt{\frac{E_T}{E_0}}\right), \tag{3.7}$$

where log is the natural logarithm, δ is a measure of the initial uncertainty and Δ a tolerance on the final result. To quantify this time in our context, we use energies rather than amplitudes as indicated in the right-hand side of equation (3.7). A random perturbation having initial energy 10^{-4} would grow to an energy of 10^{-3} in an estimated time of $T_L \approx 4.73$, which is more than twice our chosen target time. Thus, we are confident that the positive Lyapunov exponents will not hinder the convergence of the optimisation algorithm.

Concerning the initial perturbation energy, we should choose a value sufficiently large to have a non-negligible effect on the turbulent flow, but limited to a small fraction of the turbulent kinetic energy to have physically meaningful results. We tried values in the interval $[10^{-6}, 10^{-4}]$. In the following, results are shown only for the largest value, because lower values of energy have very similar but less noticeable effects. This value is $(1.4 \pm 0.1)\%$ of the pre-existing turbulent kinetic energy of the unperturbed initial snapshots $\boldsymbol{u}_u(t_0)$ used to compute the optimal. The results will show *a posteriori* that the effect of this small perturbation on the flow is consistent with the *natural* dynamics of the turbulent flow.

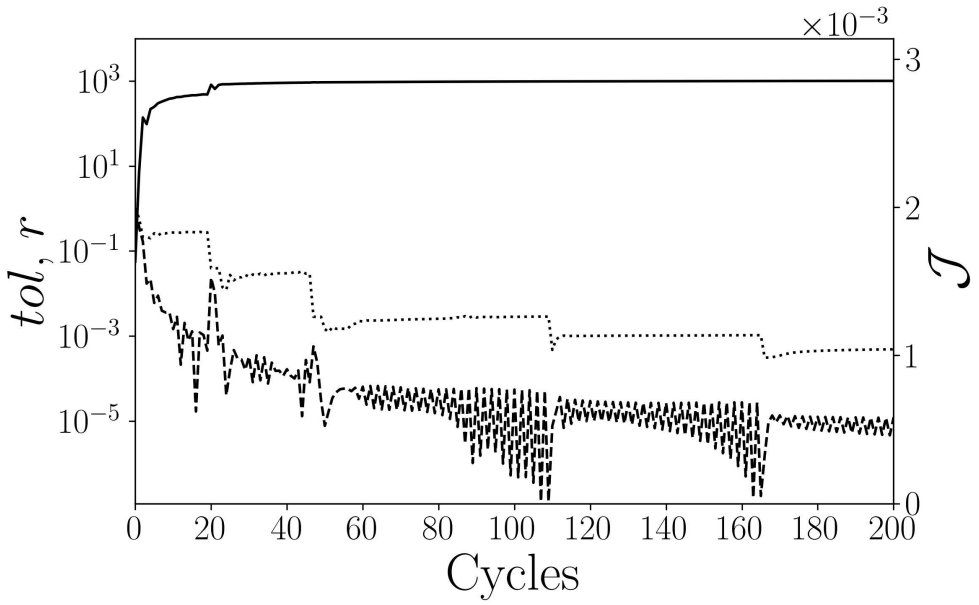

Figure 3.1: Convergence of the nonlinear turbulent optimisation. The solid line indicates the objective function (3.3) (right axis); the dashed line indicates $tol = (\mathcal{J}^n - \mathcal{J}^{n-1})/\mathcal{J}^{n-1}$ and the dotted line the convergence ratio (3.8) (left axis).

3.3.2 Results

Following previous studies, the convergence of the iterative optimization procedure is measured by the successive variation of the objective function between two cycles, $tol = (\mathcal{J}^n - \mathcal{J}^{n-1})/\mathcal{J}^{n-1}$ (Cherubini et al., 2010), and by the ratio between the component of the gradient normal to $\tilde{\boldsymbol{u}}_0$ and the full gradient (Foures et al., 2013).

$$r = \frac{\left\|\boldsymbol{G}^{\perp}\right\|}{\|\boldsymbol{G}\|}, \qquad \boldsymbol{G} = u^{\dagger}(t_0), \quad \boldsymbol{G}^{\perp} = \boldsymbol{G} - \frac{\langle \boldsymbol{G}, \tilde{\boldsymbol{u}}(t_0)\rangle}{\|\tilde{\boldsymbol{u}}(t_0)\|^2}\tilde{\boldsymbol{u}}(t_0). \tag{3.8}$$

The behaviour of these two quantities is plotted in figure 3.1 (left panel) together with $\mathcal{J}$. It can be seen that we attain a good convergence on the value of $\mathcal{J}$, with tol decreasing by five orders of magnitude. The ratio r decreases by three orders of magnitude, which is comparable to the drop achieved in previous studies (Foures et al., 2013; Kerswell, 2018). Two optimisations have been started (at the same t_0) with two different random fields. They gave essentially the same result, meaning that they attained the same value of the objective function (within the 10^{-5} tolerance) and the two optimal perturbations $\tilde{\boldsymbol{u}}_0$ differed only by small-scale details. Therefore, the choice of the initial guess does not impact our conclusions. Moreover, the optimisation procedure converges well for any chosen t_0.

The initial optimal perturbation for $E_0 = 10^{-4}$ and $T = 2$ computed with respect to a turbulent snapshot extracted from the DNS at $t_0 = 300$ is provided in figure 3.2, which shows a rather complex structure. The associated pre-multiplied energy spectra are rather broad and do not show any clearly leading mode (figure 3.3). Nevertheless, we can note some relevant features, which are common to the

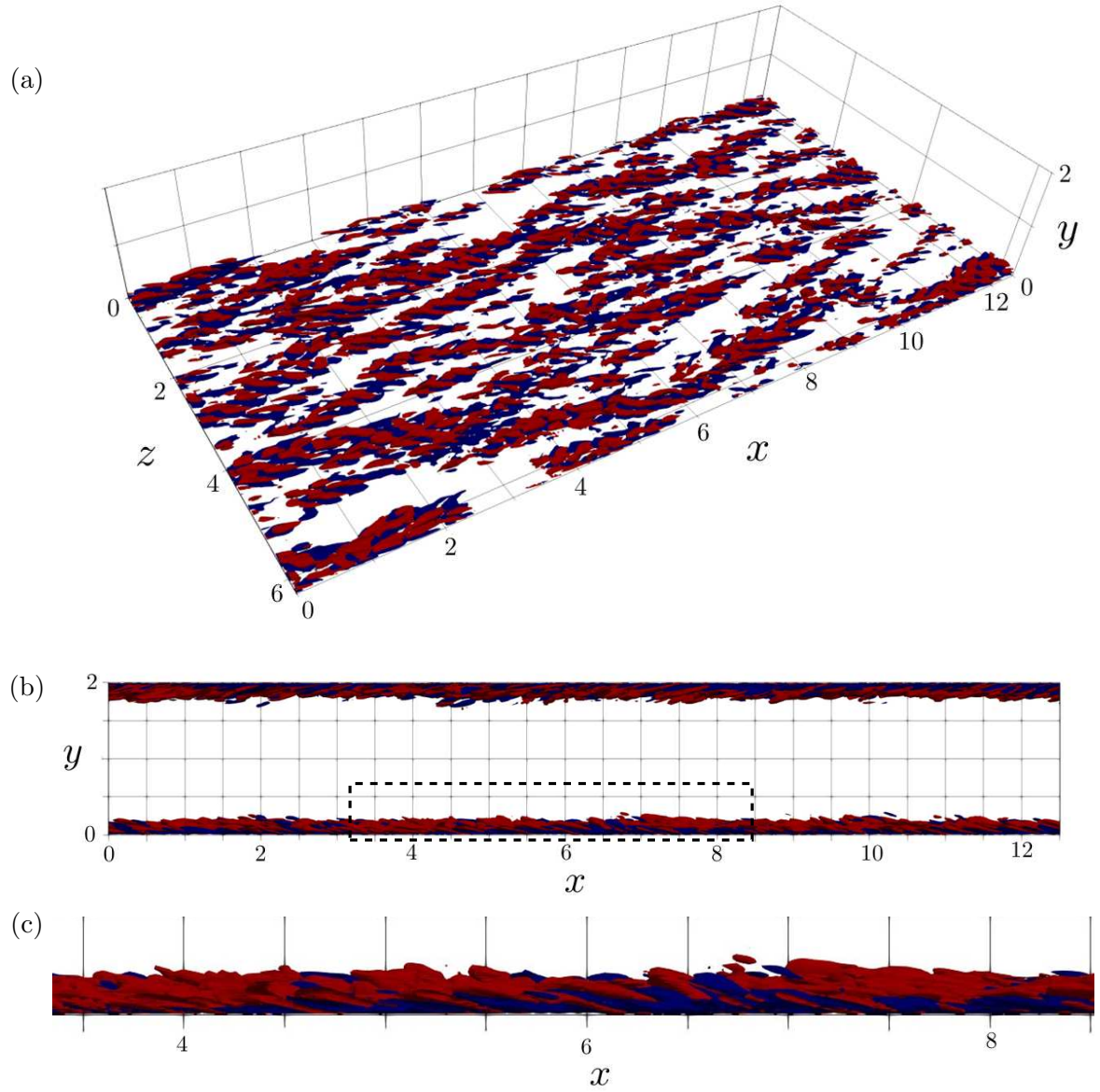

Figure 3.2: Optimal streamwise velocity perturbation isocontours ($|\tilde{\boldsymbol{u}}| = 0.02$, $|\tilde{\boldsymbol{u}}|_{max} \approx 0.21$), red/blue for positive/negative. (a) Perspective view; (b) $x-y$ view; (c) close-up on the dashed rectangle of the (b) panel.

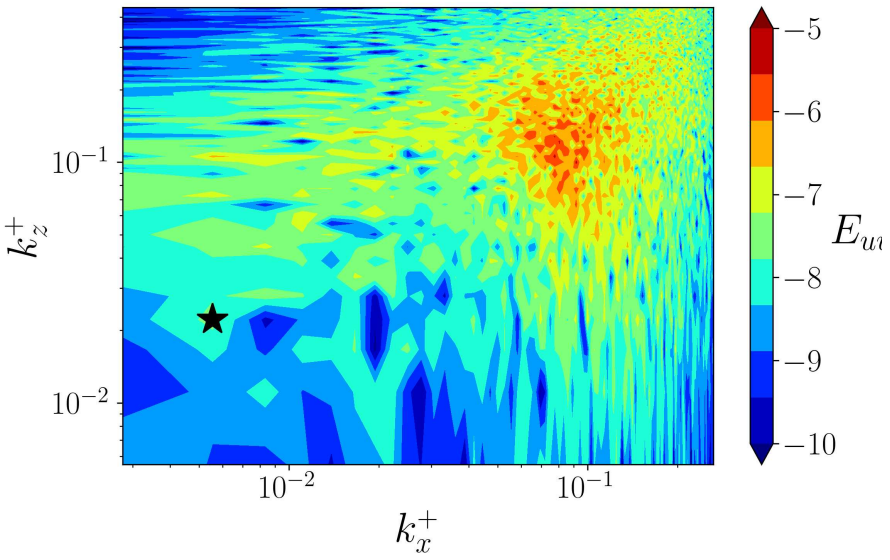

Figure 3.3: Contours of the pre-multiplied spectrum of the streamwise component of the perturbation $\tilde{\boldsymbol{u}}(t_0 = 300)$ at $y^+ = 10$ (log scale). The starred point is $k_x^+ = 5.56 \cdot 10^{-3}$, $k_z^+ = 2.22 \cdot 10^{-2}$.

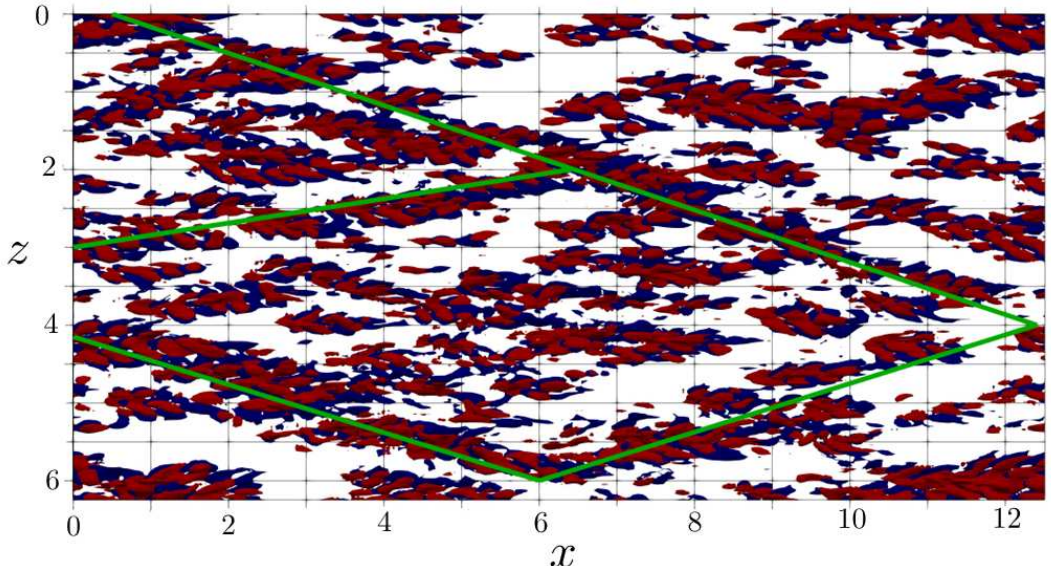

Figure 3.4: Top view of the optimal streamwise velocity perturbation isocontours (as in figure 3.2). The green lines highlight the romboidal pattern.

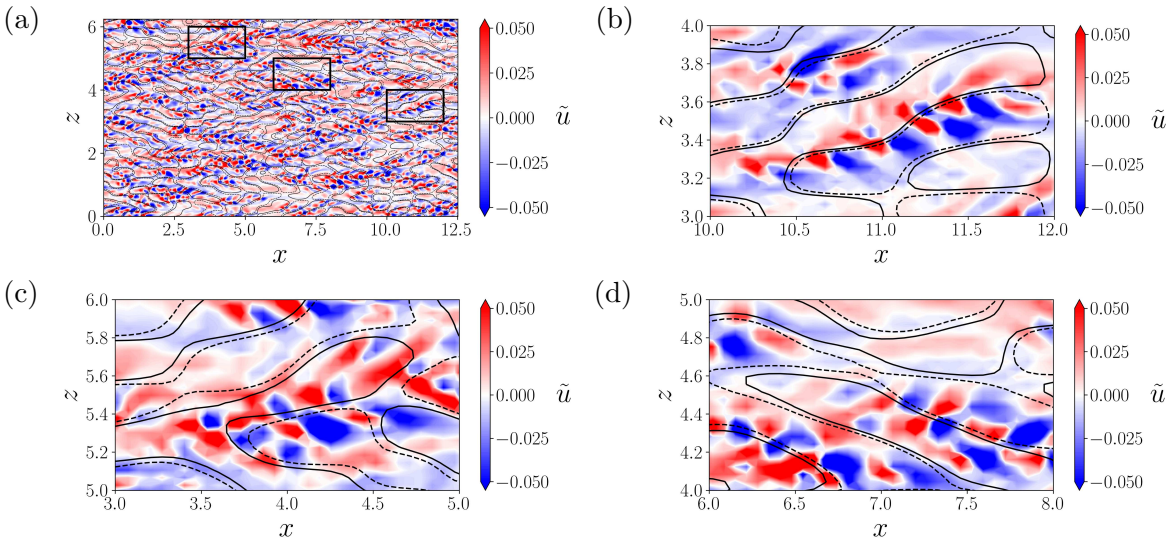

Figure 3.5: Distribution of the optimal streamwise perturbation (shaded contours) superposed to filtered streaks of the unperturbed flow at t_0 (black lines, solid for positive and dashed for negative) at $y^+ = 10$. (a) Whole domain; (b-d) close-ups on the zones framed in black in (a). The streaks are obtained by filtering the unperturbed flow and retaining modes having wavenumbers between $0.02 < k_x^+ < 0.05$ and $0.03 < k_z^+ < 0.1$.

optimal perturbations computed for all the considered turbulent snapshots.

The structures are inclined against the flow (which, in figure 3.2, goes from left to right) as reported in all previous studies about optimal perturbations (Pringle and Kerswell, 2010; Farano et al., 2015), probably to exploit Orr's mechanism (Jiménez, 2013; Encinar and Jiménez, 2020). This mechanism is known to produce turbulent bursts and seems to have a role in the initiation of turbulence production at small scale allowing an energy transfer of the wall-normal energy from large to small scales. This was recently shown for a minimal shear stress-driven flow model by Doohan et al. (2021) and in the case of a plane Couette flow subject to an adverse pressure gradient by Jiao et al. (2022).

Moreover, the perturbation forms oblique patterns, as emphasised in figure 3.4 by the green lines. These lines form an angle with the streamwise direction included between 10° and 20°. The angle varies in this range also for perturbations computed with respect to different initial snapshots. These large-scale modulations can be seen as local peaks in the spectrum. For example, the starred point in figure 3.3 corresponds to an angle $\theta = \tan^{-1}(k_x^+/k_z^+) \approx 14°$. It is not clear at present if this large-scale pattern has anything to do with oblique laminar-turbulent patterns, which are observed at significantly lower Re (see Section 1.2.2 and Chapters 5 and 6).

We conjecture that the shape of the NLOP is influenced by the coherent structures of the unperturbed turbulent flow. This is demonstrated in figure 3.5, which shows the optimal perturbation along with the pre-existing coherent velocity streaks of $\boldsymbol{u}_u(t_0)$ on a wall-parallel plane at $y^+ = 10$. To obtain the streak field, the streamwise velocity component of $\boldsymbol{u}_u(t_0)$ was filtered. The spanwise filter was centred around the typical spacing of streaks, $\lambda_z^+ \approx 100$ ($0.03 < k_z^+ < 0.1$, $62 < \lambda_z^+ < 210$). For the streamwise filter, several intervals were tested. Figure 3.5 shows the streaks with $0.02 < k_x^+ < 0.05$

($125 < \lambda_x^+ < 314$), but a fair agreement is also obtained with $0.003 < k_x^+ < 0.02$ ($314 < \lambda_x^+ < 2095$). The local-view panels show that the optimal perturbations are positioned along the interfaces between high- and low-momentum streaks. The figure shows the streamwise velocity component, but similar considerations also apply to the other velocity components. In these regions, the shear is maximum, leading to an optimal production of energy. Moreover, local inflexion points may be present and could give rise to localised instabilities (Schoppa and Hussain, 2002). Moreover, spanwise perturbations of the streak can induce strong (transient or asymptotic) energy growth due to the transport of the spanwise shear by the streamwise and spanwise perturbations (Hoepffner et al., 2005). This mechanism of streak instability and/or transient growth has recently been shown to trigger turbulence dissipation events in a two-scale shear stress-driven flow model of near-wall turbulence (Doohan et al., 2021, 2022).

Therefore, the structure of the optimal perturbation obtained here suggests that this streak instability/transient growth, inducing the breakdown of the coherent structures into fine scales, might be at the origin of the increase in the local dissipation within the flow. This point, and its connection with the generation of EEs, will be addressed in Section 3.5. In the following section, the overall effect of the optimal perturbation on the flow will be analysed.

3.4 Temporal evolution analysis

3.4.1 Turbulent dissipation analysis

This subsection focuses on the analysis of the local turbulent dissipation rate:

$$\varepsilon(\boldsymbol{x},t) = \frac{1}{Re} s'_{ij} s'_{ij}, \qquad \text{with } s'_{ij} = \frac{1}{2}\left(\frac{\partial u'_i}{\partial x_j} + \frac{\partial u'_j}{\partial x_i}\right). \tag{3.9}$$

Note that this quantity differs from the integrand of the objective function (3.3) by a negligible transport term (Pope, 2000).
We also considered the volume average of this quantity, namely

$$\mathcal{E}(t) = \int_V \frac{1}{Re} s'_{ij} s'_{ij} \, d\boldsymbol{x}, \tag{3.10}$$

and the volume-averaged turbulent kinetic energy

$$K(t) = \int_V \frac{u'_i u'_i}{2} \, d\boldsymbol{x}. \tag{3.11}$$

The evolution of two DNSs starting from the optimally perturbed and unperturbed (turbulent) flows is now compared. The top frames of figure 3.6 provide snapshots extracted at the same time instant from these two simulations, showing the contours of ε on a horizontal near-wall plane ($y^+ = 10$) at the target time. In the perturbed flow (panel (b)), there is a much higher density of small-scale structures. This observation, together with the positioning of the perturbation along the pre-existing streaks, let us conjecture that the effect of the optimal perturbation is to destabilise the pre-existing coherent structures and engender an intense energy cascade towards the small scales.

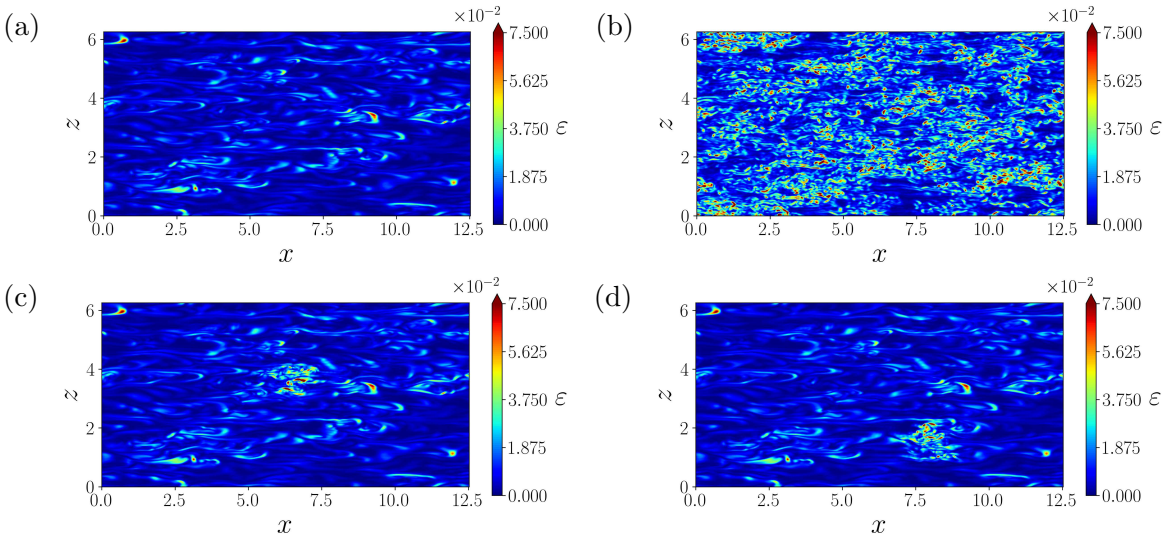

Figure 3.6: Contours of the dissipation at $t = t_0 + T = 302$ at $y^+ = 10$. (a) Unperturbed flow; (b) optimally perturbed flow; (c,d) two examples of locally perturbed flow.

The (c) and (d) frames of the same figure show the contours of ε for a flow perturbed only in a subset of the computational domain with a *clipping* of the original optimal perturbation (see also figure 3.14). The clipped perturbation is obtained by multiplying the original global perturbation by a Gaussian function:

$$w(x,z) = exp\left\{-\left[\left(\frac{x-x_c}{\ell_x/2}\right)^n + \left(\frac{z-z_c}{\ell_z/2}\right)^n\right]\right\}, \tag{3.12}$$

and subsequently projecting it on a divergence-free field. In the above equation, $\ell_x = 2$ and $\ell_z = 1$ are the streamwise and spanwise dimensions of the localised perturbation, respectively, x_c and z_c are the coordinates of the centroid of the perturbation, for which several values have been chosen, and the integer n is set equal to 30. It is striking that, at the target time, the flow surrounding the perturbed region is not at all modified by the perturbation and displays the same structures as the unperturbed flow. This clearly shows that the mechanisms exploited by this optimal perturbation have a local nature and that the numerous instabilities developing in the fully perturbed flow are independent of each other.

Figure 3.7 shows the time evolution of the volume-averaged quantities $K(t)$ and $\mathcal{E}(t)$, for the unperturbed and optimally perturbed flow, as well as for two other different perturbations of the undisturbed turbulent flow. In the optimally-perturbed case, a peak in K and $\mathcal{E}$ is observed at the target time. This also results in a peak of the mean wall shear stress (monitored through the friction Reynolds number on the right-most frames). The wall shear stress must increase with the dissipation rate because all simulations have the same flow rate. Note that the peak in $\mathcal{E}$ always follows the one in K, consistently with the time-lag found by Yin et al. (2024) in the time correlations of the same volume-averaged quantities.

The same figure shows that a generic, non-optimal perturbation, rescaled with the same initial energy as the optimal perturbation, does not generate any energy or dissipation peak, even if its effect

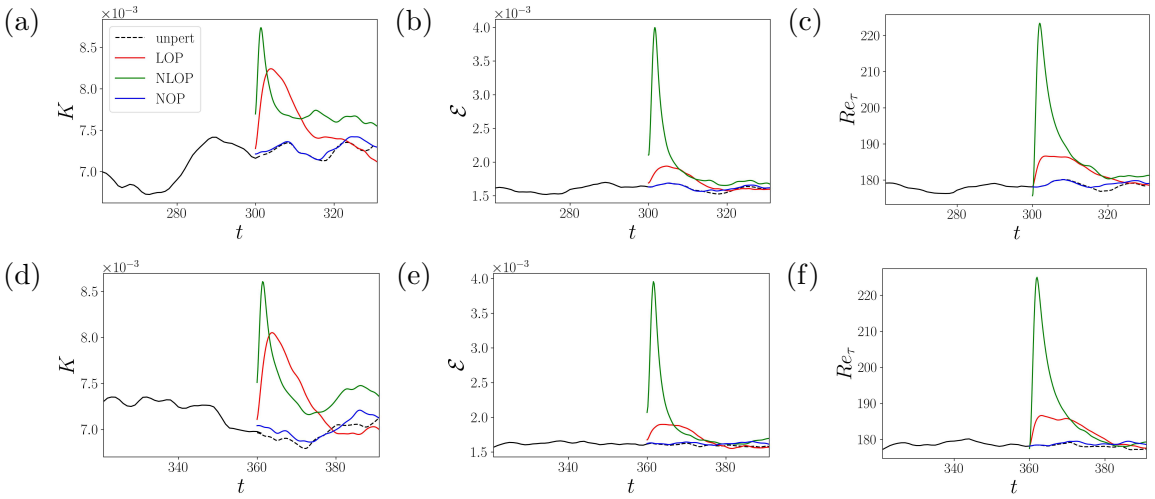

Figure 3.7: Time history of the volume averaged turbulent kinetic energy (a,d), dissipation (b,e) and friction Reynolds number (c,f). Four flows are compared: the optimally perturbed flow (NLOP, green line); the unperturbed flow (unpert, dashed black line); the flow perturbed by a non-optimal perturbation (NOP, blue line); the flow perturbed by a linear optimal perturbation (LOP, red line). (a-c) $t_0 = 300$, (d-f) $t_0 = 360$.

on these quantities is not negligible, due to the positive Lyapunov exponents. Moreover, for comparison, we superposed to the turbulent snapshot also a monochromatic linear optimal perturbation (LOP) with zero streamwise wavenumber and spanwise wavenumber equal to 10, obtained with an optimisation around the mean flow similar to that of Del Alamo and Jimenez (2006) (see also figure 3.9). In this case, even if a peak of turbulent kinetic energy is indeed produced, $\mathcal{E}$ does not increase very much (red line in the figure). This confirms that the peak of dissipation is given by the instability of the pre-existing structures, since the linear optimisation does not take them into account, being computed with respect to the mean flow. Indeed, we have tested that even if one uses the NLOP computed with respect to a given turbulent snapshot to perturb a different snapshot, the obtained effect is not the same.

The effect of the NLOP can be globally described as a turbulence overshoot. This, however, is not a sustained state. After the target time, there is a relaxation towards the unperturbed flow. The flow comes back to the statistically-steady turbulent state after $\Delta T_R \approx 15$ ($\Delta T_R^+ \approx 174$). We have verified that the long-time statistics of the relaxed flow are the same as the reference DNS.
Finally, it is noteworthy that this behaviour is independent of the initial unperturbed snapshot chosen at t_0. We have computed NLOPs and their evolutions for several snapshots, and they always gave the same qualitative behaviour, as can be seen in the bottom row of figure 3.7, where the NLOP is obtained for a turbulent snapshot extracted from the unperturbed DNS at $t_0 = 360$.

It is now worth investigating whether the optimal perturbation actually increases the number of EEs in the flow, or rather leads to an increase in the mean dissipation. Towards this aim, the PDF of ε is computed on a given wall-parallel plane. Because extreme dissipative events are rare events, one needs to compute the tail of the PDF accurately up to at least 20 times the standard deviation. To achieve this target, one simulation of the perturbed flow is not sufficient because the transient effect

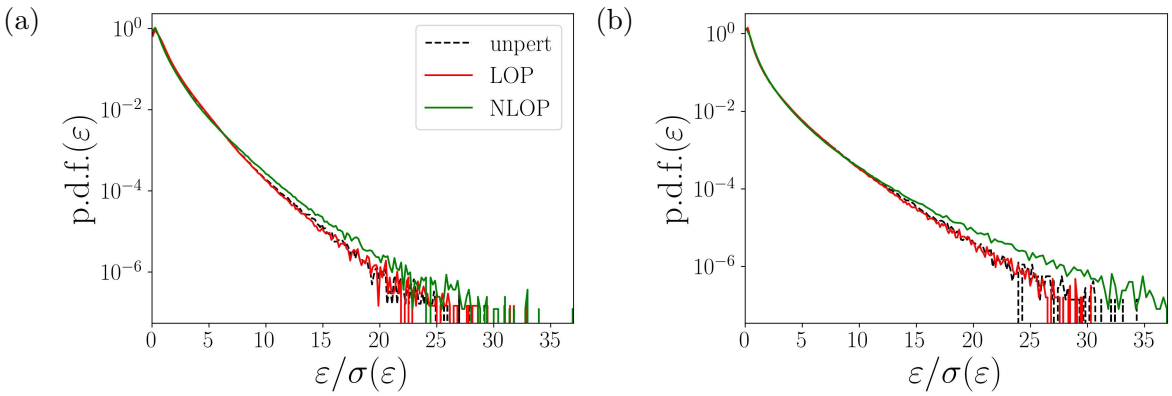

Figure 3.8: PDF of the local dissipation for the optimally perturbed flow (NLOP, green line), the unperturbed flow (unpert, dashed black line) and the flow perturbed by a linear optimal perturbation (LOP, red line). The abscissae are normalised by the respective standard deviations. (a) $y^+ = 10$ plane; (b) $y^+ = 30$ plane.

of the perturbation is quite short. For this reason, we compute an ensemble of NLOPs with respect to eight snapshots extracted from the reference DNS and equispaced in time and the corresponding ensemble of short evolutions (realisations). The dissipation is sampled on the given horizontal plane with a temporal timestep $\Delta t = 0.2$ ($\Delta t^+ \approx 2.3$) and its normalised value with respect to the standard deviation, $\sigma(\varepsilon)$, is plotted in a PDF graph in figure 3.8. One can see that the perturbed flow shows an increased tail, indicating a higher density of EEs. This feature is observed on the near-wall planes at $y^+ = 10$ and $y^+ = 30$, whereas the flow near the channel centerline ($y^+ > 90$) remains almost unperturbed (not shown). The same figure shows that the LOP (red curve) does not produce any increment of the PDF tail, *i.e.*, it does not lead to the formation of more EEs, despite increasing the volume-averaged dissipation.

3.4.2 Turbulent production analysis

It is not easy to identify the mechanism responsible for this extreme increase in dissipation rate since the initial perturbation is complex and probably exploits more than one mechanism. However, here we attempt to identify the effect of two important mechanisms of turbulent production in the channel flow: the lift-up effect (Ellingsen and Palm, 1975; Landahl, 1980) and Orr's mechanism (Orr, 1907). The former is associated with momentum transport in the $y-z$ plane, being due to streamwise-aligned vortices. In the latter, the production mechanism acts on the $x-y$ plane (Jiménez, 2013). Therefore, averaging the turbulent field in the streamwise and in the spanwise directions, we can define a lift-up-like production and an Orr-like production, respectively:

$$\mathcal{P}_{lu}(y,z,t) = -\left\langle u' \right\rangle_x \left\langle v' \right\rangle_x \frac{d\overline{U}}{dy}, \tag{3.13a}$$

$$\mathcal{P}_{Orr}(x,y,t) = -\left\langle u' \right\rangle_z \left\langle v' \right\rangle_z \frac{d\overline{U}}{dy}, \tag{3.13b}$$

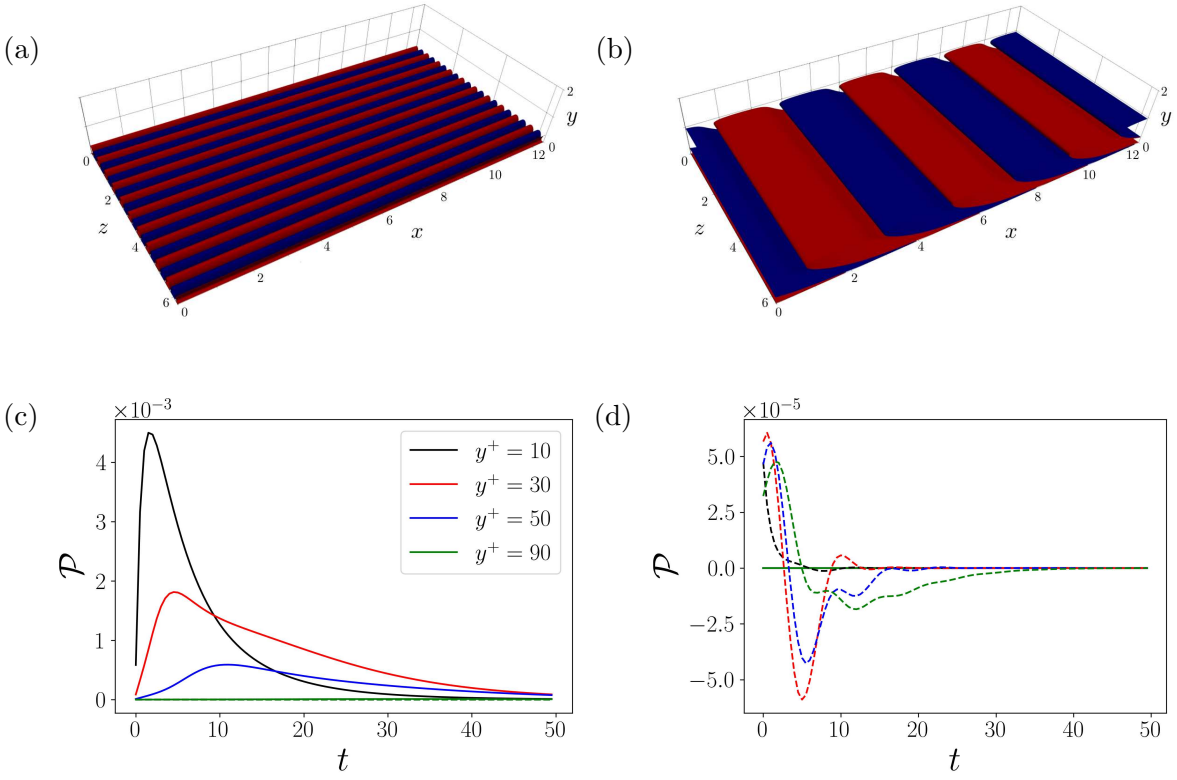

Figure 3.9: Validation of the turbulent production splitting. The top panels show the two perturbations used as test: a streak perturbation (a) and an Orr-like perturbation (b). These perturbations are evolved around the turbulent mean flow. (c) and (d) show the respective production diagrams at four different wall-normal positions. In these panels, solid lines denote the lift-up-like production $\langle \mathcal{P}_{lu} \rangle_z$, whereas dashed lines denote the Orr-like production $\langle \mathcal{P}_{Orr} \rangle_x$. The streaks on the left (a,c) show only non-zero lift-up-like production, while the Orr-like perturbation on the right (b,d) shows only non-zero Orr-like production.

where $\overline{U}(y)$ is the turbulent mean profile and $\langle \cdot \rangle_x$, $\langle \cdot \rangle_z$ denote, respectively, the streamwise and spanwise average.

The meaning of these production terms is exemplified in figure 3.9. Two monochromatic perturbations were computed using linear optimal growth analysis around the mean profile (Del Alamo and Jimenez, 2006; Cossu et al., 2009; Pujals et al., 2009). A streak-like perturbation with $k_x = 0$ and $k_z = 10$ and an Orr-like perturbation with $k_x = 1.5$ and $k_z = 0$ were computed (figure 3.9 (a) and (b), respectively). These wavenumbers were selected by looking at the peak in the turbulent pre-multiplied spectra. These perturbations were added to the mean profile with a certain amplitude and evolved with the DNS code: they generate transient energy growth and then vanish. As can be seen in the bottom panels of figure 3.9, the streaks show a non-zero $\mathcal{P}_{lu}$ ($\mathcal{P}_{Orr}$ is zero), whereas the backward inclined perturbation shows a non-zero $\mathcal{P}_{Orr}$ ($\mathcal{P}_{lu}$ is zero).

Figure 3.10 shows the time evolution of these production terms averaged along the free wall-parallel direction for the optimally perturbed (solid lines) and the unperturbed (dashed lines) flow. One can see that the averaged lift-up-like production shows a peak at several wall-normal distances:

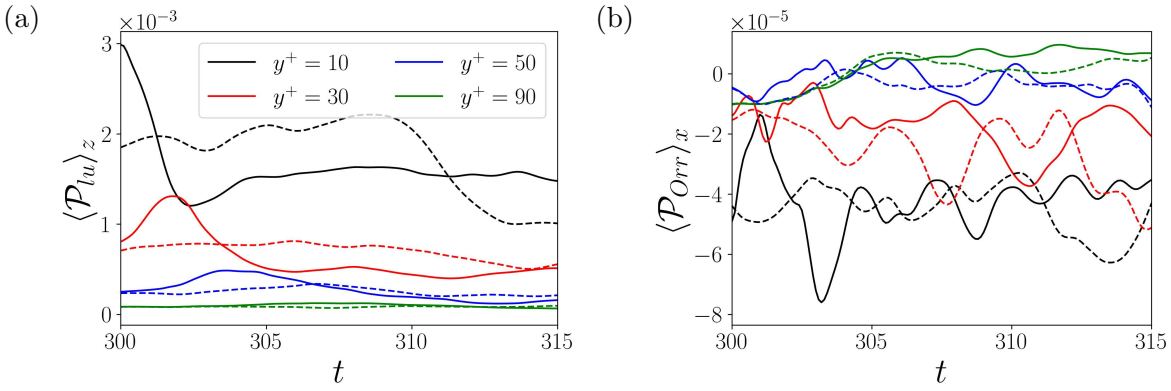

Figure 3.10: Time evolution of the turbulent split production on different horizontal planes. (a) Lift-up-like production $\langle \mathcal{P}_{lu} \rangle_z$; (b) Orr-like production $\langle \mathcal{P}_{Orr} \rangle_x$. Solid lines denote the optimally perturbed flow, dashed lines the unperturbed flow.

the perturbation initially produces energy near the wall ($y^+ = 10$, where the mean shear is maximum) and then reaches the upper layers below $y^+ = 90$. Instead, a relevant effect on the Orr-like production can be observed only in the near-wall layer ($y^+ = 10$). Note also that the Orr-like production is almost two orders of magnitude smaller than the lift-up production term and has a negative average value. Nevertheless, a peak in the curve of Orr-like production at $y^+ = 10$ can be observed for the perturbed flow. The peak in the Orr-like production is clearly linked to the backward inclination of the optimal perturbations, whereas the reason behind the peak in the lift-up-like production is better clarified by figure 3.11. This figure shows, at times $t \geqslant t_0$ (from top to bottom), the generation of intense positive-sign streaks in the near-wall region, induced by an increased streamwise vorticity, absent in the unperturbed flow. The intensified streaks increase the wall friction in the perturbed flow. Consequently, the energy extracted from the mean flow through wall friction also increases, leading to an increase of dissipation at small scales.

These observations are consistent with those of recent works showing that the Orr and lift-up mechanisms coexist for perturbations having non-zero wavenumbers in both wall-parall directions, as none of the related terms vanish (Jiao et al., 2021), and that the Orr mechanism can energise the lift-up effect sustaining the wall cycle (Doohan et al., 2021). Thus, a sharp distinction between these two mechanisms is not possible. However, a further insight can be gained by looking at the spacetime plot of these production terms. Figure 3.12 shows that the perturbation increases the production in the regions where the undisturbed flow is characterised by local production peaks. This is directly linked to the previous remarks on the positioning of the perturbation over the pre-existing coherent structures. Again, it appears that the perturbation exploits the pre-existing structures and enhances their turbulent production. Moreover, the close-ups in figure 3.5 show that the optimal perturbations are located at the interface between low- and high-momentum streaks, and are mostly characterised by a varicose symmetry with respect to this interface. This suggests the presence of a varicose instability of the streaks, which might be enhanced by the strengthening of the streaks due to the lift-up mechanism.

To investigate whether an exponential instability is involved in these dissipative events, the time

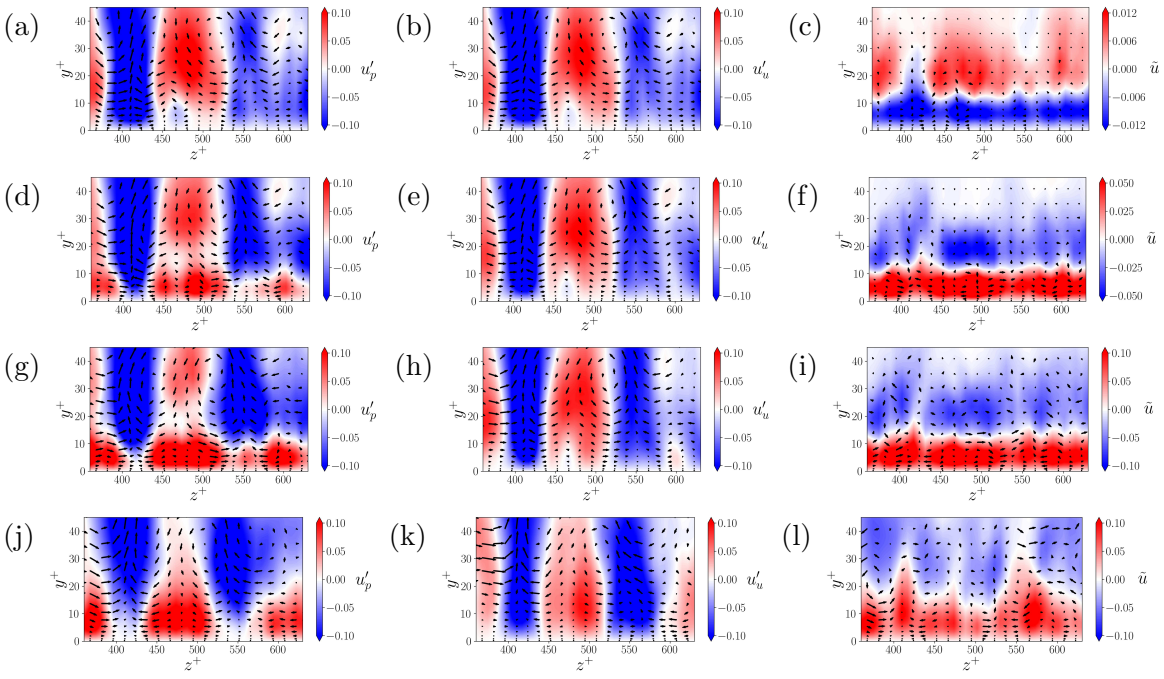

Figure 3.11: Time evolution of the flow averaged along the streamwise direction: isocontours of the streamwise velocity component and arrows for the transverse components. From top to bottom $t = [t_0, t_0+1, t_0+2, t_0+5]$. (a,d,g,j) Perturbed flow; (b,e,h,k) unperturbed flow; (c,f,i,l) perturbation. Panels (a,d,g,j) and (b,e,h,k) show the turbulent fluctuation, *i.e.* the instantaneous velocity minus the turbulent mean profile.

evolution of the optimal perturbation energy is shown in figure 3.13 for three different realisations (solid lines). In all cases, in the first time instants, the perturbation is amplified exponentially by approximately one order of magnitude in energy. This is not true for a generic non-optimal perturbation (see the blue dashed line in the figures), which grows much more slowly than the optimal and does not have any relevant effects on the dissipation. This significantly supports the idea that the optimal perturbation is exploiting a modal instability of the streaks. Moreover, due to the spatial distribution of the disturbances with respect to the streaks, this instability appears mostly of a varicose type.

3.4.3 Local dynamics

It is interesting to investigate the behaviour of the nonlinear optimal perturbation in the phase space and, in particular, to address the question of whether the optimally perturbed flow belongs to the turbulent attractor. Indeed, Blonigan et al. (2019) constructed their optimal perturbation combining POD modes of the reference turbulent flow to constrain the perturbed flow evolution inside the turbulent attractor. Despite the differences between our study and their approach (namely, they searched for an optimal turbulent field, not a small perturbation to a pre-existing turbulent field), whether the optimal flow structures may be representative precursors of real EEs represents an important issue concerning the physical validity of the present results.

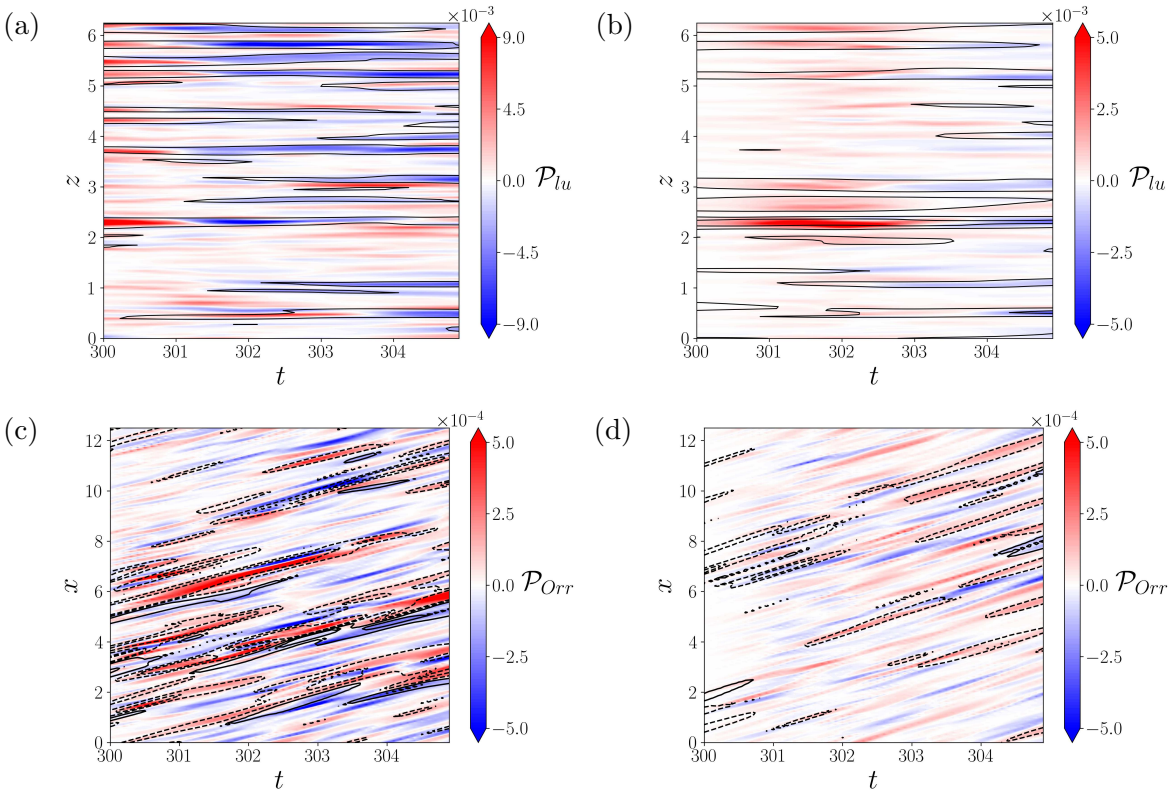

Figure 3.12: Spacetime plots of the turbulent production splitted. Solid black lines are the baseflow production contours (solid for positive values, dashed for negative) while shaded contours are the increment due to the perturbation ($\mathcal{P}^p_{lu/Orr} - \mathcal{P}^u_{lu/Orr}$). (a,c) $y^+ = 10$ plane; (b,d) $y^+ = 30$ plane. (a,b) Lift-up-like production $\mathcal{P}_{lu}$; (c,d) Orr-like production $\mathcal{P}_{Orr}$.

Indeed, the perturbed flow peaks in K and $\mathcal{E}$ (figure 3.7) appear too strong to be realistic. However, one has to consider that these are integral quantities. The fact that the optimal perturbation occupies the whole domain and induces many "synchronised" EEs (while realistic EEs are local, small-scale and not synchronised) is a possible cause of the non-realistic increase of the integral quantities. In a real flow, the optimal mechanisms may be triggered locally, providing realistic overshoots on the local ε, thus being representative of a realistic extreme event evolving inside the turbulent attractor.

To investigate in detail this issue, a series of simulations initialised with the optimal perturbation artificially localised in different places of the domain is run for each of the eight realisations used before for the PDF. The perturbations are *clipped* with the weight function (3.12). In particular, for each of the considered turbulent snapshots, the domain is divided into 36 rectangles having dimension $\ell_x = 2$, $\ell_z = 1$ and the portion of the optimal perturbation corresponding to each of these rectangles was used to obtain a locally perturbed flow. One example of local perturbation is shown in figure 3.14 (a-b). For each local perturbation, a short DNS was run to obtain its evolution (figure 3.14 (c-d)). In each of these simulations, the perturbed zone was tracked in time, taking into account the local mean advection velocity as done by Hack and Schmidt (2021) and the dissipation ε was sampled inside this

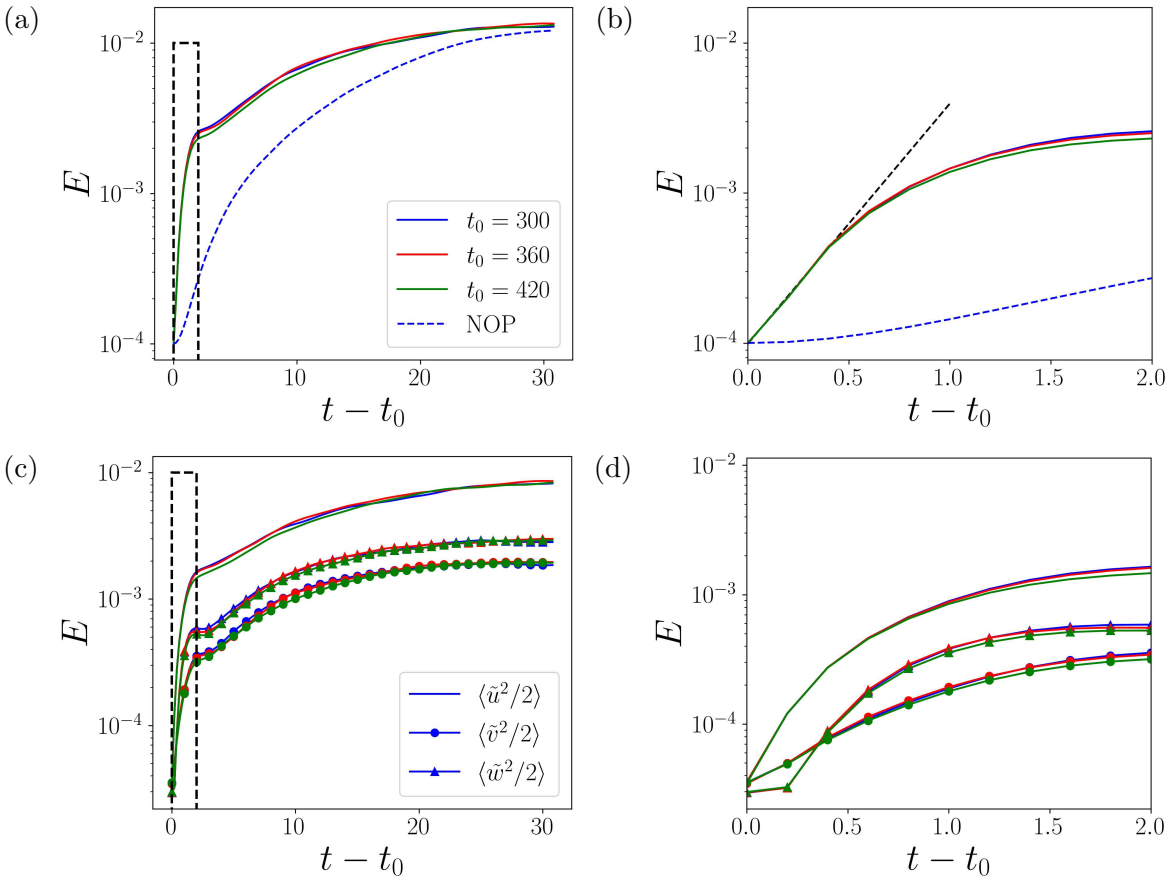

Figure 3.13: (a,b) Time evolution of the volume-integrated perturbation energy $1/2\langle \tilde{\boldsymbol{u}} \cdot \tilde{\boldsymbol{u}} \rangle$ for different realizations of the perturbed flow. The dashed blue line is the evolution of a flow perturbed with a random non-optimal perturbation. (c,d) Time evolution of the individual volume-integrated perturbation energy budgets $\langle \tilde{u}^2/2 \rangle$, $\langle \tilde{v}^2/2 \rangle$ and $\langle \tilde{w}^2/2 \rangle$ (colors as in top panels). The (b) and (d) are close-ups of the dashed black rectangles. The growth rate which corresponds to the dashed black line in (b) is $\approx 3.69 U_b^*/h^*$ for the energy, *i.e.* $\approx 1.84 U_b^*/h^*$ for the perturbation amplitude.

zone (see the dashed rectangle shown in figure 3.14).

Figure 3.15 (a) shows a $K - \mathcal{E}$ phase space. The reference DNS trajectory is plotted in grey and represents the long-time turbulent attractor. The trajectory of the fully perturbed flow resides out of the attractor already at the initial time (the starred point in the figure), continues its excursion far away from it and finally falls back. In contrast, each of the locally perturbed flows remains within the attractor at any time. Therefore, at least in this low-dimensional phase-space, the locally perturbed flows are compatible with *natural* turbulence.

It remains to show that the local perturbation drives, locally, dissipative EEs. This is reported in figure 3.15(b), where the PDF of ε sampled in the perturbed zones of the locally perturbed flows displays an increased tail with respect to the unperturbed flow, similarly to the fully perturbed flow (figure 3.8).

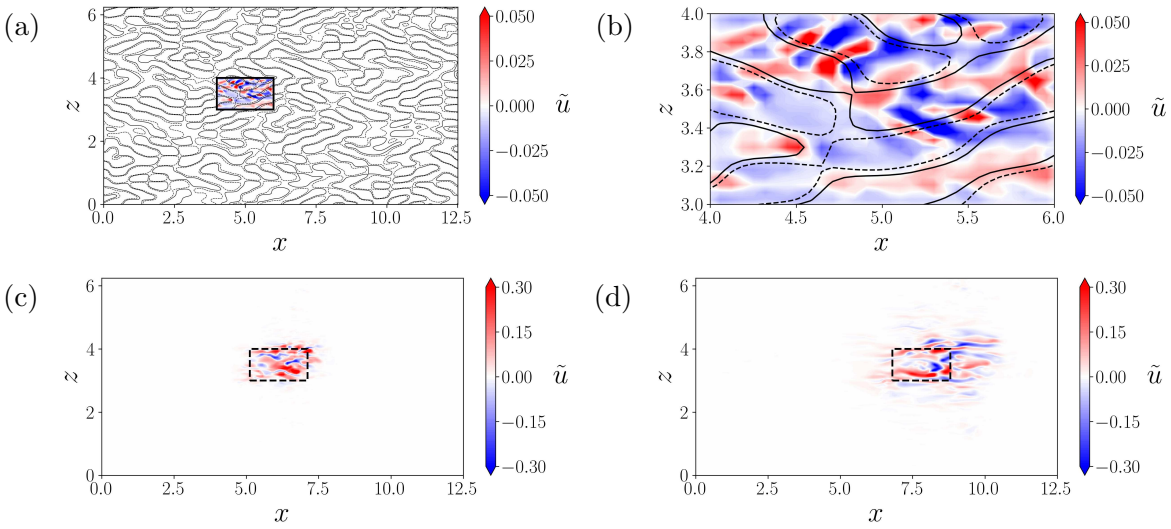

Figure 3.14: Contours of the streamwise perturbation $\tilde{u}(\boldsymbol{x},t) = u_p(\boldsymbol{x},t) - u_u(\boldsymbol{x},t)$ for an artificially localized optimal perturbation. (a,b) Contours of the streamwise perturbation superposed to the filtered streaks of the unperturbed flow at t_0 (black lines, solid for positive and dashed for negative) at $y^+ = 10$; (b) shows a close-up of (a). (c,d) Contours of the streamwise perturbation on the same plane at $t = 302, 305$.

In summary, the fully perturbed flow does not reside in the projection of the turbulent attractor because the bursting mechanism is triggered everywhere at the same time. On the other hand, this is not true for locally perturbed flows, even if the perturbation is still effective in producing EEs. However, this analysis alone is not enough to prove that the locally perturbed flow is equivalent to a naturally bursting flow. This will be better investigated by means of the CST-POD analysis in the next section. It will be shown that the perturbed and the unperturbed flows share the same local structure during an extreme event.

3.5 POD analysis

The aim of this section is twofold: (i) to show that, locally, the mechanisms activated by the NLOP are representative of those observed during the generation of EEs in a *natural* turbulent flow; (ii) to show that EEs happen at the interface between a positive and a negative streamwise velocity streak, exactly where the perturbation was placed by the optimization (figure 3.5) and consistently with the unstable modes of these structures (Waleffe, 1997; Andersson et al., 2001; Schoppa and Hussain, 2002). To this aim, we use the CST-POD analysis proposed by Schmidt and Schmid (2019) and already used for the case of the turbulent channel flow by Hack and Schmidt (2021). Details on the method are given in Section 2.5. For this study, an EE is defined as a local spatio-temporal dissipation peak. In particular, Hack and Schmidt (2021) considered the 99.9th percentile of the most intense ε peaks, corresponding to about to $20 - 30$ times the mean local[2] dissipation. However, the Reynolds number considered here is significantly smaller than the one considered by Hack and Schmidt (2021)

[2]Here local means at a given wall distance.

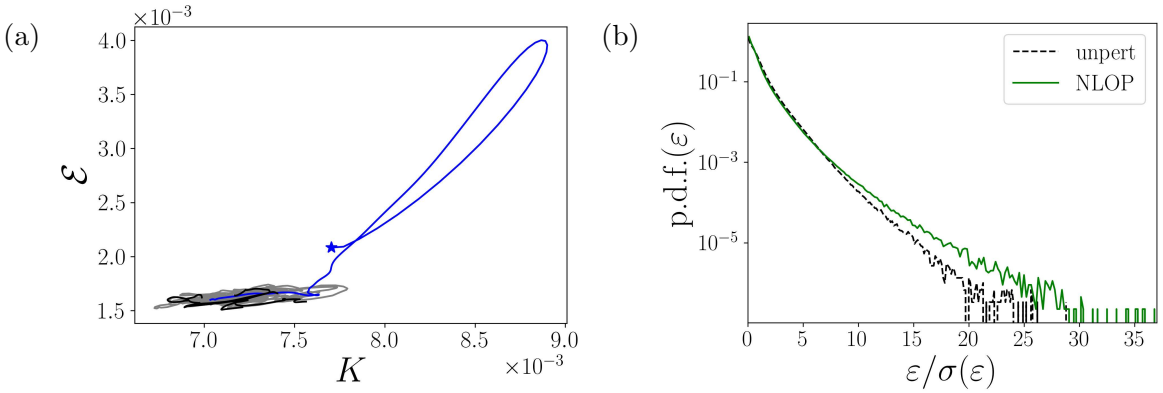

Figure 3.15: (a) Turbulent attractor projected on the $K - \mathcal{E}$ plane: reference DNS (solid grey line), optimally perturbed flow (solid blue), locally perturbed flows (solid black). (b) Dissipation PDF sampled on the perturbed zone in the locally perturbed flows (solid green line) and on the corresponding points in the unperturbed flow (dashed black) at $y^+ = 10$.

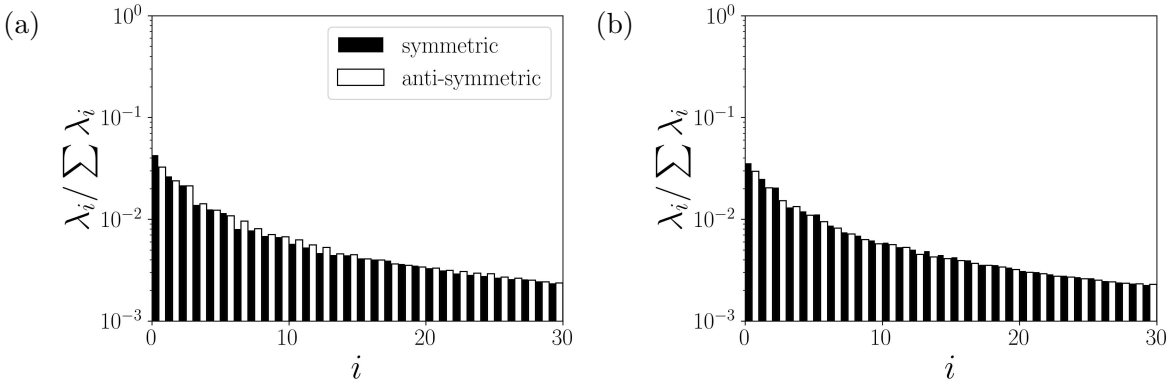

Figure 3.16: Distribution of the 30 leading eigenvalues of the POD. (a) Unperturbed flow; (b) optimally perturbed flow.

($Re_\tau = 180$ vs 2000), leading to a much smaller number of EEs, which are statistically characterised by a lower intensity. For this reason, a lower threshold is chosen, equal to 10 times the mean local dissipation.

The velocity field is sampled around each extreme event in a box having spatial dimension $\ell_x^+ \times \ell_y^+ \times \ell_z^+ \approx 785 \times 75 \times 320$ comparable to that employed by Hack and Schmidt (2021). Moreover, in order to include information on the temporal dynamics in the analysis, the field is sampled at two instants of time before the dissipation peak and two instants of time after the peak. The spacing between these instants of time is $\Delta t_{POD} = 1.0$ in outer units, which corresponds to $\Delta t_{POD}^+ \approx 11.7$ in wall units. The set of these five velocity fields constitutes a *spatio-temporal snapshot* for the CST-POD. We remark that the events are sampled as they appear in the flow, *i.e.* randomly in space and time.

The local reference frame centred on the EE is denoted by $(\tilde{\boldsymbol{x}}, \tilde{t})$. Before performing the POD, the velocity field has been split into a symmetric and antisymmetric part with respect to the $\tilde{z}$ axis:

$$\boldsymbol{u}_S = \frac{1}{2}\begin{bmatrix} u(\tilde{x},\tilde{y},\tilde{z},\tilde{t}) + u(\tilde{x},\tilde{y},-\tilde{z},\tilde{t}) \\ v(\tilde{x},\tilde{y},\tilde{z},\tilde{t}) + v(\tilde{x},\tilde{y},-\tilde{z},\tilde{t}) \\ w(\tilde{x},\tilde{y},\tilde{z},\tilde{t}) - w(\tilde{x},\tilde{y},-\tilde{z},\tilde{t}) \end{bmatrix}, \qquad \boldsymbol{u}_A = \frac{1}{2}\begin{bmatrix} u(\tilde{x},\tilde{y},\tilde{z},\tilde{t}) - u(\tilde{x},\tilde{y},-\tilde{z},\tilde{t}) \\ v(\tilde{x},\tilde{y},\tilde{z},\tilde{t}) - v(\tilde{x},\tilde{y},-\tilde{z},\tilde{t}) \\ w(\tilde{x},\tilde{y},\tilde{z},\tilde{t}) + w(\tilde{x},\tilde{y},-\tilde{z},\tilde{t}) \end{bmatrix}.$$

The following analysis refers to events sampled in the $y^+ = 30$ plane; the results in other near-wall planes are similar.

For the unperturbed flow, for which a long DNS is available, up to 2000 snapshots were used. For the optimally perturbed flow, the ensemble of realisations used to compute the dissipation PDF has been employed, which leads to 950 snapshots. Taking the unperturbed case as a reference, it was possible to verify that there is a negligible difference between the modes obtained with 1000 and 2000 snapshots. Thus, both POD analyses were performed using ≈ 1000 snapshots. Note that, in the CST-POD, the underlying expected value operator is not temporal averaging but ensemble averaging (Schmidt and Schmid, 2019; Berkooz et al., 1993), which is consistent with the approach of taking different realisations of the numerical experiment.

Figure 3.16 shows that the distribution of the energy among the modes, given by the eigenvalues of the correlation matrix, is comparable in the perturbed and in the unperturbed cases. The same is true for the subdivision of energy between the symmetric and the antisymmetric parts: 51.4% vs 48.6% and 50.8% vs 49.2%, respectively, in the optimally perturbed case and the unperturbed case. The results agree quite well with those of Hack and Schmidt (2021), although they found a stronger imbalance in favour of the symmetric part ($\approx 58\%$ vs 42%). This discrepancy may be due to the very different Reynolds numbers.

Figure 3.17 provides the comparison of the leading POD modes of the EEs generated in the optimally perturbed flow and in the undisturbed flow. The topology of the structures is globally the same: the antisymmetric mode (panels (a) and (b)) is made of two intense streaks of opposite sign approaching each other at $y^+ = 30$; the symmetric mode (panels (e) and (f)) shows a three lobe structure encircling a streak of opposite sign; lastly, the shear layer in the longitudinal plane is inclined of the same angle with respect to the streamwise direction both for the antisymmetric mode (panels (c) and (d)) and for the symmetric one (panels (g) and (h)). The slight differences between the modes are due to an intrinsic variability of the turbulent flow in which these events are immersed, as confirmed by performing the CST-POD on a different set of turbulent snapshots (*i.e.*, perfect convergence of the POD modes is actually too hard to achieve). The comparison is very good also for instants of time before and after the peak.

Ultimately, the NLOP is found to reproduce very accurately the local mechanism behind the generation of EEs in a turbulent flow. The perturbation interacts with the high shear at the interface region between coherent low- and high-momentum regions to break down the larger structures and drive energy to small scales.

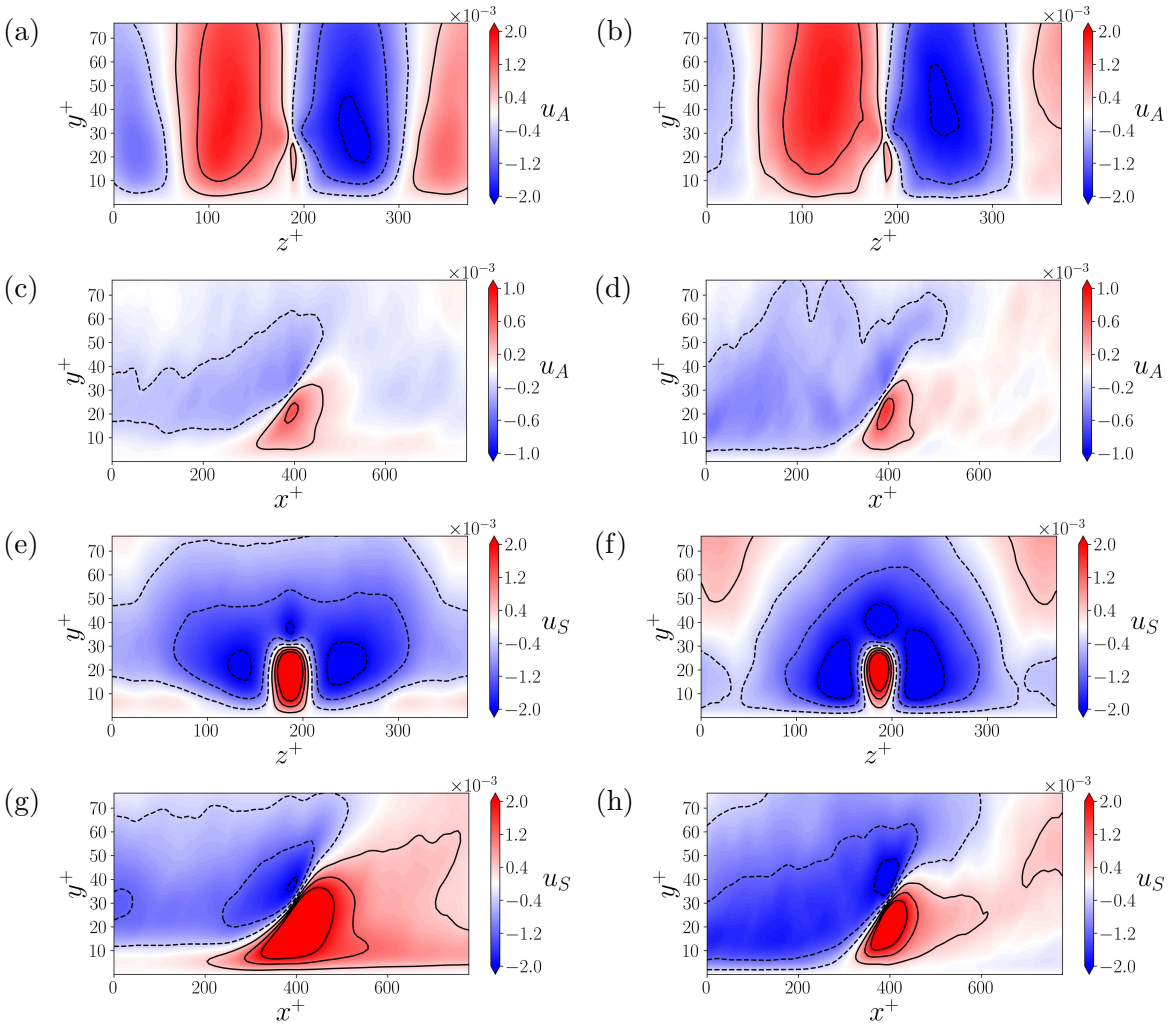

Figure 3.17: Leading POD modes of the extreme events: streamwise velocity fluctuation contours. (a,b) Transverse view of the leading antisymmetric mode; (c,d) longitudinal view of the leading antisymmetric mode; (e,f) transverse view of the leading symmetric mode; (g,h) longitudinal view of the leading symmetric mode. (a,c,e,g) Unperturbed flow; (b,d,f,h) optimally perturbed flow (NLOP).

3.6 Discussion

Turbulent flows are characterised by intermittency at small scales, consisting of the alternation of long space-time events of weak fluctuation intensity with short events of high intensity, known as EEs, with gradients increasing by orders of magnitude. We have investigated this aspect in the turbulent channel flow, searching for a perturbation that generates such EEs and, therefore, can be conceived as a precursor of such events.

The work of Hack and Schmidt (2021) suggested a link between such EEs and the streak varicose instability. Therefore, we have chosen to perturb a fully resolved turbulent flow field instead of a mean flow. The optimisation was therefore performed on a turbulent *trajectory* evolving according to the

initial perturbation. This approach is challenging both for the computational cost and for the chaotic nature of the turbulent trajectory, which, in a loose sense, is expected to make the objective function ill-conditioned. In our case, it turned out that the optimisation procedure converged essentially to the same result in different runs and allowed us to describe a consistent picture. This is probably due to the short target time considered, which, in turn, is relevant to EEs because they are characterised by short time-scales. Application of this method to other problems, for example, the large-scale instabilities considered in the next chapters, is not straightforward because the relevant target times can be much larger and the optimisation less robust.

One of the most clear results is the fact that the perturbation follows the pre-existing structures and acts to destabilise them and drive their energy to the small scales. This increases both the mean and the local dissipation rate. However, the dynamics of the perturbed flow are more complex because the perturbation also drives an overshoot of the turbulence production rate. The analysis demonstrated that several processes take place at the same time. In particular, while the pre-existing structures are broken by the perturbation, new intense near-wall streaks are created through the lift-up effect. How this process is induced by the perturbation is not clear at present. Therefore, it remains difficult to untangle the precise role of each mechanism in the highly nonlinear dynamics of the perturbed flow. It is even difficult to establish whether such *precise roles* exist.

Another clear result of this study is that the NLOP is more efficient than any other perturbation in enhancing the generation of EEs. Despite the flow exiting the turbulent attractor if the whole domain is perturbed, it can be argued that the local process is physically relevant. This was demonstrated by computing the CST-POD modes of the *natural* EEs sampled from the DNS and the *artificial* EEs sampled in several realisations of the perturbed flow. These modes provide the conditionally averaged local structure of EEs. The CST-POD results are similar for the *natural* and the *artificial* events, both in terms of distribution of energy between symmetric and antisymmetric modes and shape of the eigenfunctions. This *a posteriori* validation implies that the perturbed dynamics analysed in this chapter are relevant to the physics of turbulent flows.

Chapter 4

Large-Scale Motions at high Reynolds number

4.1 Introduction to the chapter

The turbulent channel flow is characterised by two length scales: the viscous length $\delta_\nu^* = \nu^*/u_\tau^*$ and the channel half-gap h^*. The relation between them, $\delta_\nu^* = h^*/Re_\tau$, implies that, at high Reynolds number, the two scales become well separated, leading to an increasingly broad range of turbulent motions. Therefore, at high Reynolds number, one can discriminate between the eddies having size proportional to δ_ν^* and those with size proportional to h^*. The former class includes the near-wall streaks, whose spanwise wavelength is around $100\delta_\nu^*$. The latter includes large-scale motions (LSM) and very-large-scale motions (VLSM) (Guala et al., 2006; Hutchins and Marusic, 2007). These large-scale eddies carry most of the turbulent kinetic energy and Reynolds shear stress. Since most applications involve high Reynolds number flows, these highly energetic structures are an interesting target for control strategies aiming at the reduction of friction drag (Marusic et al., 2021).

Previous studies, summarised in Chapter 1, have shown that large-scale motions are self-sustained and can draw energy directly from the mean shear through a cyclic process similar to the near-wall cycle (Hwang and Cossu, 2010c, 2011; Hwang and Bengana, 2016). They can eventually be subject to instabilities which transfer energy to smaller scales (Park et al., 2011). However, other studies have described the reversed scenario where the large-scale eddy results from a superposition (Adrian et al., 2000; Deshpande et al., 2023) or an instability (Toh and Itano, 2005) of smaller structures (bottom-up process). In this chapter, we investigate the second scenario with a modal stability approach. A synthetic base flow including small-scale[1] near-wall streaks will be considered. The question addressed is whether such base flow can sustain the growth of a large-scale mode. If this is the case, this study will corroborate the existence of a bottom-up scenario for the origin of large-scale motions. Importantly, the unstable mode must feature wavelengths and overall structure compatible with the observations made in direct numerical simulations (DNS) and experiments. For practical reasons, we will consider

[1]Small and large are relative concepts. In this chapter, small-scale denotes lengths proportional to δ_ν^*, like the wavelength of near-wall streaks, as opposed to large-scale motions whose size is proportional to h^*.

only moderately high Reynolds numbers ($Re_\tau \leqslant 2000$). This rules out VLSM, which is supposed to exist only at higher Reynolds numbers ($Re_\tau \geqslant 10^4$).

The chapter is organised as follows. First, the governing equations are recalled from Chapter 2 and the modal stability problem for the turbulent streaks is formulated in Section 4.2. Then, the computation of the base flow is addressed in Section 4.3 using, in this case, Proper Orthogonal Decomposition (POD). Results of the stability analysis follow in Section 4.4 along with a comparison to DNS and experiments. Lastly, the main results and the limits of the methodology are discussed in Section 4.5. The exposition in this chapter is adapted from the published paper Ciola et al. (2024).

4.2 Problem formulation

The incompressible flow in a channel is considered. Periodic boundary conditions are imposed in the streamwise (x or x_1) and spanwise (z or x_3) directions. No-slip conditions are imposed in the wall-normal direction (y or x_2). The periodic domain has dimensions $[L_x, L_y, L_z]$. Quantities without any superscript are made dimensionless with the channel half-gap h^* (such that $L_y = 2$ and $0 \leqslant y \leqslant 2$) and the bulk velocity $U_b^* = \int_0^2 \int_0^{L_z} u^* \, dydz/2L_z$ (outer units). Quantities with a + superscript are made dimensionless with the viscous length $\delta_\nu^* = \nu^*/u_\tau^*$ and the friction velocity $u_\tau^* = \sqrt{\tau_w^*/\rho^*}$ (inner or wall units), where ρ^* is the fluid density, ν^* the kinematic viscosity, and τ_w^* the measured mean wall shear stress. The streamwise, wall-normal and spanwise velocity components are denoted, respectively, by u, v and w or u_1, u_2 and u_3 when using index notation.

The instantaneous flow is governed by the Navier-Stokes equations for incompressible flows

$$\begin{cases} \dfrac{\partial \boldsymbol{u}}{\partial t} + \boldsymbol{u} \cdot \boldsymbol{\nabla} \boldsymbol{u} = -\boldsymbol{\nabla} p + \dfrac{1}{Re} \nabla^2 \boldsymbol{u} + \boldsymbol{f}_b, \\ \boldsymbol{\nabla} \cdot \boldsymbol{u} = 0, \end{cases} \tag{4.1}$$

where $Re = U_b^* h^*/\nu^*$ is the Reynolds number and $\boldsymbol{f}_b$ is a time-varying forcing that keeps the flow rate constant. The long-time average of the instantaneous velocity $\boldsymbol{u}$ is denoted by $\overline{\boldsymbol{U}} = \overline{U}(y)\boldsymbol{e}_x$.

Modal stability analysis of turbulent structures can be performed by considering a base flow constituted by the long-time mean flow plus a *primary* structure $\boldsymbol{u}'$:

$$\boldsymbol{U} = \overline{\boldsymbol{U}} + \boldsymbol{u}'. \tag{4.2}$$

In this work, the primary structures are near-wall streaks. Their stability analysis raises two questions. The first is how to compute a relevant $\boldsymbol{u}'$ for the problem under consideration. This point will be addressed in the next section. The second concerns the governing equations of the base flow and related *secondary* perturbation. Indeed, the analysis is focused on coherent structures, but the turbulent flow also contains incoherent fluctuations whose effect needs to be modelled. In this chapter, following Park et al. (2011) and Alizard (2015), incoherent fluctuations are taken into account through an eddy viscosity term. The Cess (1958) eddy viscosity formula, as reported by Reynolds and Tiederman

(1967), is employed:

$$\nu_t(y) = \frac{1}{2Re}\left\{\left[1+\left(\frac{Re_\tau k}{3}\left(2y-y^2\right)\left(3-4y+2y^2\right)\left(1-e^{(|y-1|-1)Re_\tau/A}\right)\right)^2\right]^{1/2}-1\right\}, \tag{4.3}$$

with $k = 0.426$, $A = 25.4$ (Del Alamo and Jimenez, 2006) and $y \in [0, 2]$.
The eddy viscosity (4.3) can be used to compute an approximate mean flow profile similarly to Reynolds and Tiederman (1967). As usual, we work with a constant bulk velocity equal to 1. To impose this constraint, we do not use the integral formula proposed by Reynolds and Tiederman (1967). Rather, we discretise and invert the following linear system:

$$\begin{cases} \dfrac{1}{Re}\dfrac{d^2}{dy^2}\overline{U} + \dfrac{d}{dy}\left(\nu_t\dfrac{d\overline{U}}{dy}\right) + f_b = 0, \\ \displaystyle\int_0^2 \overline{U}(y)\,dy = 1, \end{cases} \tag{4.4}$$

complemented by the boundary conditions $\overline{U}(0) = 0$ and $\overline{U}(2) = 0$.

Unresolved turbulent motions are also needed to sustain the primary structure $\boldsymbol{u}'$ through nonlinear interactions (as in the Waleffe cycle). These nonlinear terms are lumped in a forcing term $\boldsymbol{f}$.
In summary, the model system for the stability analysis is:

$$\begin{cases} \dfrac{\partial \boldsymbol{u}}{\partial t} + \boldsymbol{u}\cdot\boldsymbol{\nabla}\boldsymbol{u} = -\boldsymbol{\nabla}p + \dfrac{1}{Re}\nabla^2\boldsymbol{u} + \boldsymbol{\nabla}\cdot\left[\nu_t\left(\boldsymbol{\nabla}\boldsymbol{u} + (\boldsymbol{\nabla}\boldsymbol{u})^T\right)\right] + \boldsymbol{f}_b + \boldsymbol{f}, \\ \boldsymbol{\nabla}\cdot\boldsymbol{u} = 0, \end{cases} \tag{4.5}$$

where $\boldsymbol{f}$ is defined such that the base flow $\boldsymbol{U}$ is a steady state of the system. As discussed in Chapter 2 and Section 5.4.2, this definition of $\boldsymbol{f}$ is artificial and essentially corresponds to the frozen base flow assumption. Numerous previous studies of streak instabilities rely on this assumption (Schoppa and Hussain, 2002; Marquillie et al., 2011; Park et al., 2011; Hack and Zaki, 2014; Alizard, 2015; Hack and Moin, 2018), which is needed in practice because the linear stability model does not take into account all the interactions occurring in the turbulent flow.

The stability of the streaks $\boldsymbol{u}'$ is thus addressed linearizing the above equations (4.5) around $\boldsymbol{U}$:

$$\begin{cases} \dfrac{\partial \boldsymbol{u}''}{\partial t} = -\boldsymbol{U}\cdot\boldsymbol{\nabla}\boldsymbol{u}'' - \boldsymbol{u}''\cdot\boldsymbol{\nabla}\boldsymbol{U} - \boldsymbol{\nabla}p'' + \dfrac{1}{Re}\nabla^2\boldsymbol{u}'' + \boldsymbol{\nabla}\cdot\left[\nu_t\left(\boldsymbol{\nabla}\boldsymbol{u}'' + (\boldsymbol{\nabla}\boldsymbol{u}'')^T\right)\right], \\ \boldsymbol{\nabla}\cdot\boldsymbol{u}'' = 0, \end{cases} \tag{4.6}$$

where $\boldsymbol{u}''$ and p'' are the secondary perturbations.

It will be shown, in the next section, that the base flow considered in this chapter is uniform along a wall-parallel direction $\overline{x}$, mildly inclined with respect to x. The direction perpendicular to $\overline{x}$ is denoted $\overline{z}$.
Then, a normal mode *ansatz* with complex frequency σ and real streamwise wavenumber $\overline{k}_x$, namely,

$$\boldsymbol{q}''\left(\overline{x}, y, \overline{z}, t\right) = e^{\sigma_r t}\tilde{\boldsymbol{q}}(y,\overline{z})e^{\iota(\overline{k}_x\overline{x}+\sigma_i t)} + \text{ c.c. }, \tag{4.7}$$

can be injected in the linearised equations (4.6) for the secondary perturbation $\boldsymbol{q}'' = [\boldsymbol{u}'', p'']^T$ and the following generalized eigenvalue problem is obtained:

$$\sigma \mathscr{B} \tilde{\boldsymbol{q}} = \mathscr{A} \tilde{\boldsymbol{q}}. \tag{4.8}$$

with:

$$\mathscr{B} = \begin{bmatrix} 1 & 0 & 0 & 0 \\ 0 & 1 & 0 & 0 \\ 0 & 0 & 1 & 0 \\ 0 & 0 & 0 & 0 \end{bmatrix}; \qquad \mathscr{A} = \begin{bmatrix} \mathscr{L} & -\dfrac{\partial U}{\partial y} + \iota \overline{k}_x \dfrac{d\nu_t}{dy} & -\dfrac{\partial U}{\partial \overline{z}} & -\iota \overline{k}_x \\ 0 & \mathscr{L} - \dfrac{\partial V}{\partial y} + \dfrac{d\nu_t}{dy}\dfrac{\partial}{\partial y} & -\dfrac{\partial V}{\partial \overline{z}} & -\dfrac{\partial}{\partial y} \\ 0 & -\dfrac{\partial W}{\partial y} + \dfrac{d\nu_t}{dy}\dfrac{\partial}{\partial \overline{z}} & \mathscr{L} - \dfrac{\partial W}{\partial \overline{z}} & -\dfrac{\partial}{\partial \overline{z}} \\ \iota \overline{k}_x & \dfrac{\partial}{\partial y} & \dfrac{\partial}{\partial \overline{z}} & 0 \end{bmatrix};$$

$$\mathscr{L} = -\iota \overline{k}_x U - V \frac{\partial}{\partial y} - W \frac{\partial}{\partial \overline{z}} + \left(\frac{1}{Re} + \nu_t \right) \nabla^2 + \frac{\nu_t}{dy} \frac{\partial}{\partial y},$$

where $\nabla^2 = -\overline{k}_x^2 + \frac{\partial^2}{\partial y^2} + \frac{\partial^2}{\partial \overline{z}^2}$ is the laplacian operator. After discretization, (4.8) becomes an algebraic generalised eigenvalue problem $\sigma \mathbf{B}\tilde{\mathbf{q}} = \mathbf{A}\tilde{\mathbf{q}}$.

The streaks are constructed as periodic fields in the $\overline{z}$ direction (see next section). This periodicity is reflected in the block-circulant structure of the matrix $\mathbf{A}$. Therefore, the method proposed by Schmid et al. (2017) and described in Section 2.6.3 is used to efficiently compute the stability of a large array of streaks. Using this method, the computation of the stability of a system composed of N_u repeated periodic units (sub-units) is reduced to N_u sub-unit-size computations, each associated with a root of unity $\rho_j = \exp(2\pi\iota j/N_u)$ with $j = 0, 1, \ldots, N_u - 1$. In this case, one sub-unit is a positive-negative streak couple. The development of sub-harmonic or detuned modes on the streaks corresponds to the bottom-up scenario of LSMs generation because these modes feature a fundamental wavelength which is greater than the streak wavelength.
The full spectrum associated with problem (4.8) is obtained by merging N_u spectra of the smaller matrices $\hat{\mathbf{A}}^{(j)}$ obtained with the root of unity ρ_j. Similarly, provided $\mathbf{v}_j$ is an eigenvector of $\hat{\mathbf{A}}^{(j)}$, the eigenfunctions of the full system can be retrieved and take the form

$$\begin{bmatrix} \mathbf{v}_j \\ \rho_j \mathbf{v}_j \\ \rho_j^2 \mathbf{v}_j \\ \vdots \\ \rho_j^{N_u - 1} \mathbf{v}_j \end{bmatrix} \tag{4.9}$$

for a given ρ_j. Full details on the method can be found in Chapter 2.

Case	Re	Re_τ	L_x	L_z	N_x	N_y	N_z	Δx^+	Δz^+	Δy_w^+	Δy_c^+
C180	2800	≈ 180	π	$\pi/2$	72	129	60	≈ 7.85	≈ 4.71	≈ 0.05	≈ 4.42
C590	11000	≈ 590	$\pi/2$	$\pi/4$	96	257	96	≈ 9.65	≈ 4.83	≈ 0.04	≈ 7.24
C1000	21000	≈ 1000	$\pi/2$	$\pi/4$	200	385	200	≈ 7.85	≈ 3.93	≈ 0.03	≈ 8.2
C1000$_L$	21000	≈ 1000	3π	3π	800	385	1200	≈ 11.8	≈ 7.85	≈ 0.03	≈ 8.2
C2000	45000	≈ 2000	$\pi/2$	$\pi/4$	400	633	400	≈ 8.09	≈ 4.04	≈ 0.03	≈ 10.2

Table 4.1: Parameters of the direct numerical simulations. Re and Re_τ are the Reynolds numbers based, respectively, on the bulk velocity and the friction velocity (the channel is forced with constant flow rate). L_x and L_z are the domain dimensions, respectively, in the streamwise and spanwise direction (in units of channel half-gap). N_x and N_z are the number of Fourier modes in the streamwise and spanwise direction before dealiasing. N_y is the number of Chebyshev collocation points in the wall-normal direction. Δx^+ and Δz^+ are the grid spacings in wall units in the streamwise and spanwise direction. Δy_w^+ and Δy_c^+ are the wall-normal spacings, respectively, near the wall and at the channel centre.

4.3 Base flow computation

Having settled the mathematical framework that models the instability of turbulent streaks, we now turn to the problem of the base flow definition. One option would be to consider invariant solutions of the Navier-Stokes equations. These solutions have the advantage of removing the frozen base flow assumption because they are self-sustained. Moreover, such solutions have already been computed with turbulence models in the past (Rawat et al., 2015; Hwang et al., 2016). However, these solutions are always three-dimensional and including several repetitions of them in the stability analysis would imply the solution of a very large algebraic eigenvalue problem, which is out of reach at the moment. Moreover, invariant solutions usually sit far from the turbulent attractor in the phase space (Doohan et al., 2019), thus their relevance for the investigation of a turbulent process may be questionable.

Instead, the coherent structure contained in the base flow (the *primary* structure $\boldsymbol{u}'$) is determined relying on empirical arguments. Several options are available. For example, Park et al. (2011) and Alizard (2015) used an optimal perturbation obtained with the Navier-Stokes-Cess system linearised around the mean flow. Since large-scale structures are the most energetic structures of the flow, they found that the optimal structure is a large streak filling the whole channel gap. In contrast, we need to compute structures that are localised near the wall and have a small wavelength. For this reason, Direct Numerical Simulations (DNSs) in small computational domains are performed, and the relevant structures for the stability analysis are computed by Proper Orthogonal Decomposition (POD). On one hand, this strategy has the advantage that the resulting structures are statistically representative of the turbulent flow, thanks to the definition of the POD modes, which are the most correlated structures present in the data. On the other hand, it has the disadvantage of requiring a small DNS for each base flow considered.

4.3.1 Direct Numerical Simulations

DNSs of the flow are performed with the channelflow code developed by Gibson et al. (2021) in rather small computational domains. Validation of the DNS data can be found in Chapter 2. Four

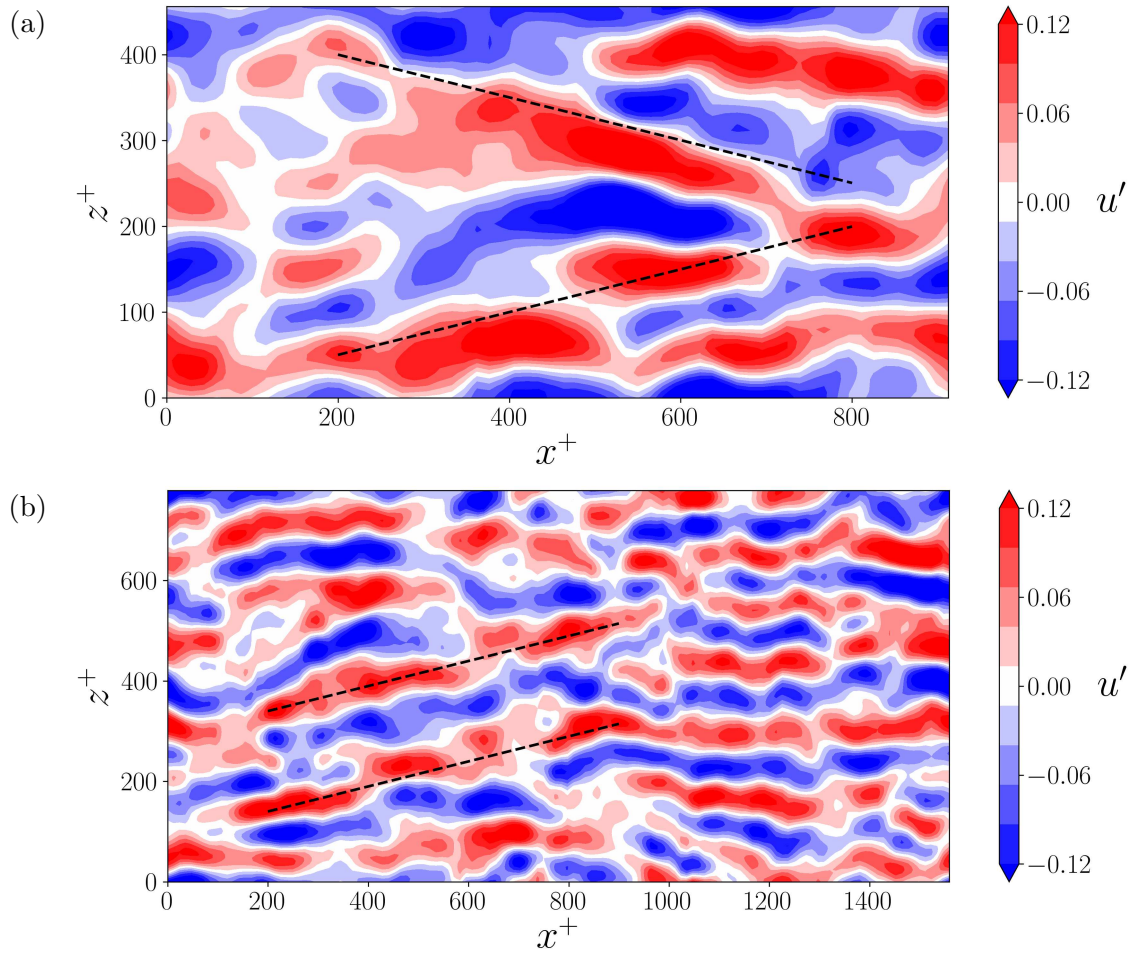

Figure 4.1: DNS snapshots of the streamwise velocity fluctuation at (a) $Re_\tau = 590$ and (b) $Re_\tau = 1000$ in a wall-parallel plane at $y^+ \approx 40$. The velocity field is filtered in the spanwise direction with wavelengths $80 < \lambda_z^+ < 220$. The dashed lines, having angle $\theta = 14°$ with respect to the streamwise direction, show the mild inclination of the coherent structures in the wall region.

different Reynolds numbers are considered for this study. They are reported in table 4.1 along with the domain dimensions and the discretisation parameters. The flow is simulated with a constant flow rate. Hence, the input Reynolds number for the simulations is the one based on the bulk velocity $Re = U_b^* h^*/\nu^*$. However, results are presented using the friction Reynolds number $Re_\tau = u_\tau^* h^*/\nu^*$ to ease comparison with the literature. Table 4.1 includes an additional simulation at $Re_\tau = 1000$ in a larger domain to allow the presence of large-scale motions to be compared with linear stability analysis (LSA) results.

The small domains contain relevant near-wall dynamics but are not reliable at the channel centre. For example, for $Re_\tau = 1000$ we have used a minimal box for the logarithmic layer as in Jiménez (2013), which is known to have incorrect statistics above $y \approx L_z/3 \approx 0.25$ (Flores and Jiménez, 2010; Lozano-Durán and Jiménez, 2014). Since the only purpose of these simulations is to extract the near-

wall coherent structures used for LSA, this should not be an issue. However, LSA will allow domains of much larger spanwise size and virtually infinite streamwise size.

4.3.2 Proper Orthogonal Decomposition

It has been shown in previous studies (Moin and Moser (1989); Alfonsi and Primavera (2007)) that the leading POD mode for the turbulent channel flow is constituted by streamwise uniform streaks. However, in the near-wall region of turbulent flows, as indicated by the early works of Hamilton et al. (1995) and more recently discussed in Jiménez (2022), due to the establishment of the wall cycle, velocity streaks exhibit small inclinations with respect to the streamwise direction.
This can be visualised in figure 4.1, which provides a snapshot of the DNS velocity field after filtering out the flow structures with spanwise wavelengths $\lambda_z^+ < 80$ and $\lambda_z^+ > 220$. The dashed lines, having an angle $\theta = 14^\circ$ with respect to the streamwise direction, show a mild inclination of the coherent structures in the wall region. Qualitatively similar structures are found in the larger domain DNS at $Re_\tau = 1000$. However, it must be noted that these streaks are inclined at different angles, resulting in a complex three-dimensional field. To make the stability analysis cheaper, we will consider a more idealised situation where the streaks are periodic along a given direction, *i.e.* they are all inclined with the same angle. This is a necessary approximation to apply the block-circulant matrix method described above.

For this reason, we extract by POD arbitrarily inclined coherent structures considering the Fourier decomposition of the instantaneous flow field $\boldsymbol{u}$ in the streamwise (x) and spanwise (z) directions (Muralidhar et al., 2019):

$$\boldsymbol{u}(\boldsymbol{x},t) = \sum_{m_x,m_z} \hat{\boldsymbol{u}}_{m_x,m_z}(y,t) e^{2\pi\iota\left(\frac{m_x x}{L_x}+\frac{m_z z}{L_z}\right)}, \tag{4.10}$$

where ι denotes the imaginary unit, m_x and m_z are the normalised wavenumbers[2], and the sum is extended to all the Fourier modes used for the discretisation of the domain, while y denotes the wall-normal direction. For a given wavenumber couple $\{m_x, m_z\}$, POD is performed using the profiles $\hat{\boldsymbol{u}}_{m_x,m_z}(y,t)$ obtained from the $x-z$ Fourier transform of the three-dimensional snapshots of the small domain DNS.

For most of the POD computations, 2000 snapshots equi-spaced in time with nondimensional time-step $\Delta t^* U_b^*/h^* = 0.25$ are employed. The resulting leading POD modes $\hat{\boldsymbol{\psi}}_{m_x,m_z}(y)$ are shown in figure 4.2. It can be noted that they are not symmetric with respect to the channel mid-plane. For this reason, the POD was repeated for $Re_\tau = 590$, $m_x = 1$ and $m_z = 2$ with 4000 snapshots instead of 2000. Comparing panel (a) with panel (c) in figure 4.2, it can be observed that the asymmetry persists. We remark that the first two POD modes have comparable eigenvalues and seem to be always in phase opposition (compare panel (a) versus panel (b) and panel (c) versus panel (d)). Hence, the first two POD modes represent a couple of modes having (almost) the same eigenvalue and characterised by an opposed asymmetry with respect to the channel midplane. A linear combination of these two modes

[2]For example, the streamwise wavelength of a mode with $m_x = 3$ is 1/3 of L_x. m_x has nothing to do with the quasi-streamwise wavenumber of the secondary perturbation $\overline{k}_x$.

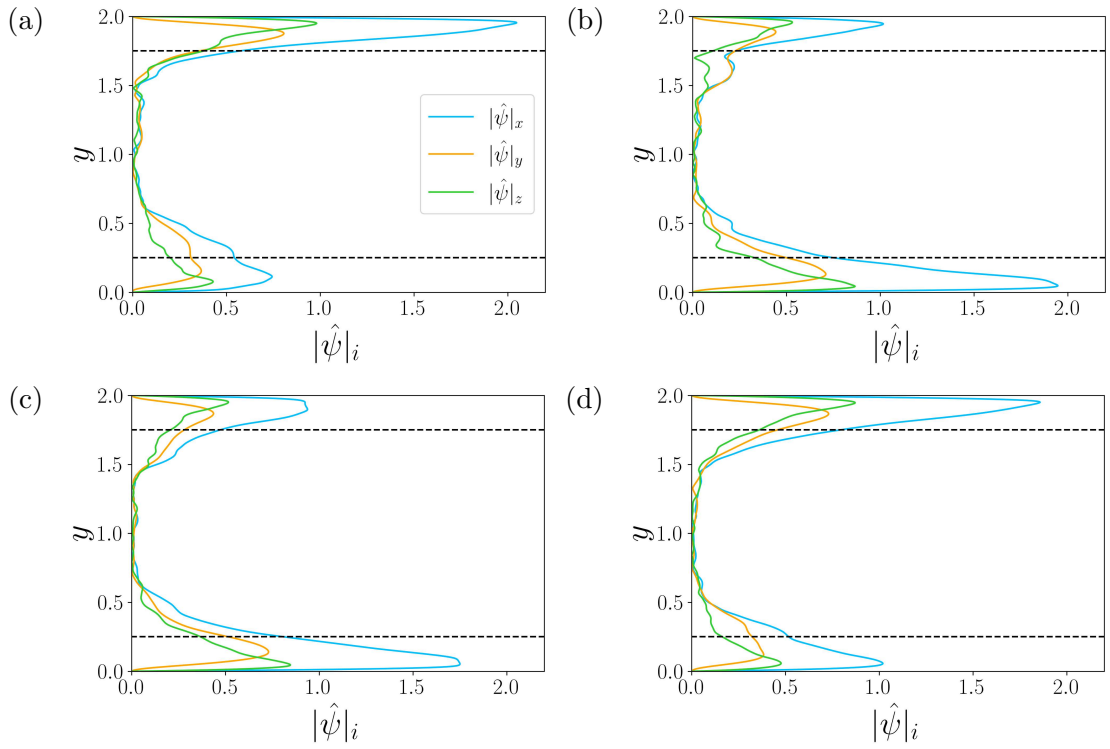

Figure 4.2: Absolute value of the POD leading modes $\boldsymbol{\psi}_{m_x,m_z}(y)$ at $Re_\tau = 590$ with $m_x = 1$ and $m_z = 2$. The POD modes are obtained from (a,b) 2,000 DNS snapshots and (c,d) 4,000 DNS snapshots spaced by $\Delta t = 0.25$ in time. (a,c) First leading mode; (b,d) second leading mode. The dashed lines denote $y = 0.25$ and $y = 1.75$ and delimit the wall regions where the turbulent flow is well resolved in the minimal domains.

would be arbitrary because their amplitudes are not defined (we define only a relative amplitude of the streaks with respect to the mean flow, as described below). Therefore, a single asymmetric mode was retained.

In figure 4.2, it can also be noted that the POD mode decreases rapidly when the distance from the wall is greater than $0.25h^*$, as demarcated by the dashed black lines. The flow in the minimal unit is well resolved in this region (Flores and Jiménez, 2010). For larger m_x and m_z, the mode is even more localised near the wall. Conversely, it is dislocated towards the channel centre for $m_x = 1$ and $m_z = 1$. However, it will be seen in the following that this particular combination of wavenumbers is not much relevant for the conclusions of this chapter and is included in the results only for completeness.

The leading POD profile, $\hat{\boldsymbol{\psi}}_{m_x,m_z}(y)$, is used to reconstruct a three-dimensional flow field as:

$$\boldsymbol{u}_s(\boldsymbol{x}) = \hat{\boldsymbol{\psi}}_{m_x,m_z}(y) e^{2\pi\iota\left(\frac{m_x x}{L_x}+\frac{m_z z}{L_z}\right)} + \text{ c.c.} \tag{4.11}$$

(c.c.: complex conjugate). The properties of the POD (Berkooz et al., 1993) ensure that the mode obtained in this way is still a POD mode of the three-dimensional channel. In addition, using this method, the inclination of the resulting coherent structures can be freely chosen by selecting m_x and m_z. Note that, being selected *a priori*, this inclination is not expected to vanish as the number of

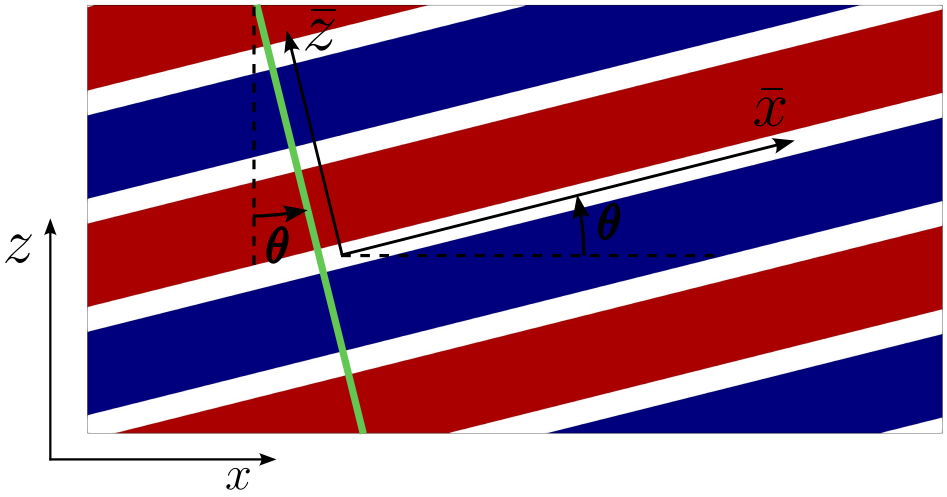

Figure 4.3: Visualisation of the POD mode at $Re_\tau = 590$ in the $x - z$ plane and sketch of the rotated frame $\overline{x} - \overline{z}$ ($\theta \approx 14°$). The thick green line is the trace of the $y - \overline{z}$ plane on which LSA is performed.

snapshots used for the POD is increased. Moreover, for a given couple $\{m_x, m_z\}$, there is a paired $\{m_x, -m_z\}$ mode which provides streaks inclined with the same angle in the opposite direction. However, to obtain a two-dimensional base flow, the two modes can not be employed together.

Figure 4.3 shows that the structures computed in this way are uniform along the direction $\overline{x}$, which is inclined with respect to x of an angle $\theta = \arctan\left[(m_x L_z) / (m_z L_x)\right]$. To make the stability analysis computationally cheaper, the POD mode is defined as a two-dimensional field in the $y - \overline{z}$ plane (green line in the figure), where $\overline{z}$ is the axis perpendicular to $\overline{x}$. The mean flow and the POD mode, which define the base flow, are therefore projected in this rotated frame.

4.3.3 Streak amplitudes

The POD modes are defined up to an arbitrary multiplicative constant. Therefore, we need to introduce an amplitude definition for the streaks. We follow Alizard (2015) and define the *streak amplitude* as:

$$A_s = \frac{\max_{y,\overline{z}} u - \min_{y,\overline{z}} u}{2U_c}, \tag{4.12}$$

where u (scalar) is the $\overline{x}$ velocity component of a two-dimensional field and U_c is the centerline velocity of the mean turbulent profile.

Accordingly, $\boldsymbol{u}_s$ is rescaled such that:

$$\frac{\max_{y,z} u_s - \min_{y,z} u_s}{2\overline{U}_c} = 1, \tag{4.13}$$

where u_s (as a scalar field) is the $\overline{x}$ component of $\boldsymbol{u}_s$. Then, the new base flow $\boldsymbol{U}$ is constructed as

$$\boldsymbol{U} = \overline{\boldsymbol{U}} + A_s \boldsymbol{u}_s, \tag{4.14}$$

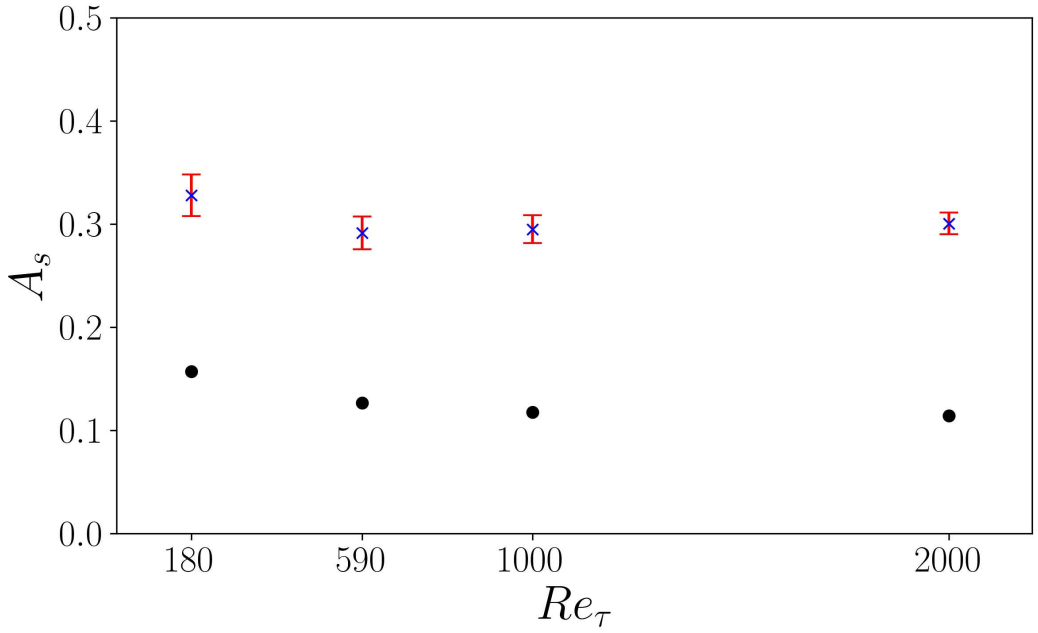

Figure 4.4: A_s (4.12) measured in DNS at different Reynolds numbers; the × symbols denote the mean value, whereas the error bars denote the standard deviation of the respective temporal fluctuations. The circles are the peaks in the r.m.s. profiles of the streamwise fluctuation scaled with U_c.

with $A_s > 0$, the parameter that plays the role of streak amplitude.

In order to define a realistic variability range for A_s, some quantitative measurements are performed on the DNS data. For each snapshot, the equation (4.12) is applied to every $y-z$ plane and averaged in the streamwise direction and in time. The result is an amplitude of $\approx 0.3 \pm 0.01$ (blue crosses in figure 4.4) for all four Reynolds numbers considered, where the uncertainty is given by the standard deviation of this quantity with respect to time. Evidently, this is a rough estimate because the formula (4.12) is applied to an instantaneous turbulent field, which is rather different from the base flow constituted by periodic streaks. Using equation (4.12), the amplitude is computed using the maximum and minimum values of the streamwise component of velocity, irrespective of the structural topology of the velocity field, in a sort of worst-case scenario. Therefore, this can be considered an upper estimate of the streak amplitude.

On the other hand, the root mean square (r.m.s.) peak value of the streamwise velocity fluctuation (scaled with the centerline velocity for comparison) is around 0.1, as shown by the black circles in figure 4.4. Given the definition of r.m.s., it is sure that a greater value will be attained by the velocity fluctuation at least at some instant of time. Thus, it is argued that a realistic amplitude for the coherent structures must fall in the range $0.1 \div 0.3$.

This estimation from the DNS is performed on the full velocity fluctuation, whereas the considered base streaks are made up of only one Fourier mode. The energy contained in one Fourier mode of the DNS fields is not so substantial because of the broadband character of the turbulent velocity

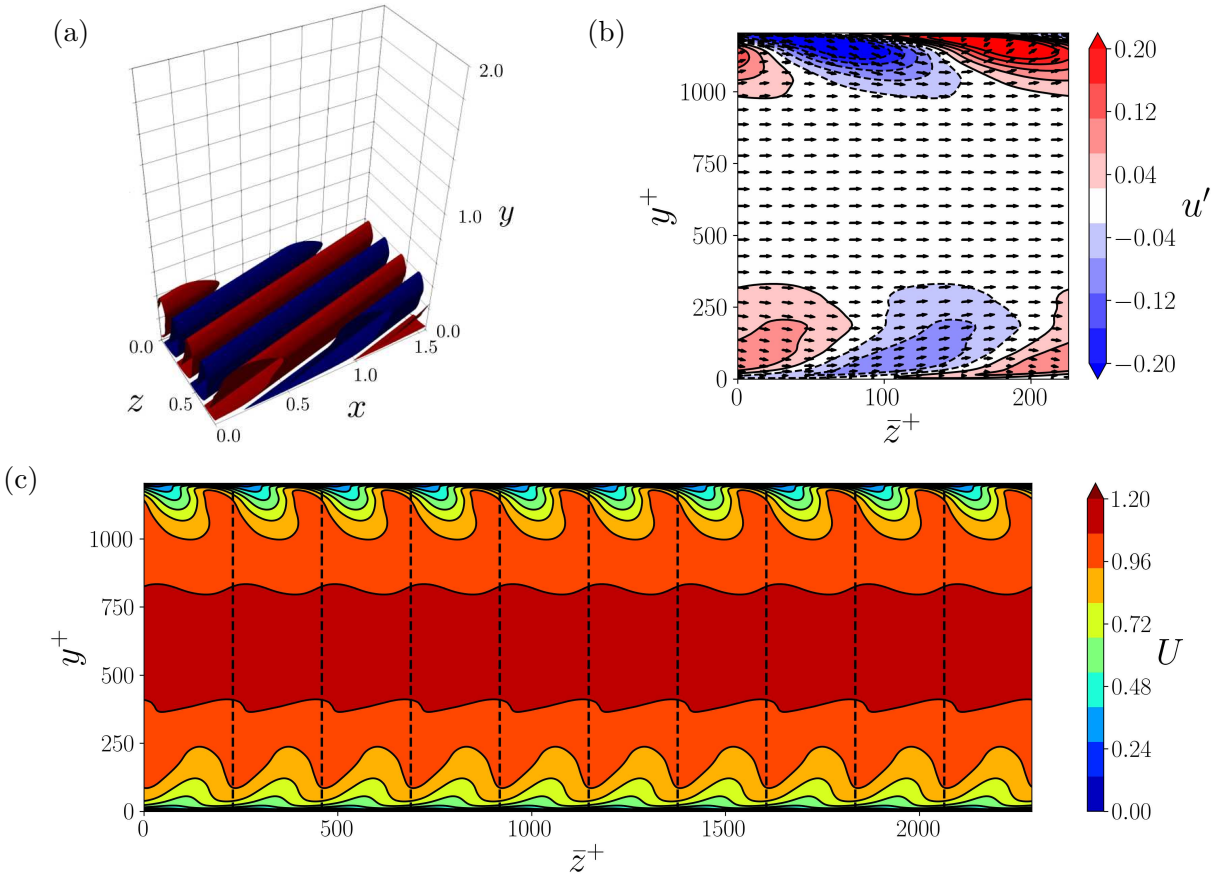

Figure 4.5: Base flow for the $Re_\tau = 590$ case. (a) Isocontours of the streamwise component of the POD mode with $m_x = 1$ and $m_z = 2$ ($\theta \approx 14°$). (b) POD mode rescaled with $A_s = 0.25$ visualised in the $y - \bar{z}$ plane: isocontours of the streamwise component and arrows for the transverse components. (c) Base flow (mean flow plus POD mode) in the $y - \bar{z}$ with $N_u = 10$. The dashed lines delimit a single periodic unit.

spectrum. Therefore, the extracted mode should not be seen as representative of the (m_x, m_z) Fourier mode alone but, rather, as an idealised representative of the whole ensemble of near-wall coherent turbulent fluctuations. Note, also, that the values used by Park et al. (2011) and Alizard (2015) are included in the same range.

The field $\boldsymbol{u}_s$ developed in the three-dimensional space from the leading POD profile with $\{m_x, m_z\} = \{1, 2\}$ and $Re_\tau = 590$ is shown in figure 4.5 (a). This POD mode projected in the $y - \overline{z}$ frame with amplitude $A_s = 0.25$ is shown in figure 4.5 (b). As can be remarked from the arrows on this panel, the streamwise velocity modulations are subject to a nonzero mean flow component in the $\overline{z}$ direction, due to their inclination with respect to the streamwise direction. Finally, panel (c) of the same figure shows the complete base flow (mean flow plus POD mode) with $N_u = 10$ periodic units.

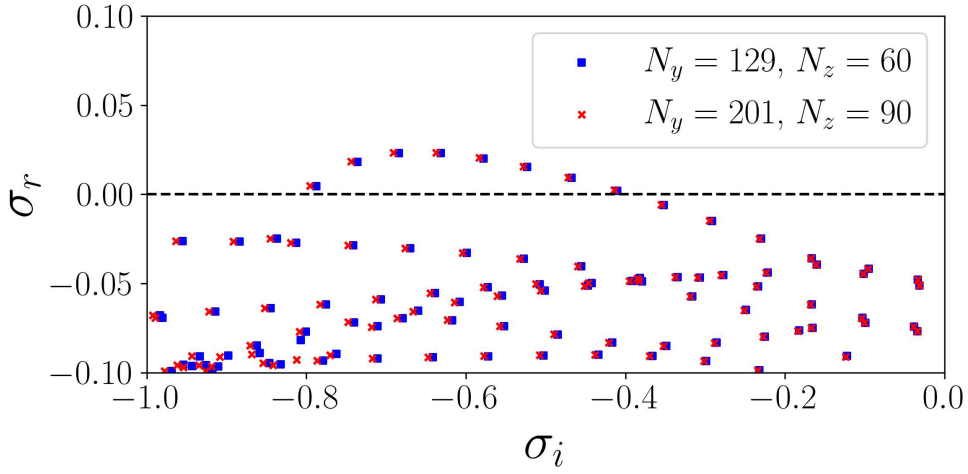

Figure 4.6: Eigenvalues at $Re_\tau = 2000$ for the $A_s = 0.2$ and $\overline{k}_x = 1.0$ case ($N_u = 60$, $\theta \approx 14°$) in the complex plane for two different numerical resolutions (N_y number of points in the y direction and N_z number of points in the $\overline{z}$ direction).

4.4 Stability analysis results

4.4.1 Numerical parameters

The differential operators in (4.8) are discretised using Fourier collocation in the $\overline{z}$ direction and Chebyshev collocation in the wall-normal direction. The matrices are modified to enforce no-slip conditions (zero perturbation velocity) at the walls ($y = 0$ and $y = 2$). Two grids are tested: the first has $N_z = 60$ collocation points in $\overline{z}$ and $N_y = 129$ collocation points in y; the second has $N_z \times N_y = 90 \times 201$. We compare the two grids at the highest Re considered ($Re_\tau = 2000$), which, in principle, is the most sensible to the discretisation because velocity gradients are stronger. Figure 4.6 shows that the two grids give comparable results with a variation of the order of 2% on the leading eigenvalue. Similar small deviations are measured on the leading eigenmodes. These small deviations do not impact the conclusions of our study. Therefore, the coarser discretisation is considered appropriate and used for all the other computations.

Another numerical parameter that may affect the results of LSA is the number of DNS snapshots used to compute the POD mode (N_s). This is verified in figure 4.7 for two base flows obtained at $Re_\tau = 1000$ with two different POD modes: the first obtained with 1200 snapshots and the second obtained with 2000 snapshots. Despite there are some differences between the spectra, the leading unstable branch is almost the same. Since most of the results commented on in the following subsections are based on the leading modes, these differences should not affect the conclusions of our study. The observed discrepancies between the eigenvalues obtained with different N_s are the consequence of differences in the respective POD modes. This was already observed in figure 4.2, which shows that, even increasing the number of snapshots to 4000, the convergence of the POD modes is not satisfactory. This slow convergence is a drawback of the POD method and motivates

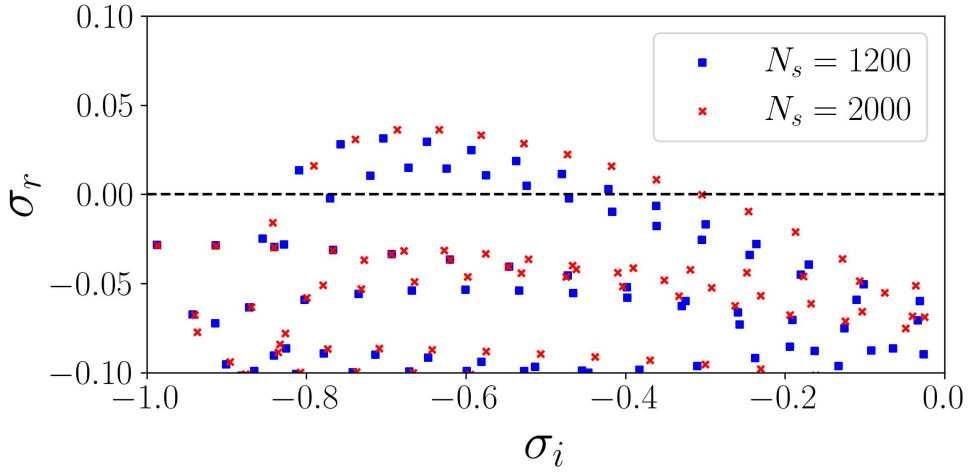

Figure 4.7: Eigenvalues at $Re_\tau = 1000$ for the $A_s = 0.2$ and $\overline{k}_x = 1.0$ case ($N_u = 60$, $\theta \approx 14°$) in the complex plane as a function of the number of snapshots used for the POD N_s.

the change of approach in the next chapter. The baseline value of N_s used for all the following computations is 2000.

Lastly, an important numerical parameter is the number of periodic units considered N_u, *i.e.* the number of periodic streaks on which sub-harmonic or detuned modes can develop. The value of this parameter indirectly sets the total spanwise size of the LSA domain. $Re_\tau = 2000$ is considered again to test this parameter. The variation of the leading growth rate is displayed in figure 4.8 (a) for $\overline{k}_x = 0.5$ and $\overline{k}_x = 1.0$. We observe a variation in the leading growth rate between $N_u = 60$ and $N_u = 90$ of the 2.4% for $\overline{k}_x = 0.5$ and of the 1.8% for $\overline{k}_x = 1.0$. The figure clearly shows that this variation is negligible with respect to the variation due to *e.g.* the wavenumber $\overline{k}_x$. Therefore, N_u has a minor influence on the eigenvalues. Concerning the influence on the eigenmodes, figure 4.8 (b-d) shows the spectral energy content in $\overline{z}$ of the leading modes for $\overline{k}_x = 0.5$ (b) and $\overline{k}_x = 1.0$ (c-d). This type of figures are better explained and interpreted in the following subsection (see figure 4.12 and related text). The point here is that the structure of the eigenmodes is not influenced by N_u. The only difference that may be encountered, depending on the case, is illustrated by the two panels (c) and (d). The leading mode obtained with $N_u = 60$ corresponds to a root of unity index $j = 56$, whereas with $N_u = 90$ the leading mode corresponds to $j = 85$. These unstable modes are compared in panel (c). In panel (d), we plot the $N_u = 90$ unstable mode corresponding to $j = 84$ instead of 85 (together with leading modes obtained from $N_u = 30$ and 60). We see that the $j = 84$ mode matches well those obtained with $N_u = 30$ and 60 (indeed $84/56 = 1.5 = 90/60$), while the truly most unstable mode at $N_u = 90$ ($j = 85$) has a slightly different large-scale wavelength. Hence, this slight shift in the large-scale wavelength is what may happen to the most unstable eigenmode when increasing the total number of periodic units. However, this does not alter the conclusions of this study because the shift is negligible with respect to other parametric variations. For this reason, $N_u = 60$ is used throughout the rest of the chapter.

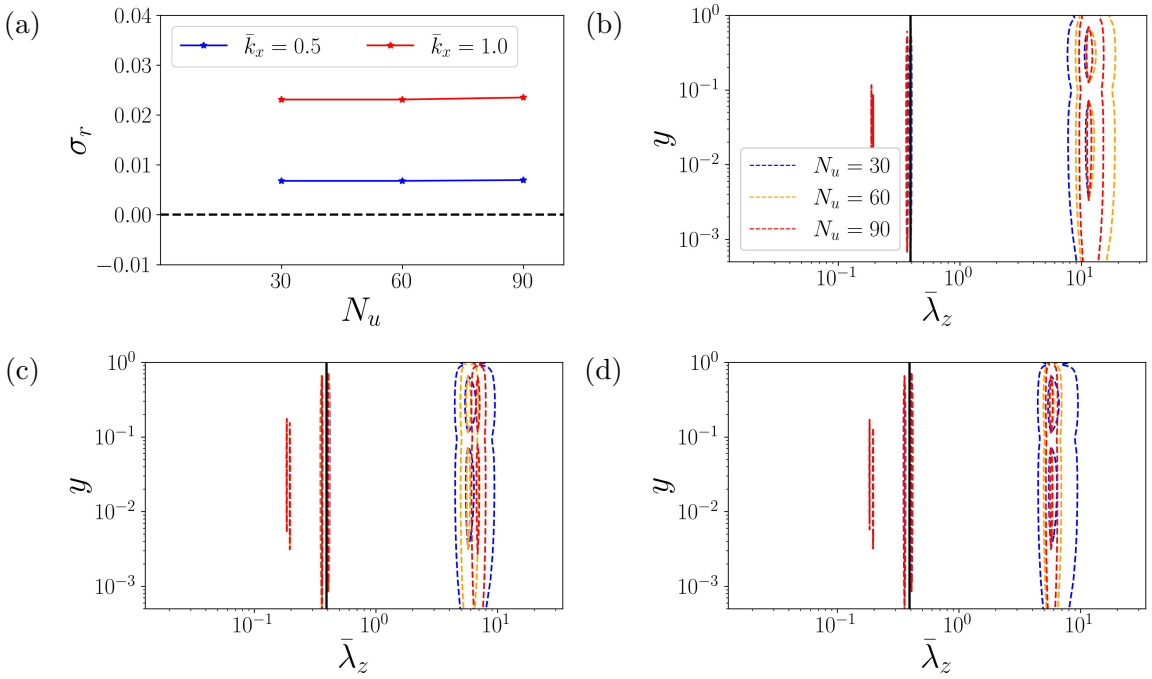

Figure 4.8: (a): Growth rate of the leading unstable mode ($\star$) as a function of the number of periodic units N_u at $Re_\tau = 2000$ for two different values of $\bar{k}_x$, $m_z = 2$ and $A_s = 0.20$. (b-d): Spectral energy content along the $\overline{z}$ direction of the streamwise component of the leading unstable eigenmodes (E_{uu} in the text) for (b) $\bar{k}_x = 0.5$ and (c,d) $\bar{k}_x = 1.0$. The vertical black line denotes the width of the periodic units. The eigenmode is normalised to have kinetic energy equal to one. The contour levels are for $E_{uu} = [10^{-4}, 10^{-1}]$. The difference between (c) and (d) is that a different root unity index is selected for the $N_u = 90$ mode (see text).

4.4.2 Leading growth rates

An example of eigenspectra is given in figure 4.9 for two of the four Re_τ considered, $Re_\tau = 180$ (a) and $Re_\tau = 590$ (b). The colorbar shows the respective detuning factor ($\gamma = j/N_u$) of the instability, which is allowed to take N_u discrete equi-spaced values in the interval $[0, 1)$. Due to the high number of periodic units considered, the eigenspectra show numerous branches. Figure 4.9 shows that one of these branches is almost marginally stable at $Re_\tau = 180$ and becomes prone to a detuned instability ($0.9 < \gamma < 1$) at higher Reynolds numbers. However, it must be noted that the detuning factor depends on the reference frame, so that the effective detuning factor in the streamwise aligned ($x - z$) reference frame is lower. The conversion is not done here because the detuning factor, per se, is of minor importance. We will convert the wavelengths of the eigenmodes from the $\overline{x} - \overline{z}$ system to the $x - z$ system in the following. The important message of figure 4.9 is that an unstable branch is present at sufficiently high Reynolds number, with the leading mode corresponding to a detuned instability.

In the previous subsection, we have seen that the number of periodic units has a weak impact both on the eigenspectra and on the eigenmodes, provided that it is sufficiently large ($N_u \geqslant 60$). This behaviour is expected because the number of units fixes the maximum allowable spanwise size of the modes. If this size is too small, modes linked to a large-scale spanwise modulation might not be

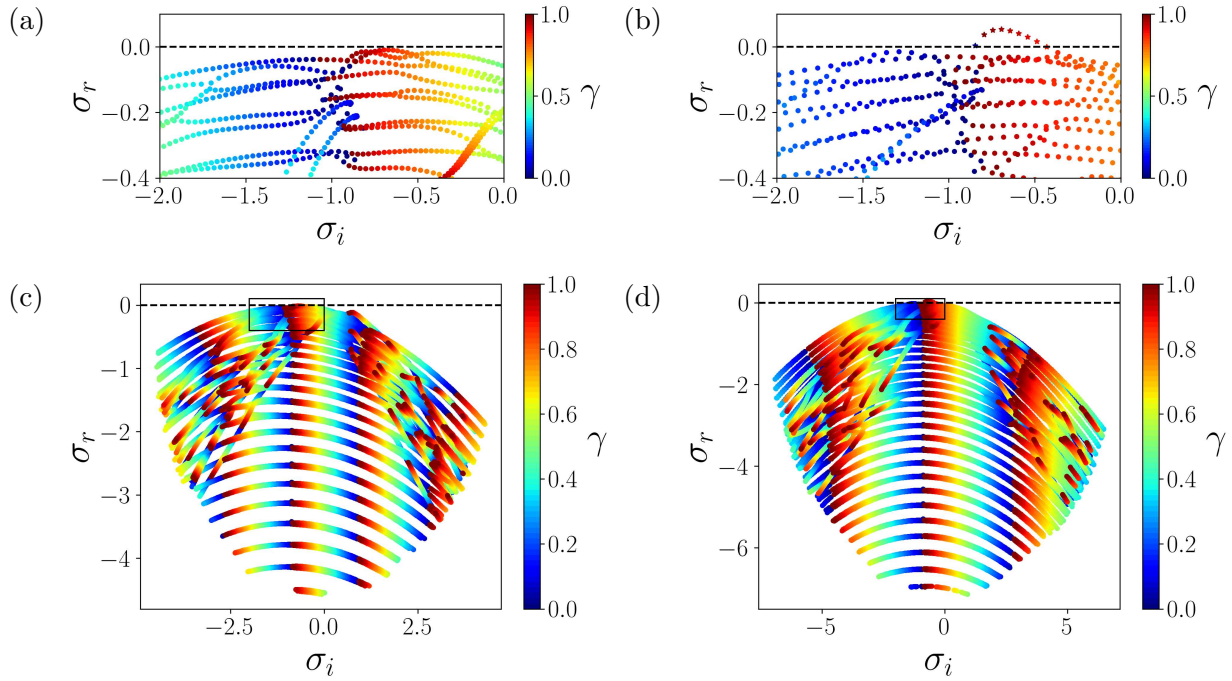

Figure 4.9: Eigenvalues for the $A_s = 0.25$ and $\overline{k}_x = 1.0$ case ($N_u = 60$, $\theta \approx 14^\circ$) at: (a-c) $Re_\tau = 180$; (b-d) $Re_\tau = 590$. The colors denote the detuning factor $\gamma = j/N_u$ for $j = 0, \ldots, N_u - 1$. The top row panels are close-ups on the portion of the spectrum denoted by solid line rectangles in the bottom row panels. The dashed black line denotes the marginal stability limit ($\sigma_r = 0$). The point with maximum growth rate σ_r defines the leading unstable mode in case of instability ($\max \sigma_r > 0$) or the least stable mode in case of stability ($\max \sigma_r < 0$).

properly resolved. On the other hand, if the domain is sufficiently large, the leading mode is properly resolved and becomes independent of the domain size. Conversely, the streak amplitude A_s and the inclination of the base flow streaks θ strongly affect the outcome of the stability analysis, as shown in figure 4.10. The growth rates of the most unstable modes have similar values and trends for $Re_\tau = 590$, $Re_\tau = 1000$ and $Re_\tau = 2000$ (blue, red and yellow lines), while the $Re_\tau = 180$ (green) cases show a different behaviour.

The dependence of the most unstable mode growth rate on A_s is displayed in figure 4.10 (a). As expected, the growth rate increases linearly with this parameter so that instability is found for $A_s > 0.1$ for $Re_\tau = 590, 1000, 2000$. For $Re_\tau = 180$, instability is found only at a very large amplitude $A_s > 0.25$.

Concerning the base flow inclination, figure 4.10 (b) shows that there is a peak in the growth rate at $\theta \approx 14^\circ$ for $Re_\tau = 590, 1000$ slightly displaced at $\theta \approx 7.1^\circ$ for $Re_\tau = 2000$, while the flow remains stable at $Re_\tau = 180$. This decrease of the optimal angle with the friction Reynolds number might indicate a trend towards the destabilisation of more streamwise-aligned streaks at higher Reynolds numbers. However, streaks that are totally aligned with the streamwise direction are found to be stable with respect to detuned instabilities, also at high Reynolds numbers.

For $Re_\tau = 180$ and $A_s < 0.25$, the base flow remains stable no matter the angle of the POD mode. The

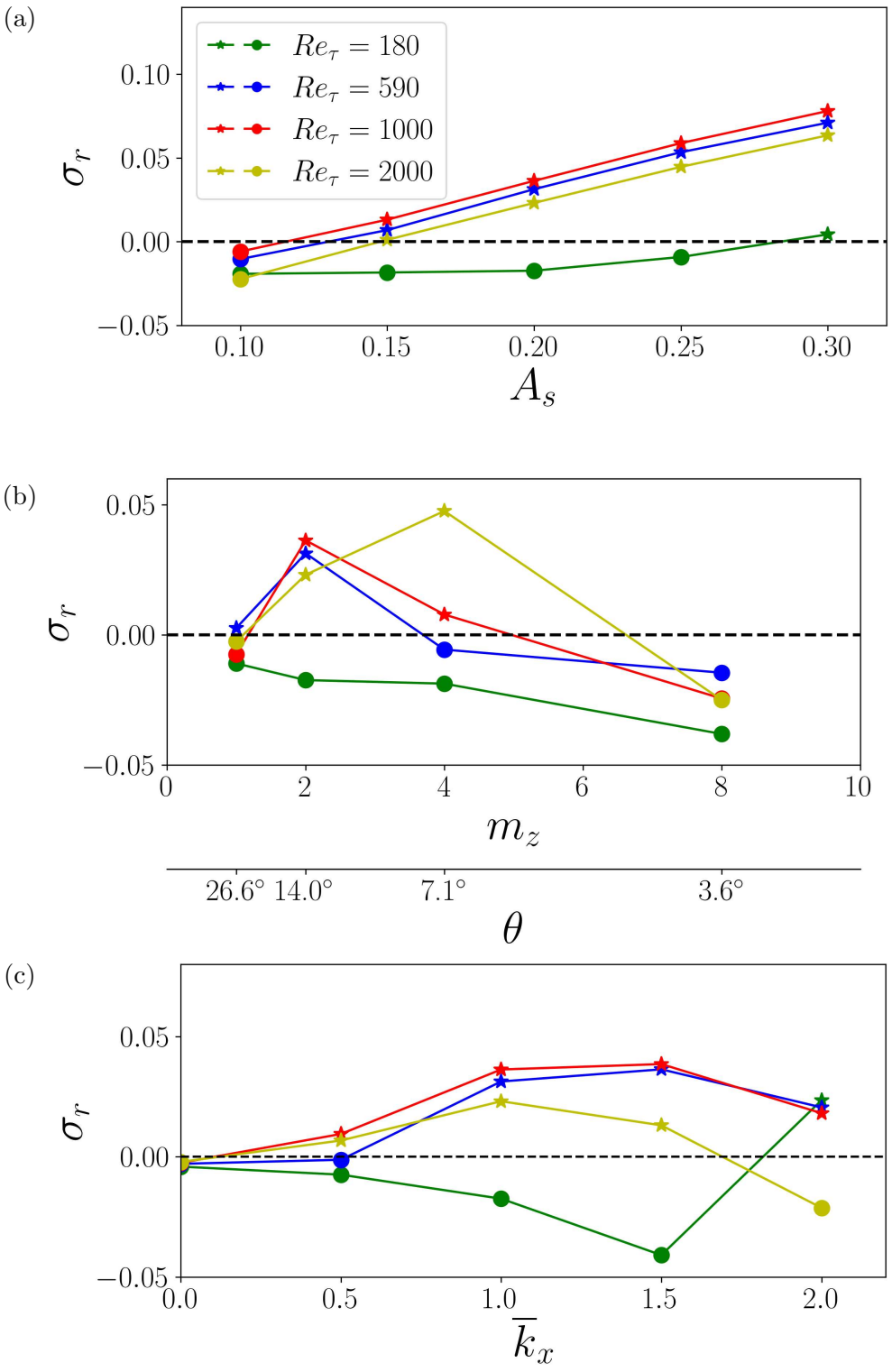

Figure 4.10: Growth rate of the leading unstable mode ($\star$) or least stable mode ($\bullet$) as a function of: (a) A_s (with $k_x = 1.0$ and $m_z = 2$); (b) θ (with $k_x = 1.0$ and $A_s = 0.20$); (c) $\overline{k}_x$ (with $A_s = 0.20$ and $m_z = 2$). All computations were performed with $m_x = 1$ and $N_u = 60$.

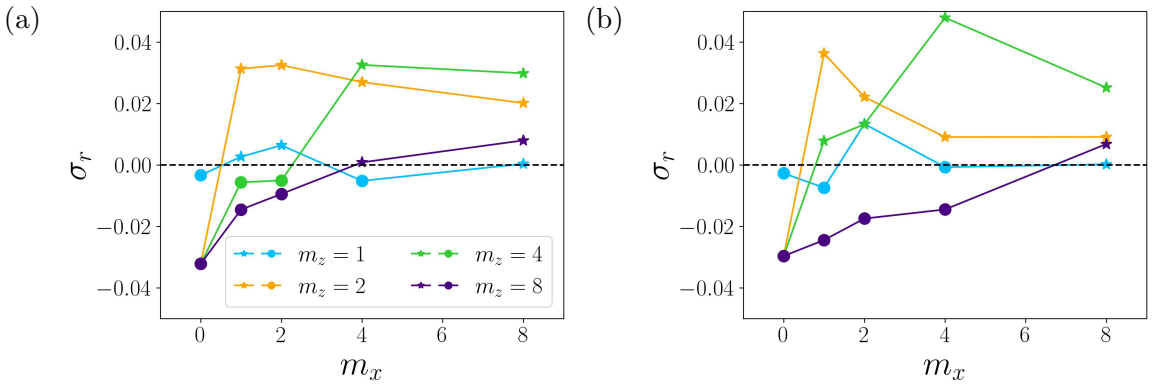

Figure 4.11: Growth rate of the leading unstable mode ($\star$) or least stable mode ($\bullet$) as a function of base flow wavenumbers $\{m_x, m_z\}$ for (a) $Re_\tau = 590$ and (b) $Re_\tau = 1000$. All computations were performed with $\overline{k}_x = 1.0$, $A_s = 0.20$ and $N_u = 60$.

stability of the $Re_\tau = 180$ cases can be attributed to low Reynolds number effects and is compatible with the poor evidence of large-scale structures in these flow conditions (Smits et al., 2011).

The wavenumber along $\overline{x}$, namely, $\overline{k}_x$, is a free parameter of the problem as well. Figure 4.10 (c) shows that for the intermediate Reynolds number considered (590, 1000) there is a plateau in the growth rate for $\overline{k}_x \in [1.0, 2.0]$. The plateau is shifted towards smaller wavenumbers ($\overline{k}_x \in [0.5, 1.5]$) for $Re_\tau = 2000$. Conversely, for $Re_\tau = 180$ the growth rate is found positive with $A_s = 0.2$ only for $\overline{k}_x = 2.0$.
Hence, the influence of $\overline{k}_x$ on the growth rate gives a range of unstable wavenumbers depending on the friction Reynolds number. The fact that the most unstable wavenumber decreases when Re_τ grows is consistent with the observation of coherent structures having larger streamwise wavelength at higher friction Reynolds number (compare the pre-multiplied energy spectra at different Re_τ in figure 4.14, and the work of Del Alamo et al. (2004)). As will be shown in the next section, this range of $\overline{k}_x$ gives a range of streamwise and spanwise wavelengths in the DNS reference frame.

Finally, one may ask what happens when both the base flow wavenumbers $\{m_x, m_z\}$ are changed. To investigate this point several computations spanning $m_x = [0, 1, 2, 4, 8]$ and $m_z = [1, 2, 4, 8]$ for the two intermediate Reynolds numbers considered ($Re_\tau = [590, 1000]$) are performed having fixed $A_s = 0.20$ and $\overline{k}_x = 1.0$. The resulting growth rates are shown in figure 4.11. Two aspects can be remarked: (i) the streamwise independent ($m_x = 0$) structures are always stable; (ii) increasing m_z, the maximum growth rate moves towards larger m_x. This means that the instability is found in a given range of the ratio m_z/m_x which corresponds to a range of inclination angles $\theta \approx 7^\circ \div 28^\circ$.

4.4.3 Leading eigenmodes

In this subsection, some observations on the leading unstable modes (or least stable modes in some cases) are presented. The $Re_\tau = 180$ case, for which evidence of large-scale motions is not compelling, will not be considered. Moreover, we fix $m_x = 1$ and $m_z = 2$ for most of the section to simplify the

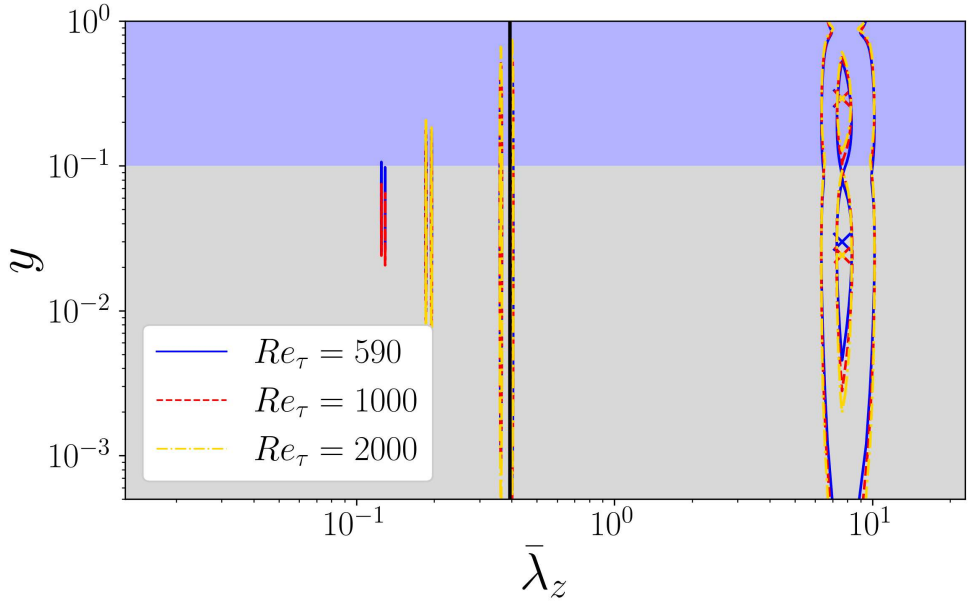

Figure 4.12: Spectral energy content along the $\overline{z}$ direction of the streamwise component of the leading unstable eigenmodes (E_{uu} in the text) for $\overline{k}_x = 1.0$ and different Reynolds numbers ($A_s = 0.20$, $m_x = 1$, $m_z = 2$). The vertical black line denotes the wavelength of the periodic units (the base flow is periodic along $\overline{z}$ with this wavelength). The eigenmode is normalised to have kinetic energy equal to one. The contour levels are for $E_{uu} = [10^{-4}, 10^{-1}]$. The two different background colours indicate the inner layer (light grey, for $y < 0.1$) and the outer layer (light blue, for $y > 0.1$).

analysis. It will be argued that other combinations of base flow wavenumbers $\{m_x, m_z\}$ lead to similar conclusions. Different $\overline{k}_x \in [0.5, 2]$ will be considered unless otherwise specified.

A closer look at the eigenmodes' spatial structure is provided in figure 4.12, where the energy content of the mode is represented with respect to the wavelength along $\overline{z}$ ($\overline{\lambda}_z$) and to the wall-normal position. To compute this quantity, we consider, the Fourier tranform of the eigenvector $\tilde{\boldsymbol{q}}(y, \overline{z}) = [\tilde{u}(y, \overline{z}), \tilde{v}(y, \overline{z}), \tilde{w}(y, \overline{z}), \tilde{p}(y, \overline{z})]^T$ in the $\overline{z}$ direction, denoted by $\hat{\boldsymbol{q}}$. The quantity plotted in figure 4.12 is $E_{uu}(y, \overline{\lambda}_z) = \hat{u}\hat{u}^*$, where * denotes the complex conjugate.
It can be seen in the figure that the eigenmodes are made up of several waves with different wavelengths. Among them, one is characterised by a large wavelength and extends up to the outer region of the flow ($y > 0.1$). In the figure, the spanwise wavelength characterising the base flow is denoted by the black solid line. Therefore, it is evident that the large wavelength component of the eigenmode is much more extended than the base flow structures. We postulate that the large-wavelength modulation found in the unstable eigenmode is a large-scale structure engendered by the interaction of several base flow sub-units, *i.e.* several near-wall streaks.
In the wall normal direction, the eigenmodes have two peaks at large wavelength: one in the wall layer ($y < 0.1$) and the other in the outer layer ($y > 0.1$). The outer one is the presumed large-scale structure, while the inner one can be interpreted as the near-wall footprint of this structure, as described by Hutchins and Marusic (2007). The other short-wavelength modulations, which are

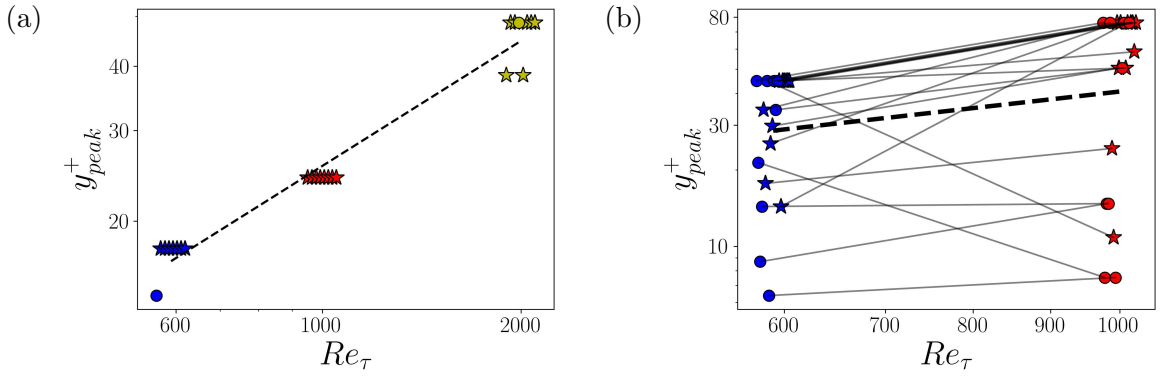

Figure 4.13: Wall-normal position of the inner peak as a function of Re_τ. Leading unstable modes ($\star$) or least stable modes ($\bullet$) for (a) $Re_\tau = [590, 1000, 2000]$, $\overline{k}_x = [0.5, 1, 1.5, 2]$ and $A_s = [0.20, 0.25]$ ($m_x = 1$, $m_z = 2$, $N_u = 60$) and (b) $Re_\tau = [590, 1000]$, $m_x = [0, 1, 2, 4, 8]$ and $m_z = [1, 2, 4, 8]$ ($\overline{k}_x = 1.0$, $A_s = 0.20$, $N_u = 60$). The abscissae of the symbols are jittered to avoid overlapping of the symbols. In both (a) and (b) the black dashed line is the scaling law found by least-squares regression of all the points contained in the two plots, respectively $y^+_{peak} \propto Re_\tau^{0.81}$ and $y^+_{peak} \propto Re_\tau^{0.674}$. In (b), the grey lines join the points corresponding to a given $\{m_x, m_z\}$ couple from one Reynolds number to the other.

present near the wall, can be attributed to the near-wall cycle (Hamilton et al. (1995)).

It is interesting to investigate how the wall-normal position of the inner peak at large wavelength depends on the Reynolds number. Experimental works in boundary layers (Vincenti et al., 2013) and pipes (Vallikivi et al., 2015) have shown that the wall-normal position of the peak of the pre-multiplied streamwise energy spectrum scales as $y^+_{peak} \propto Re_\tau^{0.5}$ (or $y_{peak}/h \propto Re_\tau^{-0.5}$), meaning that even large-scale structures are affected by viscous effects (Hwang, 2016). In figure 4.13 (a), the wall-normal position of the inner peak for the leading eigenmodes computed with $Re_\tau = [590, 1000, 2000]$, $\overline{k}_x = [0.5, 1, 1.5, 2]$ and $A_s = [0.20, 0.25]$ is plotted as a function of the friction Reynolds number. A power-law least-squares regression applied to all these points gives the scaling law $y^+_{peak} \propto Re_\tau^{0.81}$ (dashed line in the figure). This result is between the experimental findings recalled above and the scaling $y^+_{peak} \propto Re_\tau^{0.898}$ found by Hwang (2016) from the primary transient growth of the mean flow. Note that we considered the spectrum with respect to $\overline{\lambda}_z$ instead of the spectrum with respect to λ_x, but the location of the inner peak remains unchanged when the reference frame is rotated from $\overline{z}$ to x. Therefore, the scaling law we found can be directly compared to the previously mentioned ones.

To assess if the large-scale modulations observed in the leading eigenmodes can represent large-scale structures populating turbulent flows, a comparison of their wavelengths with DNS data is presented. Again, the leading eigenmodes computed with $Re_\tau = [590, 1000, 2000]$, $\overline{k}_x = [0.5, 1, 1.5, 2]$ and $A_s = [0.20, 0.25]$ are considered. For each of these, the prominent $\overline{\lambda}_z$ is extracted from the Fourier spectrum (the $\overline{\lambda}_z$ corresponding to the peaks in figure 4.12). Then, the streamwise and spanwise wavelengths in the DNS frame (λ_z, λ_x) must be obtained from those in the rotated frame ($\overline{\lambda}_z$ and $\overline{\lambda}_x = 2\pi/\overline{k}_x$). This can be done considering the large-scale modes as waves whose crests are inclined with respect to the $\overline{z}$ axis of an angle $\beta = \arctan(\overline{\lambda}_x/\overline{\lambda}_z)$. The inclination with respect to the z axis

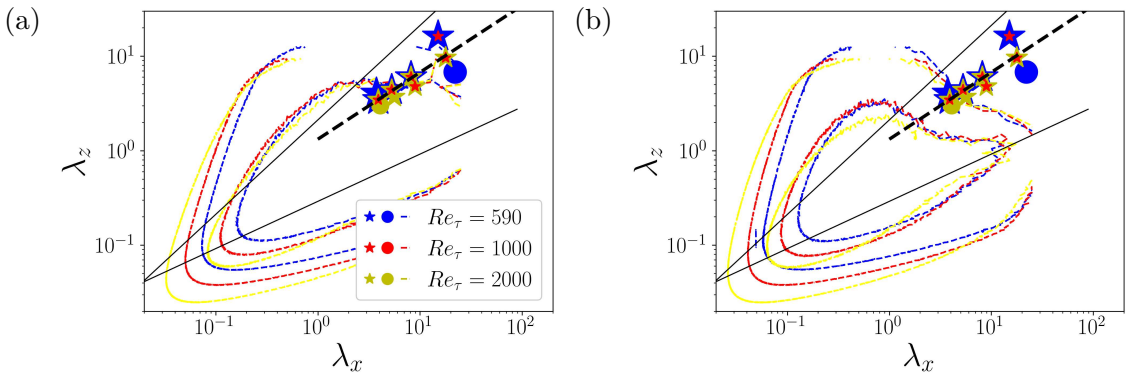

Figure 4.14: Wavelengths of the (a) streamwise and (b) wall-normal velocity component of the leading unstable modes ($\star$) or least stable modes ($\bullet$) reported in the DNS reference frame for several cases. The contours are the reference DNS pre-multiplied spectra at $y \approx 0.3$ for the (a) streamwise and (b) wall-normal velocity fluctuations by Del Alamo et al. (2004) and Hoyas and Jiménez (2006). The wavelengths of the eigenmodes follow the thick dashed line given by $\lambda_z = 1.32\lambda_x^{0.71}$. The solid black lines are the scaling laws $\lambda_z \propto \lambda_x$ and $\lambda_z \propto \lambda_x^{0.5}$ reported in Del Alamo et al. (2004).

is $\beta + \theta$, hence:

$$\lambda_x = \overline{\lambda}_x \frac{\cos(\beta)}{\cos(\beta+\theta)}, \qquad \lambda_z = \overline{\lambda}_z \frac{\sin(\beta)}{\sin(\beta+\theta)}, \tag{4.15}$$

with θ the angle of inclination of the rotated frame. These transformations are equivalent to a rotation by θ of the wavenumber vector:

$$\begin{pmatrix} \frac{2\pi}{\overline{\lambda}_x} \\ \frac{2\pi}{\overline{\lambda}_z} \end{pmatrix} = \begin{pmatrix} \cos\theta & -\sin\theta \\ \sin\theta & \cos\theta \end{pmatrix} \begin{pmatrix} \frac{2\pi}{\lambda_x} \\ \frac{2\pi}{\lambda_z} \end{pmatrix}. \tag{4.16}$$

The results for the streamwise and wall-normal velocity components are shown in figure 4.14 along with the respective DNS pre-multiplied spectra by Del Alamo et al. (2004) and Hoyas and Jiménez (2006). The characteristic sizes of the unstable modes (blue/red/yellow stars) are included in the large-wavelength portion of the DNS spectra, showing that these eigenmodes may represent the large-scale modulations found in the turbulent flow. The spectra are taken at a wall-normal position $y \approx 0.3$, which is not far from the outer peak of the mode (see figure 4.12 and figure 4.16). The premultiplied energy spectra of the spanwise component are equivalent to the wall-normal ones, hence are not shown.

Particularly, the wavelengths of the eigenmodes are found to scale according to the law $\lambda_z \propto \lambda_x^\gamma$ with $\gamma \approx 0.71$ (thick dashed line in figure 4.14). This scaling law is comprised between the scalings reported by Del Alamo et al. (2004), namely $\lambda_z \propto \lambda_x^{0.5}$ and $\lambda_z \propto \lambda_x$. Del Alamo et al. (2004) report the laws in terms of λ_x/y and λ_z/y, whereas we are considering only the eigenmode outer peak wall-normal position. So, y is fixed and included in the proportionality constant. This is because the eigenmode is representative only of one large-scale structure at a time, whereas the scaling of the DNS spectra with respect to y is due to the whole hierarchy of structures present in the flow. These two scaling laws are reported in the panels of figure 4.14 as solid black lines. The first one is mainly followed by the streamwise velocity fluctuation, the second characterises the transverse fluctuations (wall-normal

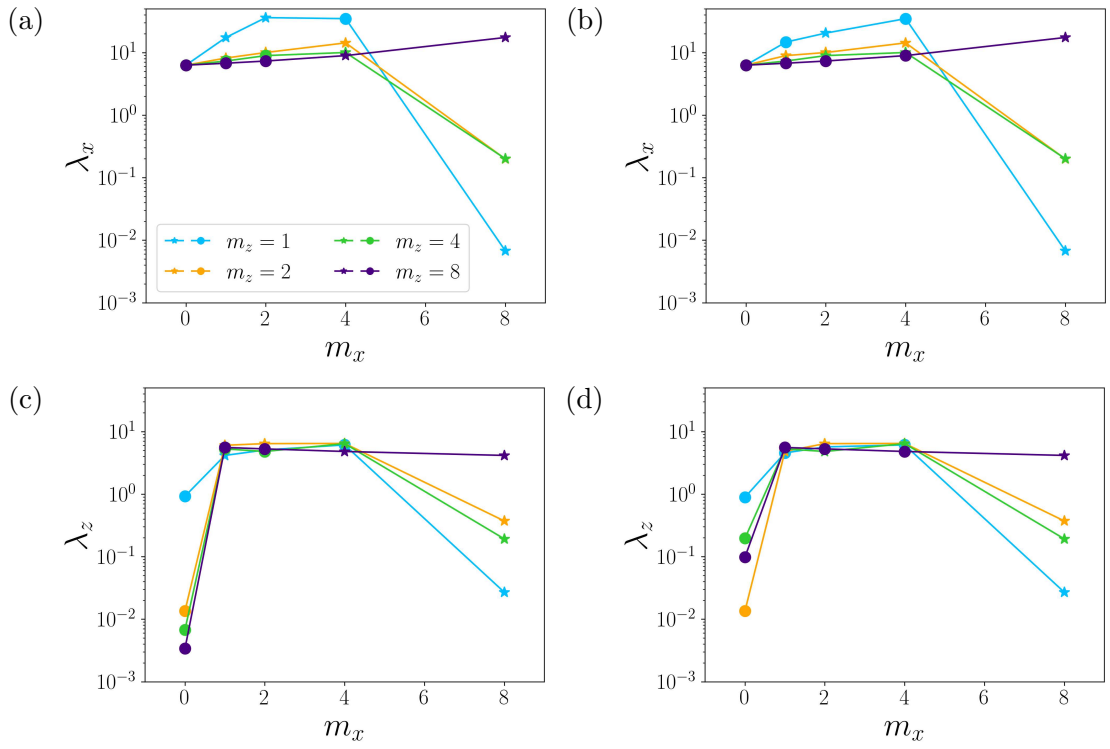

Figure 4.15: Streamwise (a,b) and spanwise (c,d) wavelengths of the streamwise velocity component of the leading unstable modes ($\star$) or least stable modes ($\bullet$) reported in the DNS reference frame as functions of $\{m_x, m_z\}$ for (a,c) $Re_\tau = 590$ and (b,d) $Re_\tau = 1000$. All computations were performed with $\overline{k}_x = 1.0$, $A_s = 0.20$ and $N_u = 60$.

and spanwise). Our eigenmodes display the same prominent wavelengths both for the streamwise and for the wall-normal component (the same is true also for the spanwise component, not shown). Consistently, the scaling law is intermediate between the two given by Del Alamo et al. (2004).

Until now, only the couple $\{m_x, m_z\} = \{1, 2\}$ of base flow wavenumbers has been considered. In figure 4.15, it is shown how the choice of these parameters affects the characteristic wavelengths of the eigenmodes (reported in the DNS reference frame as explained above). It can be remarked that the wavelengths are rather independent of both wavenumbers except in two cases: (i) when $m_x = 0$, but this is not much relevant because these streaks are always stable; (ii) when $m_x = 8$ and $m_z < 8$, but this case also is not much relevant because corresponds to structures inclined of an angle $\theta \geqslant 45^\circ$ with respect to the streamwise direction. These large inclination angles are unlikely to be found near the wall and are included only for completeness. Also, the Reynolds number dependence illustrated in figure 4.13 (a) is generally not affected by the variation of m_x and m_z, as it is demonstrated by panel (b) of the same figure. It can be seen that for most of the $\{m_x, m_z\}$ couples, the position of the peak increases and, on average, the trend is consistent with the law reported in panel (a). Therefore, it can be concluded that the main features of the eigenmodes are robust enough to allow us to focus only on a given couple $\{m_x, m_z\}$ for the rest of the chapter.

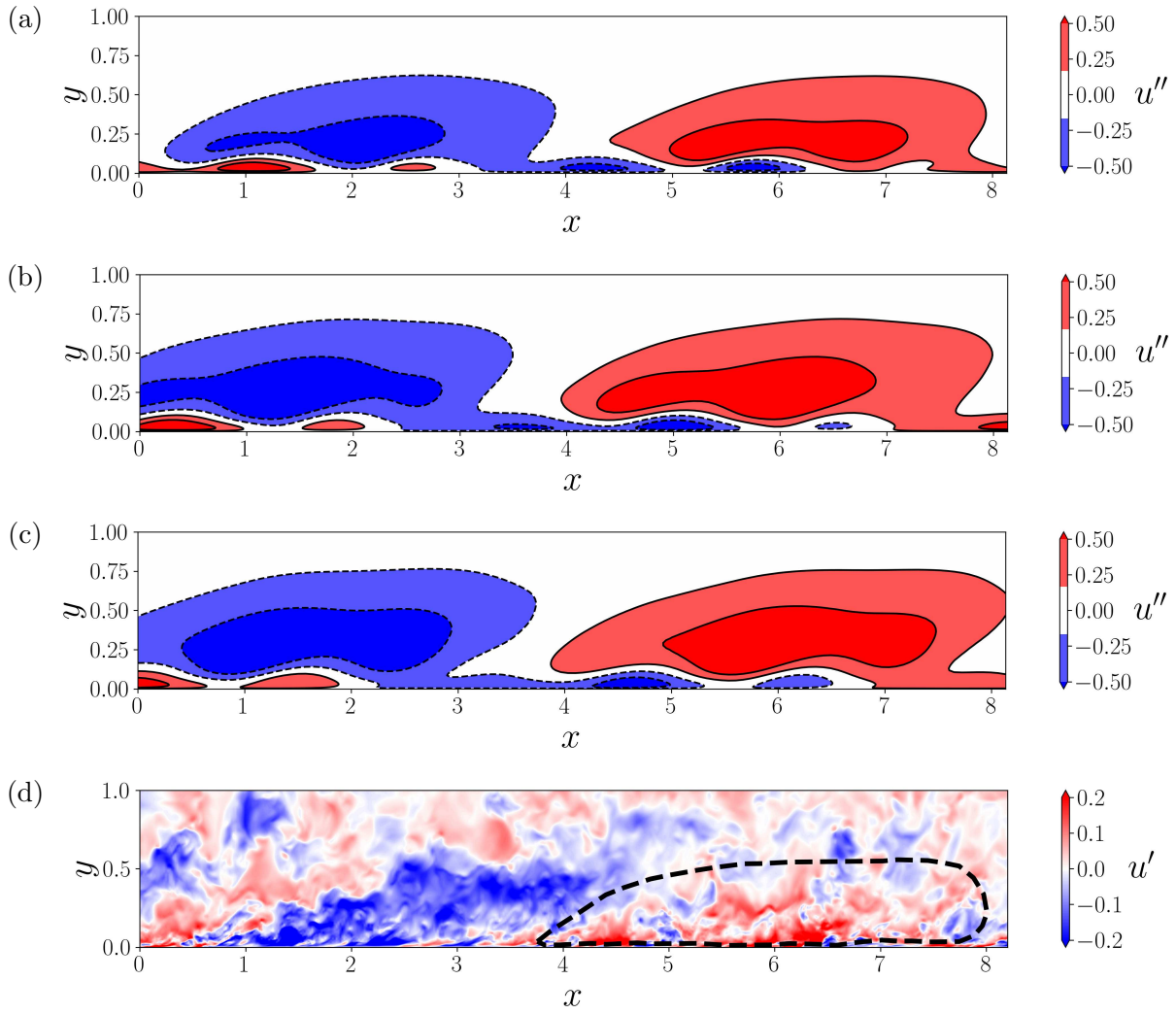

Figure 4.16: (a-c) Streamwise component of the leading unstable eigenmode reported in the DNS $x-y$ reference frame at (a) $Re_\tau = 590$, (b) $Re_\tau = 1000$ and (c) $Re_\tau = 2000$ ($\overline{k}_x = 1.0$, $A_s = 0.20$, $\theta \approx 14°$, $N_u = 60$). The amplitude of the mode is normalised to one. (d) Instantaneous streamwise component of the turbulent fluctuation extracted from a snapshot of the large-domain DNS at $Re_\tau = 1000$ (C1000_L in table 4.1). The dashed line is a conceptual representation of a superstructure (from figure 13 of Deshpande et al. (2023)).

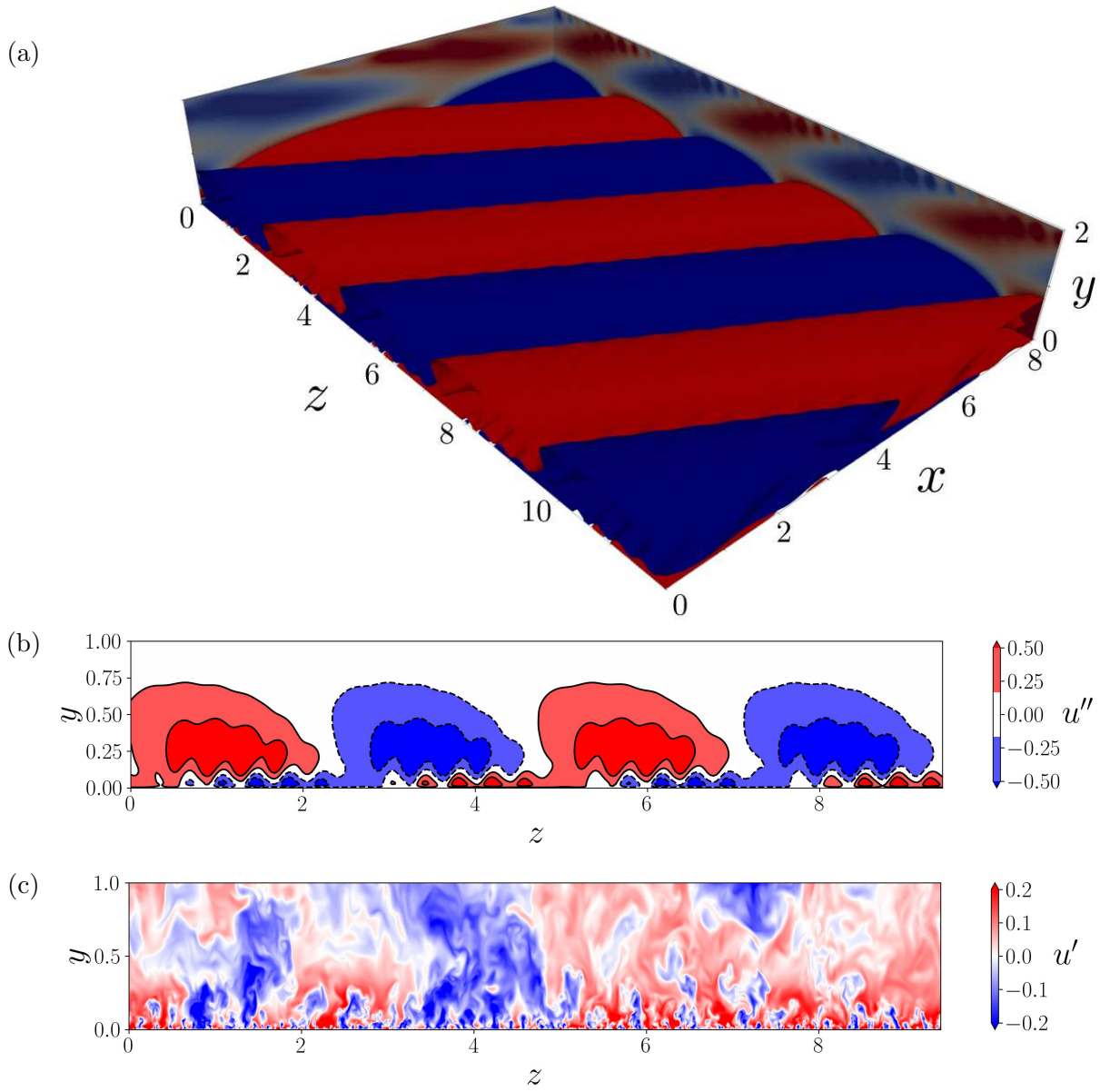

Figure 4.17: (a) Streamwise velocity component iso-contours (mode amplitude normalized to one, contour value 0.1) of the leading unstable eigenmode reported in the DNS $x-y-z$ reference frame at $Re_\tau = 1000$ ($\overline{k}_x = 1.0$, $A_s = 0.20$, $\theta \approx 14°$, $N_u = 60$). (b) $y-z$ cut of the same mode in (a). (c) Instantaneous streamwise component of the turbulent fluctuation extracted from a snapshot of the large-domain DNS at $Re_\tau = 1000$ ($\mathrm{C1000}_L$), $y-z$ cut.

The spatial structure of the unstable modes is presented in figure 4.16 (a-b-c). One of the leading unstable eigenmodes is shown in a $x-y$ plane for each $Re_\tau \in [590, 1000, 2000]$. It can be seen that the Reynolds number does not have a major influence on the shape of the eigenmode. This visualisation recalls a conceptual sketch suggested in figure 13 of Deshpande et al. (2023), where an experimental boundary layer is considered. Despite the Reynolds number considered in this study being much lower than the experimental one, the large-scale modulation of the eigenmode is found to reproduce the shape of a *superstructure*. To make a direct comparison, following Deshpande et al. (2023), the outline of the superstructure is superposed to a snapshot taken from our large-domain DNS at $Re_\tau = 1000$ ($\mathrm{C1000}_L$ in table 4.1) in figure 4.16 (d). Considering the channel half-height as the equivalent boundary layer thickness, it can be seen that the instantaneous structures of the channel form a large-scale structure of the same height and shape as that found in the boundary layer. Comparing the frames of figure 4.16, one can conclude that the unstable mode is reminiscent of the superstructures.

To further illustrate the structure of the unstable eigenmode, its three-dimensional shape, in the DNS frame of reference, is shown in figure 4.17 (a) for $Re_\tau = 590$. The modes at other Reynolds numbers are totally equivalent, as can be deduced by the various panels of figure 4.16. In a wall-parallel plane, the mode has the shape of a travelling wave. Therefore, the only meaningful information in this plane is the streamwise and spanwise wavelengths, already compared to DNS results in figure 4.14. To improve the comparison of the wall-normal structure of the leading unstable mode with DNS results, spanwise-wall-normal cuts of the two are included in figure 4.17 (panels (b) and (c)). Like the base streaks, the resulting modes also have infinite length along a given axis. However, they have larger dimensions in the cross-plane. Therefore, they effectively represent structures of a larger scale with respect to the base streaks.

The panels of figures 4.16 and 4.17 show that a sign change is present in the mode at $y \approx 0.1$. This feature of the eigenmodes is currently not understood. It can be noted, especially in the wall-normal-spanwise plane (figure 4.17 (c)), that similar sign changes can be observed at some locations in the DNS snapshots. However, it does not present a net phase shift as it seems to be present in the unstable mode. One should take into account that the eigenmode is a linear, therefore idealised, structure, whereas the actual structures found in the DNS are the result of nonlinear interactions between several modes. In particular, the nonlinear development of the mode may alter the relative amplitude of the near-wall small-wavelength wave with respect to the amplitude of the large-wavelength wave, such that the sign of the large-wavelength wave would prevail and mostly remove the sign change.

4.5 Discussion

In this study, the detuned stability of turbulent near-wall streaks and its connection to the appearance of large-scale motions in turbulent channel flow are investigated. Streaky structures with an arbitrarily small inclination in the streamwise-spanwise plane are extracted by POD from minimal-flow-unit DNS data. A periodic N_u-array of such structures superposed to the turbulent mean profile is considered as base flow for the stability analysis. Unresolved turbulent motions were included in the linear operator using an eddy viscosity model, as in previous works (Park et al., 2011; Alizard,

2015). This method allows the study of turbulent coherent structures without the need for heavy computations in large domains.

However, the employed approach has several limitations:

- First of all, the streaks need to be forced. Without the forcing, they are rapidly dissipated, and the instability can not grow (Moffatt, 1989; Schoppa and Hussain, 2002). As we will see in the next chapter, in general, one can always find a forcing that makes a given flow field steady. This forcing is artificial, as the base flow itself, but, as for the base flow, we can argument that the forcing models physically important mechanisms such as the nonlinearities that close the wall cycle (Waleffe, 1997). Still, this empirical argument is too vague and does not eliminate the ambiguity of using synthetic base flows.

- We have used POD to compute the base flow streaks because POD structures are the prominent turbulent structures in a statistical sense (the POD mode is the most correlated structure present in the data). However, this method needs DNS data for every Reynolds number considered, and the convergence of the results with the number of snapshots is slow. There are other methods to compute streaks for a stability analysis. Alternative approaches will be considered in the next chapter.

- To make the computational cost of the stability analysis acceptable, we considered a two-dimensional base flow, *i.e.* streaks that are uniform along a given direction. In reality, near-wall streaks can have different inclination angles in the $x-z$ plane, making the candidate base flows three-dimensional.

- The base flow is constructed with a POD mode computed from a given wavenumber couple $\{m_x, m_z\}$. Actual near-wall streaks can be multi-modal. This mode is then equipped with an amplitude that takes into account the energy contained in the whole turbulent spectrum. This is a strong approximation, as it means that a complex chaotic field is ideally represented by only one Fourier mode.

- As pointed out by Cossu (2022), there is no universal agreement in the literature on how to close the linear equations (and whether to employ a closure at all). Recent comparative studies (Illingworth et al., 2018; Morra et al., 2019; Symon et al., 2023) have shown that including the (Cess, 1958) eddy viscosity in the linear operator ameliorates the predictions of the linear model. Still, there are plenty of other possibilities, like computing an eddy viscosity from DNS data.

Some of the above shortcomings are shared by most previous studies on the secondary instability of streaks (Schoppa and Hussain, 2002; Marquillie et al., 2011; Hack and Zaki, 2014; Hack and Moin, 2018; Park et al., 2011; Alizard, 2015) and also by various works on the stability of mean flows (for example, see Cossu (2022) and McKeon and Sharma (2010)). The questions raised during this work will be tackled in more detail in the next chapter.

Notwithstanding the various approximations made, the results display a certain consistency with the features of large-scale structures reported in the literature. The results show that for sufficiently

high friction Reynolds numbers, near-wall streaks can trigger a large-scale instability, suggesting a possible origin of large-scale motions (LSMs) in wall-bounded turbulence. There is little qualitative difference between the unstable modes at $Re_\tau = [590, 1000, 2000]$ and this is compatible with the fact that large structures scale in outer units (Hutchins and Marusic (2007); Cossu and Hwang (2017)). Conversely, the $Re_\tau = 180$ case is always stable except for very large amplitudes of the streaks and small wavelengths of the instability, corroborating the observation that developed large-scale structures are not expected at this low Reynolds number.

A comparison of the computed unstable eigenmodes with DNS and experimental results was attempted. It was found that the eigenmodes reproduce some features of turbulent large-scale motions (LSMs). The streamwise and spanwise wavelengths of the large-scale modulation are compatible with the DNS spectra of Del Alamo et al. (2004) and Hoyas and Jiménez (2006). They also scale according to a power law that is included between the two power laws $\lambda_z \propto \lambda_x^{0.5}$ and $\lambda_z \propto \lambda_x$ proposed by Del Alamo et al. (2004). In addition, the scaling of the wall-normal position of the spectrum inner peak with Re_τ agrees reasonably well with experimental findings (Vincenti et al., 2013; Vallikivi et al., 2015), with a slight improvement with respect to previous linear computations (Hwang, 2016).
Moreover, it was found that these traits of the eigenmodes are rather robust with respect to the variation of the base streaks wavenumber couple $\{m_x, m_z\}$. This consistency supports at least in part the applicability of the assumptions made, since it shows that the choice of a given wavenumber couple is not critical as long as it respects some physical constraints (moderate inclination of the streaks with respect to the streamwise direction).

As the employed base flow, the eigenmode itself is an idealised structure, as it resembles an oblique travelling wave. Nevertheless, it contains interesting elements. The shape of the structure in the streamwise/wall-normal plane conceptually recalls the structures found in recent experimental findings (Deshpande et al., 2023) and in the large domain DNS performed in this study. Similar considerations apply to the structure in the spanwise/wall-normal plane. Even if in the comparison there are unclear elements (*e.g.* a near-wall phase shift not well understood at the moment), which are probably due to the linear nature of the eigenmode, it can be concluded that the instability returns the correct streamwise/spanwise wavelengths and a fair wall-normal structure.

Therefore, this study brings numerical evidence that the large-scale motions (LSMs) found in numerical simulations and experiments of wall-turbulence can be the result of an instability of near-wall structures. An important point to highlight here is that this evidence does not imply in any way that the detuned instability is the sole mechanism to generate large-scale structures. Indeed, it is well-known that large-scale motions are self-sustained (Hwang and Cossu, 2010c; Hwang, 2015; Hwang and Bengana, 2016). Therefore, they can directly extract energy from the mean flow. However, the turbulent flow is characterised by plenty of energy transfer interactions between different scales. The present results suggest that LSMs can also be generated by an instability of smaller scales, which should be interpreted as a possible scale interaction mechanism. Lastly, we mention that similar considerations may apply to VLSMs, although the considered Re are too low to give direct evidence on this subject.

Chapter 5

Turbulence Modulations at low Reynolds number

5.1 Introduction to the chapter

In the previous chapter, we have seen that large-scale motions (LSMs) can be generated by the instability of near-wall streaks. This instability appears when the Reynolds number (Re) is increased above a certain threshold, which is compatible with the fact that LSMs are observed at high Re. In contrast, when Re is decreased, a different class of large-scale coherent structures arises: turbulence modulations and laminar-turbulent patterns. A detailed discussion of this phenomenology is given in Section 1.2.2. These coherent structures appear as modulations of small-scale fluctuations and are always coupled with a large-scale flow (Tuckerman and Barkley, 2011; Duguet and Schlatter, 2013).

Kashyap et al. (2022) showed that these modulations result from a linear instability of the unmodulated (*featureless*) turbulent flow. With their numerical protocol, they were able to compute a statistical dispersion relation and extrapolate the critical Re and wavenumbers. To gain further insights on the instability mechanism, the same authors tried to retrieve this result from a *more classic* modal linear stability analysis (LSA) of the mean flow (Kashyap et al., 2024). The advantage of such analysis is that, in addition to the growth rates, it also provides the eigenmodes. However, in order to perform an eigenvalues/eigenmodes computation, a relevant base flow to linearise about and a closure for the unresolved turbulent fluctuations are needed. Kashyap et al. (2024) linearised around the turbulent mean profile and tested both the no closure option and two eddy viscosity closures. It was found that this linear model does not detect the observed instability.
The failure of the mean flow model suggests that the instability needs to interact with the turbulent fluctuations and that they must be included more explicitly in the computation. This can be done in two ways: adding a dynamical equation for the Reynolds stress closure as in Benavides and Barkley (2025) or including coherent structures in the base flow as we have done, at high Re, in the previous chapter. An attempt at the first strategy will be discussed in the next chapter. In this chapter, we focus on the second strategy.

We do not follow exactly the same methodology as Chapter 4. Rather, we try to overcome some

of the shortcomings that were pointed out in the last discussion section. Particularly, we look for a better way to compute the base flow. The first idea is to consider finite-time temporal averaging. If one considers a domain of medium size and an averaging interval of width T_a, it will be shown that there is a range of T_a for which the obtained mean flow is approximately two-dimensional, which provides a good candidate for LSA. It will be shown that the analysis of this base flow gives only a partial improvement with respect to the mean flow analysis (Kashyap et al., 2024). Accordingly, we keep looking for a consistent base flow and consider the structures obtained by the resolvent analysis of the mean profile. This second strategy is appealing for several reasons: (i) it does not require a precursor DNS; (ii) resolvent modes are robust and characterised by a high degree of symmetry; (iii) the resulting structures are periodic by construction in the spanwise direction, which makes them suitable for the block-circulant matrix method; (iv) the dominant resolvent modes are the result of a steady forcing, which makes it a natural setting for the frozen base flow approximation.

The chapter is organised as follows. Generalities on the problem and the governing equations are recalled in Section 5.2. The finite-time average approach is explained and analysed in Section 5.3. This section also includes a comparison between different types of closures for the unresolved incoherent fluctuations and discusses the results of LSA performed around this type of base flows. Then, we explain in Section 5.4 how a better base flow can be computed using resolvent analysis. The stability of the new base flow is addressed in Section 5.5. The results of this second LSA are further analysed using an energy budget decomposition in Section 5.6, while the nonlinear simulation of the instability is briefly illustrated in Section 5.7. Finally, a discussion covering several important points of this work is given in Section 5.8. Part of this chapter is adapted from the paper Ciola et al. (2025).

5.2 Problem formulation

We continue to consider the pressure-driven incompressible flow in a channel. Periodic boundary conditions are imposed in the streamwise (x or x_1) and spanwise (z or x_3) directions. No-slip conditions are imposed in the wall-normal direction (y or x_2). The periodic domain has dimensions $[L_x, L_y, L_z]$. Quantities without any superscript are made dimensionless with the channel half-gap h^* (such that $L_y = 2$ and $0 \leqslant y \leqslant 2$) and the bulk velocity $U_b^* = \int_0^2 \int_0^{L_z} u^* \, dydz/2L_z$ (outer units). Quantities with a + superscript are made dimensionless with the viscous length $\delta_\nu^* = \nu^*/u_\tau^*$ and the friction velocity $u_\tau^* = \sqrt{\tau_w^*/\rho^*}$ (inner or wall units), where ρ^* is the fluid density, ν^* the kinematic viscosity and τ_w^* the measured mean wall shear stress. The streamwise, wall-normal and spanwise velocity components are denoted, respectively, by u, v and w or u_1, u_2 and u_3 when using index notation.

The instantaneous flow is governed by the incompressible Navier-Stokes (NS) equations

$$\begin{cases} \dfrac{\partial \boldsymbol{u}}{\partial t} + \boldsymbol{u} \cdot \boldsymbol{\nabla} \boldsymbol{u} = -\boldsymbol{\nabla} p + \dfrac{1}{Re} \nabla^2 \boldsymbol{u} + \boldsymbol{f}_b, \\ \boldsymbol{\nabla} \cdot \boldsymbol{u} = 0, \end{cases} \tag{5.1}$$

where $Re = U_b^* h^*/\nu^*$ is the Reynolds number and $\boldsymbol{f}_b$ is a time-varying forcing that keeps the flow rate constant. The long-time average of the instantaneous velocity $\boldsymbol{u}$ is denoted by $\overline{\boldsymbol{U}} = \overline{U}(y)\boldsymbol{e}_x$.

In this chapter, similarly to Chapter 4, the stability of a base flow composed of the long-time average $\overline{\boldsymbol{U}}$ plus a coherent fluctuation is considered. The stability of such base flow is addressed with the linearised NS equations augmented with a closure term for the incoherent fluctuations. In general, the LSA model can be written

$$\begin{cases} \dfrac{\partial \boldsymbol{u}''}{\partial t} + \boldsymbol{U}\cdot\boldsymbol{\nabla}\boldsymbol{u}'' + \boldsymbol{u}''\cdot\boldsymbol{\nabla}\boldsymbol{U} = -\boldsymbol{\nabla}p'' + \dfrac{1}{Re}\nabla^2\boldsymbol{u}'' + \mathcal{M}\boldsymbol{u}'', \\ \boldsymbol{\nabla}\cdot\boldsymbol{u}'' = 0, \end{cases} \tag{5.2}$$

where $\boldsymbol{U}$ is the base flow, $\boldsymbol{u}''$ is the secondary coherent perturbation[1] and $\mathcal{M}$ denotes the linear operator of the turbulence closure. When $\mathcal{M}\boldsymbol{u}'' \equiv \boldsymbol{0}$, the system is called quasi-laminar model (see Section 1.2.3).

The results of different base flows and different closures will be compared in the following sections for the problem of turbulent modulations at low Re. Below, we consider 7 different Re. The computations are performed imposing the Re based on the bulk velocity, namely $Re = [1000, 1100, 1200, 1300, 1350, 1400, 1500]$. However, results are presented using Re_τ, computed a posteriori from DNS, to ease comparison with previous literature. The Re_τ corresponding to the considered Re are, respectively, $[71, 78, 85, 92, 95, 99, 106]$. The range of Re considered is centred on the critical Re_τ reported by Kashyap et al. (2022) (*i.e.* 95). At the lowest Reynolds number considered here ($Re_\tau = 71$), the turbulent flow appears as a pattern of oblique bands (figure 5.1 (c)). The alternance of extended blue and red regions indicates the presence of the large-scale flow which coexists with the pattern (Duguet and Schlatter, 2013). At a higher value of $Re_\tau = 92$, such a pattern of alternatively laminar and turbulent regions is replaced in DNS by a weaker modulation of a more standard streaky turbulent flow (figure 5.1 (a)). Instead, for Re_τ above 95, turbulence appears in DNS unmodulated by large-scale oblique structures, consistently with Kashyap et al. (2022), and will be qualified as *featureless* after Shimizu and Manneville (2019).

The simulations illustrated in figure 5.1 are performed in a domain of size $L_x \times L_y \times L_z = 250 \times 2 \times 150$, respectively, in the streamwise, wall-normal and spanwise directions. The collocation points (before dealiasing) are $N_x \times N_y \times N_z = 1500 \times 65 \times 1800$, leading to resolutions comparable to previous DNSs (Kashyap et al., 2020, 2022; Shimizu and Manneville, 2019). Equivalent resolutions are used for the other simulations mentioned in the chapter.

Figure 5.1 clearly shows that the modulated flow is constituted by two types of coherent structures: the streaks and the large-scale modulations. The idea of this chapter is to perform the LSA of mean flow plus streaks and retrieve the modulations. This analysis is performed using the linear system (5.2). The closure model $\mathcal{M}\boldsymbol{u}''$ and the base flow $\boldsymbol{U}$ will be specified for each of the different approaches considered in the next sections.

[1] A double prime is introduced here to keep the notation consistent with the following sections.

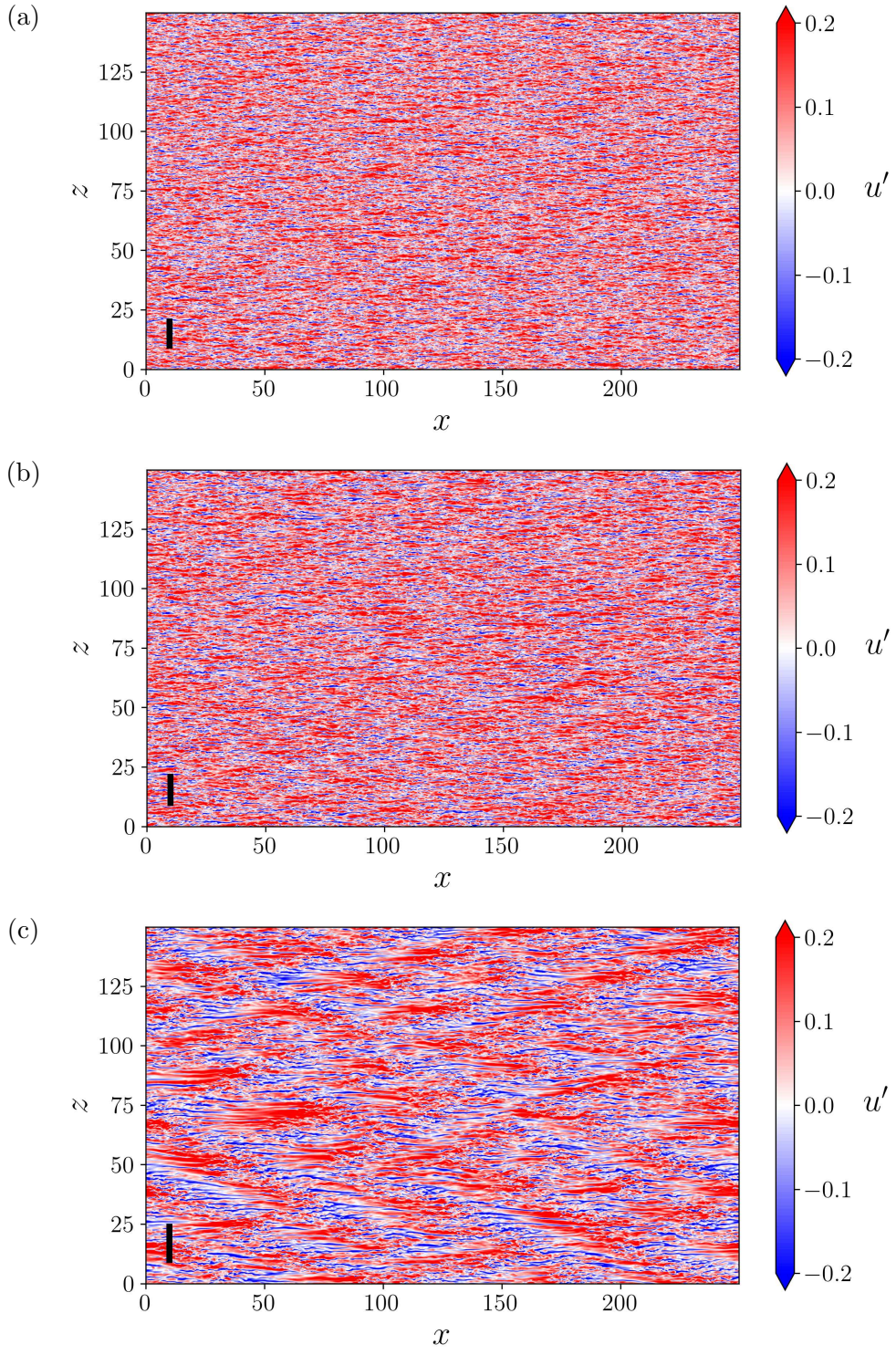

Figure 5.1: Contours of streamwise velocity fluctuations in the plane $y^+ \approx 35$ from a DNS at (a) $Re_\tau = 99$, (b) $Re_\tau = 92$ and (b) $Re_\tau = 71$ ($y \approx 0.36$ for $Re_\tau = 98, 92$ and $y \approx 0.49$ for $Re_\tau = 71$). The black vertical segment at the bottom left corner of each panel indicates a spanwise length of 1000 wall units.

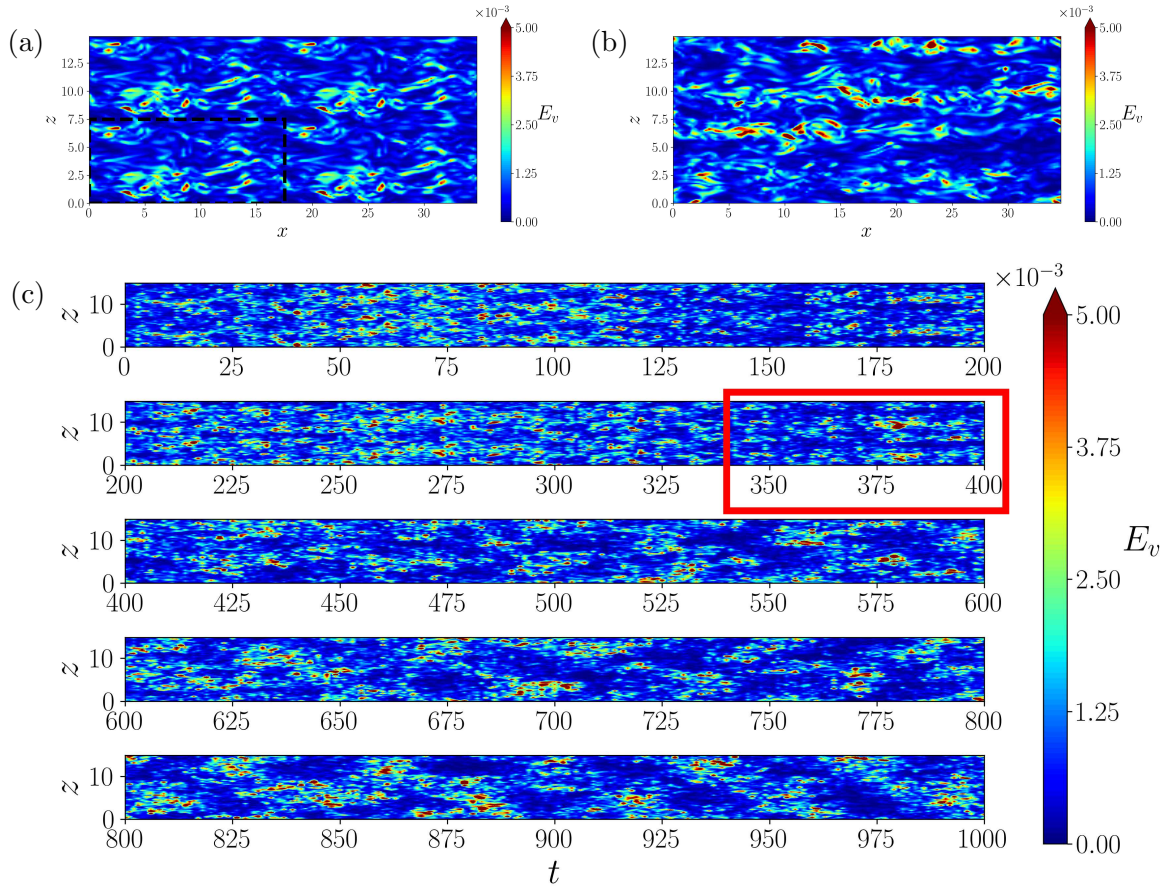

Figure 5.2: Contours of the wall-normal-integrated wall-normal kinetic energy (E_v) at $Re_\tau = 71$ in the $x - z$ plane at (a) $t = 0$ and (b) $t = 400$ and (c) in the $t - z$ plane at $x = 0$. The black dashed rectangle in (a) indicates the domain which is *periodically tiled* in the larger domain. The red rectangle in (c) indicates the interval considered for finite time averaging without the pattern.

5.3 Finite-time average

5.3.1 Resulting base flow

Finite-time averaging provides a hierarchy of base flows. If T_a is the width of the averaging interval, when $T_a \to 0$, one recovers a three-dimensional instantaneous field. When $T_a \to \infty$, the mean profile $\overline{\boldsymbol{U}}(y)$, as considered by Kashyap et al. (2024), is obtained. For intermediate T_a, one should retain the coherent fluctuations and average out the incoherent ones. In a turbulent channel flow, one expects from the literature (Kline et al., 1967; Hamilton et al., 1995) that the coherent fluctuations are elongated streaks.

Finite-time-averaged turbulent fields are computed using DNS. These simulations are performed in a domain of size $L_x \times L_z = 35 \times 15$. The choice of these domain lengths is driven by the critical wavenumbers reported by Kashyap et al. (2022), which correspond to $k_x^c \approx 0.18 \approx 2\pi/L_x$ and $k_z^c \approx$

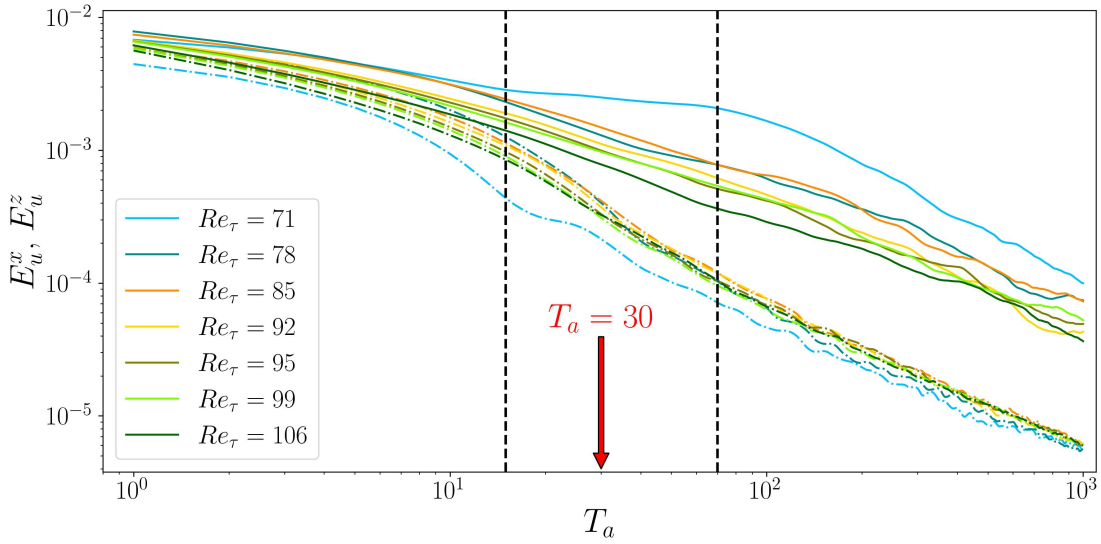

Figure 5.3: Streamwise kinetic energy contained in the $x-$varying modes (E_u^x, dash-dotted lines) and $z-$varying modes (E_u^z, solid lines) of a finite-time averaged flow as a function of the averaging width T_a. $T_a = 30$ is the baseline value used for most of the computations. The vertical dashed lines are at $T_a = 15$ and $T_a = 70$.

$0.42 \approx 2\pi/L_z$. As such, the 35×15 domain contains exactly one turbulent band for $Re_\tau < 95$. The domain is discretised using $N_x \times N_z = 180 \times 180$ Fourier modes in the wall-parallel directions (before dealiasing with the 2/3 rule) and 65 Chebyshev collocation points in the wall-normal directions. This gives a resolution comparable to previous studies (Kashyap et al., 2020).
The base flow needs to be computed without the modulations. This is trivial for Re above the critical value, where featureless turbulence is the asymptotic state. When modulations naturally arise in the flow, a strategy needs to be devised to simulate at least transiently featureless turbulence. We applied the following protocol. A simulation is run in a smaller domain (17.5×7.5), which is too small to contain a laminar-turbulent band. When the flow reaches a statistically steady state in this domain, a snapshot is *periodically tiled* in the larger domain, as illustrated in figure 5.2 (a). Then, the simulation is restarted in the larger domain: the flow keeps its original periodicity for a certain period of time (Nikitin, 2008) and then gradually loses it. At this point, the flow is developed on the larger domain and still does not feature the modulation (figure 5.2 (b)). A turbulent band will develop later and become fully formed after $\approx 1,000$ convective time units (h^*/U_b^*), as illustrated in the space-time plot of figure 5.2 (c). The panels in figure 5.2 show contours of the wall-normal-integrated wall-normal kinetic energy, namely

$$E_v(x,z,t) = \int_0^2 \frac{v^2}{2}(\boldsymbol{x},t)\ dy. \tag{5.3}$$

Therefore, the finite-time average is performed during the transient in which the flow does not have the modulations, as highlighted by the red rectangle in figure 5.2 (c). In general, the result of averaging over a time T_a is a three-dimensional field

$$\langle \boldsymbol{u} \rangle_{T_a}(\boldsymbol{x}) = \frac{1}{T_a}\int_{t_0}^{t_0+T_a} \boldsymbol{u}(\boldsymbol{x},t)\ dt. \tag{5.4}$$

Note that t_0 is fixed and its choice does not qualitatively affect the results. Then, when T_a increases, we expect that the three-dimensional content of $\langle \boldsymbol{u} \rangle_{T_a}$ is gradually averaged out. To examine the effect of the averaging, we consider the energy contained in the $x-$varying modes of the temporally averaged field

$$E^x_{u_i} = \frac{1}{V} \int_V \frac{1}{2} \left(\langle u_i \rangle_{T_a} - \left\langle \langle u_i \rangle_{T_a} \right\rangle_x \right)^2 d\boldsymbol{x}, \tag{5.5}$$

and, similarly, the energy contained in the $z-$varying modes

$$E^z_{u_i} = \frac{1}{V} \int_V \frac{1}{2} \left(\langle u_i \rangle_{T_a} - \left\langle \langle u_i \rangle_{T_a} \right\rangle_z \right)^2 d\boldsymbol{x}, \tag{5.6}$$

where V is the volume of the computational domain and $\langle \cdot \rangle_x$ and $\langle \cdot \rangle_z$ are, respectively, the streamwise and the spanwise averages.

These quantities are plotted in figure 5.3 as a function of T_a using the streamwise velocity component. It can be seen that there is a range of T_a between 15 and 70 (delimited by the vertical dashed lines in the figure) for which E^z_u (solid lines) and E^x_u (dash-dotted lines) spread apart. In this range, the $z-$varying modes have a non-negligible energy while the $x-$varying modes have almost an order of magnitude less energy. This is because the coherent structures of the channel (the streaks) are approximately invariant in x and highly varying in z (hence belong to the $z-$varying modes), while the streak meandering belonging to the $x-$varying modes is less coherent in time. Therefore, the flow averaged for $T_a \in [15, 70]$ can be seen as an approximately 2D field ($x-$invariant). This feature can be exploited to perform LSA in the $y - z$ plane as in the previous chapter. The residual $x-$varying modes are discarded considering the streamwise average $\left\langle \langle \boldsymbol{u} \rangle_{T_a} \right\rangle_x \equiv \langle \boldsymbol{u} \rangle_{x,T_a}$. For $T_a > 70$, the finite-time-averaged flow is still approximately 2D (even more), but the $z-$varying modes become too weak to be relevant.

Some of the resulting base flows are reported in figure 5.4 for $T_a = 30$ and $Re_\tau = 71, 92, 106$ and figure 5.5 for $Re_\tau = 71$ and $T_a = 15, 30, 70$. These figures plot the deviation from the mean flow $\langle u \rangle_{x,T_a} - \overline{U}$. The averaged flows are characterised by chaotic streaks. Increasing Re, the streaks are squeezed nearer to the walls because the mean shear is more localised there. In contrast, figure 5.5 shows that T_a has a weak influence on the shape of $\langle u \rangle_{x,T_a}$.

5.3.2 Reynolds stress closures

Assuming that the streamwise and finite-time average $\langle \cdot \rangle_{x,T_a}$ is a Reynolds average[2], the equations for the averaged flow should contain a Reynolds stress term

$$R_{ij} = -\left\langle u'_i u'_j \right\rangle_{x,T_a}, \tag{5.7}$$

where, in this section, $u'_i = u_i - \langle u_i \rangle_{x,T_a}$. This term should be taken into account in the LSA through the $\mathcal{M}\boldsymbol{u}''$ term in (5.2). Still, one possibility is to completely neglect it using, therefore, the quasi-laminar model.

[2]This is introduced here as a working assumption. Actually, this is not the case.

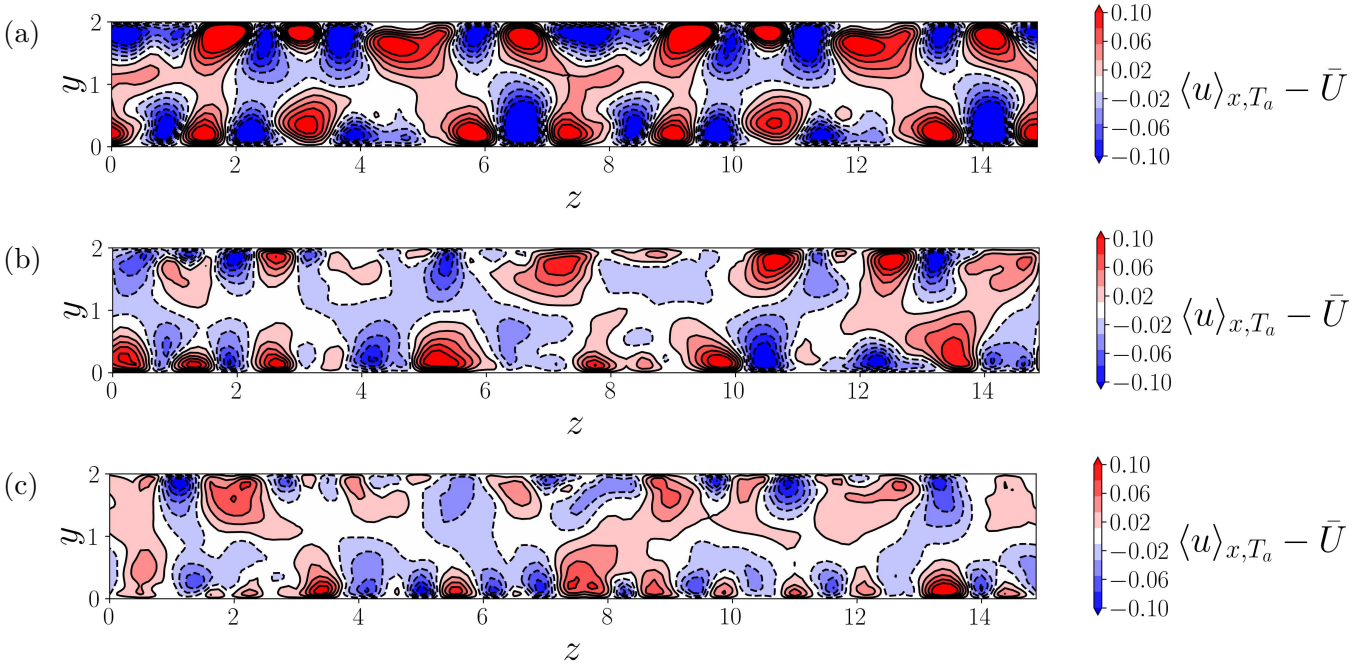

Figure 5.4: Streamwise velocity fluctuation of $\langle \boldsymbol{u} \rangle_{x,T_a}$ for $T_a = 30$ and (a) $Re_\tau = 71$, (b) $Re_\tau = 92$ and (c) $Re_\tau = 106$.

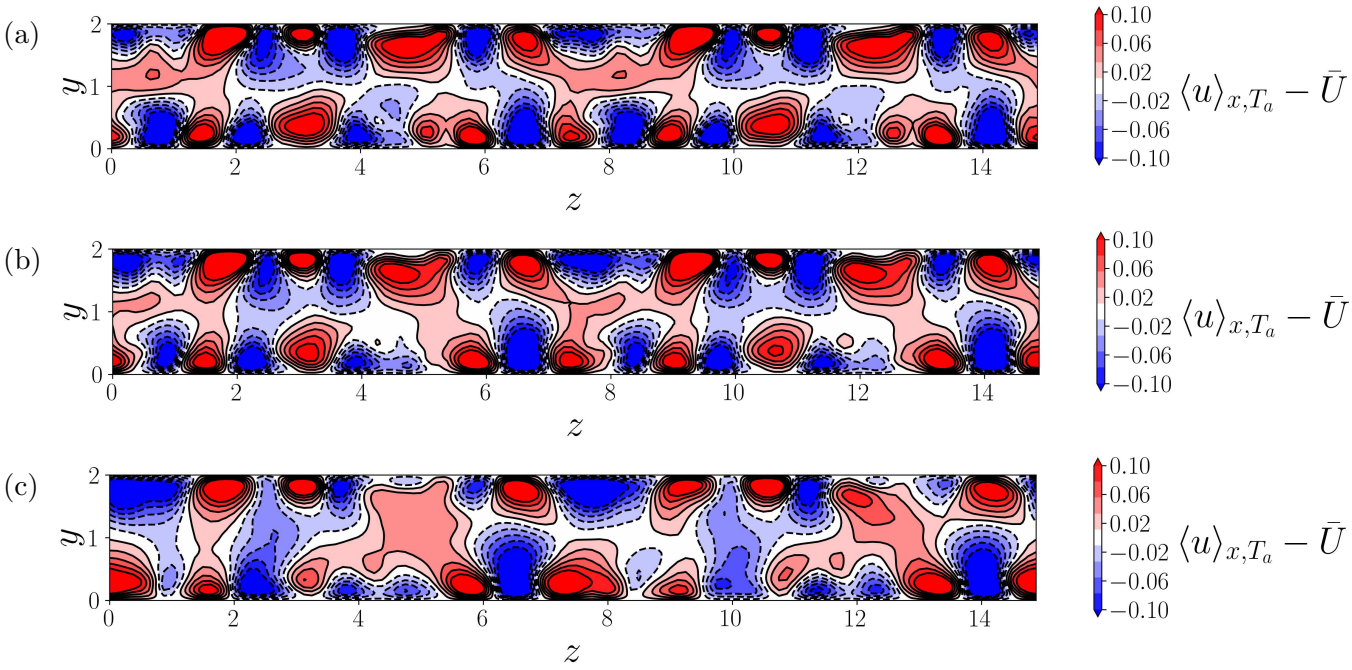

Figure 5.5: Streamwise velocity fluctuation of $\langle \boldsymbol{u} \rangle_{x,T_a}$ for $Re_\tau = 71$ and (a) $T_a = 15$, (b) $T_a = 30$ and (c) $T_a = 70$.

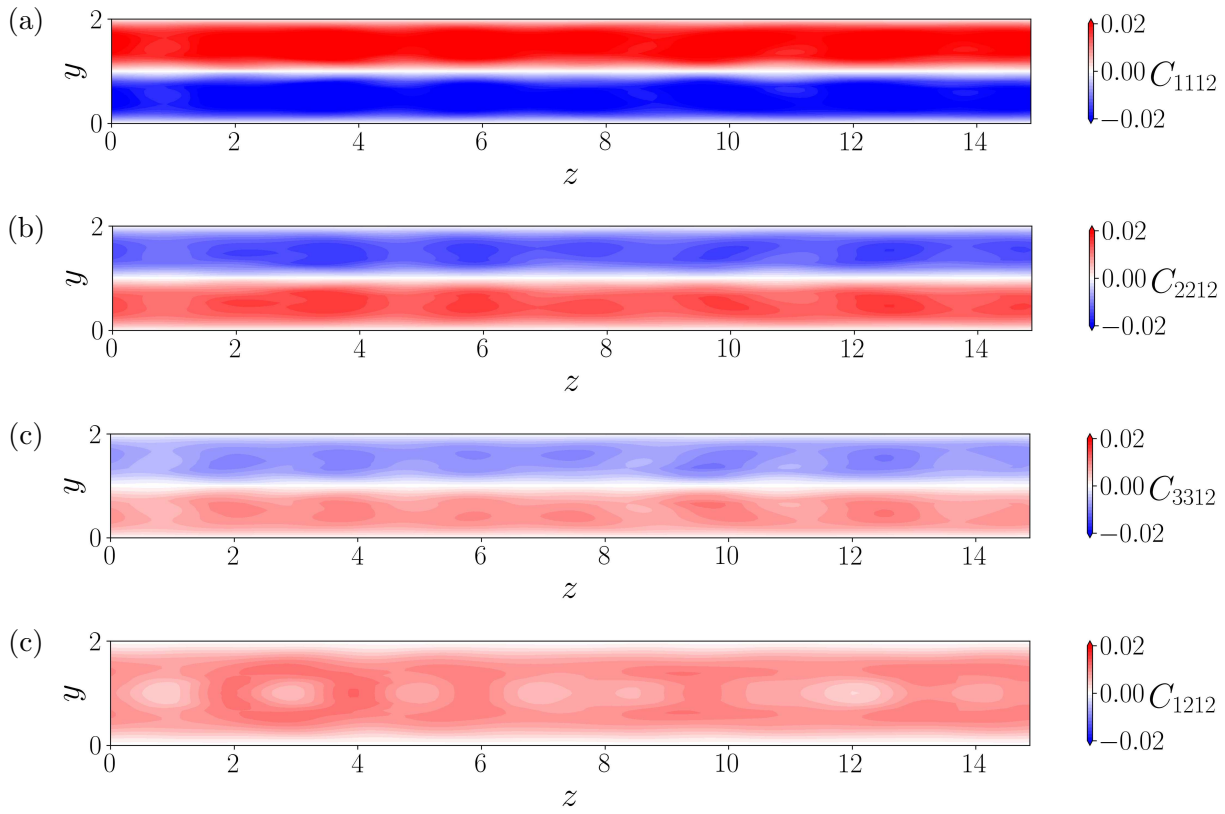

Figure 5.6: Principal components of the anisotropic eddy viscosity tensor C_{ijkl} (filtered and symmetrized) for $Re_\tau = 106$ and $T_a = 30$. (a) C_{1112}, (b) C_{2212}, (c) C_{3312} and (d) C_{1212}.

Another possibility, in the channel flow, is to follow the approach of the previous chapter (and many previous studies (Del Alamo and Jimenez, 2006; Pujals et al., 2009; Hwang and Cossu, 2010a; Park et al., 2011; Alizard, 2015)) and use the Cess (1958) eddy viscosity formula, as reported by Reynolds and Tiederman (1967), namely

$$\nu_t(y) = \frac{1}{2Re}\left\{\left[1 + \left(\frac{Re_\tau k}{3}\left(2y - y^2\right)\left(3 - 4y + 2y^2\right)\left(1 - e^{(|y-1|-1)Re_\tau/A}\right)\right)^2\right]^{1/2} - 1\right\}, \tag{5.8}$$

with $k = 0.426$, $A = 25.4$ (Del Alamo and Jimenez, 2006) and $y \in [0, 2]$. In this case the tensor $\boldsymbol{R}$ is modeled with the Boussinesq approximation (Pope, 2000):

$$R^a_{ij} = R_{ij} - \frac{1}{3}R_{ii}\delta_{ij} = \nu_t\left(\frac{\partial\langle u_i\rangle_{x,T_a}}{\partial x_j} + \frac{\partial\langle u_j\rangle_{x,T_a}}{\partial x_i}\right). \tag{5.9}$$

However, in this case, the tensor $\boldsymbol{R}$ can be computed together with the averaged flow $\langle\boldsymbol{u}\rangle_{x,T_a}$. So, the finite-time average approach provides an opportunity to challenge the choice of the Cess (1958) model.

The validity of the Boussinesq approximation (5.9) is questionable in most situations, because the Reynolds stress tensor and the mean deformation tensor are generally not aligned (Schmitt, 2007).

In the past, non-Boussinesq turbulence models have been proposed which used nonlinear polynomials of the mean deformation and mean rotation tensors (Pope, 1975). Nevertheless, to perform the LSA, we are looking for a linear model. In principle, the nonlinear models could be linearised around the base flow, but it is simpler to look directly for a more general linear model. The most general linear relation between two $2nd-$order tensors, is given by a $4th-$order tensor:

$$R^a_{ij} = C_{ijkl} S_{kl}, \qquad \text{with } S_{kl} = \frac{1}{2}\left(\frac{\partial \langle u_k \rangle_{x,T_a}}{\partial x_l} + \frac{\partial \langle u_l \rangle_{x,T_a}}{\partial x_k}\right). \tag{5.10}$$

In general, C_{ijkl} has $3^4 = 81$ components. However, both R^a_{ij} and S_{kl} are symmetric. This implies the *minor* symmetries of C_{ijkl}, namely $C_{ijkl} = C_{ijlk}$ and $C_{ijkl} = C_{jikl}$. These consitute 45 independent relations which reduce the number of independent coefficients to $81 - 45 = 36$. By analogy with the theory of linear elasticity (Barber, 2004), we also assume the major symmetries $C_{ijkl} = C_{klij}$, which remove another 15 degrees of freedom from the tensor. Therefore, the *supersymmetric* tensor C_{ijkl} has 21 free components. Moreover, $\langle \boldsymbol{u} \rangle_{x,T_a}$ is uniform in x, which implies $S_{11} = 0$ and, by incompressibility, $S_{33} = -S_{22}$. This allows us to discard 3 of the 21 free components.

At each point of the $y-z$ domain, R^a_{ij} and S_{kl} can be computed using the $\langle \cdot \rangle_{x,T_a}$ average. Then, at each point, equation (5.10) gives an underdetermined linear system with 6 equations and 18 unknowns. The least-squares solution of this system can be found with the singular value decomposition (SVD) of the system matrix (Quarteroni et al., 2006). In practice, it is found that only 4 components are non-negligible (the others show only small fluctuations near the channel centre), namely C_{1112}, C_{2212}, C_{3312} and C_{1212}. This is not surprising because the dominant components of R^a_{ij} are R^a_{11}, R^a_{22}, R^a_{33} and R^a_{12} and the dominant component of S_{kl} is S_{12}. The resulting components of C_{ijkl} are shown in figure 5.6. This figure shows the results of the local least-squares regression after they have been filtered and symmetrised to regularise the spatial behaviour of the tensor. The C_{ijkl} tensor, as shown in figure 5.6 consitutes our anisotropic eddy viscosity data-driven model.

A simpler model can be formulated using the C_{1212} component alone. This component is the proportionality constant between R^a_{12} and S_{12}, which means that it plays the role of the classic eddy viscosity (indeed, it is always positive). An eddy viscosity can be seen as an isotropic $4th-$order tensor. An isotropic tensor is defined by $C^I_{ijkl} = C(\delta_{ik}\delta_{jl} + \delta_{il}\delta_{jk})$ where C is a scalar. We can identify C with the C_{1212} component and denote it by ν_t^{DD} because it represents a data-driven eddy viscosity. This is seen considering the identity

$$R^a_{ij} = C^I_{ijkl} S_{kl} = \nu_t^{DD} \left(\delta_{ik}\delta_{jl} + \delta_{il}\delta_{jk}\right) S_{kl} = 2\nu_t^{DD} S_{ij}.$$

C^I_{ijkl} (ν_t^{DD}) contitutes our isotropic eddy viscosity data-driven model. Contours of ν_t^{DD} are illustrated in figure 5.7 for three Re. Moreover, ν_t^{DD} averaged in the spanwise direction is compared, in figure 5.8, to the Cess (1958) eddy viscosity profile for all the Re considered.

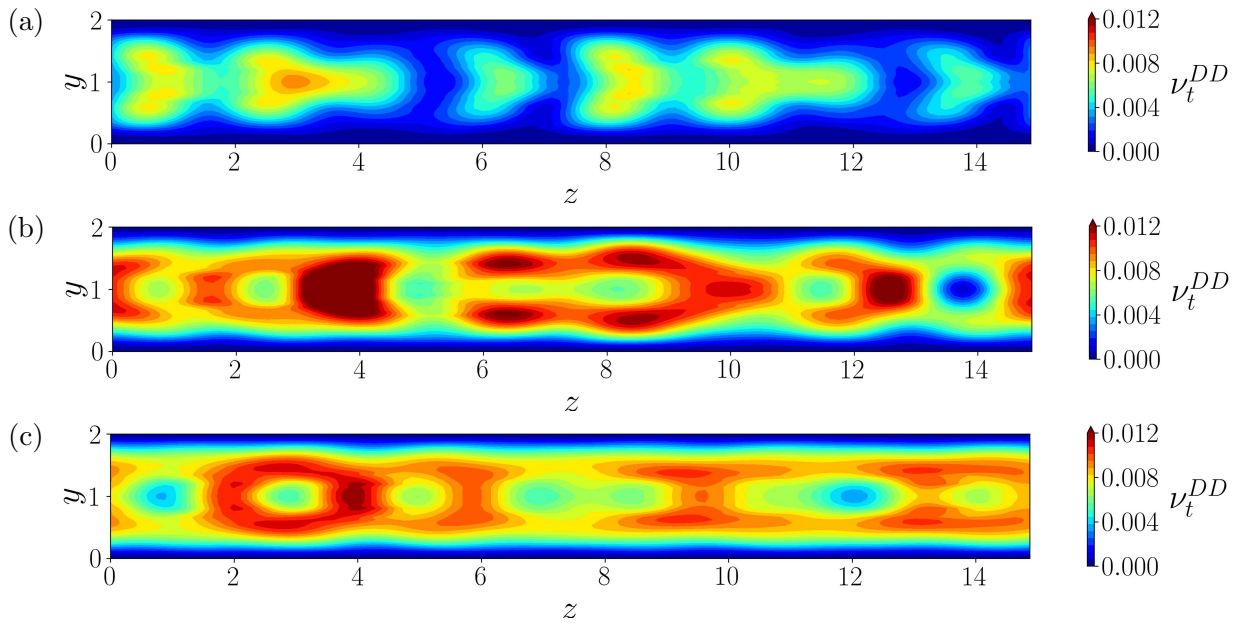

Figure 5.7: Scalar component of the isotropic eddy viscosity tensor ν_t^{DD} for $T_a = 30$ and (a) $Re_\tau = 71$, (b) $Re_\tau = 92$ and (c) $Re_\tau = 106$.

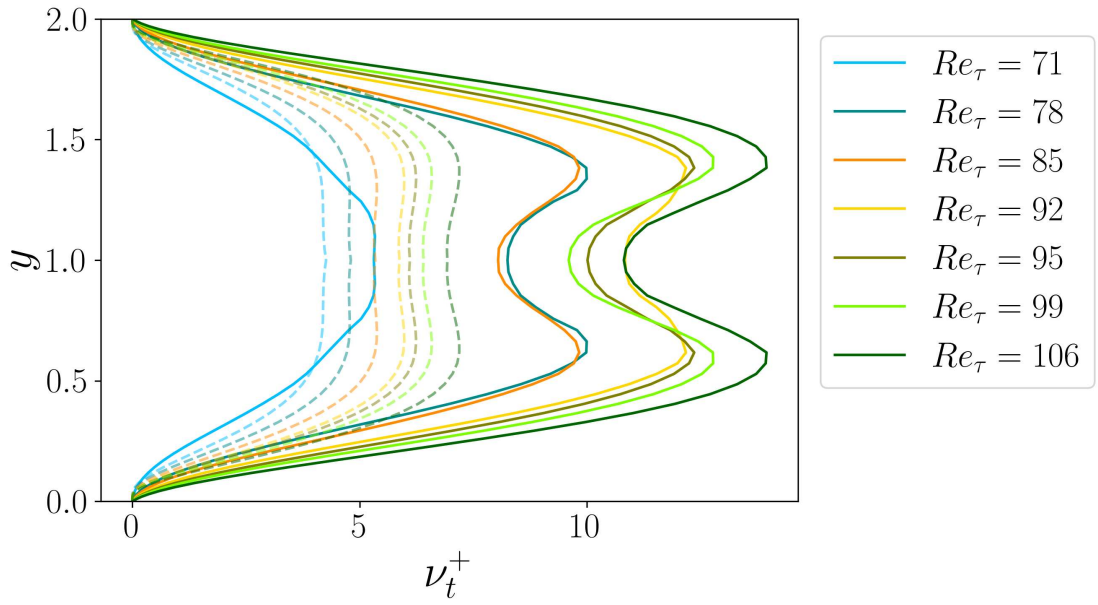

Figure 5.8: Spanwise averaged ν_t^{DD} obtained with $T_a = 30$ (solid lines) compared to the Cess (1958) eddy viscosity (dashed lines) at different Reynolds numbers. The two eddy viscosities are plotted in inner units, *i.e.* $\nu_t^+ = \nu_t Re$.

5.3.3 Stability analysis results

LSA is performed using (5.2) with $\boldsymbol{U} = \langle \boldsymbol{u} \rangle_{x,T_a}$ and

$$\left(\mathcal{M}\boldsymbol{u}''\right)_i = \frac{\partial}{\partial x_j}\left[\nu_t\left(\frac{\partial u_i''}{\partial x_j} + \frac{\partial u_j''}{\partial x_i}\right)\right] \tag{5.11}$$

for the Cess (1958) eddy viscosity model and the isotropic data-driven model and

$$\left(\mathcal{M}\boldsymbol{u}''\right)_i = \frac{\partial}{\partial x_j}\left[C_{ijkl}\left(\frac{\partial u_k''}{\partial x_l} + \frac{\partial u_l''}{\partial x_k}\right)\right] \tag{5.12}$$

for the anisotropic data-driven model.
Modal stability analysis assumes the following perturbation *ansatz* (ι denotes the imaginary unit):

$$\boldsymbol{u}'' = \tilde{\boldsymbol{u}}(y,z)e^{\sigma t + \iota k_x x} + \text{complex conjugate}, \quad \sigma \in \mathbb{C} \text{ and } k_x \in \mathbb{R}, \tag{5.13}$$

and an equivalent one for the pressure p''. This *ansatz* is substituted in (5.2) and the resulting equations are discretised with Fourier collocation in z and Chebyshev collocation in y. $N_y \times N_z = 65 \times 180$ collocation points are used in the domain $L_y \times L_z = 2 \times 15$, giving the same resolution of the DNS. Some tests with $N_y \times N_z = 101 \times 180$ points gave a variation of 3% on the growth rate and 0.005% on the frequency of the leading eigenvalues.

The scope of this study is to look for unstable modes that feature a large-scale flow, which can be associated with turbulence modulations. The choice of L_z was guided by this aim because 15 is the wavelength approximately corresponding to the critical spanwise wavenumber $k_x = 0.42$ reported by Kashyap et al. (2022). Analogously, the streamwise wavenumber is fixed to the critical value reported in the same study, namely $k_x = 0.18$. In this section, it will not be changed.
Figure 5.9 and 5.10 show the resulting eigenvalues in the complex plane obtained with the Cess (1958) eddy viscosity model and for, respectively, different Re and T_a. In these figures, the eigenvalues are coloured according to the scalar r_{LS} that quantifies the large-scale character of the corresponding eigenmode. Let $\check{\boldsymbol{u}}(y,k_z)$ be the Fourier transform of the eigenmode $\tilde{\boldsymbol{u}}(y,z)$ along z. r_{LS} is the ratio between the eigenmode energy at large k_z and the total eigenmode energy[3]:

$$r_{LS} = \frac{\displaystyle\int_0^2 |\check{\boldsymbol{u}}(y,k_z^1)|^2 \, dy}{\displaystyle\int_0^2 \sum_{k_z} |\check{\boldsymbol{u}}(y,k_z)|^2 \, dy}, \tag{5.14}$$

where $k_z^1 = 2\pi/L_z \approx 0.42$.
Figure 5.9 shows that, with the Cess model, the finite-time-averaged base flow is stable at every Re. However, the least stable modes have an important large-scale character. Changing T_a does not seem to bring any qualitative change to the results.

[3]The eigenmode energy is defined up to a multiplicative constant. This ambiguity is eliminated by considering the ratio between two eigenmode energies.

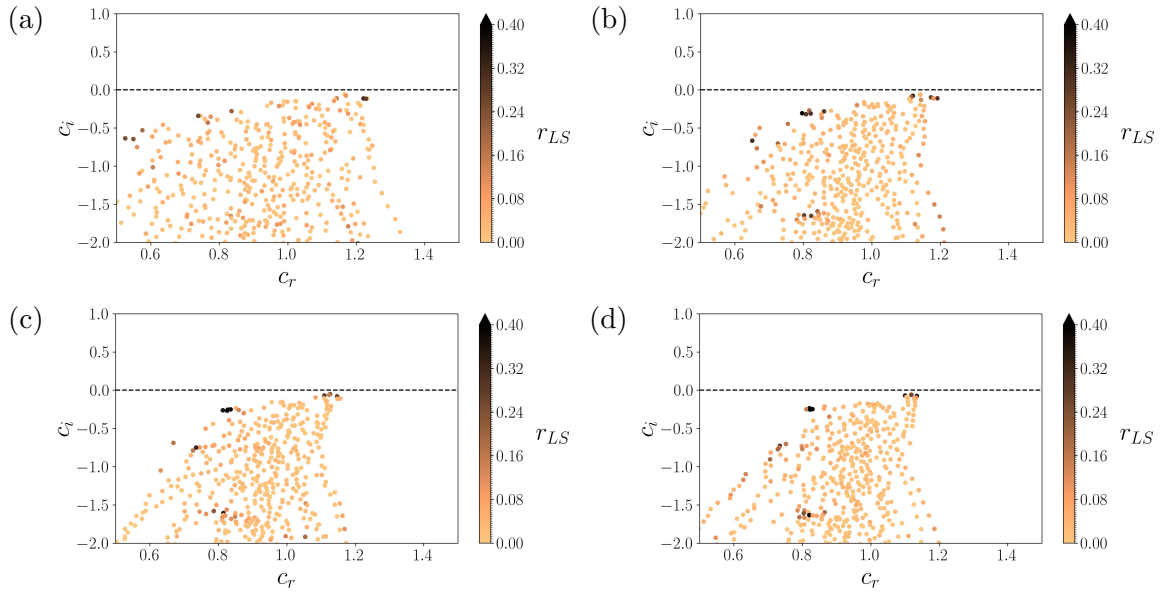

Figure 5.9: Eigenvalues coloured by the large-scale spanwise energy ratio r_{LS} for the $T_a = 30$ averaged base flows at (a) $Re_\tau = 71$, (b) $Re_\tau = 85$, (c) $Re_\tau = 99$ and (d) $Re_\tau = 106$. Cess eddy viscosity model and $k_x = 0.18$.

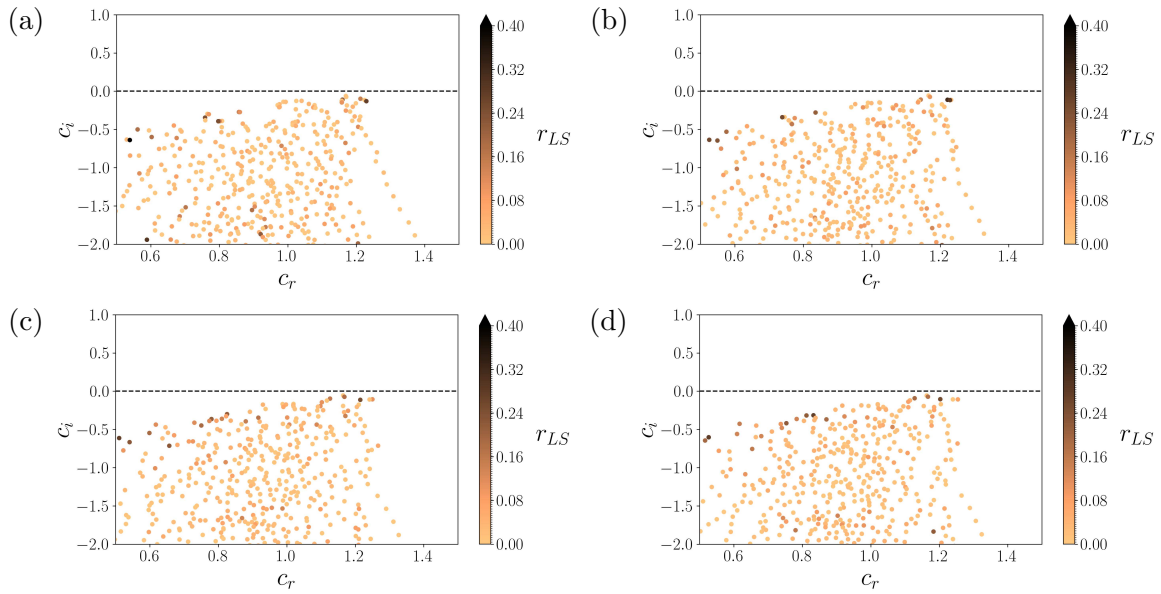

Figure 5.10: Eigenvalues coloured by the large-scale spanwise energy ratio r_{LS} for the (a) $T_a = 15$, (b) $T_a = 30$, (c) $T_a = 50$ and (d) $T_a = 70$ averaged base flow at $Re_\tau = 71$. Cess eddy viscosity model and $k_x = 0.18$.

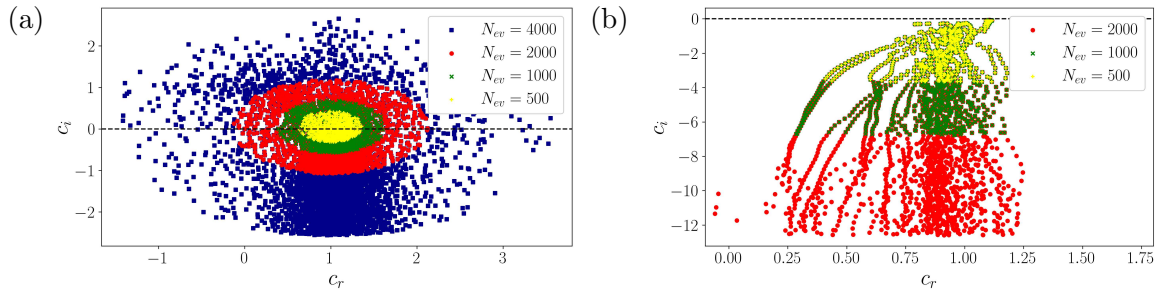

Figure 5.11: Influence of the number of computed eigenvalues on the eigenspectra for the anisotropic eddy viscosity data-driven model (a) and the isotropic eddy viscosity data-driven model (b). Computation at $Re_\tau = 106$ for the $T_a = 30$ base flow and $k_x = 0.18$.

Next, we address the influence of the closure model on the spectra. In the previous subsection, two data-driven eddy viscosity models were formulated: the anisotropic and the isotropic ones. Figure 5.11 shows that the anisotropic model is problematic. Apparently, it produces an enormous number of unstable modes. Increasing the number of computed eigenvalues, the number of unstable modes increases too, in such a way that the spectrum seems to be almost symmetric with respect to the zero growth rate line. We suspect that this behaviour is related to the C_{1112}, C_{2212} and C_{3312} components of the tensor. They change sign in the domain (see figure 5.6(a-b-c)) and, therefore, might introduce anti-dissipation in the system. This argument is substantiated by the fact that when these components are removed, in the isotropic model, the model behaves *well*: increasing the number of computed eigenvalues, only highly dissipated modes are added to the spectrum. The Cess (1958) eddy viscosity model behaves analogously to figure 5.11 (b).

Therefore, we compare only the Cess (1958) eddy viscosity model, the data-driven isotropic model and the quasi-laminar model (zero eddy viscosity) in figure 5.12. It can be seen that the quasi-laminar model does not give large-scale eigenmodes among the least stable ones (no dark points near the stability limit). Conversely, the data-driven isotropic eddy viscosity model gives a spectrum which is very close to the one obtained with the Cess (1958) model.

We define the leading eigenmodes as the least stable modes featuring $r_{LS} > 0.1$. The streamwise velocity component of these modes is shown in figure 5.13 for $T_a = 30$ and $Re_\tau = 71$, 92 and 106. The mode is characterised by a wavelength of ≈ 35 in x. Along z, it is multiscale, featuring a predominant large-scale character that corresponds to the wavelength 15 (*i.e.* the spanwise domain length). The Re impacts only the details of the mode. Indeed, most of the features of the mode depend on the t_0 used to start the finite-time average (the particular realisation of the base flow). Consequently, only the qualitative character of the mode is robust in this analysis. The modes at different Re share the same large-scale character. Therefore, there is no clear dependence of the shape of the modes on this parameter.

More interesting is the influence of the closure models. Figure 5.14 shows the leading modes for $Re_\tau = 106$ and $T_a = 30$ for the quasi-laminar model, the Cess (1958) eddy viscosity model and the data-driven isotropic eddy viscosity model. For the quasi-laminar model, there is no mode with $r_{LS} > 0.1$. Therefore, we simply took the least stable mode. The difference between the quasi-laminar

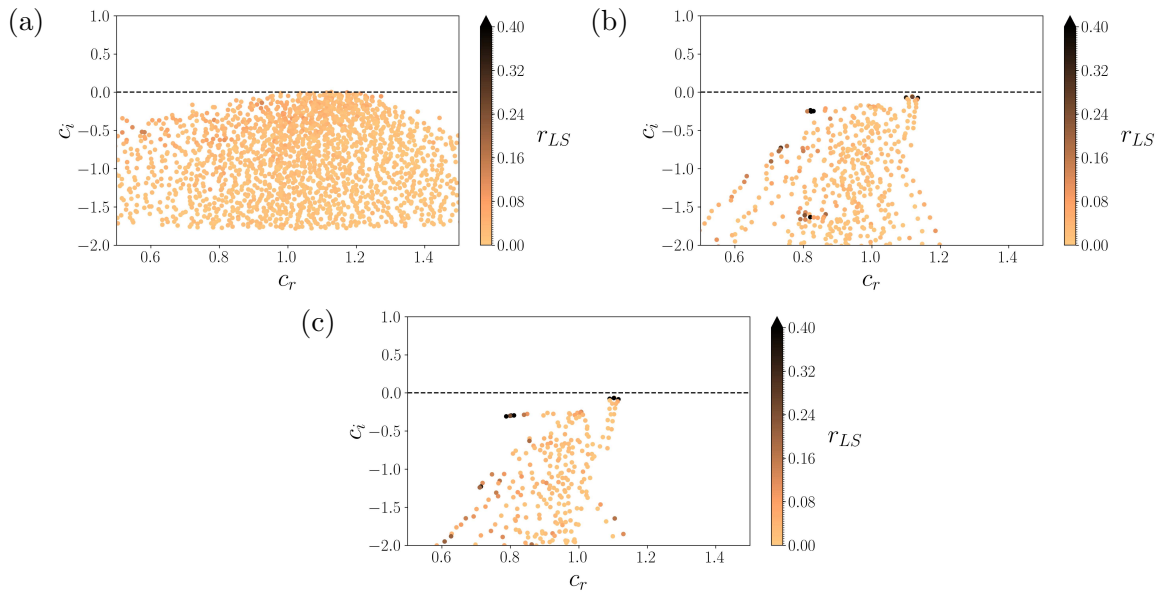

Figure 5.12: Eigenvalues coloured by the large-scale spanwise energy ratio r_{LS} at $Re_\tau = 106$ for the $T_a = 30$ averaged base flow and different models: (a) quasi-laminar model, (b) Cess eddy viscosity model and (c) data-driven eddy viscosity model. $k_x = 0.18$.

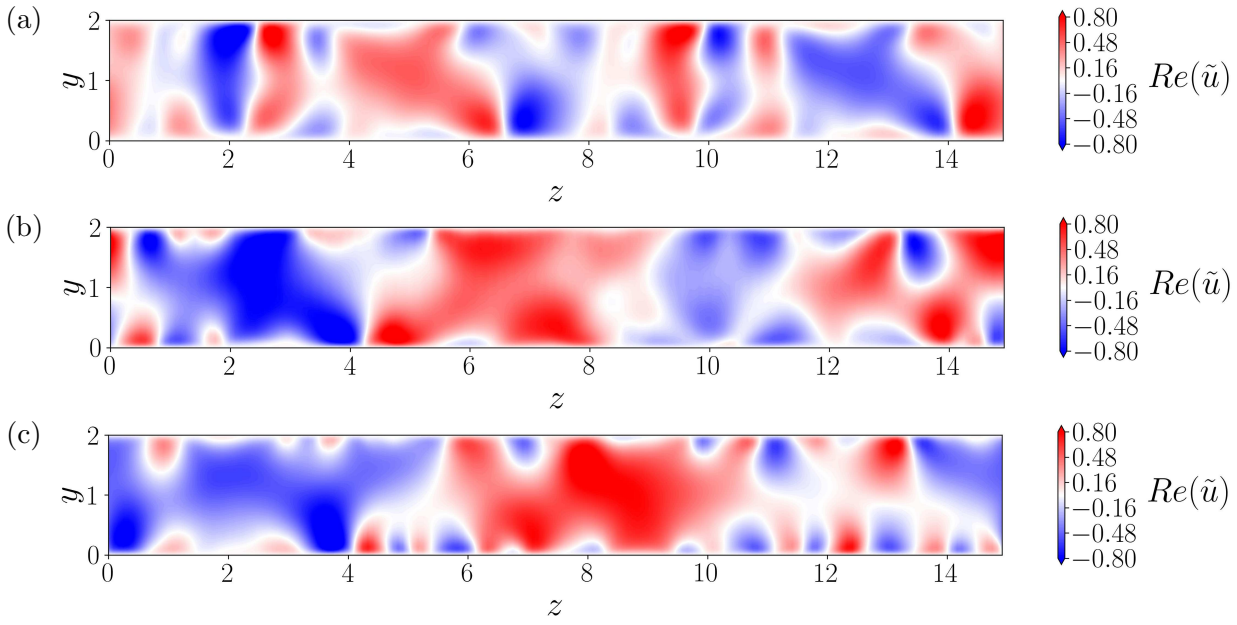

Figure 5.13: Real part of the streamwise velocity component of the leading mode for $T_a = 30$ and (a) $Re_\tau = 71$, (b) $Re_\tau = 92$ and (c) $Re_\tau = 106$. Cess eddy viscosity model and $k_x = 0.18$.

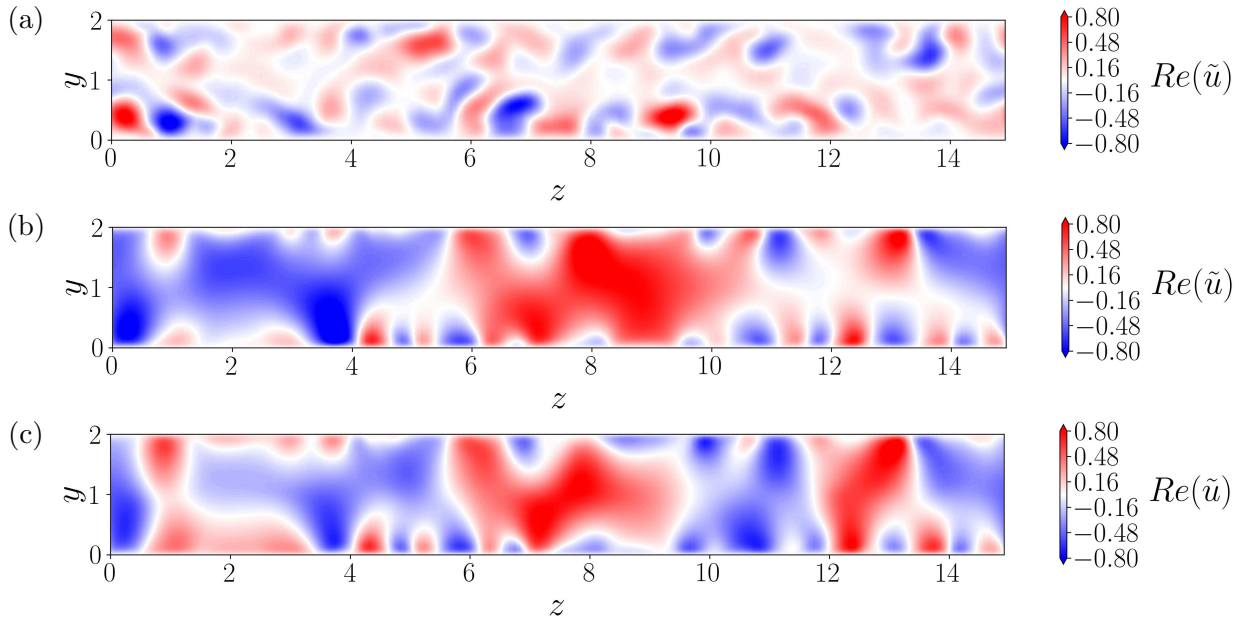

Figure 5.14: Real part of the streamwise velocity component of the leading mode at $Re_\tau = 106$ for the $T_a = 30$ averaged base flow and different models: (a) quasi-laminar model, (b) Cess eddy viscosity model and (c) data-driven eddy viscosity model. $k_x = 0.18$.

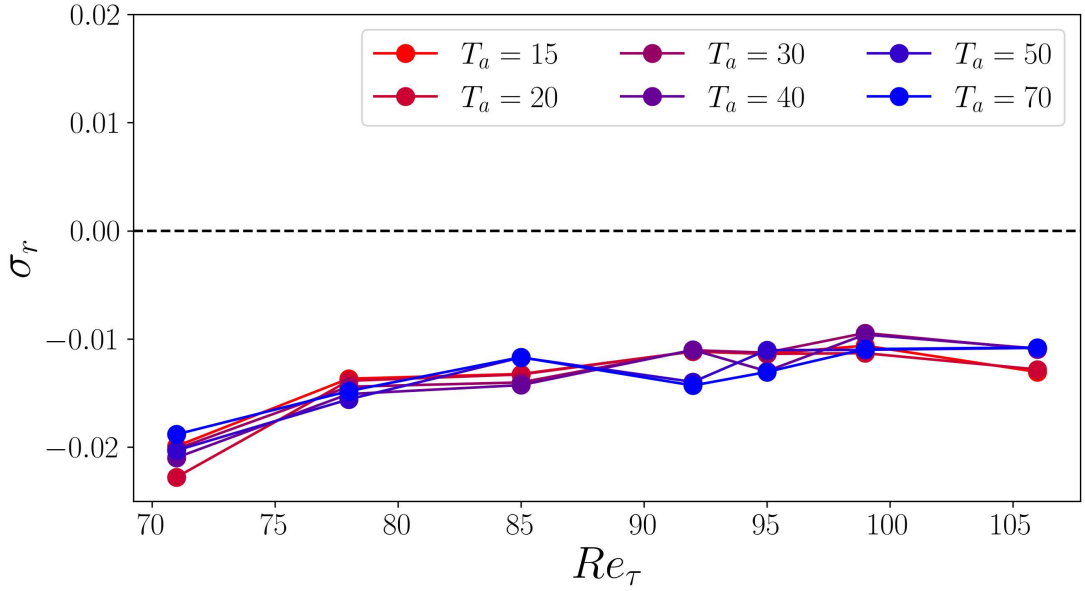

Figure 5.15: Growth rate of the leading mode of the finite time averaged base flow as a function of Re_τ and T_a. Cess eddy viscosity model.

mode and the other two modes is clear: no large-scale character exists without the eddy viscosity. We also note that the mode obtained with the Cess (1958) eddy viscosity and the one obtained with the data-driven eddy viscosity are remarkably similar.

5.3.4 Discussion

The results obtained with the finite-time-averaged base flows are encouraging for several reasons. When the incoherent turbulent motions are taken into account either by the Cess (1958) eddy viscosity or by the data-driven eddy viscosity, the system has some large-scale eigenmodes which may be representative of the modulations observed by Kashyap et al. (2022). The results show that there is an essential qualitative difference between the eddy viscosity models and the quasi-laminar model, demonstrating the need for modelling unresolved scales. This finding agrees with recent studies which compared different linear models of wall-bounded flows (Illingworth et al., 2018; Morra et al., 2019; Symon et al., 2023). Importantly, the Cess (1958) model and the data-driven eddy viscosity model give, qualitatively, similar results.

On the other hand, the approach presented in this section still fails to detect a critical Re. This is depicted in figure 5.15, which plots the growth rates of the leading large-scale eigenmodes as a function of Re_τ and T_a. The selected large-scale modes are always stable, and there is only a weak dependence on Re, which, in addition, is in the wrong direction (growth rate slightly increasing with Re). Moreover, the growth rates do not seem to depend on T_a. Therefore, tuning this parameter does not help to solve the issue. This is not surprising, since the base flows do not differ much for different T_a (see figure 5.5). In conclusion, concerning the Re dependence of the instability, the use of finite-time-averaged base flows does not improve with respect to the mean profile approach of Kashyap et al. (2024).

The reason for this failure is not well understood at this point. One possible explanation is given at the end of the chapter. In the following sections, we consider a different strategy to compute a relevant base flow, based on the resolvent analysis of the mean profile. As explained in Section 5.1, this approach has several advantages. We will see that these advantages are translated into better results.

5.4 Streaks computation by resolvent analysis

A wealth of previous studies have demonstrated that typical near-wall structures can be computed using the Navier-Stokes operator linearised around the mean flow either by considering the harmonic forcing problem (Hwang and Cossu, 2010a; McKeon and Sharma, 2010; Sharma and McKeon, 2013; Moarref et al., 2013) or the initial value problem (Del Alamo and Jimenez, 2006; Pujals et al., 2009). The results of this analysis are briefly revised here at low Re.

Using the Reynolds decomposition, the solution of (5.1) can be partitioned as the sum of the mean flow $\overline{\boldsymbol{U}} = \overline{U}(y)\boldsymbol{e}_x$ plus fluctuations. Then, following Reynolds and Hussain (1972), the effect of

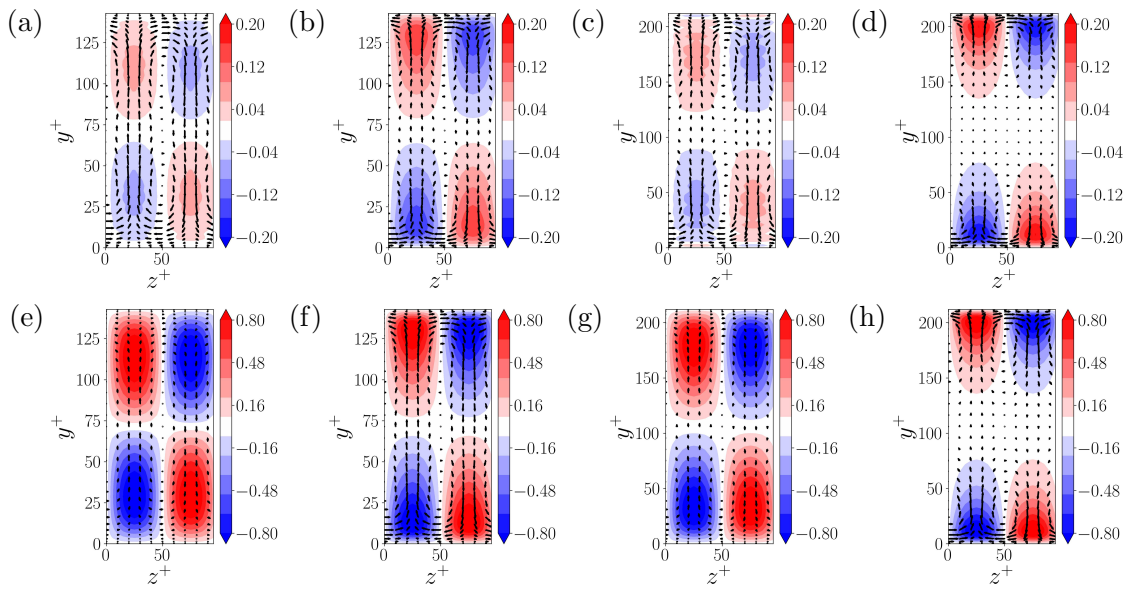

Figure 5.16: Optimal harmonic forcing (a-d) and response velocity field (e-h) obtained from the resolvent analysis of the mean flow for (a,b,e,f) $Re_\tau = 71$ and (c,d,g,h) $Re_\tau = 105$. In all panels, contours denote the streamwise component while quivers stand for transverse components. The scale of the arrows in the top row is ten times larger than in the bottom row. Streamwise uniform case ($k_x = 0$). (a,c,e,g) Quasi-laminar model; (b,d,f,h) eddy viscosity model.

incoherent fluctuations is modelled using an eddy viscosity term. Therefore, one obtains the system

$$\begin{cases} \dfrac{\partial \boldsymbol{u}'}{\partial t} + \overline{\boldsymbol{U}} \cdot \boldsymbol{\nabla} \boldsymbol{u}' + \boldsymbol{u}' \cdot \boldsymbol{\nabla} \overline{\boldsymbol{U}} + \boldsymbol{\nabla} p' - \dfrac{1}{Re} \nabla^2 \boldsymbol{u}' - \boldsymbol{\nabla} \cdot \left[\nu_t \left(\boldsymbol{\nabla} \boldsymbol{u}' + (\boldsymbol{\nabla} \boldsymbol{u}')^T \right) \right] = \boldsymbol{f}, \\ \boldsymbol{\nabla} \cdot \boldsymbol{u}' = 0, \end{cases} \tag{5.15}$$

for the coherent velocity fluctuation $\boldsymbol{u}'$ (resp. p' for the coherent pressure fluctuation), where $\boldsymbol{f}$ is a generic forcing term (*cf.* Morra et al. (2019)). The coherent fluctuation is interpreted mainly as the large scales, but it also includes the streaks because of their temporal and spatial coherence. Smaller scales as well as the remaining other flow structures, that by default we consider as "incoherent", are not explicitly resolved, instead they are modelled as an eddy viscosity.

The results of the previous section have demonstrated that the Cess (1958) eddy viscosity and the data-driven eddy viscosity give the same results up to minor details. For this reason and in order to simplify the analysis, we will use only the eddy viscosity given by equation (5.8) for the rest of the chapter. Therefore, from now on, the Cess (1958) model will be simply referred to as the eddy viscosity model. We will also perform computations without the eddy viscosity (quasi-laminar model) and compare the results for the two models. Note, however, that in both cases the eddy viscosity given by equation (5.8) is used to compute the mean profile solving the one-dimensional boundary value problem (4.4).

5.4.1 Resolvent modes

The linear nature of the system (5.15) greatly simplifies its analysis: by considering the Fourier transform of the equation in the wall-parallel directions and in time, the harmonic response is computed as $\hat{\boldsymbol{u}}(y;k_x,k_z,\omega) = \mathcal{H}(y;k_x,k_z,\omega)\hat{\boldsymbol{f}}(y;k_x,k_z,\omega)$, where $\mathcal{H}(y;k_x,k_z,\omega)$ is the resolvent operator, the hats denote Fourier transforms in x, z and t), ω is the angular frequency of both the forcing and the response, and k_x and k_z are the streamwise and spanwise wavenumbers. For a given $\{\omega,k_x,k_z\}$ triplet, the optimal harmonic forcing is defined as the function $\hat{\boldsymbol{f}}(y)$ that maximises the amplitude ratio between response and forcing (cf. Hwang and Cossu (2010a)):

$$R(k_x,k_z,\omega) = \max_{\hat{\boldsymbol{f}}\neq\boldsymbol{0}} \frac{\|\hat{\boldsymbol{u}}\|^2}{\left\|\hat{\boldsymbol{f}}\right\|^2} = \|\mathcal{H}(y;k_x,k_z,\omega)\|^2 \tag{5.16}$$

where the standard L^2 norm in y is used both for $\hat{\boldsymbol{u}}$ and $\hat{\boldsymbol{f}}$. The optimal harmonic forcing problem is solved using an in-house code which performs the Singular Value Decomposition of the discretised resolvent operator (see Section 2.7 and Schmid and Brandt (2014); Symon et al. (2018)). After Fourier transform in x, z and t and discretisation in y, the system (5.15) can be written as $(\iota\omega\mathbf{B}-\mathbf{L})\,\hat{\mathbf{q}} = \mathbf{B}\hat{\mathbf{f}}$, where $\hat{\mathbf{q}}$ contains the four primitive variables $\hat{u}$, $\hat{v}$, $\hat{w}$ and $\hat{p}$ for each point of the computational grid, $\mathbf{B}$ is the prolongation matrix (Cerqueira and Sipp, 2014), $\mathbf{L}$ is the discretised linear Navier-Stokes operator and ι the imaginary unit. The discretised resolvent operator can be computed by a matrix inversion as $\mathbf{H} = (\iota\omega\mathbf{B}-\mathbf{L})^{-1}\mathbf{B}$ and decomposed such that $\mathbf{W}^{1/2}\mathbf{H}\mathbf{W}^{-1/2} = \mathbf{U}\mathbf{\Sigma}\mathbf{V}^T$ ($\mathbf{W}$ contains the quadrature weights). The most amplified harmonic forcing is given by the first column of $\mathbf{V}$, the corresponding response mode by the first column of $\mathbf{U}$ and the energy amplification factor R by the square of the leading singular value of $\mathbf{H}$, which is the first diagonal element of $\mathbf{\Sigma}$. For the discretisation of differential operators, $N_y = 65$ Chebyshev collocation points have proven sufficient at the low values of Re considered. The code was validated by reproducing the results of Hwang and Cossu (2010a) and Symon et al. (2018) (see Section 2.7.3).

Resolvent analysis is not the main focus of this study. It is used here to define the streaks that are relevant to the stability analysis. Of course, there are other alternative ways to define two-dimensional streak modes, including the POD modes employed in the previous chapter (and not employed here to avoid the drawbacks discussed at the end of that chapter) but also the eigenmodes from the associated Stokes operator (Waleffe, 1997) or data-driven techniques where streaks are directly extracted from DNS (Hack and Zaki, 2014) or experimental data (Liu et al., 2024). The present choice of the resolvent modes was motivated mainly by the robustness of the resolvent modes, which makes the results more easily reproducible. Since this is the aim of our resolvent analysis, we do not explore systematically the optimal harmonic response. It is well known that typical near-wall structures in the considered flow are streaks characterised by a dominant spanwise wavelength $\lambda^+_{z,s} \approx 100$, defined in wall units. Moreover, in a first approximation, they can be seen as streamwise-independent structures (*straight streaks* following Liu et al. (2024)). Therefore, the optimal harmonic forcing problem is solved here for $k_x = 0$ and $k_z^+ = 2\pi/100$ and using 20 equi-spaced ω values in $[0,2\pi]$. Optimal amplification is found for steady forcing ($\omega = 0$) as in Hwang and Cossu (2010a). The problem is solved for the same range of Re considered in the previous section, namely $Re_\tau = [71,78,84,91,95,98,105]$.

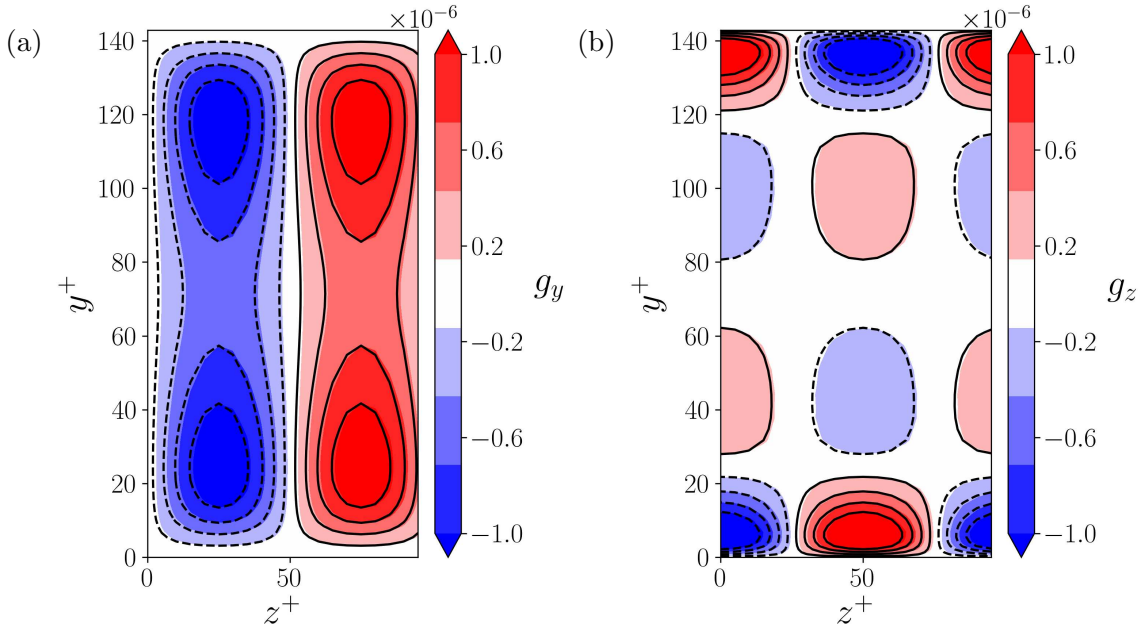

Figure 5.17: Forcing term $\boldsymbol{g}$ in equations (5.19-5.20) (shaded contours) compared to the forcing term $\boldsymbol{f}$ in equation (5.15) (black lines: solid for positive values, dashed for negative values) for $A_s = 1 \times 10^{-4}$. (a) Wall-normal component; (b) spanwise component. The line contours have the same iso-levels as the shaded contours to make the comparison meaningful.

Streamwise streaks are routinely explained by the advection of streamwise vortices by the lift-up effect (Ellingsen and Palm, 1975; Landahl, 1980), known as a linear mechanism, although explaining their persistence in turbulent flows requires nonlinear concepts such as the self-sustaining process (SSP). As it happens, resolvent analysis with the operator linearised around the mean flow is well-suited to compute such structures, including the one optimally amplified by linear mechanisms. In the resolvent framework, the forcing $\boldsymbol{f}$ represents the vortices and the response $\boldsymbol{u}'$ the streak field. Indeed, the forcing is found to be mainly directed in the wall-normal and spanwise directions, while the response is primarily dominated by the streamwise velocity component. Figure 5.16 shows the streamwise component of the forcing and response as shaded contours and the transverse components as arrows in the $y-z$ plane for two values of Re_τ. The typical picture of streamwise rolls and induced streaks is recognised here. Comparing the quasi-laminar model (panels a-c-e-g) with the eddy viscosity model (panels b-d-f-h), it is found that the eddy viscosity squeezes both streaks and vortices towards the wall. This effect increases with the Reynolds number. This is likely due to the wall-normal dependence of the eddy viscosity (5.8). We now turn to the linear stability analysis of the streaks. Before doing so, however, we briefly explain how the resolvent framework helps to define a steady base flow.

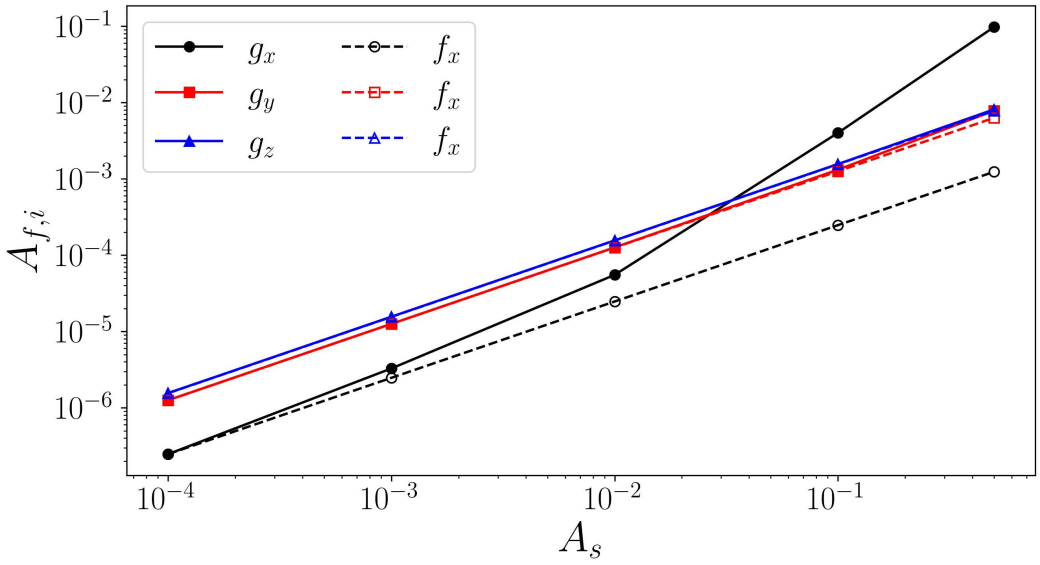

Figure 5.18: Comparison of the streak forcing amplitude ($A_{f,i} = (\max_{y,z} f_i - \min_{y,z} f_i)/2$) as a function of the streak amplitude (A_s). $\boldsymbol{f}$ and $\boldsymbol{g}$ defined as in figure 5.17.

5.4.2 Steady forcing for steady base flow

As illustrated in the previous section, the resolvent analysis identifies an optimal response with zero frequency. The velocity field associated with this response is hereafter denoted by $\boldsymbol{u}_s$. Due to the linearity of equation (5.15), $\boldsymbol{u}_s$ is defined up to a multiplicative constant. Analogously to the previous chapter, $\boldsymbol{u}_s$ is rescaled such that:

$$\frac{\max_{y,z} u_s - \min_{y,z} u_s}{2\overline{U}_c} = 1, \tag{5.17}$$

where u_s (scalar field) is the streamwise velocity component of the streak field and $\overline{U}_c$ is the centreline velocity of the turbulent mean profile.

A new base flow $\boldsymbol{U}$ is constructed from the knowledge of the mean flow $\overline{\boldsymbol{U}}$ and the streak field $\boldsymbol{u}_s$ as

$$\boldsymbol{U} = \overline{\boldsymbol{U}} + A_s \boldsymbol{u}_s, \tag{5.18}$$

with $A_s > 0$ interpreted as the *streak amplitude*. Consistently with the previous subsection, $\boldsymbol{U} = (U(y,z), V(y,z), W(y,z))$ is uniform in the streamwise direction.

Since both the mean flow and the optimal response are steady, we expect that the base flow $\boldsymbol{U}$ verifies an equation of the generic form

$$\begin{cases} \boldsymbol{U} \cdot \boldsymbol{\nabla} \boldsymbol{U} + \boldsymbol{\nabla} P - \dfrac{1}{Re} \nabla^2 \boldsymbol{U} - \boldsymbol{\nabla} \cdot \left[\nu_t \left(\boldsymbol{\nabla} \boldsymbol{U} + (\boldsymbol{\nabla} \boldsymbol{U})^T \right) \right] - \boldsymbol{f}_b = \boldsymbol{g}, \\ \boldsymbol{\nabla} \cdot \boldsymbol{U} = 0. \end{cases} \tag{5.19}$$

with some forcing term $\boldsymbol{g}$ to be determined. Such a forcing term is necessary since $\boldsymbol{U}$ is not an explicit solution to the unforced Navier-Stokes equations. Nevertheless, this forcing term $\boldsymbol{g}$ differs from the

forcing term $\boldsymbol{f}$ in equation (5.15) because equation (5.15) is linear with respect to $\boldsymbol{u}_s$ whereas equation (5.19) implicitly contains the nonlinear term $A_s^2 \boldsymbol{u}_s \cdot \boldsymbol{\nabla} \boldsymbol{u}_s$, with A_s not vanishing. $\boldsymbol{g}$ can be computed explicitly using a nonlinear time-stepping algorithm, as detailed below.

Once $\boldsymbol{g}$ is known, the following nonlinear system is fully specified by

$$\begin{cases} \dfrac{\partial \boldsymbol{u}}{\partial t} + \boldsymbol{u} \cdot \boldsymbol{\nabla} \boldsymbol{u} + \boldsymbol{\nabla} p - \dfrac{1}{Re} \nabla^2 \boldsymbol{u} - \boldsymbol{\nabla} \cdot \left[\nu_t \left(\boldsymbol{\nabla} \boldsymbol{u} + (\boldsymbol{\nabla} \boldsymbol{u})^T \right) \right] - \boldsymbol{f}_b = \boldsymbol{g}, \\ \boldsymbol{\nabla} \cdot \boldsymbol{u} = 0. \end{cases} \tag{5.20}$$

By construction, the base flow $\boldsymbol{U}$ is a steady state solution of this system.

The forcing $\boldsymbol{g}$ in the above equations can be numerically determined using the nonlinear time-stepping code channelflow (Gibson et al., 2021). To detail the procedure, let us denote the left-hand side of the first equation in (5.20) as $\partial \boldsymbol{u}/\partial t + \boldsymbol{\mathcal{N}}(\boldsymbol{u})$. We seek $\boldsymbol{g}$ such that, by construction, $\boldsymbol{U}$ verifies (5.19), *i.e.* $\boldsymbol{\mathcal{N}}(\boldsymbol{U}) = \boldsymbol{g}$. To approximate $\boldsymbol{\mathcal{N}}(\boldsymbol{U})$ using a timestepper, and only for this purpose, we consider the initial value problem:

$$\begin{cases} \dfrac{\partial \boldsymbol{u}}{\partial t} = -\boldsymbol{\mathcal{N}}(\boldsymbol{u}), \\ \boldsymbol{\nabla} \cdot \boldsymbol{u} = 0, \\ \boldsymbol{u}(t = 0) = \boldsymbol{U}. \end{cases} \tag{5.21}$$

Advancing this system of one time step Δt, one obtains a velocity field $\boldsymbol{U}^1 \neq \boldsymbol{U}$. Then, the forcing term $\boldsymbol{g} = \boldsymbol{\mathcal{N}}(\boldsymbol{U})$ can be approximated by the finite difference $-\left(\boldsymbol{U}^1 - \boldsymbol{U}\right)/\Delta t$.

This approach comes with a numerical error due to the finite difference approximation. In practice, however, it turns out to be accurate enough. Indeed, advancing the system (5.20) with the timestepping code starting from $\boldsymbol{U}$, this field remains steady up to a small numerical error, as expected by construction of the forcing. Moreover, the forcing computation can be validated considering a small A_s. In the limit $A_s \to 0$, equations (5.15) and (5.19) coincide with $\boldsymbol{u}' = \boldsymbol{u}_s$ and $\boldsymbol{g} \to \boldsymbol{f}$ because the difference between the equations, $A_s^2 \boldsymbol{u}_s \cdot \boldsymbol{\nabla} \boldsymbol{u}_s$, becomes negligible. This is shown in panels (a) and (b) of figure 5.17 for $A_s = 1 \times 10^{-4}$. As A_s increases, the two forcings differ, especially on the streamwise component (figure 5.18). This difference at finite A_s motivates the need for a specific procedure to compute $\boldsymbol{g}$.

Since $\boldsymbol{U}$ is now a steady solution of equation (5.20), LSA can be used rigorously. By perturbing the base flow $\boldsymbol{U}$ with a small perturbation $\boldsymbol{u}''$ such that $\boldsymbol{u} = \boldsymbol{U} + \boldsymbol{u}''$ and neglecting quadratic perturbation terms, one gets the linear system (5.2) for $\boldsymbol{u}''$ and the corresponding pressure perturbation p''. The forcing term $\boldsymbol{g}$ cancels out in the secondary perturbation equation because it is constant, *i.e.*, it depends only on $\boldsymbol{U}$ and not on $\boldsymbol{u}''$. Similarly, $\boldsymbol{f}_b$ cancels out because we assume that $\boldsymbol{u}''$ does not modify the flow rate.

It is important to highlight that this "derivation" of the linear stability equations is not essentially different from the frozen base flow assumption advocated in the previous chapter. However, this presentation has two merits: (i) it helps to *frame* this assumption in the forcing $\boldsymbol{g}$, which is a *lumped* representation of the nonlinear feedback of the SSP; (ii) it allows to identify the nonlinear equations

verified by the base flow plus perturbation flow (5.20), which can be numerically integrated to perform nonlinear simulations of the instability.

5.5 Stability analysis of resolvent streaks

5.5.1 Stability equations

Consistently with the analysis in Section 5.4, we will consider for the stability analysis both the quasi-laminar and the Cess (1958) eddy viscosity model. Therefore, the LSA equations are (5.2) either with $\mathcal{M}\boldsymbol{u}'' \equiv \boldsymbol{0}$ or with (5.9).

Modal stability analysis is performed assuming the *ansatz* (5.13). After substitution into equation (5.2), the following eigenvalue problem is obtained:

$$\begin{cases} \sigma\tilde{u} = -\imath k_x U\tilde{u} - V\dfrac{\partial\tilde{u}}{\partial y} - W\dfrac{\partial\tilde{u}}{\partial z} - \tilde{v}\dfrac{\partial U}{\partial y} - \tilde{w}\dfrac{\partial U}{\partial z} - \imath k_x\tilde{p} + \left(\dfrac{1}{Re} + \nu_t\right)\nabla^2\tilde{u} + \dfrac{d\nu_t}{dy}\left(\dfrac{\partial\tilde{u}}{\partial y} + \imath k_x\tilde{v}\right), \\ \sigma\tilde{v} = -\imath k_x U\tilde{v} - V\dfrac{\partial\tilde{v}}{\partial y} - W\dfrac{\partial\tilde{v}}{\partial z} - \tilde{v}\dfrac{\partial V}{\partial y} - \tilde{w}\dfrac{\partial V}{\partial z} - \dfrac{\partial\tilde{p}}{\partial y} + \left(\dfrac{1}{Re} + \nu_t\right)\nabla^2\tilde{v} + 2\dfrac{d\nu_t}{dy}\dfrac{\partial\tilde{v}}{\partial y}, \\ \sigma\tilde{w} = -\imath k_x U\tilde{w} - V\dfrac{\partial\tilde{w}}{\partial y} - W\dfrac{\partial\tilde{w}}{\partial z} - \tilde{v}\dfrac{\partial W}{\partial y} - \tilde{w}\dfrac{\partial W}{\partial z} - \dfrac{\partial\tilde{p}}{\partial z} + \left(\dfrac{1}{Re} + \nu_t\right)\nabla^2\tilde{w} + \dfrac{d\nu_t}{dy}\left(\dfrac{\partial\tilde{w}}{\partial y} + \dfrac{\partial\tilde{v}}{\partial z}\right), \\ 0 = \imath k_x\tilde{u} + \dfrac{\partial\tilde{v}}{\partial y} + \dfrac{\partial\tilde{w}}{\partial z}, \end{cases} \tag{5.22}$$

with $\nabla^2 = -k_x^2 + \partial_y^2 + \partial_z^2$.

As before, the secondary stability problem is solved in a two-dimensional $y-z$ domain using Fourier collocation in the spanwise direction and Chebyshev collocation in the wall-normal direction. Assuming that $\boldsymbol{u}_s$ is periodic in z with wavelength $\lambda_{z,s}$, the spanwise size of the domain for the secondary stability analysis is chosen as an integer multiple of this wavelength. In this way, we include in the analysis perturbations characterised by a large-scale modulation developing over several repetitions of the base flow unit (cf. Chapter 4). Hereafter, the number of periodic units is denoted by N_u, the total spanwise size of the domain is therefore $N_u\lambda_{z,s}$.

After spatial discretisation, the stability problem (5.22) becomes a generalised eigenvalue problem of the form

$$\sigma\mathbf{B}\tilde{\mathbf{q}} = \mathbf{A}\tilde{\mathbf{q}}, \tag{5.23}$$

where $\tilde{\mathbf{q}}$ contains the four primitive variables $\tilde{u}$, $\tilde{v}$, $\tilde{w}$ and $\tilde{p}$ for each point of the computational grid. The matrix $\mathbf{B}$, referred to as the prolongation matrix (see *e.g.* Cerqueira and Sipp (2014)), is almost the identity matrix except for the vanishing diagonal terms associated with the pressure. The matrix $\mathbf{A}$ is block-circulant owing to the spanwise periodicity of the base flow. This particular structure of the problem can be exploited to reduce the computational cost of the analysis by performing N_u smaller computations, with each sub-problem having a computational cost proportional to the size of the base flow domain (see Schmid et al. (2017) and Section 2.6.3). We briefly recall the peculiarities of this method. Each sub-problem is associated with a root of unity $\exp(2\pi\gamma\imath)$, with γ taking N_u equi-spaced

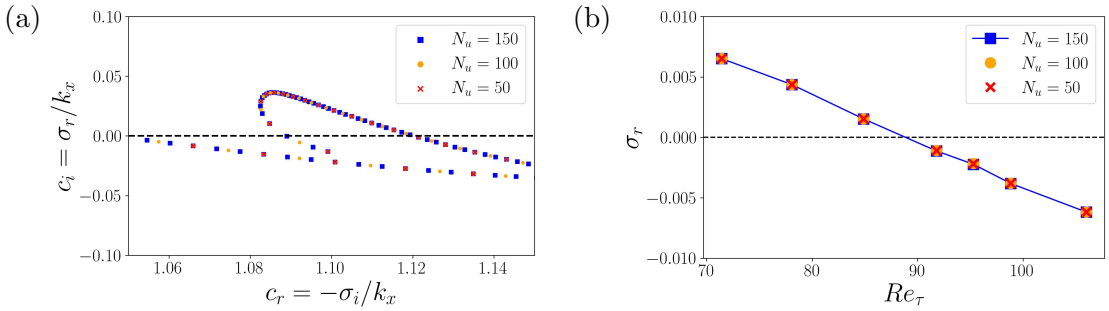

Figure 5.19: Convergence of the eigenvalues with the number N_u of base flow units (eddy viscosity model). (a) Eigenvalues for $Re_\tau = 71$, $k_x = 0.18$ and $A_s = 0.5$. (b) Leading growth rate as a function of Reynolds number for $k_x = 0.18$ and $A_s = 0.5$.

values in $[0, 1)$. The union of the eigenspectra of the sub-problems yields the eigenspectrum of the original problem.

The γ exponents are ideally interpreted, for a given eigenvector, as the ratio between the wavelength of the base flow and that of the eigenvector. In the particular case where $\gamma = 0$ ($\rho_1 = 1$), the eigenvector has the same periodicity as the base flow, *i.e.* $N_u = 1$. One recovers thus the classical LSA results, since $\rho_1 = 1$ and $\gamma = 0$. In the special case where γ is of the form $1/Q$ with Q a non-zero integer, then the fundamental wavelength of the eigenvector is exactly $Q\lambda_{z,s}$, and it can be labelled *subharmonic*. In the general case, for N_u finite, only rational values of γ can be tackled using this method and irrational values are excluded. The physical range of meaningful values of γ is continuous and involves irrational values as well. In practice, it is advised to consider a value of N_u as large as possible in order to have access to a well-discretised range of values of γ in $[0 : 1)$. As a consequence, γ can be interpreted as a *detuning factor* (Jouin et al., 2024). Note moreover that the symmetry $z \leftarrow -z$, inherent to the base flow, implies that γ and $1 - \gamma$ are associated with the same eigenvalue and eigenvector. This restricts the study of the eigenspectrum to the range of values $\gamma \in [0, 0.5]$. Finally, the union of the spectra of the sub-matrices $\hat{\mathbf{A}}_\mathbf{j}$ yields the spectrum of the original matrix $\mathbf{A}$. In practice, the latter is found by looping over $j = 0, ..., N_u - 1$, which is indirectly a loop over the values of γ in $[0, 0.5]$. This is the basis of the computation shown in Figure 5.21.

The exponent γ plays the same role as the Floquet modulation parameter in spatial Floquet theory (Herbert, 1988), although the block-circulant matrix method and spatial Floquet analysis (also called Bloch formalism) are formally different. However, *a posteriori* the two methods give identical results (Jouin et al., 2024).

5.5.2 Numerical parameters

LSA involves, as numerical parameters, the number of collocation points for the discretisation of the problem (N_y in the wall-normal direction and N_z in the spanwise direction) and the number of periodic units which effectively imposes the spanwise size of the domain (N_u).

Figure 5.19(a) shows the effect of increasing the number of independent base flow units on the

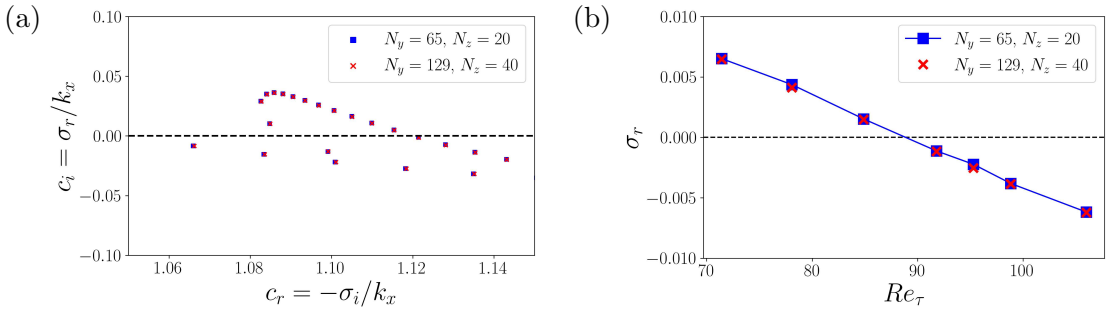

Figure 5.20: Convergence of the eigenvalues with the number of collocation points (eddy viscosity model). (a) Eigenvalues for $Re_\tau = 71$, $k_x = 0.18$ and $A_s = 0.5$. (b) Leading growth rate as a function of Re for $k_x = 0.18$ and $A_s = 0.5$.

spectrum: the branches of detuned modes tend towards continuous branches. However, as demonstrated by figure 5.19(b), the leading eigenvalue (and corresponding mode) is already well captured with $N_u = 50$, which means that the branch is sufficiently well discretised for this number of units.

Similarly, figure 5.20(a) shows that doubling the number of collocation points in both spatial directions affects the eigenvalues minimally. Identical considerations also apply to the spatial structure of the eigenmodes (not shown). Moreover, figure 5.20(b) shows that the Re-dependence of the leading growth rate is not affected either.

Therefore, the choice of $N_y = 65$, $N_z = 20$[4] and $N_u = 50$ does not affect the conclusions of our study and is employed for all the computations described in the following.

5.5.3 Critical Reynolds number

The first question addressed in this section is whether a critical Reynolds number exists below which spatial modulations appear. In the work of Kashyap et al. (2024), based on a linearisation around the asymptotic mean flow (without streaks), no such critical threshold was identified. The same was found in Section 5.3. Note, however, that in Section 5.3 no streak amplitude was explicitly introduced, contrary to Chapter 4. It is well established that streaks become unstable for sufficiently large amplitude (Schoppa and Hussain, 2002). However, classical streak instability is characterised by wavelengths which are either identical ($\gamma = 1$) or double ($\gamma = 0.5$) of the wavelength of the streak (Andersson et al., 2001), whereas the focus of this work is on instabilities that modulate the streaky flow over much larger scales. Therefore, the second point to be addressed is whether the unstable mode at criticality features an important large-scale component. In this subsection, we focus specifically on $k_x = 0.18$, the critical streamwise wavenumber reported by Kashyap et al. (2022).

The effect of the streak amplitude A_s on the eigenvalues associated with (5.23) is documented in figure 5.21. This figure shows a close-up view in the complex plane of the leading branch of eigenvalues, *i.e.*, the least stable (or the most unstable) one. It shows the eigenvalues in the form of complex phase velocities $c = -\sigma/\imath k_x$. The figure displays only a small part of the computed eigenspectrum. There is

[4]The number of points in the spanwise direction refers to the discretisation of a single streak wavelength.

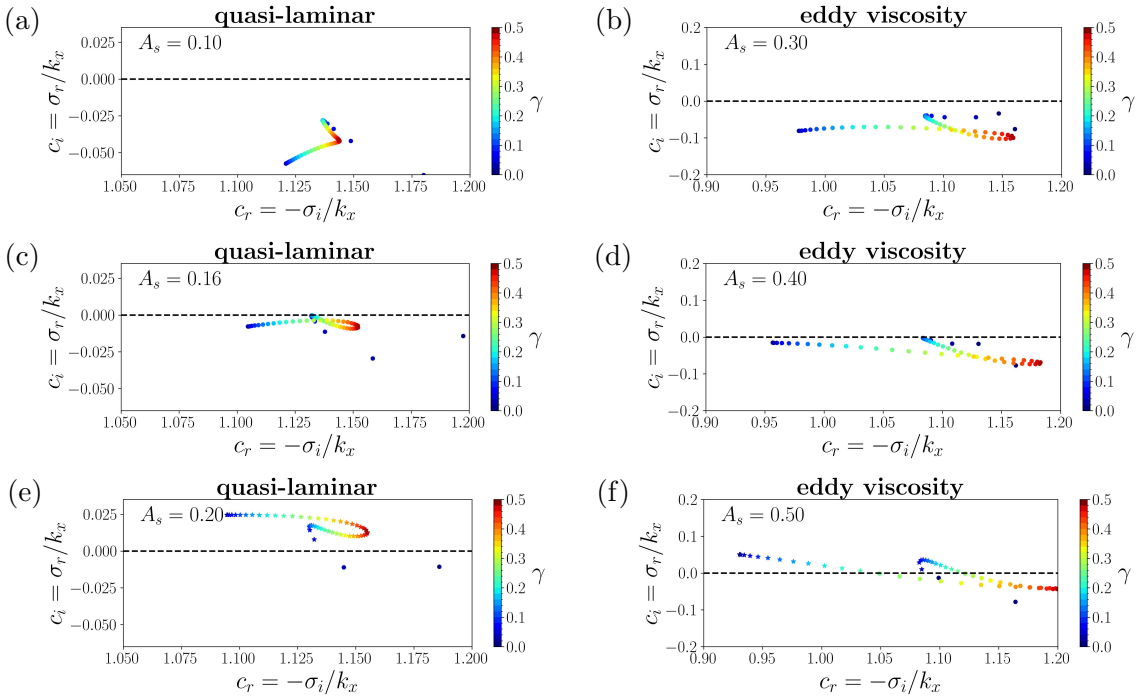

Figure 5.21: Eigenvalues for the streak stability problem (only a subset of the computed spectra is shown) for $Re_\tau = 71$ and $k_x = 0.18$. The eigenvalues ($\bullet$ for stable modes, $\star$ for unstable modes) are coloured with the corresponding root of unity factor $\gamma = j/N_u$ for $j = 0, \ldots, N_u/2$ (the eigenvalues for $\gamma \in (0.5, 1.0)$ are equal to those for $\gamma \in (0, 0.5)$ and the corresponding modes are the same up to a reflection in the spanwise direction). (a,c,e) Quasi-laminar model; (b,d,f) eddy viscosity model. Streak amplitudes increase from top to bottom and are (a) 0.10, (c) 0.16 and (e) 0.20 for the quasi-laminar cases and (b) 0.30, (d) 0.40 and (f) 0.50 for the cases with eddy viscosity.

no instability elsewhere in the range of parameters investigated. As explained in the previous section, these spectra are the union of N_u sub-spectra, each associated with a different root of unity. Therefore, in figure 5.21 the eigenvalues are coloured according to the respective factor γ, which identifies the relevant root of unity (see previous section) and takes values in $[0, 1)$. In practice, only the range $[0, 0.5]$ needs to be shown since the eigenmodes corresponding to γ in $(0.5, 1)$ are obtained from those in $(0, 0.5)$ by spanwise reflection. Focusing on $Re_\tau = 71$ and $k_x = 0.18$, the figure shows that the branch becomes unstable as the A_s is increased. The critical amplitude for the quasi-laminar model (left panels) is ≈ 0.16, whereas for the eddy viscosity model it is larger, ≈ 0.4 (right panels). After inspection of the eigenvalues for several A_s, we report that, for both models, the first mode that becomes unstable at $k_x = 0.18$ has $\gamma > 0$.

The Re_τ-dependence of the leading eigenvalue is documented in figure 5.22 for varying A_s. The first row shows the leading growth rates for the two models considered, respectively, quasi-laminar and using an eddy viscosity. In the quasi-laminar model, the growth rates become positive without any apparent dependence on Re. A critical amplitude can still be defined, independently of Re_τ, but no critical Reynolds number exists. For the eddy viscosity model, the growth rate increases with A_s and depends also on the value of Re_τ. As a result, for A_s large enough, as Re_τ is decreased, the

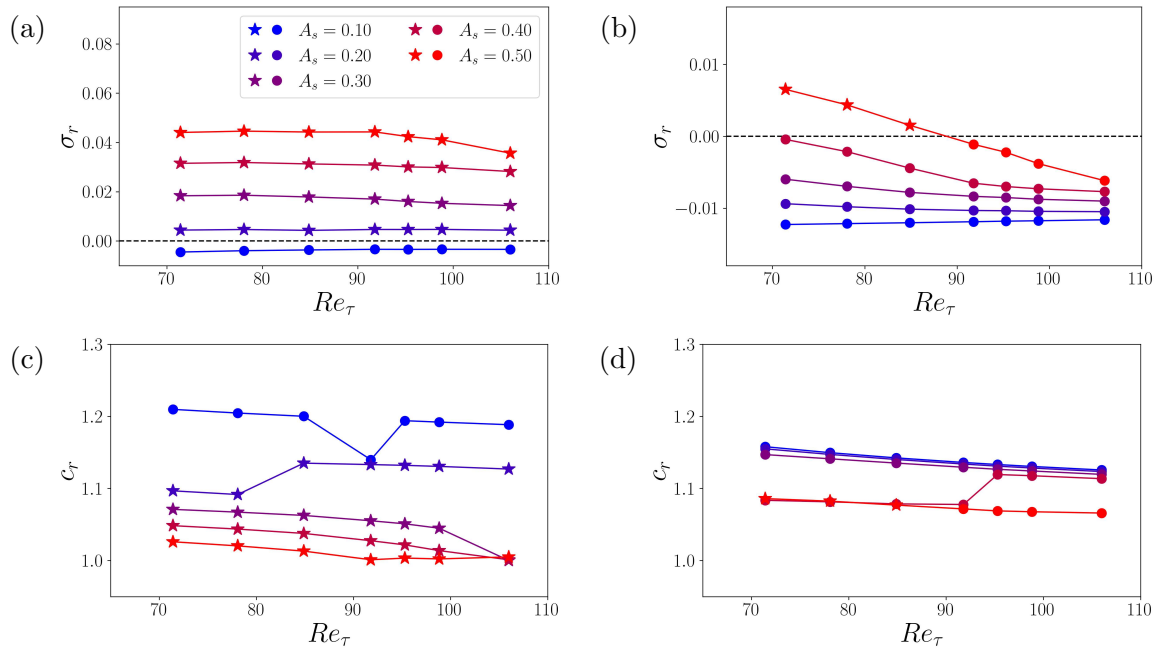

Figure 5.22: Variation of the leading eigenvalues with Re and streak amplitude A_s for $k_x = 0.18$ (• for stable modes, ⋆ for unstable modes). (a,b): growth rate. (c,d): phase velocity. (a,c) Quasi-laminar model; (b,d) eddy viscosity model.

growth rate of the most unstable mode becomes positive at a well-defined critical Reynolds number. A striking point is the qualitative difference between the results of the two models. The presence of a critical Re with the eddy viscosity model is a qualitative improvement with respect to the mean flow analysis in Kashyap et al. (2024).

The bottom panels of figure 5.22 show the phase velocity of the leading modes with respect to Re_τ and A_s. The values globally overestimate by roughly $5 - 10\%$ the advection velocities of turbulent bands measured from DNS (Tuckerman et al., 2014), however, they display a similar decrease with Re.

Besides the fact that the critical value itself depends on the value of A_s, another point of concern is the fact that the instability and the Reynolds number dependence are observed only for large amplitudes. The issue of whether these amplitudes are realistic will be addressed in the discussion section.

5.5.4 Unstable (large-scale) modes

The above results are encouraging and call for an examination of the unstable eigenmodes. Notably, no spanwise wavelength of the modes is explicitly imposed in the *ansatz* in (5.13). All detuned eigenmodes contain energy in wavelengths larger than the base flow wavelength $\lambda_{z,s}$, yet the question arises whether some eigenmodes have a particularly prominent large-scale component. In this respect, the detuning factor γ yields only partial information. Therefore, as was done in Section 5.3, an

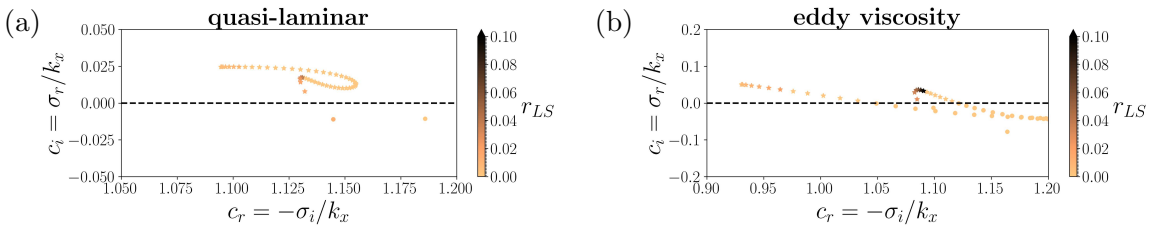

Figure 5.23: Eigenvalues coloured by the large-scale spanwise energy ratio r_{LS} (only a subset of the computed spectra is shown) for $Re_\tau = 71$ and $k_x = 0.18$ ($\bullet$ for stable modes, $\star$ for unstable modes). (a) Quasi-laminar model and $A_s = 0.2$; (b) eddy viscosity model and $A_s = 0.5$.

additional quantification of the large-scale property is introduced by

$$r_{LS} = \frac{\displaystyle\int_0^2 \sum_{|k_z|<k_z^c} |\check{\boldsymbol{u}}(y,k_z)|^2 \, dy}{\displaystyle\int_0^2 \sum_{k_z} |\check{\boldsymbol{u}}(y,k_z)|^2 \, dy}, \tag{5.24}$$

where $\check{\boldsymbol{u}}$ denotes the Fourier transform of the mode in z and k_z^c is a cutoff wavenumber that represents a higher limit for a Fourier mode to be considered large-scale. The value $k_z^c = 0.5$ was chosen after inspection of the DNS and it corresponds to a wavelength which is roughly 10 times greater than the wavelength of the streaks depending on Re. Analogously to the previous section, the quantity r_{LS} is the ratio of the eigenmode's energy at large wavelengths to the total eigenmode energy. It is used to color the eigenvalues in *e.g.* figure 5.23, where darker points correspond to eigenmodes with a pronounced large-scale character. Again, the qualitative difference between the quasi-laminar model and the eddy viscosity model is significant. For the eddy viscosity model the leading mode has a large-scale factor near 10%, to be compared with much weaker values for the quasi-laminar model.

The spatial structure of this interesting eigenmode for the eddy viscosity model is shown in figure 5.24 in the $y-z$ plane. The eigenmode is characterised by a small-scale modulation with the same spanwise periodicity as the base flow streaks, and by a large-scale modulation. In particular, the large-scale modulation of the wall-normal velocity component appears as an amplitude modulation. On the spanwise component, it appears as a large-scale flow. As for the streamwise component, the large-scale character is less clear, but the large-scale modulating feature is still clearly observed. These qualitative observations are confirmed by looking at the Fourier decomposition of the modes along z. The real part of each eigenmode component $\hat{u}_i(y,z)$ is decomposed in Fourier series. The wall-normal integrated squared modulus of the Fourier coefficients gives energies as a function of spanwise wavenumber $E_i(k_z)$, which are plotted in figure 5.25 for the three velocity components. The figure shows that the eigenmode can be seen as a superposition of waves. The first wave has a small wavenumber and gives the large-scale character of the eigenmode. We note that r_{LS} was designed to give the ratio of the energy of this large-scale component with respect to the total energy of the eigenmode. The other waves have wavelengths near $\lambda_{z,s}$ (dashed line in the figure) or smaller. Moreover, figure 5.25 shows that the large-scale wave is dominant in the spanwise velocity component. Lastly, we note that the large-scale spanwise wavenumber of this mode is $k_z \approx 0.36$. Given that $k_x = 0.18$ for this eigenmode, it means

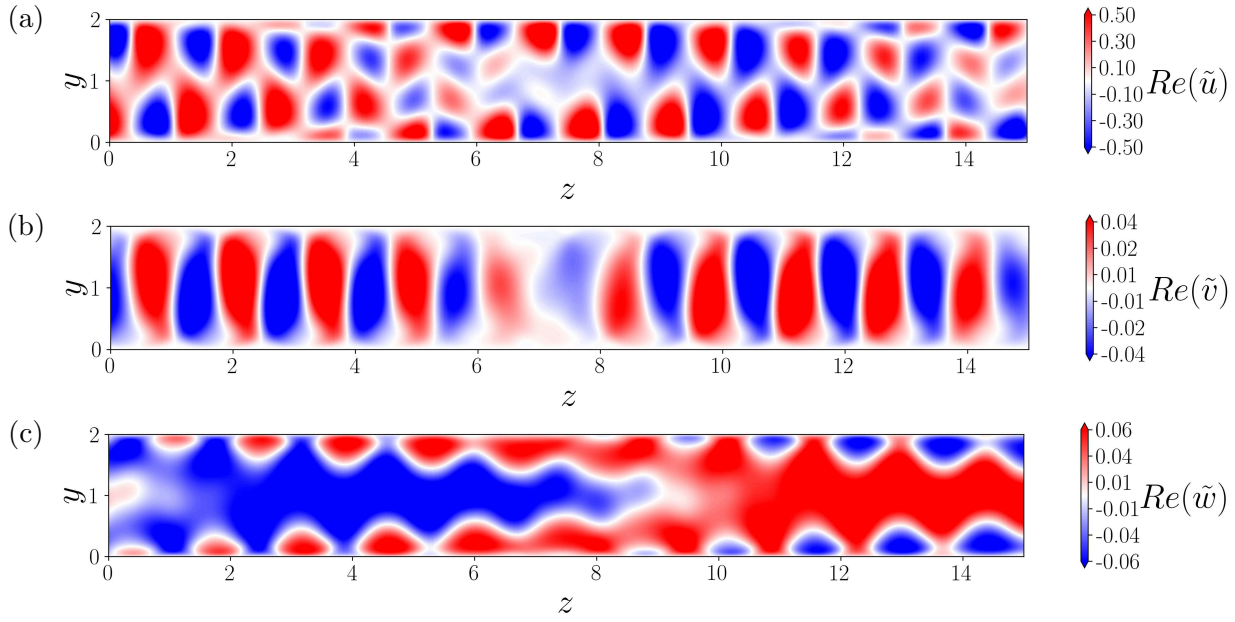

Figure 5.24: Leading eigenmode for the root of unity corresponding to $\gamma = 4/50$ for the eddy viscosity model with $Re_\tau = 71$, $k_x = 0.18$ and $A_s = 0.50$. The modes are normalised to $\max_{y,z}|Re(\tilde{u})| = 1$. Real part of (a) streamwise velocity component, (b) wall-normal velocity component and (c) spanwise velocity component.

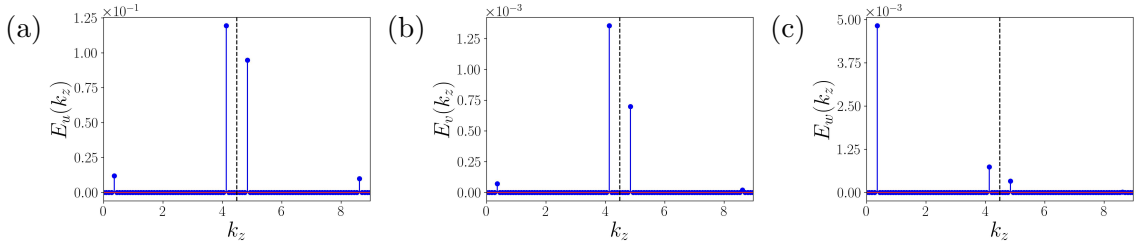

Figure 5.25: Spanwise Fourier decomposition of the leading eigenmode for the same parameters as Fig. 5.24. The figure shows the wall-normal integrated squared Fourier coefficient of the real part of the (a) streamwise, (b) wall-normal and (c) spanwise velocity components. The black dashed line denotes the wavenumber of the base flow $2\pi/\lambda_{z,s}$.

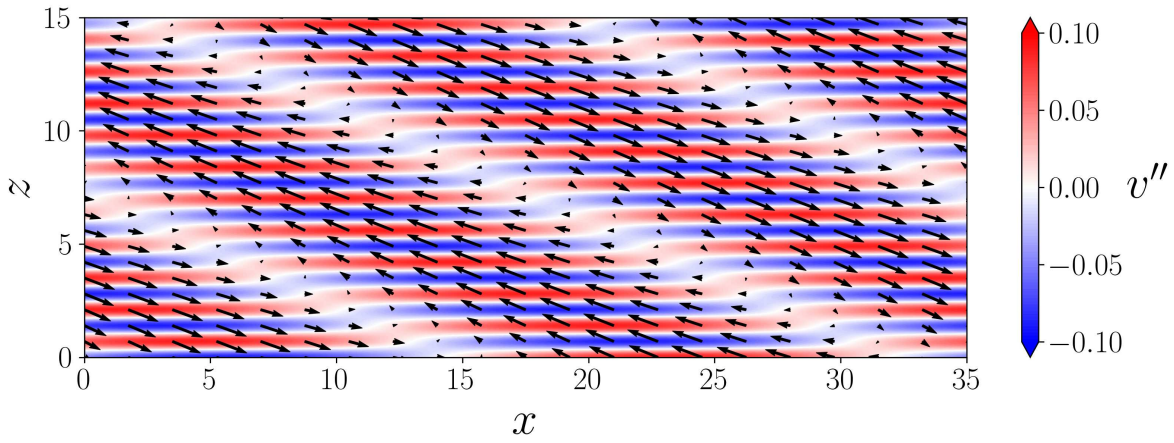

Figure 5.26: Leading eigenmode (real part of the full *ansatz*) for the same parameters as Fig. 5.24. Wall-normal velocity component (shaded contours) at midplane and wall-parallel large-scale flow (black arrows) in the $x-z$ plane. The large-scale flow is obtained by integrating the wall-parallel velocity components in the wall-normal direction.

that the modulation forms an angle of $\tan^{-1}(k_x/k_z) \approx 26.6^\circ$ with respect to the streamwise direction. This angle is not far from the 23° reported by Kashyap et al. (2022) and the 22.5° found by Benavides and Barkley (2025).

The above analysis is consistent with DNS observations interpreted as an amplitude modulation of the small scales together with a wall-parallel large-scale flow. This ideal picture is confirmed by figure 5.26, which shows the eigenmode integrated along the wall-normal direction y in the horizontal plane $x-z$. The arrows portray the streamwise and spanwise velocity components forming the large-scale flow. The displayed velocity field is fully consistent with most observations in the patterning regime (Duguet and Schlatter, 2013; Tuckerman et al., 2014). Similar observations also apply to other unstable eigenmodes that belong to the branch and are detuned. There are also unstable modes which do not show any large-scale modulation, related to classical sinuous/varicose streaks instabilities which are involved in the self-sustaining cycle (Hamilton et al., 1995; Waleffe, 1997). Their presence is expected from the classical literature on streak instabilities, and they are hence not the focus of this work.

When the streamwise wavenumber is fixed to a value consistent with the value from Kashyap et al. (2022), namely $k_x = 0.18$, the eddy viscosity model gives a group of eigenmodes characterised by a large-scale modulation that becomes unstable as the Re_τ is lowered. It is now necessary to assess which streamwise wavenumber is selected by the system. Figure 5.27 shows the dependence of the leading growth rate on the streamwise wavenumber for several values of A_s and for all Re under consideration. For low A_s, the growth rate monotonically decreases with k_x both for the quasi-laminar model and for the eddy viscosity model. The same behaviour was reported in Kashyap et al. (2024) for the stability analysis of the mean flow, *i.e.* the case $A_s = 0$. As the streak amplitude is increased, the growth rate is maximal for a non-zero streamwise wavenumber. For the quasi-laminar model, the maximum is unique and the curves for the different Re_τ overlap. Moreover, the maximum occurs for $k_x \approx 1$, which implies $\lambda_x \approx 3-6$. These wavelengths are too short to be representative of the large-scale patterns

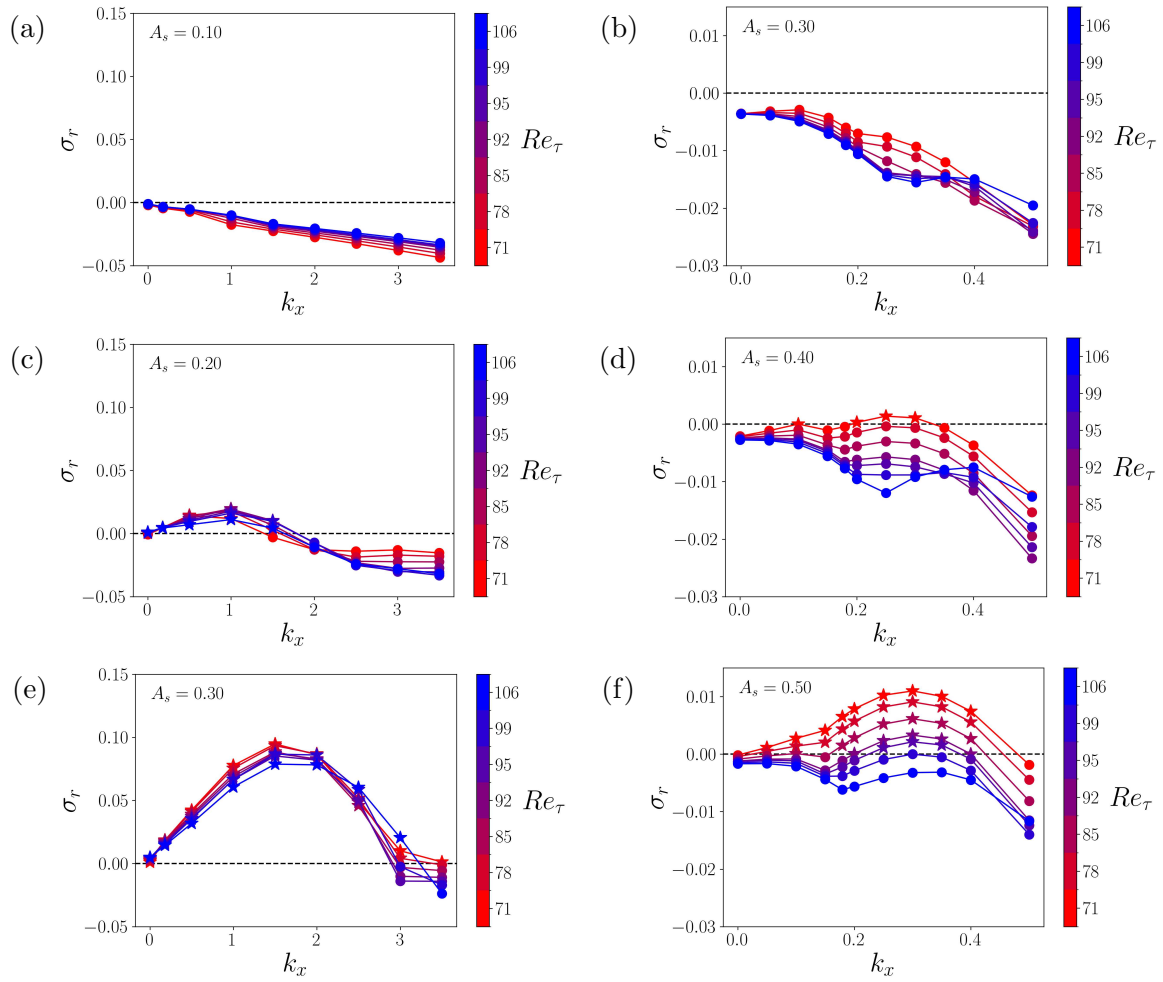

Figure 5.27: Variation of the leading growth rate σ_r with Re and streamwise wavenumber k_x (• for stable modes, ⋆ for unstable modes). (a,c,e) Quasi-laminar model; (b,d,f) eddy viscosity model. Note the different scale in k_x between left and right panels. Streak amplitudes A_s increase from top to bottom and are (a) 0.10, (c) 0.20 and (e) 0.30 for the no-closure cases and (b) 0.30, (d) 0.40 and (f) 0.50 for the cases with eddy viscosity.

of interest. Instead, with the eddy viscosity model, the instability is limited to $k_x \approx \mathcal{O}(0.1)$, *i.e.* $\lambda_x \approx 30 - 40$, which is consistent with expectations. In conclusion, only when incoherent fluctuations are taken into account does stability analysis select a relevant large-scale streamwise wavenumber.

5.5.5 Critical Amplitude and Wavelengths

This subsection is devoted to a deeper analysis of the eddy viscosity model at critical conditions. The critical parameters are defined as the parameters for which the leading mode has zero growth rate. Usually in linear stability studies, as in Kashyap et al. (2022), a critical Re and critical wavenumbers are reported. In our model, we have a degree of freedom given by the streak amplitude. One can either define a critical Re for a given A_s (note that the critical Re is defined only for sufficiently

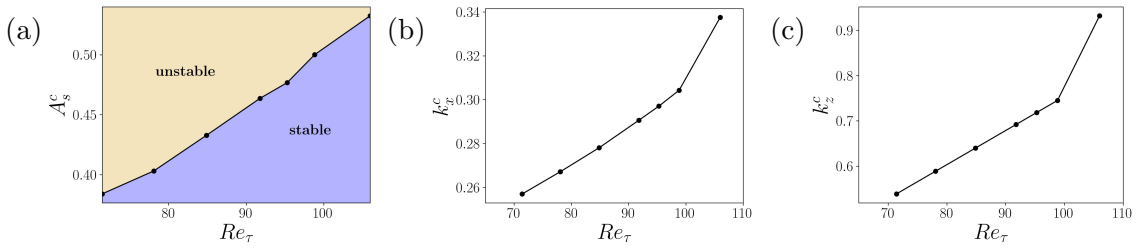

Figure 5.28: Critical A_s, k_x and large-scale k_z as a function of Re_τ for the eddy viscosity model.

high A_s, figure 5.22 (b)) or define a critical A_s for each Re, so that a neutral curve $Re - A_s$ can be computed. For each point on this neutral curve, there is a critical eigenmode with a streamwise wavenumber k_x^c. Moreover, a critical spanwise wavenumber k_z^c can also be defined since the eigenmodes are characterised by one single large-scale wavelength (see figure 5.25).

The neutral curve is computed for the considered value of Re_τ by coupling a line search algorithm in k_x with a bisection algorithm for A_s. In the inner loop, we look for the k_x giving the maximum growth rate for a given A_s. Then, A_s is bisected until the absolute value of the maximum growth rate falls below a tolerance of 10^{-5}. The result is presented in figure 5.28 (a). It can be seen that the critical amplitude grows almost linearly with Re. This means that for fixed A_s the instability is obtained by decreasing Re, as explained in Subsection 5.5.3 and consistently with Kashyap et al. (2022). The neutral curve has not been computed for the quasi-laminar model since the results presented in figure 5.22 already suggest that the critical amplitude is independent of Re in the considered range.

Panels (b) and (c) of figure 5.28 show the critical wavenumbers. They increase with Re, indicating that the instability tends towards smaller wavelengths at high Re. This is also consistent with DNS observations (Kashyap et al., 2020). At $Re_\tau = 95$, we obtain $k_x^c \approx 0.3$ and $k_z^c \approx 0.71$, which are slightly greater than the $k_x^c \approx 0.18$ and $k_z^c \approx 0.42$ of Kashyap et al. (2022). However, the ratio between the wavenumbers, hence the angle of the eigenmode with the streamwise direction, is approximately the same ($\approx 23^\circ$). We report that our critical angle slowly decreases with Re from 25.5° at $Re_\tau = 71$ to 20.0° at $Re_\tau = 106$ (not shown).

5.6 Energy budget analysis

To physically interpret the results of the stability analysis of the streaky base flow, an equation equivalent to the Reynolds-Orr equation for the most unstable eigenvector is derived in this section (Schoppa and Hussain, 2002; Schmid and Henningson, 2012; Albensoeder et al., 2001; Alizard, 2015). For a simpler derivation, the index notation is used. We recall that x_1, x_2 and x_3 correspond, respectively, to x, y and z and u_1, u_2 and u_3 to u, v and w. Summation over repeated indices is implicit, and i takes the values 1, 2 and 3, whereas j takes only the values 2 and 3. Moreover, in this section, an asterisk denotes the complex conjugate (and not a dimensional quantity as in the rest of the thesis).

5.6.1 Derivation

By taking the scalar product of $\tilde{\boldsymbol{u}}^*$ with the momentum equation in (5.22), one obtains the following scalar equation

$$\begin{aligned}\sigma\tilde{u}_i^*\tilde{u}_i = &-\iota k_x U\tilde{u}_i^*\tilde{u}_i - U_j\tilde{u}_i^*\frac{\partial\tilde{u}_i}{\partial x_j} - \tilde{u}_i^*\tilde{u}_j\frac{\partial U_i}{\partial x_j} - \iota k_x\tilde{u}^*\tilde{p} - \tilde{u}_j^*\frac{\partial\tilde{p}}{\partial x_j} - k_x^2\left(\frac{1}{Re}+\nu_t\right)\tilde{u}_i^*\tilde{u}_i \\ &+\left(\frac{1}{Re}+\nu_t\right)\tilde{u}_i^*\frac{\partial^2\tilde{u}_i}{\partial x_j\partial x_j} + \tilde{u}_i^*\frac{d\nu_t}{dy}\frac{\partial\tilde{u}_i}{\partial y} + \iota k_x\tilde{u}^*\tilde{v}\frac{d\nu_t}{dy} + \tilde{u}_j^*\frac{d\nu_t}{dy}\frac{\partial\tilde{v}}{\partial x_j}.\end{aligned} \tag{5.25}$$

Moreover, the following identities are considered:

$$-\iota k_x\tilde{u}^*\tilde{p} - \tilde{u}_j^*\frac{\partial\tilde{p}}{\partial x_j} = -\frac{\partial}{\partial x_j}\left(\tilde{u}_j^*\tilde{p}\right) \qquad \text{(using the continuity equation);} \tag{5.26}$$

$$\frac{1}{Re}\tilde{u}_i^*\frac{\partial^2\tilde{u}_i}{\partial x_j\partial x_j} = \frac{1}{Re}\frac{\partial}{\partial x_j}\left(\tilde{u}_i^*\frac{\partial\tilde{u}_i}{\partial x_j}\right) - \frac{1}{Re}\frac{\partial\tilde{u}_i^*}{\partial x_j}\frac{\partial\tilde{u}_i}{\partial x_j}; \tag{5.27}$$

$$\nu_t\tilde{u}_i^*\frac{\partial^2\tilde{u}_i}{\partial x_j\partial x_j} = \frac{\partial}{\partial x_j}\left(\nu_t\tilde{u}_i^*\frac{\partial\tilde{u}_i}{\partial x_j}\right) - \nu_t\frac{\partial\tilde{u}_i^*}{\partial x_j}\frac{\partial\tilde{u}_i}{\partial x_j} - \tilde{u}_i^*\frac{d\nu_t}{dy}\frac{\partial\tilde{u}_i}{\partial y}. \tag{5.28}$$

Substituting the above identities in equation (5.25), then integrating on the secondary-stability $y-z$ domain (Ω) and normalizing the eigenmode such that $\int_\Omega \tilde{u}_i^*\tilde{u}_i\, d\Omega = 1$, a decomposition for the complex eigenvalue σ is obtained :

$$\sigma = T_a + \mathcal{P} - \mathcal{D} - \mathcal{D}^c + C, \tag{5.29}$$

where

$$T_a = \underbrace{-\iota k_x\int_\Omega U\tilde{u}_i^*\tilde{u}_i\, d\Omega}_{T_{a1}} \underbrace{-\int_\Omega U_j\tilde{u}_i^*\frac{\partial\tilde{u}_i}{\partial x_j}\, d\Omega}_{T_{a2}}; \tag{5.30}$$

$$\mathcal{P} = \underbrace{-\int_\Omega \tilde{u}^*\tilde{v}\frac{\partial U}{\partial y}\, d\Omega}_{\mathcal{P}_{uy}} \underbrace{-\int_\Omega \tilde{u}^*\tilde{w}\frac{\partial U}{\partial z}\, d\Omega}_{\mathcal{P}_{uz}} \underbrace{-\int_\Omega \tilde{v}^*\tilde{v}\frac{\partial V}{\partial y}\, d\Omega}_{\mathcal{P}_{vy}} \underbrace{-\int_\Omega \tilde{v}^*\tilde{w}\frac{\partial V}{\partial z}\, d\Omega}_{\mathcal{P}_{vz}} \tag{5.31}$$

$$\underbrace{-\int_\Omega \tilde{w}^*\tilde{v}\frac{\partial W}{\partial y}\, d\Omega}_{\mathcal{P}_{wy}} \underbrace{-\int_\Omega \tilde{w}^*\tilde{w}\frac{\partial W}{\partial z}\, d\Omega}_{\mathcal{P}_{wz}}; \tag{5.32}$$

$$\mathcal{D} = \frac{k_x^2}{Re}\int_\Omega \tilde{u}_i^*\tilde{u}_i\, d\Omega + \frac{1}{Re}\int_\Omega \frac{\partial\tilde{u}_i^*}{\partial x_j}\frac{\partial\tilde{u}_i}{\partial x_j}\, d\Omega; \tag{5.33}$$

$$\mathcal{D}^c = k_x^2\int_\Omega \nu_t\tilde{u}_i^*\tilde{u}_i\, d\Omega + \int_\Omega \nu_t\frac{\partial\tilde{u}_i^*}{\partial x_j}\frac{\partial\tilde{u}_i}{\partial x_j}\, d\Omega; \tag{5.34}$$

$$C = \underbrace{\iota k_x\int_\Omega \tilde{u}^*\tilde{v}\frac{d\nu_t}{dy}\, d\Omega}_{C_1} + \underbrace{\int_\Omega \frac{d\nu_t}{dy}\tilde{u}_j^*\frac{\partial\tilde{v}}{\partial x_j}\, d\Omega}_{C_2}. \tag{5.35}$$

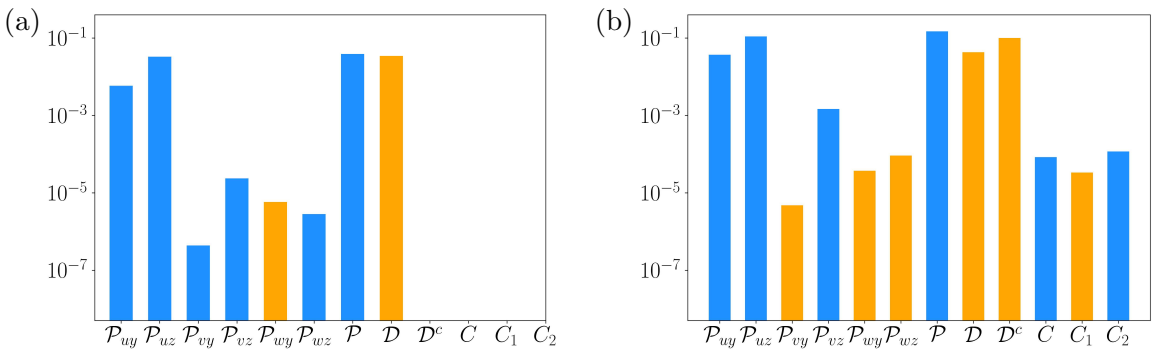

Figure 5.29: Energy budget for the leading eigenmode at $Re_\tau = 71$ and $k_x = 0.18$ for (a) the quasi-laminar model ($A_s = 0.2$) and (b) the eddy viscosity model ($A_s = 0.5$). Blue bars denote positive contributions to the growth rate, while orange bars denote negative contributions. For the meaning of the labels, see equations (5.29-5.35) in the text.

The equation (5.29) represents a Reynolds-Orr type energy budget for an eigenvector perturbation to the two-dimensional base flow, extended to the turbulent regime modelled by the turbulent eddy viscosity. We should note that the following terms integrate to zero because of the boundary conditions in y and z:

$$T_p = -\int_\Omega \frac{\partial}{\partial x_j}\left(\tilde{u}_j^* \tilde{p}\right)\, d\Omega \equiv 0; \tag{5.36}$$

$$T_d = \frac{1}{Re}\int_\Omega \frac{\partial}{\partial x_j}\left(\tilde{u}_i^* \frac{\partial \tilde{u}_i}{\partial x_j}\right)\, d\Omega \equiv 0; \tag{5.37}$$

$$T_d^c = \int_\Omega \frac{\partial}{\partial x_j}\left(\nu_t \tilde{u}_i^* \frac{\partial \tilde{u}_i}{\partial x_j}\right)\, d\Omega \equiv 0. \tag{5.38}$$

The relation (5.29) shows that the complex-valued eigenvalue σ associated with one given eigenmode results from several contributions: advective transport (T_a), production due to base flow gradients ($\mathcal{P}$), dissipation due to molecular viscosity ($\mathcal{D}$), dissipation due to eddy viscosity ($\mathcal{D}^c$) and production due to eddy viscosity gradients (C). Of course, the last two terms are present only when the eddy viscosity model is active. Some remarks need to be made about these quantities: (i) T_a is purely imaginary, hence it contributes to the angular frequency $Im(\sigma)$ but does not contribute to the growth rate $Re(\sigma)$ (as expected for a transport term); (ii) $\mathcal{D}$, $\mathcal{D}^c$ and C are purely real with $\mathcal{D} \geqslant 0$ and $\mathcal{D}^c \geqslant 0$ and thus contribute to the damping of the mode, whereas C generally contributes positively to the growth rate; (iii) $\mathcal{P}$ is complex but contributes mainly to the real part of the eigenvalue with a positive amount. The main contribution to the imaginary part of σ (hence to the phase velocity of the mode) comes from T_{a1}, *i.e.* from the mean flow advection.

The terms contributing to the real part of the eigenvalues (the modal growth rate) are analysed in more detail on specific examples. We focus on the parameter values $Re_\tau = 71$, $k_x = 0.18$, $A_s = 0.2$ for the quasi-laminar model and $A_s = 0.5$ for the eddy viscosity model. Figure 5.29 shows the various terms from equation (5.29) for the two cases. For the quasi-laminar case, the important terms are $\mathcal{P}_{uy}$, $\mathcal{P}_{uz}$ and $\mathcal{D}$. The remaining production terms are several orders of magnitude smaller. For the

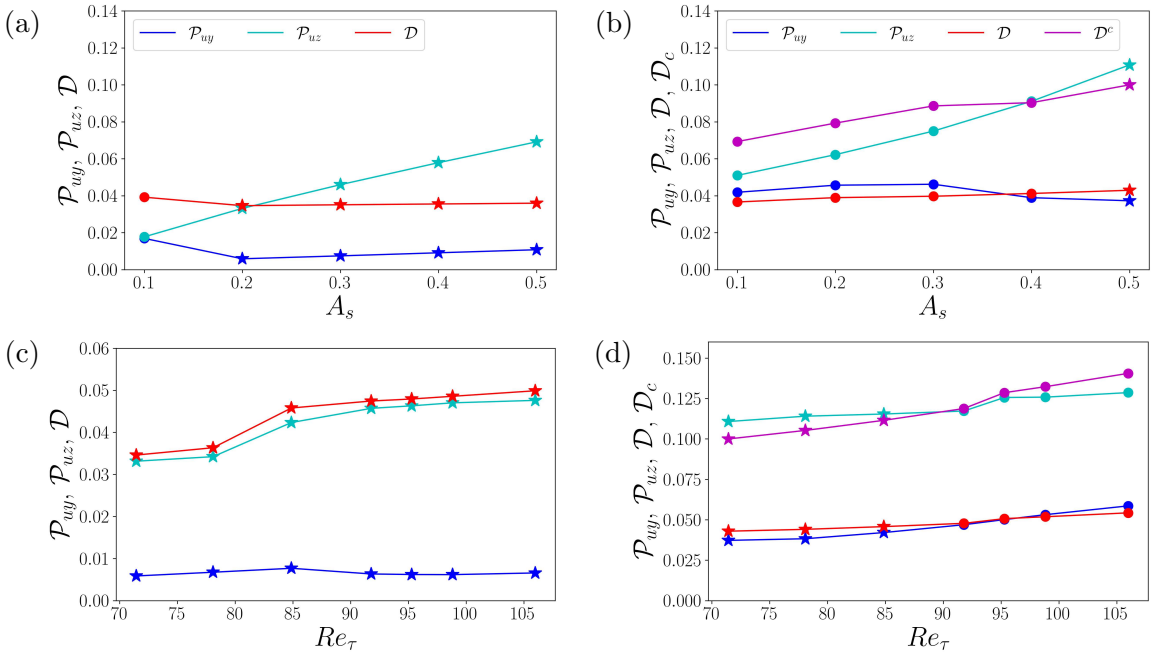

Figure 5.30: Energy the leading eigenmode for $k_x = 0.18$. (a,b) Variation with streak amplitude A_s for fixed $Re_\tau = 71$. (c,d) Variation with Re for fixed streak amplitude $A_s = 0.2$ in (c) and $A_s = 0.5$ in (d). (a,c) Quasi-laminar model; (b,d) eddy viscosity model. For the meaning of the labels, see equations (5.29-5.35) in the text.

eddy viscosity case, the eddy viscosity dissipation $\mathcal{D}^c$ is another important term. On the contrary, the production due to eddy viscosity gradients C appears as negligible. Nonetheless, this does not imply that the wall-normal variation of the eddy viscosity is not important. All the quantities plotted are integrals that involve the eigenmodes, and, in general, it can be expected that the wall-normal variation of ν_t contributes to the structure of the eigenmodes. It was verified by inspection that similar considerations apply to all the cases considered in the following analysis.

5.6.2 Results

Having identified the dominant terms, their dependence on the stability parameters is analysed in figure 5.30. Concerning the effect of A_s (panels (a) and (b)), for both models, the production term inducing instability is the one associated with spanwise gradients of the base flow, $\mathcal{P}_{uz}$. For the eddy viscosity model, a larger amplitude is needed to compensate for the dissipation due to the eddy viscosity.

The panels (c) and (d) in figure 5.30 illustrate why a critical Re is observed only within the eddy viscosity model. For the quasi-laminar model (panel (c)), production and dissipation follow essentially the same trend, resulting in a growth rate almost independent of Re_τ. Conversely, for the eddy viscosity model (panel (d)), the eddy viscosity dissipation increases faster than the production when the Re_τ is increased. Consequently, at some critical value of Re_τ, the eddy viscosity dissipation takes

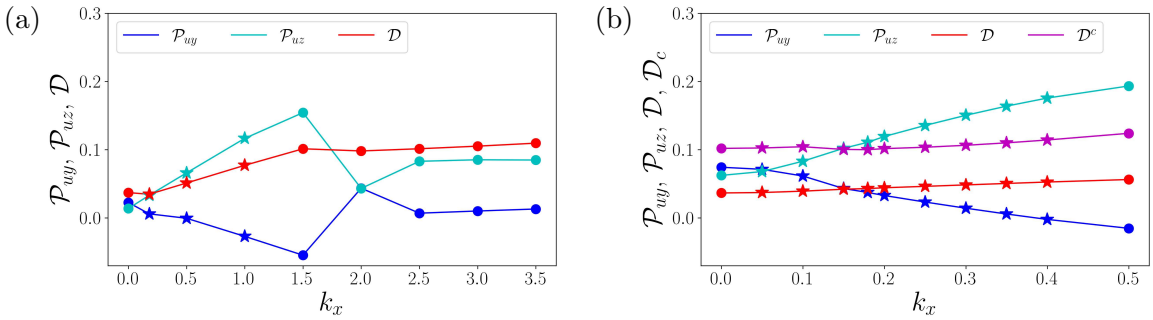

Figure 5.31: Energy budget for the leading eigenmode as k_x is varied. $Re_\tau = 71$. (a) Quasi-laminar model with $A_s = 0.2$; (b) eddy viscosity model with $A_s = 0.5$. Note the different scale of the abscissa in the two panels. For the meaning of the labels, see equations (5.29-5.35) in the text.

over the production and stabilises the eigenmode. This suggests a Re-dependence for the growth rates encoded in the Re-dependence of the eddy viscosity, an interesting result pointing at the role of the turbulent fluctuations in this instability.

The two panels of figure 5.31 illustrate how the energy budget changes with the streamwise wavenumber k_x. For both models $\mathcal{P}_{uy}$ and $\mathcal{P}_{uz}$ depart from each other, the former decreasing while the latter increases. For the quasi-laminar model in panel (a), this behaviour changes drastically beyond $k_x = 1.5$, indicating a change in the nature of the leading eigenmode. However, the main difference between the two models is again the presence of the eddy viscosity dissipation that stabilises the modes for $k_x > 0.4$.

In conclusion, the energy budget analysis shows that the inclusion of the eddy viscosity induces the observed parameter dependence mainly via the additional damping term $\mathcal{D}^c$.

5.7 Nonlinear simulation of the instability

Once the base flow forcing $\boldsymbol{g}$ is computed (see Section 5.4.2), the system (5.20) can be advanced in time starting from any initial condition. Nonlinear simulations of the modal instability are performed by adding the unstable mode rescaled with a small amplitude to the base flow. Such computations for several modes and system parameters have been performed using the channelflow code. The outcome of one of these simulations, performed in a domain of size $L_x \times L_y \times L_z = 175 \times 2 \times 70$, is illustrated in figures 5.32 and 5.33.

Figure 5.32 shows the evolution of the amplitudes of the base flow streaks and the secondary perturbation. Because the streaks are uniform in x and varying in z, the amplitude of the base flow streaks is monitored using the square root of the energy of $x-$uniform $z-$varying Fourier modes integrated in the wall-normal direction, namely

$$\overline{A}_s(t) = \sqrt{\int_0^2 \sum_{k_z=k_z^1}^{k_z^{\max}} |\hat{\boldsymbol{u}}(k_x = 0, y, k_z, t)|^2 \, dy}. \tag{5.39}$$

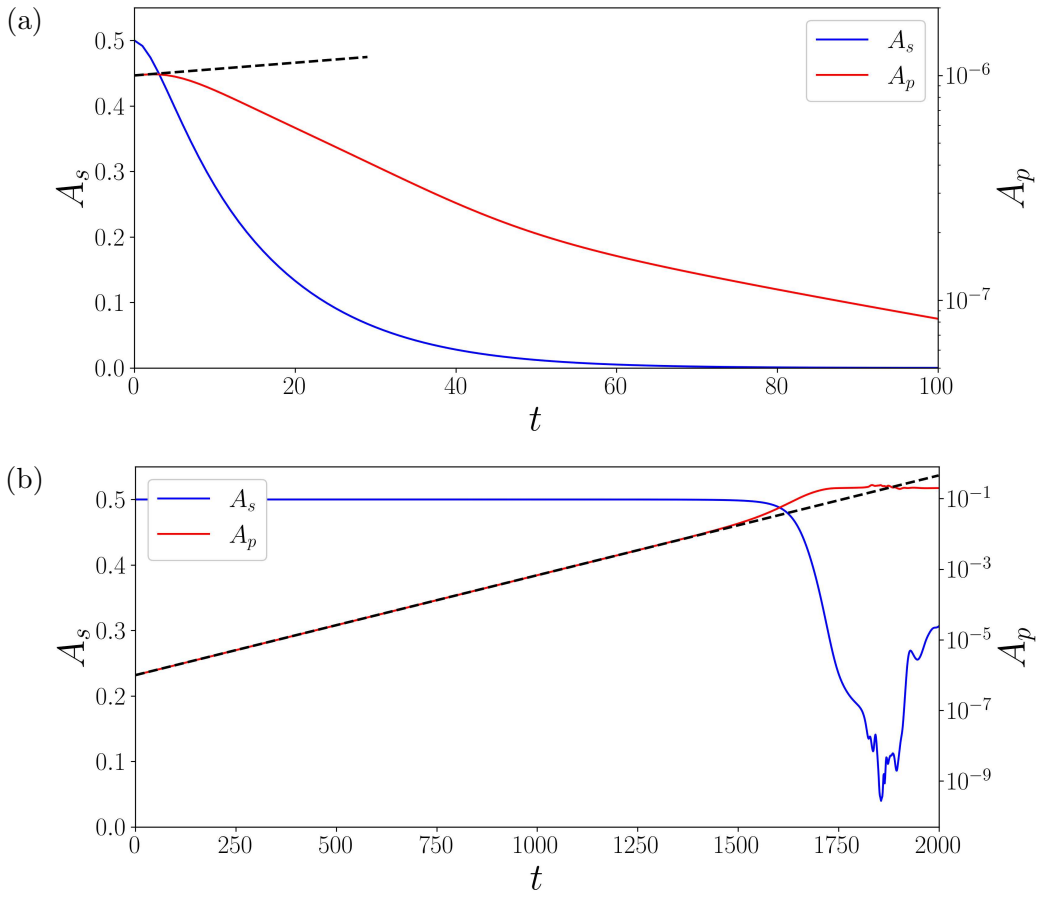

Figure 5.32: Temporal evolution of the streak amplitudes A_s and the secondary perturbation amplitude A_p in the nonlinear simulation of the instability without (a) and with (b) the forcing $\boldsymbol{g}$. The dashed black lines represent exponential growth as computed with LSA.

On the other hand, the amplitude of the secondary perturbation is defined as the square root of the energy of all the $x-$varying Fourier modes integrated in the wall-normal direction, namely

$$A_p(t) = \sqrt{\int_0^2 \sum_{k_x=k_x^1}^{k_x^{\max}} \sum_{k_z=k_z^1}^{k_z^{\max}} |\hat{\boldsymbol{u}}(k_x, y, k_z, t)|^2 \, dy}. \tag{5.40}$$

Here, k_x^1 and k_z^1 denote the first wavenumbers allowed by the computational domain and $k_x^{\max}$ and $k_x^{\max}$ the last wavenumbers allowed by the discretisation.
These definitions allow to partition the total flow energy into base flow energy and perturbation energy, even in a general nonlinear evolution of the instability. However, the definition of $\overline{A}_s$ is different from the definition of A_s given in (5.17). To be consistent with our previous definition, we define and plot in figure 5.32 $A_s(t) = \overline{A}_s(t)A_s/\overline{A}_s(0)$, such that $A_s(0) \equiv A_s$ as defined in the previous sections.

Panel (a) of the figure shows what happens to the streaks and the secondary perturbation when the forcing $\boldsymbol{g}$ in (5.20) is zeroed. The streaks are quickly damped by the (molecular and eddy)

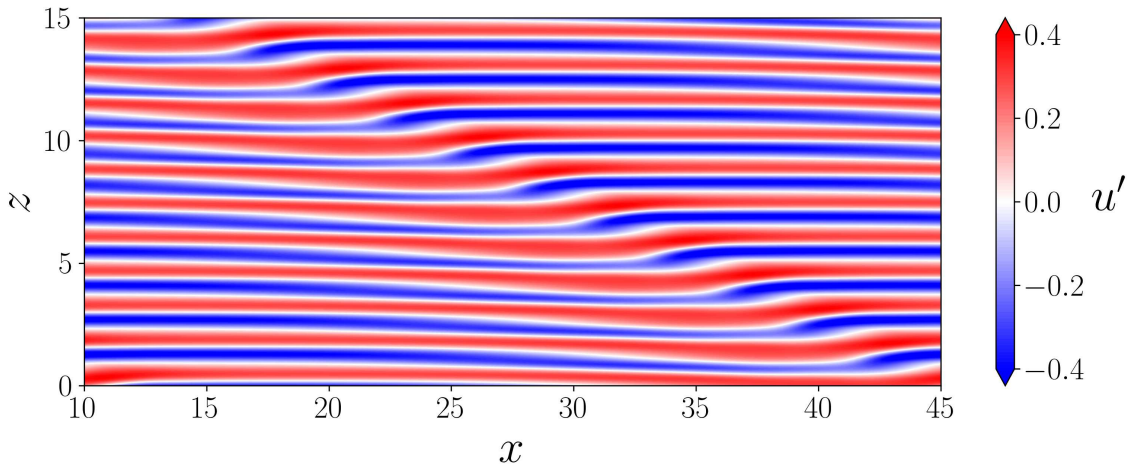

Figure 5.33: Contours of streamwise velocity fluctuations in the plane $y^+ \approx 35$ of the nonlinearly saturated streak instability at $Re_\tau = 71$. Eddy viscosity model with $k_x = 0.18$ and $A_s = 0.50$. Only a small portion of the computational domain ($L_x \times L_y \times L_z = 175 \times 2 \times 70$) is shown.

viscosity, and the instability does not have the time to grow. The modes are initially amplified with the predicted growth rate (dashed line), but they quickly start decaying with the streaks, similarly to the numerical experiments of Schoppa and Hussain (2002). Instead, when the forcing is active (panel (b)), it maintains the base flow steady, and the instability grows exponentially for several orders of magnitude. The growth rates measured from the simulations are always within a 5% relative error band with respect to those computed with the linear stability code. This error comes from the numerical discretisation of the equations. It is small if one considers that the growth rates are near zero and their sensitivity with respect to the parameters of the analysis is much higher.

There are three phases in the nonlinear simulation of the instability: modal growth, nonlinear saturation and fully nonlinear phase. The fully nonlinear phase gives a chaotically oscillating behaviour which is probably spurious: the assumptions involved in the model cease to be valid at this stage. Therefore, we do not present any analysis beyond the saturation phase.
An example of saturated large-scale instability is shown in figure 5.33. This figure shows the deviation from the mean flow of the streamwise velocity component. Therefore, it contains both the base flow streaks and the saturated mode. It can be seen that the instability results indeed in an oblique modulation of the streaks. This corresponds to the qualitative picture of wall-bounded turbulence modulations described in the introduction of the chapter.

5.8 Discussion

The streak field selected in the second part of this study corresponds to the most amplified structure by the mean shear, computed using resolvent analysis after linearising around the mean flow. An eigenvalue problem was formulated by linearising around a synthetic base flow, constructed with the mean flow, to which the optimal streaks have been added with a tunable amplitude. It was solved

numerically by allowing for detuned eigenmodes, *i.e.* spatially subharmonic modes whose wavelength is not a simple multiple of the spanwise wavelength of the streaks. Visual comparison between the most unstable large-scale eigenmode and the structure of laminar-turbulent patterns, as observed in numerical simulations, suggests that this instability is indeed relevant to the appearance of the pattern.

The starting hypothesis for this approach differs greatly from that of Liu and Gayme (2021), who have considered linearisation around the analytical laminar base flow solution. The streak instability considered here takes place in a turbulent environment whose effect needs to be modelled. In fact, this work shows that the turbulent fluctuations contribute to the sought instability in two ways. First, the coherent part of the fluctuations (the streaks) makes the flow unstable to various wavelengths. Secondly, the turbulent fluctuations, via the eddy viscosity term, damp high wavelengths, selecting specific large-scale modes, thereby introducing a cutoff in wavenumber. As a result of this competition, large-scale modes can be destabilised at low enough Re provided A_s is large enough. This result highlights the need to correctly model unresolved turbulent motions in linear studies of turbulence in agreement with other recent works (Illingworth et al., 2018; Morra et al., 2019; Symon et al., 2023). The present model is an improvement compared to the approach in Kashyap et al. (2024), which featured the eddy viscosity in the governing equations but not the streak mode in the base flow.

Another important assumption of the model is the high degree of symmetry of the optimal streaks obtained from resolvent analysis. By construction, the resolvent modes are harmonic in z and uniform in x. As a consequence of the harmonicity in z, they do not modify the mean flow. In particular, the typical 100 wall units spacing of the streaks was chosen as the spanwise wavelength for the resolvent analysis. However, if the maximum amplification factor (cf. (5.16))

$$R_{max}(k_x, k_z) = \max_{\omega} R(k_x, k_z, \omega), \tag{5.41}$$

is considered as a function of $\lambda_z = 2\pi/k_z$ for $k_x = 0$, then the maximum amplification does not correspond to $\lambda_z^+ = 100$ (see figure 5.34 (a)). Indeed, the curve is characterised by only one peak whose wavelength scales in outer rather than inner units. In contrast, at higher Re_τ, there are two peaks, one of which scales in wall units and corresponds to $\lambda_z^+ \approx 100$ (see the results of Hwang and Cossu (2010a), reproduced successfully in Section 2.7.3). As Re_τ is decreased, the peak in wall units disappears, and the curve displays only one peak, which does not match 100 wall units. This behaviour was also documented in other studies of optimal harmonic forcing at relatively low Re (Hwang and Cossu, 2010b; Willis et al., 2010; Pujals et al., 2010). One possible explanation is the strong hypothesis $k_x = 0$. Streaks are elongated in the streamwise direction, hence $k_x = 0$ is a decent first approximation. Streaks in turbulent flow, however, are characterised by a distribution of (finite) streamwise wavelengths which, according to several observations, is centred around $\lambda_x^+ \approx 1000$ wall units (Smits et al., 2011). Figure 5.34 (b) shows that, when the optimal amplification factor curves are shown for $k_x^+ = 2\pi/1000$, the peak at $\lambda_z^+ = 100$ is recovered. For the purpose of this work, this implies that the choice of a finite streamwise wavelength for the streaks would be more relevant. Moreover, the value of 100 inner units represents in real flows only the mean spanwise wavelength (Kline et al., 1967). An alternative would be the generalisation to a three-dimensional base flow featuring three-dimensional streaks. Such a choice is technically possible. However, it would make the stability computations more expensive and would require different numerical methods. It is therefore

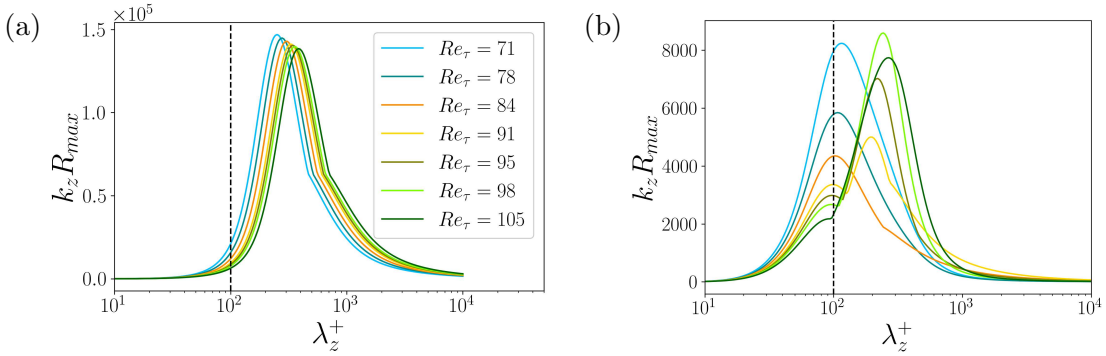

Figure 5.34: Maximum energy amplification factor as a function of the spanwise wavelength of the forcing (in wall units, λ_z^+) for streamwise wavenumber (a) $k_x = 0$ and (b) $k_x^+ = 2\pi/1000$.

outside the scope of the present work.

The values of the critical amplitude reported earlier deserve a discussion in connection with the streak amplitude found either in the literature on streak instability or in DNSs of turbulent flows. The analysis of the energy budgets in Section 5.6 shows that the desired Reynolds dependence is induced by the presence of an eddy viscosity dissipation. However, the eddy viscosity dissipation also implies an increase in the critical amplitude of the instability. This fact was already observed by Alizard (2015), who compared his critical amplitudes to those of Schoppa and Hussain (2002), after conversion of his values to the strength factor introduced by the latter. Alizard (2015) found significantly greater critical strength factors with respect to those from Schoppa and Hussain (2002) and attributed this difference to his choice of eddy viscosity. Despite the very different Re values, we can directly compare our critical values to those of Alizard (2015) since we use the same definition of streak amplitude. We find critical amplitudes that are correspondingly larger (≈ 0.40 *versus* ≈ 0.18). Conversely, in Chapter 4, where we considered Re values similar to Alizard (2015), we found similar critical amplitudes.

Therefore, we further investigate streak amplitudes at low Re using DNS data. DNS in moderate-size periodic domains ($L_x \times L_y \times L_z = 35 \times 2 \times 15$) have been performed, and the following quantities are introduced:

$$A_{s,xav} = \frac{\max_{y,z} \langle u' \rangle_x - \min_{y,z} \langle u' \rangle_x}{2\overline{U}_c}, \tag{5.42}$$

$$A_{s,xmax} = \max_x \frac{\max_{y,z} u' - \min_{y,z} u'}{2\overline{U}_c}, \tag{5.43}$$

where u' is the streamwise velocity fluctuation, $\langle \cdot \rangle_x$ denotes the streamwise average and $\overline{U}_c$ is the centreline velocity of the turbulent mean profile.
$A_{s,xav}$ measures the amplitude of streamwise-uniform streaks whereas $A_{s,xmax}$ measures the maximum local amplitude of generic streaks. The smoothing effect of the streamwise average implies $A_{s,xav} < A_{s,xmax}$. The distribution of $50,000$ temporal samples of these quantities is shown in figure 5.35 for two Re. $A_{s,xav}$ takes values between 0.10 and 0.30 whereas $A_{s,xmax}$ takes values between 0.35 and 0.50. We conclude that, for the streamwise-uniform streaks of our base flow, a critical amplitude of

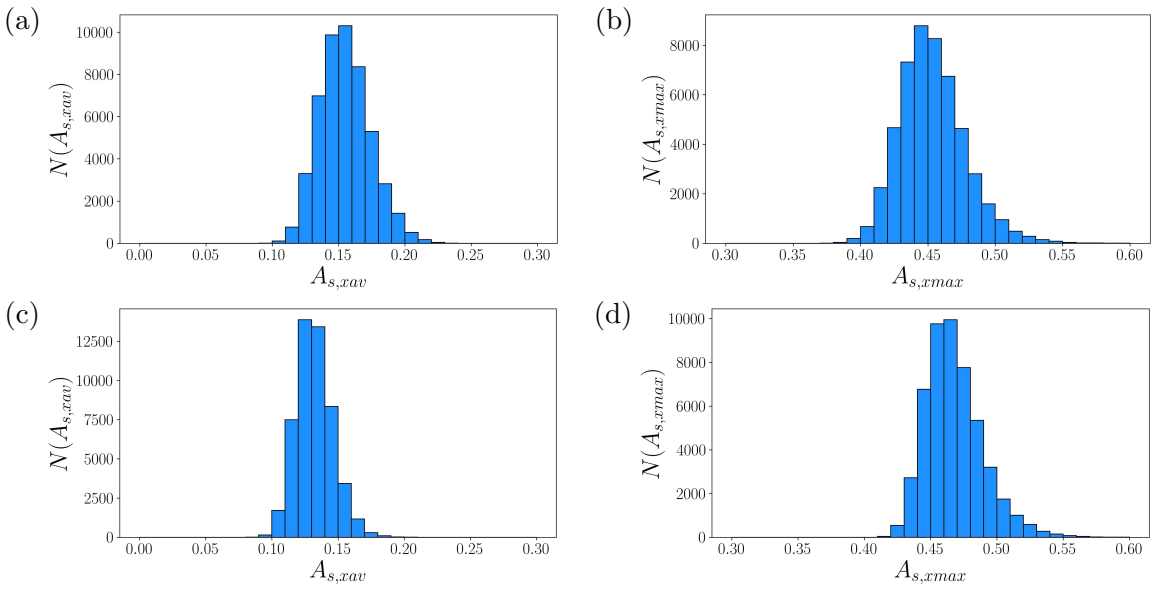

Figure 5.35: Histograms of streak amplitudes measured from DNS in a domain of size $L_x \times L_y \times L_z = 35 \times 2 \times 15$ for (a,b) $Re_\tau = 71$ and (c,d) $Re_\tau = 106$. (a,c) Amplitudes from streamwise averaged fields (5.42); (b,d) streamwise maximum amplitudes of non-averaged velocity fields (5.43).

0.4 is too high on average. We do not exclude that such an amplitude could be reached locally within a turbulent flow, thereby making a connection with *extreme events* (Hack and Schmidt, 2021; Ciola et al., 2023). The need for large A_s may be a consequence of the various approximations made in the construction of the base flow, notably its over-symmetrisation. It is not excluded that, if the base flow streaks were three-dimensional or characterised by more than one spanwise wavelength, the critical amplitude would decrease, yet this remains to be verified.

The leading resolvent modes have energy predominantly in the streamwise velocity component and almost no energy in the transverse components (Hwang and Cossu, 2010a). However, in actual turbulent flows, the velocity field possesses three genuine components, at least because, in the SSP picture, streamwise streaks are accompanied by streamwise vortices. To analyse the influence of this three-dimensionality on critical thresholds, a numerical experiment was performed (using the eddy viscosity model) by augmenting the amplitude of transverse components of the vector field $\boldsymbol{u}_s$ while A_s was kept constant. This is easily implemented since the streamwise invariance of the field $\boldsymbol{u}_s$ implies that streamwise and transverse components are decoupled in the continuity equation. Therefore, if, after the rescaling of $\boldsymbol{u}_s$, v_s and w_s are multiplied by a factor B_{vw}, the resulting velocity field is still divergence-free. The dependence of the leading growth rate on Re_τ is shown in figure 5.36(a) for different values $B_{vw} \geqslant 1$. When B_{vw} is large enough, a critical Reynolds number appears exactly as in figure 5.22(b). Thus, with a slightly modified base flow, the right Re-dependence of the growth rates can also be retrieved for $A_s = 0.2$, which is comparable with other streak instabilities' critical amplitudes (Park et al., 2011; Alizard, 2015; Ciola et al., 2024). Importantly, the augmented amplitudes of the transverse components are of the order of the mean amplitudes of the transverse fluctuations observed in DNS. Therefore, the modified base flow does not contain any extreme fluctuations in con-

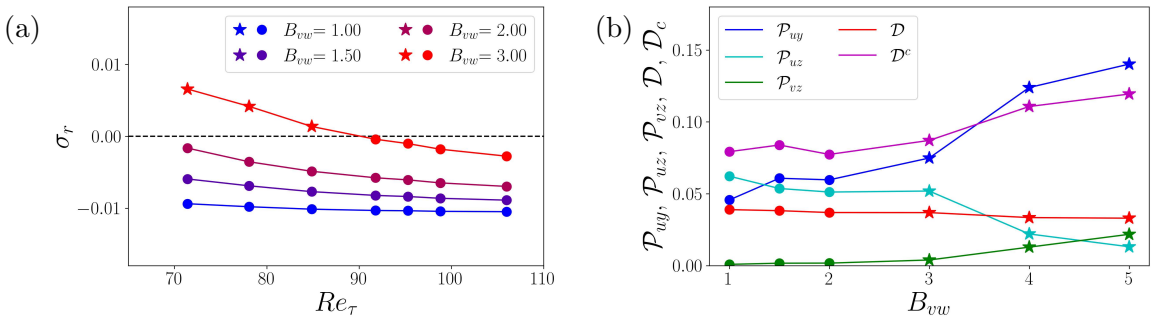

Figure 5.36: Effect of increasing the transverse components amplitude in the base flow. (a): Leading growth rate as a function of Re for $k_x = 0.18$. A_s is kept constant at 0.2 but the transverse velocity components of the base flow V and W are multiplied by a factor B_{vw}. (b): Variation of the energy budgets with the prefactor B_{vw} ($A_s = 0.2$, $Re_\tau = 71$, $k_x = 0.18$). For the meaning of the labels, see equations (5.29-5.35).

trast to the previous base flow with $A_s = 0.5$. The energy budgets obtained using the new base flow (figure 5.36 (b)) show similar dissipation trends with respect to those in figure 5.30(b) but different trends on the production contributions, with the production term $\mathcal{P}_{vz}$ playing a non-negligible role for large B_{vw}. This numerical experiment shows that certain quantitative aspects of the stability analysis depend on explicit choices in the modelling of the base flow. By contrast, the results highlighted in the previous sections are qualitatively robust to small modifications of the base flow.

The analysis of the production terms also shows that in order to have the instability and the correct Reynolds dependence, one needs strong spanwise gradients (given by strong streak amplitudes) and/or strong vortices in the base flow. Both the spanwise gradients and the vortices are filtered by the streamwise-temporal average considered in Section 5.3. This may explain why we did not obtain the correct results with the finite-time average approach.

Notwithstanding the approximations made, the results of the eddy viscosity model support the initial expectation of this work, namely that large-scale structures can emerge out of the instability of a base flow featuring smaller-scale structures. This idea is illustrated in figure 5.37, which shows the time-averaged pre-multiplied energy spectrum of the streamwise velocity component, integrated along the wall-normal direction and obtained from a DNS at $Re_\tau = 71$ in a large domain with $L_x \times L_z = 250 \times 125$. The flow for Re below critical is characterised by two scales: the streaks and the modulations. There is no marked scale separation between the two, but the two peaks are well discernible in figure 5.37. The peak corresponding to the streaks is centred around the spanwise wavelength $\lambda^+_{z,s} = 100$. Streaks also have a characteristic streamwise wavelength, yet we have supposed $k_x = 0$ as a first approximation. The modulations are characterised by $k_x \approx 0.1$ and $k_z \approx 0.5$, consistently with previous DNS studies (Kashyap et al., 2020, 2022).
In figure 5.37, the wavelengths of the unstable modes obtained with the eddy viscosity model at $Re_\tau = 71$ are superimposed on the DNS spectrum, all unstable modes with $r_{LS} > 2\%$ being selected. The range $k_x \leqslant 0.5$ was considered, but unstable modes with $r_{LS} > 2\%$ were found only for $k_x \in [0.15, 0.4]$. The spanwise wavelength of the eigenmode was extracted using a spanwise Fourier transform. The unstable modes are found in a region of the spectrum close to where the large-scale

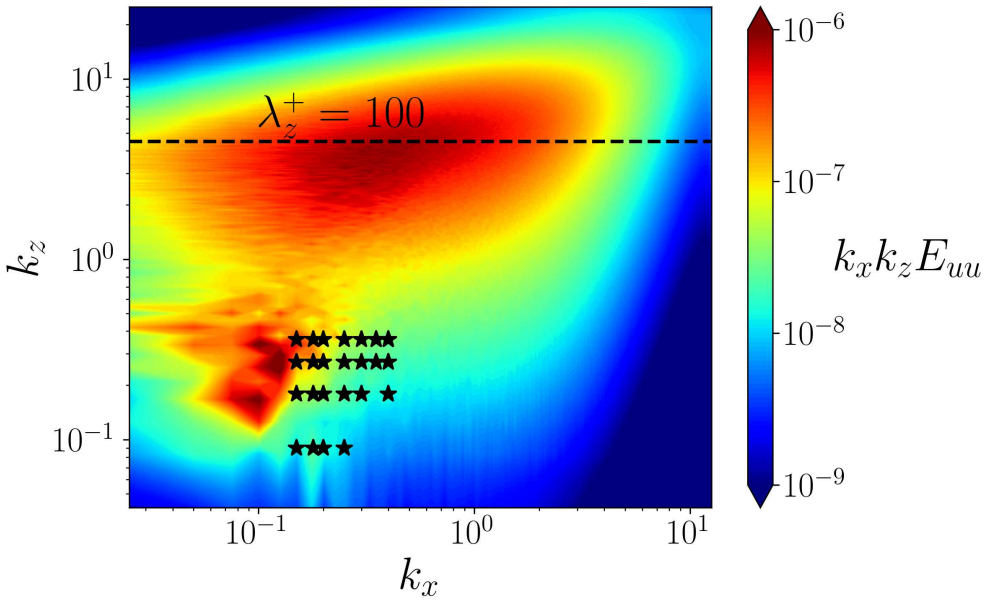

Figure 5.37: Wall-normal integrated pre-multiplied energy spectrum for the streamwise velocity component, time-averaged from DNS at $Re_\tau = 71$. The simulation domain is $L_x \times L_y \times L_z = 250 \times 2 \times 150$. Black line denotes the structures with spanwise wavelength $\lambda_z^+ = 100$ (as the base flow streaks considered in this work). Black stars denote the large-scale wavelengths of all the unstable modes obtained using the eddy viscosity model, $A_s = 0.5$, and having a large-scale energy ratio $r_{LS} \geqslant 2\%$ (see text for details).

turbulent modulations lie. Closer inspection reveals that they cover very well the spanwise wavenumber range of the modulations, but less accurately the streamwise wavenumber range. Note that by assumption, the base flow is invariant in x. Therefore, the unstable mode is monochromatic in x. As discussed above, this is a first approximation. The results may be improved if characteristic streamwise wavelengths of the streaks are taken into account in the base flow. This improvement is not straightforward from the computational point of view, but remains a stimulating perspective for future studies.

The present modelling effort is directed specifically at the analysis of the linear instability of the turbulent flow, in line with the studies of Kashyap et al. (2022, 2024). As such, the model is representative of the physics only in the incipient modulational regime, when the solution does not depart sensibly from the turbulent attractor. However, the link between the oblique structure shown in fig. 5.26 and the genuine laminar-turbulent patterns, although visually stimulating, is not trivial. Both the eigenmode and the base flow are three-dimensional vector fields, and the result of adding them together is not simple. In particular, active parts of the eigenmode can either tame the turbulence or reinvigorate it. In the next chapter, we will show that the introduction of an additional variable modelling local turbulence intensity makes it easier to interpret eigenmodes in this respect.

Fully developed laminar-turbulent patterns remain thus outside the scope of the present model. Indeed, laminar flow is not a solution of the nonlinear model equations (5.20). Therefore, nonlinear simulations of the instability following Eq. (5.20) are not expected to be physically relevant to laminar-

turbulent patterning, given that the flow would not have the possibility to develop the laminar holes observed in DNS (Kashyap et al., 2020).
Nonlinear simulations of (5.20) have been performed anyway (cf. Section 5.7) and they confirm this expectation: the oblique stripe saturates in amplitude, but no proper laminar hole can develop because the streaks are constantly forced everywhere in the domain. An improved model capturing the linear instability while allowing for both laminar and turbulent solutions is the subject of the next chapter. The recent efforts of Kashyap et al. (2024) and Benavides and Barkley (2025) are a useful starting point.

Chapter 6

Towards a Nonlinear Model of Laminar-Turbulent Pattern Formation

6.1 Introduction to the chapter

In the previous chapter, the emergence of turbulence modulations was modelled as a modal linear instability of a large array of streaks. It was argued that the considered streaky base flow is a better approximation of the turbulent flow on which the instability develops than the mean flow alone. However, the linear model of the previous chapter is relevant only for the linear phase of the instability, *i.e.* while the flow is still uniformly turbulent, for two reasons: (i) to have the streaks in the base flow, they need to be forced continuously in the flow; (ii) the eddy viscosity is uniform in the streamwise and spanwise directions implying that turbulence is uniform in these directions. To allow for the development of the instability in laminar-turbulent patterns, the turbulence model needs to be *turned off* in laminar regions. This is what happens in the very recent reduced models of laminar-turbulent patterns proposed by Benavides and Barkley (2025) and Kashyap et al. (2025). These two models have different structures but two common points: (i) there is a variable that quantifies the local turbulence intensity (q in Benavides and Barkley (2025) and W in Kashyap et al. (2025)) and (ii) when this quantity is uniformly zero, the laminar solution is obtained.

The main idea developed in this chapter is to include the above features in a nonlinear model of laminar-turbulent pattern formation. This may be done by looking at the eddy viscosity as a model variable that can be locally zero and can be modulated by the instability. Since there is an additional variable, at least an additional dynamical equation is required. Moreover, in order to let the laminar flow be a steady state solution of the model, the forcing used in the previous chapters to have a streaky steady state must be abandoned. Since it is difficult to find a model with both a streaky and a laminar steady state solution, the streaks themselves are left out of the new model, and the turbulent steady state will be just the mean profile. This choice may seem to contradict the conclusions of the previous chapter, but it does not. Indeed, in the previous chapter, the model was made up of the Navier-Stokes (NS) equations plus a *frozen* eddy viscosity term. Frozen means that the eddy viscosity does not depend on the flow variables and is unaffected by the instability. In this chapter, instead, we

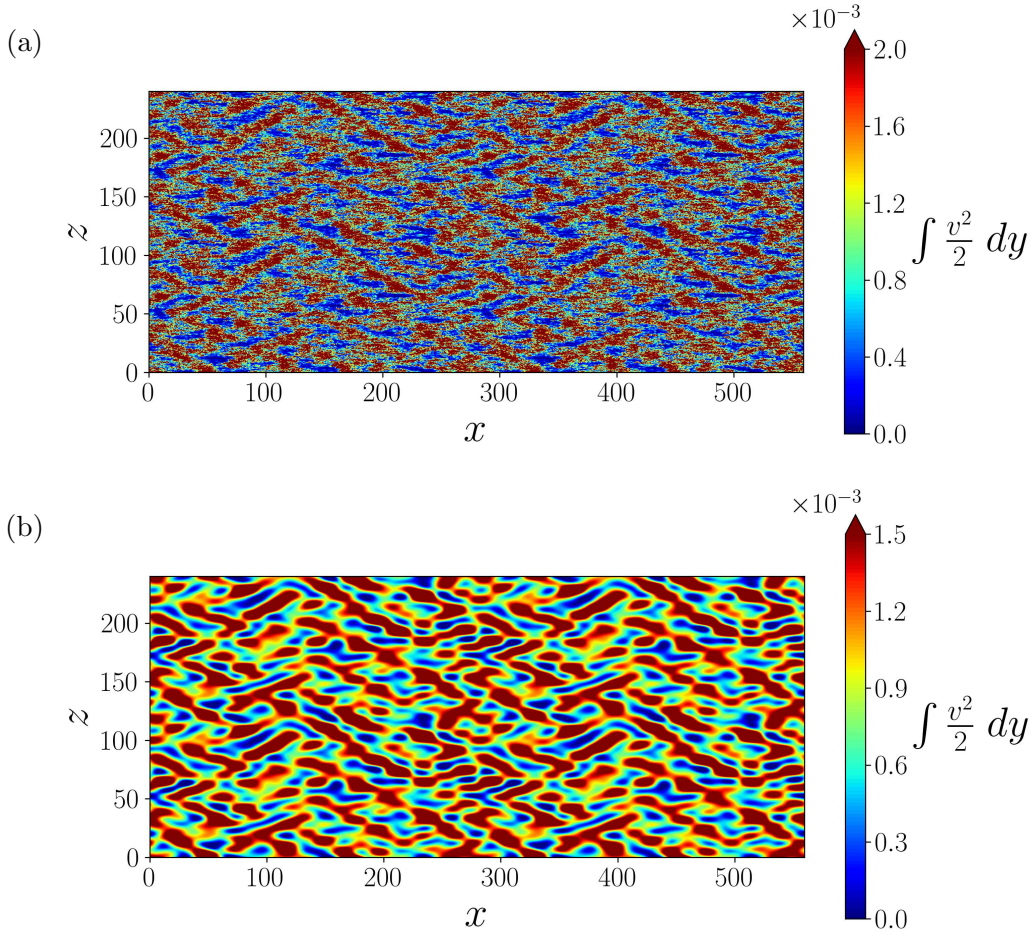

Figure 6.1: Contours of the wall-normal integrated wall-normal kinetic energy from a DNS at $Re_\tau = 71$ ($Re = 1000$). The raw field shown in (a) is filtered in (b) with the spectral filter introduced in (6.13) with $k_{x,c} = 0.2$, $\Delta k_x = 0.1$, $\Delta k_{z,c} = 0.5$ and $\Delta k_z = 0.2$. The DNS was performed in a domain of size $L_x \times L_z = 280 \times 120$ (in units of channel half-gap), and the resulting field was tiled twice in the streamwise and spanwise directions.

introduce a dynamic eddy viscosity governed by an additional equation. This equation may induce the instability even in the absence of streaks in the base flow. Indeed, our strategy will be to seek an additional equation that renders the system unstable at the wavelengths and Re values suggested by DNS observations. Therefore, the model discussed in this chapter is complementary to the model of Chapter 5.

Of course, the Navier-Stokes equations themselves are a nonlinear model of laminar-turbulent patterns, and the patterns can be simulated with DNS. However, this approach requires the accurate resolution of the turbulent motions. Figure 6.1 (a) shows an example of a laminar-turbulent pattern obtained with a DNS of the turbulent channel flow in a moderately large domain. In a DNS, the numerical grid has to be fine enough to resolve all the small-scale details that are visible in this figure, which makes the simulation in large domains quite expensive. In developing our nonlinear model,

we aim to simulate the laminar-turbulent patterns without resolving all the turbulent small scales. Therefore, the model output should resemble a filtered DNS field, as shown in figure 6.1 (b). If this intent is met, the model could be used to simulate laminar-turbulent patterns more easily with respect to DNS, as the necessary numerical resolution would be reduced.

In Section 6.2, a general formulation of the model is presented. This formulation includes some unclosed terms, notably a reaction function. In Section 6.3, a simple closure is tested by taking the reaction function from the Barkley (2011a) pipe flow model. It will be shown that the results of this model are encouraging in some respects but also evidence some limitations concerning the nonlinear development of the instability. In Section 6.4, a strategy to derive a reaction function from Direct Numerical Simulations (DNS) data is presented in two different versions, and the ensuing results are discussed. The work presented in this chapter has not reached a definitive conclusion yet. A short discussion of the current *state of affairs* is presented in Section 6.5.

6.2 General model formulation

As in the rest of the thesis, we consider the pressure-driven incompressible flow in a channel. Periodic boundary conditions are imposed in the streamwise (x or x_1) and spanwise (z or x_3) directions. No-slip conditions are imposed in the wall-normal direction (y or x_2). The periodic domain has dimensions $[L_x, L_y, L_z]$. Quantities without any superscript are made dimensionless with the channel half-gap h^* (such that $L_y = 2$ and $0 \leqslant y \leqslant 2$) and the bulk velocity $U_b^* = \int_0^2 \int_0^{L_z} u^* \; dydz/2L_z$ (outer units). The Reynolds number considered in this chapter is the one based on the bulk velocity $Re = U_b^* h^*/\nu^*$. Quantities with a $+$ superscript are made dimensionless with the viscous length $\delta_\nu^* = \nu^*/u_\tau^*$ and the friction velocity $u_\tau^* = \sqrt{\tau_w^*/\rho^*}$ (inner or wall units), where ρ^* is the fluid density, ν^* the kinematic viscosity and τ_w^* the measured mean wall shear stress. The streamwise, wall-normal and spanwise velocity components are denoted, respectively, by u, v and w or u_1, u_2 and u_3 when using index notation. We will assume that the channel is forced to keep a constant flow rate in the streamwise direction.

In the last chapter, we considered a model with an eddy viscosity term and a constant forcing (see equation 5.20). It was argued that the flow field $\boldsymbol{u}$ in (5.20) represents the coherent part of the dynamics containing the mean flow, the streaks and a (small-amplitude) modulation. In this chapter, we will continue to see $\boldsymbol{u}$ as a coherent part of the flow, but we will coarse-grain further and eliminate the streaks. Therefore, $\boldsymbol{u}$ contains only a uniform flow plus a large-scale modulation. We look for the model equations for $\boldsymbol{u}$ starting from the unforced equation (5.20):

$$\begin{cases} \dfrac{\partial \boldsymbol{u}}{\partial t} + \boldsymbol{u} \cdot \boldsymbol{\nabla} \boldsymbol{u} = -\boldsymbol{\nabla} p + \dfrac{1}{Re} \nabla^2 \boldsymbol{u} + \boldsymbol{\nabla} \cdot \left[\nu_t \left(\boldsymbol{\nabla} \boldsymbol{u} + (\boldsymbol{\nabla} \boldsymbol{u})^T \right) \right] + \boldsymbol{f}_b, \\ \boldsymbol{\nabla} \cdot \boldsymbol{u} = 0. \end{cases} \tag{6.1}$$

To have a laminar-turbulent pattern, the eddy viscosity must be zero in some regions and non-zero in other regions or, at least, be modulated such that there are regions of weaker turbulence. Therefore, the Cess (1958) eddy viscosity (5.8), used in the previous chapter, should be replaced by a

more general eddy viscosity which depends on all the space-time coordinates of the system, $\tilde{\nu}_t(\boldsymbol{x}, t)$, and is a variable in its own right. Since there is an additional variable, a further dynamical equation is required. Previous models (Barkley, 2011a; Manneville, 2012; Benavides and Barkley, 2025; Kashyap et al., 2025) suggest that an advection-reaction-diffusion equation can be assumed. This equation must model the spatio-temporal intermittent behaviour typical of laminar-turbulent patterns and the wall-normal structure of the flow (notably the mean profile). However, the formulation of the model can be simplified by decoupling the wall-normal dynamics from the wall-parallel intermittent behaviour related to the patterns. This approach is reminiscent of the shear-induced scalar dispersion theory proposed by Taylor (1953). Under appropriate assumptions, Taylor (1953) solved the passive scalar advection-diffusion problem in an axisymmetric pipe by decoupling the diffusion in the radial direction from the advection-diffusion in the streamwise direction. In a similar spirit, we assume the following separation of variables:

$$\tilde{\nu}_t(x, y, z, t) = q(x, z, t)\nu_t(y). \tag{6.2}$$

This assumption is convenient because the Cess (1958) formula (5.8) or a profile computed from data can be used for $\nu_t(y)$. This is useful to encode in the model a steady state that approximates the turbulent mean profile. The variable $q(x, z, t)$ can be interpreted as a local turbulence intensity and will characterise the spatio-temporally intermittent behaviour of the patterns. It can take any positive value, but for the purposes of the model, it should vary mostly between 0 and 1. Thereby, the problem of finding a dynamical equation for $\tilde{\nu}_t(\boldsymbol{x}, t)$, a three-dimensional field, reduces to finding an equation for $q(x, z, t)$, a two-dimensional field.

As anticipated, we consider an advection-reaction-diffusion for q:

$$\frac{\partial q}{\partial t} + \widetilde{u}\frac{\partial q}{\partial x} + \widetilde{w}\frac{\partial q}{\partial z} = R\left(q, \breve{u}\right) + \frac{D}{Re}\left(\frac{\partial^2}{\partial x^2} + \frac{\partial^2}{\partial z^2}\right) q, \tag{6.3}$$

where D is a diffusion coefficient, $\widetilde{u}$ and $\widetilde{w}$ are the advection velocities of the variable q, $R\left(q, \breve{u}\right)$ is the reaction function, and $\breve{u}$ is a scalar reaction variable related to the velocity field. This form of the reaction function relies on a strong simplification, since, in principle, R could depend on the whole velocity field. This form is inspired by the pipe flow model of Barkley (2011a) (see below for further details).

A difficulty of this formulation is that $\widetilde{u}$, $\widetilde{w}$ and $\breve{u}$ are two-dimensional fields (depending on x, z and t) and must be related to the velocity field, which is three-dimensional. The other important closure problem for this equation resides in the choice of the reaction function. Ideas to close these terms are discussed in the following sections.

In summary, the proposed model is the following system of equations:

$$\begin{cases} \dfrac{\partial \boldsymbol{u}}{\partial t} + \boldsymbol{u}\cdot\boldsymbol{\nabla}\boldsymbol{u} = -\boldsymbol{\nabla}p + \dfrac{1}{Re}\nabla^2\boldsymbol{u} + \boldsymbol{\nabla}\cdot\left[q\nu_t\left(\boldsymbol{\nabla}\boldsymbol{u} + (\boldsymbol{\nabla}\boldsymbol{u})^T\right)\right] + \boldsymbol{f}_b, \\ \boldsymbol{\nabla}\cdot\boldsymbol{u} = 0, \\ \dfrac{\partial q}{\partial t} + \widetilde{u}\dfrac{\partial q}{\partial x} + \widetilde{w}\dfrac{\partial q}{\partial z} = R\left(q, \breve{u}\right) + \dfrac{D}{Re}\left(\dfrac{\partial^2}{\partial x^2} + \dfrac{\partial^2}{\partial z^2}\right) q. \end{cases} \tag{6.4}$$

equipped with the appropriate boundary conditions and the constant flow rate constraint mentioned at the beginning of this section. If $q \equiv 0$, the classic NS equations (2.1) are recovered. Therefore, the model admits the laminar Poiseuille solution $\{u, v, w, q\} = \{1.5(2y - y^2), 0, 0, 0\}$.

Various closures will be tested by following a common procedure:

1. Find the uniform fixed points of the system and identify one of the fixed points as the uniform turbulent solution. In this chapter, the adjective uniform denotes solutions which do not depend on x and z while retaining the $y-$dependence of the velocity field;
2. Perform the linear stability analysis (LSA) of the uniform turbulent solution and compare with the results of the previous chapter;
3. If LSA identifies a reasonable large-scale instability, perform the nonlinear simulation of the model and study the related bifurcation diagram.

For the computation of uniform fixed points and their LSA, the wall-normal direction is discretised with 65 Chebyshev collocation points and the computations performed with an in-house python code. The nonlinear simulation of the model is performed with the channelflow code. Equation (6.3) is implemented in channelflow using the same third-order temporal scheme used for the velocity field with an explicit treatment for the advection and reaction terms and an implicit treatment for the diffusion term (see Section 2.3.1 for details).

We conclude this section by noting that the model does not necessarily need to be based on an eddy viscosity. One could remove the Boussinesq hypothesis, namely

$$\boldsymbol{\tau}^R = \nu_t \left(\boldsymbol{\nabla u} + (\boldsymbol{\nabla u})^T \right), \tag{6.5}$$

and modulate, more generally, the deviatoric Reynolds stress tensor $\boldsymbol{\tau}^R$. In this case the separation of variables assumption becomes $\tilde{\boldsymbol{\tau}}^R(\boldsymbol{x}, t) = q(x, z, t)\boldsymbol{\tau}^R(y)$, where $\boldsymbol{\tau}^R(y)$ is the Reynolds tensor corresponding to the mean profile and the model equations become:

$$\begin{cases} \dfrac{\partial \boldsymbol{u}}{\partial t} + \boldsymbol{u} \cdot \boldsymbol{\nabla u} = -\boldsymbol{\nabla} p + \dfrac{1}{Re} \nabla^2 \boldsymbol{u} + \boldsymbol{\nabla} \cdot \left(q \boldsymbol{\tau}^R \right) + \boldsymbol{f}_b, \\ \boldsymbol{\nabla} \cdot \boldsymbol{u} = 0, \\ \dfrac{\partial q}{\partial t} + \breve{u} \dfrac{\partial q}{\partial x} + \breve{w} \dfrac{\partial q}{\partial z} = R\left(q, \breve{u}\right) + \dfrac{D}{Re} \left(\dfrac{\partial^2}{\partial x^2} + \dfrac{\partial^2}{\partial z^2} \right) q. \end{cases} \tag{6.6}$$

This alternative version of the model, which is not equivalent to the eddy viscosity model, is tested using a data-driven closure.

6.3 Preliminary model

We start our exploration of the nonlinear model (6.4), drawing inspiration from the pipe flow model proposed by Barkley (2011a) (see Section 1.2.2.1 for the context). This model involves two variables.

The variable $\breve{u}$ (u in the original paper) which is interpreted as the streamwise velocity on the pipe axis and a variable q which is interpreted as the magnitude of transverse velocity components at a given streamwise position. The variable q is a proxy of turbulence intensity as in the present model. Therefore, it is reasonable, as a first test, to close our q equation with the reaction function of the Barkley (2011a) model. Barkley (2011b) already found a pattern-forming instability with a Couette flow model derived from the pipe flow model.

6.3.1 Formulation

In this section, we consider the eddy viscosity version of the model (6.4), keeping the Cess (1958) formula (5.8) for $\nu_t(y)$.
In the q equation, the following reaction function is considered:

$$R\left(q,\breve{u}\right)=\alpha q\left[\breve{u}+r-1-(r+\delta)(q-1)^2\right], \tag{6.7}$$

with $\delta=0.1$ (Barkley, 2011a). This function involves two new parameters (α and r) and the variable $\breve{u}$, which has to be related to the velocity field u_i. The parameter α sets the time scale of the reaction term. Since we do not have any *a priori* information on this time scale, we leave it as a free parameter (similarly to D for the $q-$diffusion term). The parameter r, according to Barkley (2011a), is proportional to the Reynolds number Re. Instead of imposing a relation between r and Re *a priori*, we treat them as two free parameters, and we search for a relation *a posteriori*. Lastly, following Barkley (2011a), the variable $\breve{u}$ is taken as the local streamwise centreline velocity:

$$\breve{u}(x,z,t)=\frac{2}{3}u(x,y=1,z,t). \tag{6.8}$$

In this way, $\breve{u}=1$ for the laminar flow and $\breve{u}<1$ for the turbulent flow, as in the pipe flow model (Barkley, 2011a).

Having specified the reaction function, one can study uniform fixed points of (6.4). Using the wall-normal and spanwise momentum equations and the continuity equation, it is easy to find that the wall-normal and spanwise velocity components are zero. Therefore, the velocity field is a streamwise velocity profile $U(y)$. Moreover, for a uniform fixed point, the field q is simply a number, Q. Capital letters denote uniform fixed-point variables. These quantities verify the system:

$$\begin{cases}\dfrac{d^2U}{dy^2}+\dfrac{d}{dy}\left(\nu_t Q\dfrac{dU}{dy}\right)+f_b=0,\\ \dfrac{1}{2}\displaystyle\int_0^2 U\,dy=1,\\ R(\breve{U},Q)=0.\end{cases} \tag{6.9}$$

This system is a linear two-point boundary value problem for $U(y)$ (with boundary conditions $U(0)=U(2)=0$) coupled to a nonlinear algebraic equation for the number Q. We remark that uniform fixed points are independent of $\widetilde{u}$ and $\widetilde{w}$. The flow rate constraint is used with the boundary value

problem to compute f_b. After numerical discretisation, the boundary value problem plus the flow rate constraint becomes $N_y + 1$ linear algebraic equations.

To go beyond the computation of uniform fixed points, the model needs to be completed with $\widetilde{u}$ and $\widetilde{w}$, which have to be related to the three-dimensional velocity field. An option is to average along the wall-normal direction the streamwise and spanwise velocity components at each $x-z$ location. In the case of uniform solutions, the wall-normal average of the streamwise component is 1 (see (6.9)), and the spanwise component is identically zero. Therefore, for uniform fixed points, $\widetilde{u} = 1$ and $\widetilde{w} = 0$. These values are used for the LSA of uniform fixed points (see (6.11) below). In nonlinear simulations, the local wall-normal average can be computed. This choice, however, leads to undesired results (further comments in Subsection 6.3.2). Therefore, we use $\{\widetilde{u}, \widetilde{w}\} = \{1, 0\}$ for all the results shown in this chapter.

The model equations (6.4) can be linearised around a uniform fixed point $\{U(y), Q\}$ to study its linear stability. The *ansatz*

$$\begin{bmatrix} u_i' \\ p' \\ q' \end{bmatrix} = \begin{bmatrix} \hat{u}_i(y) \\ \hat{p}(y) \\ \hat{q} \end{bmatrix} e^{\imath(k_x x + k_z z) + \sigma t}, \quad k_x, k_z \in \mathbb{R},\ \sigma \in \mathbb{C}, \tag{6.10}$$

can be substituted for the perturbation. The resulting LSA equations are:

$$0 = \imath k_x \hat{u} + \frac{d\hat{v}}{dy} + \imath k_z \hat{w}, \tag{6.11a}$$

$$\begin{aligned} \sigma\hat{u} = &-\imath k_x U\hat{u} - \frac{dU}{dy}\hat{v} - \imath k_x \hat{p} + \left(\frac{1}{Re} + \nu_t Q\right)\left(-k_x^2 - k_z^2 + \frac{d^2}{dy^2}\right)\hat{u} \\ &+ Q\frac{d\nu_t}{dy}\left(\frac{d\hat{u}}{dy} + \imath k_x \hat{v}\right) + \frac{d}{dy}\left(\nu_t \frac{dU}{dy}\right)\hat{q}, \end{aligned} \tag{6.11b}$$

$$\begin{aligned} \sigma\hat{v} = &-\imath k_x U\hat{v} - \frac{d\hat{p}}{dy} + \left(\frac{1}{Re} + \nu_t Q\right)\left(-k_x^2 - k_z^2 + \frac{d^2}{dy^2}\right)\hat{v} + 2Q\frac{d\nu_t}{dy}\frac{d\hat{v}}{dy} \\ &+ \imath k_x \nu_t \frac{dU}{dy}\hat{q}, \end{aligned} \tag{6.11c}$$

$$\begin{aligned} \sigma\hat{w} = &-\imath k_x U\hat{w} - \imath k_z \hat{p} + \left(\frac{1}{Re} + \nu_t Q\right)\left(-k_x^2 - k_z^2 + \frac{d^2}{dy^2}\right)\hat{w} \\ &+ Q\frac{d\nu_t}{dy}\left(\frac{d\hat{w}}{dy} + \imath k_z \hat{v}\right), \end{aligned} \tag{6.11d}$$

$$\begin{aligned} \sigma\hat{q} = &-\imath k_x \hat{q} + \alpha Q \mathcal{F}\hat{u} + \alpha\left[\check{U} + r - 1 - (r+\delta)(Q-1)(3Q-1)\right]\hat{q} \\ &- \frac{D}{Re}(k_x^2 + k_z^2)\hat{q}. \end{aligned} \tag{6.11e}$$

This is a $1D$ generalised eigenvalue problem in σ, which has to be solved for each $\{k_x, k_z\}$ wavenumber couple. The size of the discretised problem is $4N_y + 1$. The operator $\mathcal{F}$, present in the last equation,

is defined by:

$$\mathcal{F}\hat{u} = \begin{cases} \frac{2}{3}\hat{u} & \text{if } y = 1, \\ 0 & \text{otherwise.} \end{cases} \tag{6.12}$$

In practice, this operator extracts from $\hat{u}$ the $\breve{u}$ perturbation, *i.e.* the rescaled centreline value of the wall-normal profile $\hat{u}$.

Before discussing the results, another aspect of the formulation of this model needs to be covered. It was mentioned in Section 6.2 that, if $q \equiv 0$, the classic NS equations are recovered, without eddy viscosity. This is desirable because it allows to recover the laminar solution, but it is also a source of difficulty in nonlinear simulations. Indeed, the rationale of the model is that $q = 0$ implies laminar flow. But the model also admits situations in which q decays to zero and the velocity field undergoes a transition to turbulence. This behaviour is paradoxical in the logic of the model and must be avoided. One possible solution is to add a properly designed source term in the q equation, which produces q when the velocity field becomes turbulent. This production term would trigger the eddy viscosity, which, in turn, would damp the undesired small scales. A simpler solution is to filter out the turbulent scales from the velocity field and keep in $\boldsymbol{u}$ only the large-scale flow. This is reminiscent of Large Eddy Simulations (LES), in which the q equation would be the subgrid scale model.
Given the pseudo-spectral nature of our numerical code, filtering is performed directly in spectral space by multiplying the Fourier coefficients of the velocity fields by a damping function. Let the Fourier coefficients of $u_i(x, y, z, t_n)$ be denoted by $\hat{u}_i^n(k_x, y, k_z)$. And let the non-filtered updated Fourier coefficients be denoted by $\underline{\hat{u}_i^{n+1}}(k_x, y, k_z)$. Then, the filtered updated Fourier coefficients are:

$$\hat{u}_i^{n+1}(k_x, y, k_z) = S\left(\frac{k_{x,c} + \Delta k_x - k_x}{\Delta k_x}\right) S\left(\frac{k_{z,c} + \Delta k_z - k_z}{\Delta k_z}\right) \underline{\hat{u}_i^{n+1}}(k_x, y, k_z), \tag{6.13}$$

where $S(\xi)$ is the damping function:

$$S(\xi) = \begin{cases} S_0 & \text{if } \xi \leqslant 0; \\ \dfrac{1 - S_0}{1 + e^{\left(\frac{1}{\xi - 1} + \frac{1}{\xi}\right)}} + S_0 & \text{if } 0 < \xi < 1; \\ 1 & \text{if } \xi \geqslant 1. \end{cases} \tag{6.14}$$

S_0 is a parameter between 0 and 1 that we take equal to 0.5. This function realises a smooth transition from S_0 to 1.
The above formula implies that every mode with either $k_x > k_{x,c}$ or $k_z > k_{z,c}$ is multiplied by a number smaller than 1 and, therefore, is damped. Modes with both $k_x < k_{x,c}$ and $k_z < k_{z,c}$ are multiplied by one and, therefore, untouched. This realises a low-pass filter. The cutoff values are chosen such that the typical spacing of streaks in the spanwise direction ($\lambda_z^+ = 100$) and the typical streamwise size of streamwise vortices ($\lambda_x^+ = 300$) are fully damped, *i.e.* $k_{x,c} + \Delta k_x < 2\pi Re_\tau/300$ and $k_{z,c} + \Delta k_z < 2\pi Re_\tau/100$. In this way, small-scale turbulence can not be sustained by the system and, at the low Re considered, the flow relaminarises whenever q is close enough to 0. The parameters Δk_x and Δk_z are chosen such that the critical wavenumber of the modulations ($k_x \approx 0.18$ and $k_z \approx 0.42$) are left untouched, *i.e.* $k_{x,c} > 0.18$ and $k_{z,c} > 0.42$.

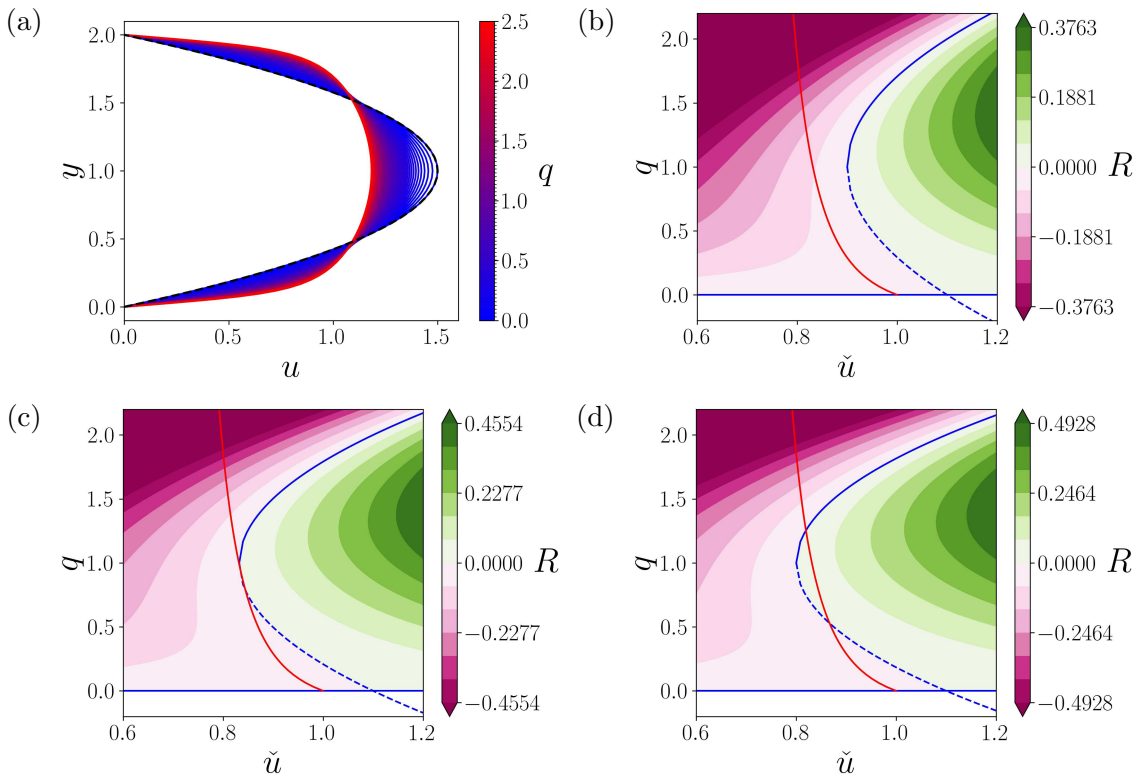

Figure 6.2: (a) One-dimensional velocity profiles obtained with the Cess (1958) eddy viscosity and different values of q. The dashed black line is the Poiseuille solution $1.5(2y-y^2)$. (b-d) Contours of the Barkley (2011a) reaction function (6.7) at $Re = 1000$ and (b) $r = 0.10$, (c) $r = 0.17$ and (d) $r = 0.20$. The blue lines are the $q-$nullclines ($R = 0$) while the red line is the $\breve{u}-$nullcline given by the centreline velocity of the profiles in (a).

6.3.2 Results

The analysis starts from the uniform fixed points. The solutions of (6.9) can be understood using the $\breve{u}-q$ plane. Unlike in Barkley (2011a), here the $\breve{u}-q$ plane is just a low-dimensional projection of the system (6.9), which includes more degrees of freedom in the wall-normal direction. Nevertheless, this projection is sufficient to identify the fixed points. In this plane, one can identify regions on which the reaction function R is either positive or negative and the points on which R is zero. The points at which $R = 0$ form curves called *nullclines* ($q-$nullclines). The reaction function (6.7) has two nullclines: $q = 0$ and a parabola whose position depends on r. By definition, the fixed points must be on the $q-$nullclines. The fixed point solution must also verify the boundary value problem for the velocity profile, which depends on q. One can solve the boundary value problem for a range of q's and obtain a continuum of profiles parametrised by q. An example of such profiles is shown in figure 6.2 (a) for $Re = 1000$. We recall that in this section we are using the Cess (1958) eddy viscosity formula (5.8). The figure shows that for $q = 0$, the parabolic laminar profile $U(y) = 1.5(2y - y^2)$ is obtained, while for increasing q, the profile becomes increasingly blunted. Each of these profiles gives $\breve{u}$ as its rescaled centreline velocity. Therefore, the boundary value problem defines a relation between

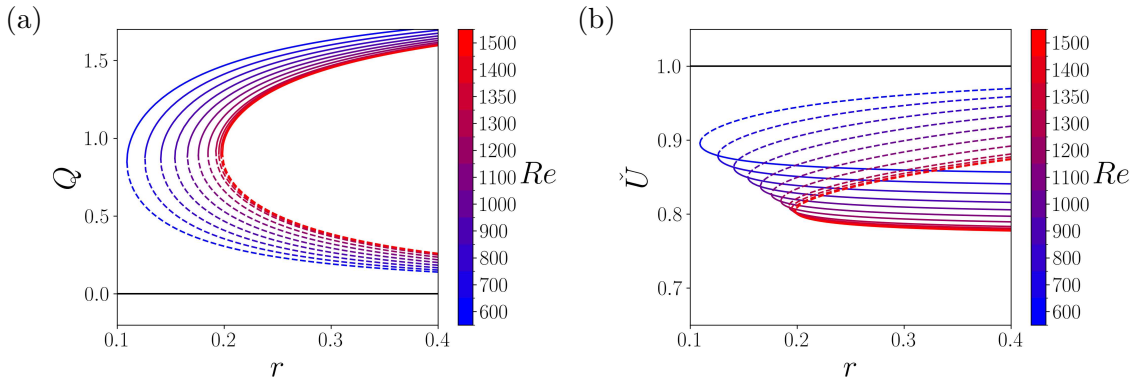

Figure 6.3: Bifuration diagrams of the fixed points as a function of r and Re for the model with the Barkley (2011a) reaction function.

$\breve{u}$ and q which, in the $\breve{u} - q$ plane, is a curve and, as a matter of fact, is the $\breve{u}-$nullcline. The fixed points, *i.e.* the solutions of (6.9), are identified in the $\breve{u} - q$ plane as the $\{U(y), Q\}$ couples for which the $q-$nullclines and the $\breve{u}-$nullcline cross.

Figure 6.2 (b,c,d) shows the $q-$nullclines in blue and the $\breve{u}-$nullcline in red for $Re = 1000$ and three different values of r. The figure also shows the contours of R in the half-plane $q > 0$. It can be seen that R changes sign across the blue nullcline. By construction, the $\{\breve{u}, q\} = \{1, 0\}$ point is always a fixed point: it is the laminar solution. It was numerically verified that the laminar solution is linearly stable for the range of Re considered. Two additional fixed points are generated in a saddle-node bifurcation when r is increased. As far as the linear stability to spatially uniform perturbations is concerned, the lower branch point is unstable while the upper branch point is stable. This upper branch fixed point represents our uniform turbulent flow solution.

The fixed points have been computed to machine precision by coupling the solver of the boundary value problem with a bisection on q. The boundary layer problem is solved by discretising the differential and integral operators with Chebyshev collocation and inverting the resulting linear system after implementation of the boundary conditions. The problem has been solved for a range of r and a range of Re. Figure 6.3 summarises the results. For each Re, there is a saddle-node bifurcation at a critical r that we denote by r_{sn}. The function $r_{sn}(Re)$ can be useful to find a relation between r and Re such that there is a single saddle-node bifurcation at a desired Re_{sn}.

Having computed the turbulent fixed point, the next important question is whether this fixed point becomes linearly unstable with respect to spatially varying perturbations. We address this point by solving (6.11). While the parameters α and D are irrelevant for fixed points, they become important for LSA. Contours of the leading growth rates as a function of k_x and k_z are reported in figure 6.4 at $Re = 1000$ and $r = 0.17$. The computations were performed for a range of k_x and k_z, which is relevant to large-scale modulations. As a reference, the critical wavevector of Kashyap et al. (2022) $\{k_x, k_z\} \approx \{0.18, 0.42\}$ is indicated by a green cross. The different panels of the figure show the growth rate contours for different combinations of α and D. In the top row, α is increased from 0.1 to 1.0 while $D = 1.0$ is kept constant. For increasing α, the instability moves to higher wavenumbers,

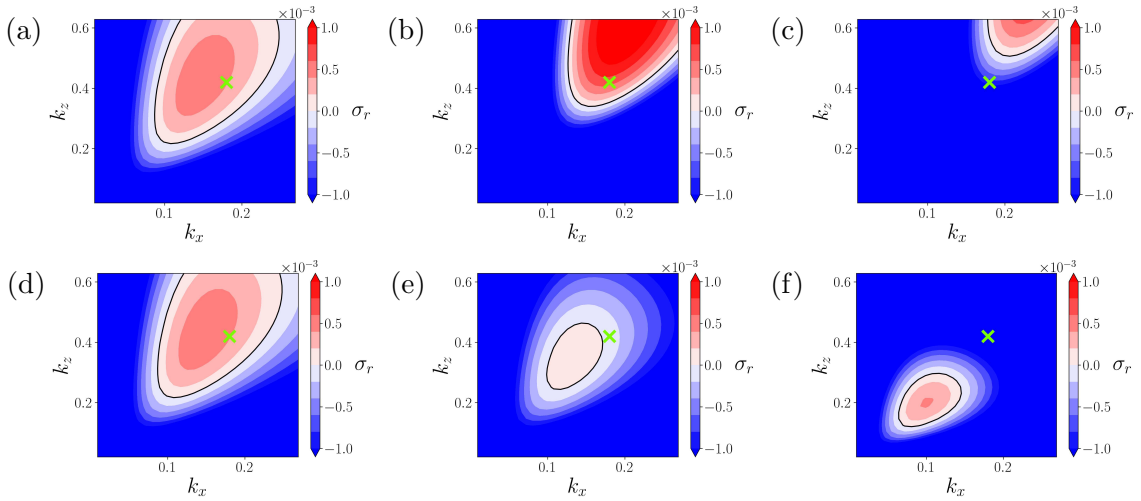

Figure 6.4: Leading growth rates from LSA of the upper branch fixed point of the model with the Barkley (2011a) reaction function as a function of k_x and k_z. $Re = 1000$ and $r = 0.17$. (a-c) Increasing α from left to right with $D = 1$ ($\alpha = 0.1, 0.5, 1.0$). (d-f) Increasing D from left to right with $\alpha = 0.1$ ($D = 1, 4, 25$). The black contour separates the stable (blue) and unstable (red) regions. The green cross denotes the critical wavenumbers of Kashyap et al. (2022), $k_x = 0.18$ and $k_z = 0.42$.

moving out of the figure for $\alpha = 1.0$. Note that it is of no interest to compute the instability for high wavenumbers. In the bottom row, D is increased from 1.0 to 25.0 while $\alpha = 0.1$ is kept constant. Increasing D has the opposite effect, namely, the instability moves towards smaller wavenumbers. We note that the location and extension of the unstable region also depend on r and Re. However, we argue that $\alpha = 0.1$ and $D = 1.0$ is a good combination of parameters, since the growth rate peaks near the reference wavenumbers (green cross). In principle, α and D can be fine-tuned to make the critical wavenumbers coincide with those of Kashyap et al. (2022). This fitting, however, was not performed in this study because it also involves the other parameters, and it is of no interest at this stage of the investigation.

Figure 6.5 shows an $y - z$ cut of the leading eigenmode for $k_x = 0.18$ and $k_z = 0.42$ (the critical wavenumbers of Kashyap et al. (2022)) for a particular parameter combination. Leading unstable eigenmodes for different parameter combinations and slightly different wavenumbers are very similar. The $x - y$ cut is also very similar. Comparison of figure 6.5 with figure 5.24 reveals a similarity between the instability obtained with the current model and that discussed in the previous chapter. The resemblance is particularly evident on the spanwise velocity component and suggests that the current eigenmode is a monochromatic version of the eigenmode shown in figure 5.24. In addition to the velocity components, the eigenmode of the present model also brings the perturbation to the variable q, q', which is shown in figure 6.5 (d). The q' field does not depend on y and is simply sinusoidal in x and z. Positive q' indicates regions where turbulence is augmented, while negative q' indicates regions where turbulence is damped. Figure 6.6 shows the same eigenmode in the $x-z$ plane. In particular, the figure shows the q' field and the wall-normal integrated $u'-w'$ flow, which represents the large-scale flow (Duguet and Schlatter, 2013). We note once again the resemblance of this figure

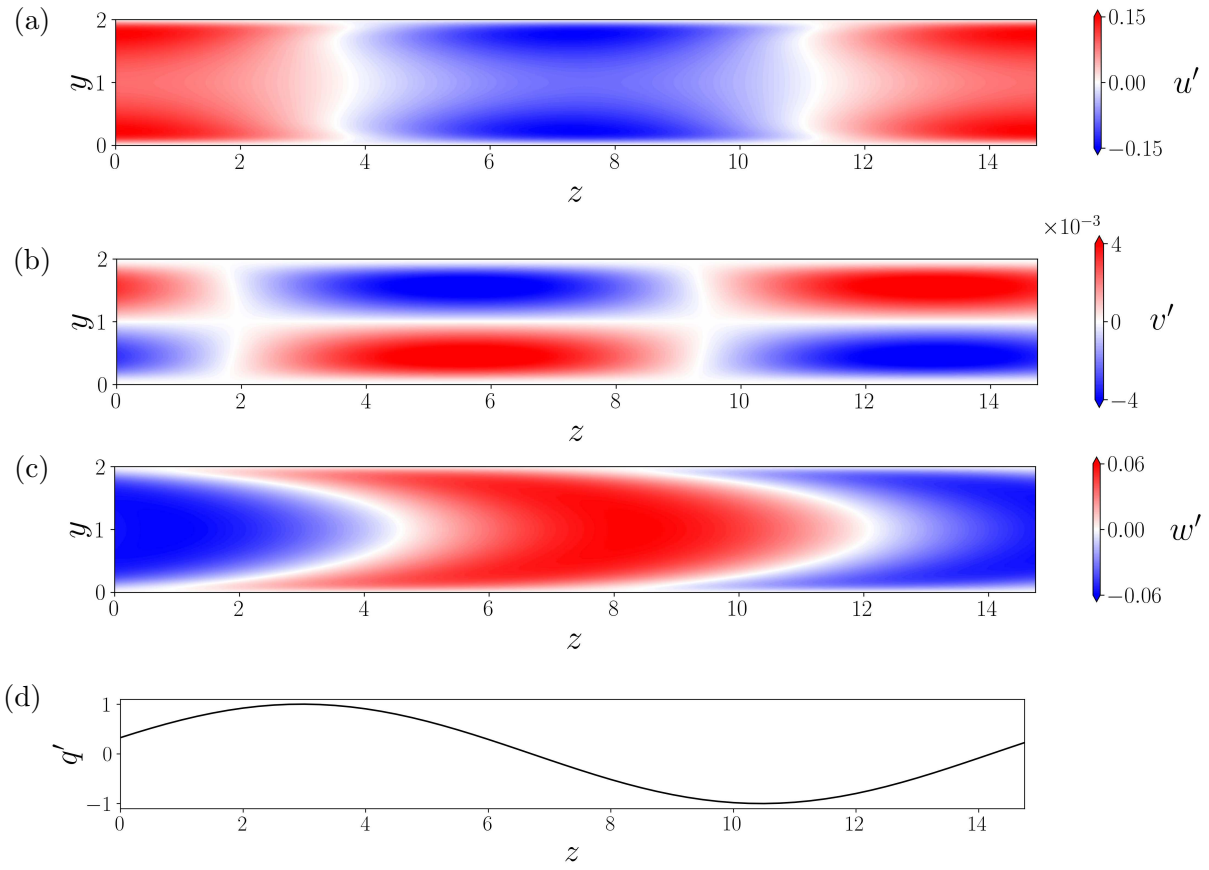

Figure 6.5: Leading eigenmode of the model with the Barkley (2011a) reaction function at $Re = 1000$ and $r = 0.17$ with $k_x = 0.18$, $k_z = 0.42$, $\alpha = 0.1$ and $D = 1$ in the $y - z$ plane. (a) Streamwise velocity component, (b) wall-normal velocity component, (c) spanwise velocity component and (d) q'.

to figure 5.26 of the previous chapter. The large-scale flow is very similar. However, the current figure shows the q perturbation instead of the wall-normal velocity perturbation. This variable makes clear that, in the linear eigenmode, the large-scale flow is located between regions of augmented and damped turbulence. However, similarly to Chapter 5, it is not possible to define a laminar-turbulent interface at the linear level, since the linear eigenmode is a modulation with unspecified amplitude.

Until now, we have discussed LSA results only for a given Re and a given r. Now, we discuss the influence of these parameters on the stability of the turbulent fixed point. Since it is generated by a saddle-node bifurcation, the turbulent fixed point exists only in a region of the $Re - r$ plane, delimited by the curve $r_{sn} = r_{sn}(Re)$. This curve can be obtained using the data reported in figure 6.3, and it is shown in figure 6.7. LSA defines a new curve $r_c = r_c(Re)$. This curve is computed by searching for the critical r at which the first mode becomes unstable for each Re. The research of critical r is performed with a bisection algorithm, which at each iteration maximises the growth rate with respect to k_x and k_z. Therefore, the algorithm also returns the critical k_x and k_z. They are not discussed here because they depend on α and D and can be eventually fitted to the desired values by fine-tuning

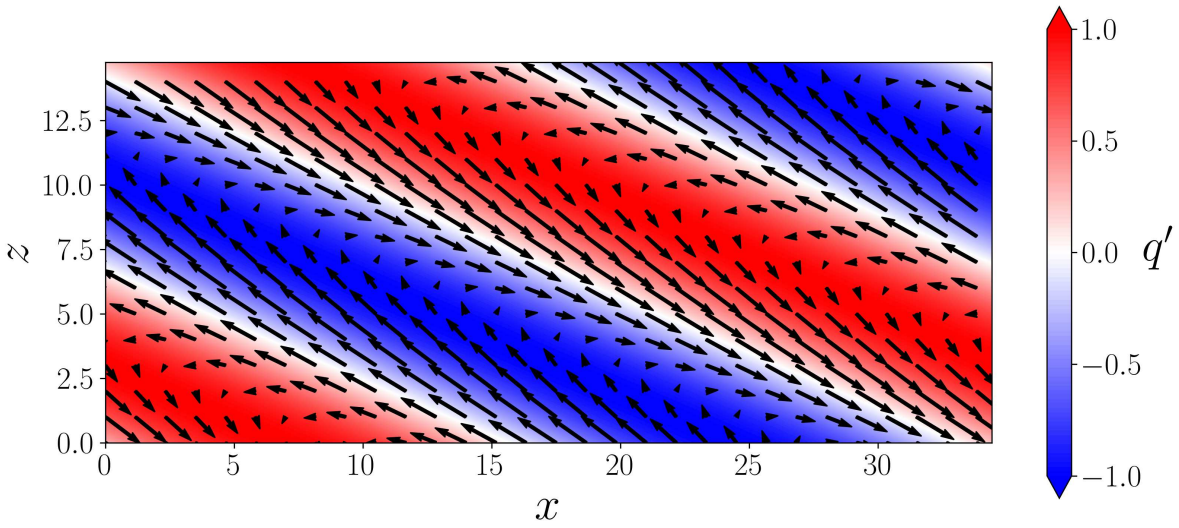

Figure 6.6: Leading eigenmode of the model with the Barkley (2011a) reaction function for the same parameters of figure 6.5. The figure shows the contours of q' and the wall-normal integrated streamwise and spanwise velocity components (arrows).

these parameters (see discussion of figure 6.4). LSA reveals that the instability is found by lowering r. Therefore, there is a range of r between r_{sn} and r_c for which the turbulent fixed point exists and is linearly unstable with respect to spatially varying perturbations. For $r < r_{sn}$ the turbulent fixed point does not exist, while for $r > r_c$ the turbulent fixed point exists and is linearly stable. Figure 6.7 shows that the width of the range $[r_{sn}, r_c]$ is relatively small and approximately constant with Re. The diagram reported in figure 6.7 can be used to find a relation between r and Re that will give the desired Re_{sn} and Re_c. We give here an example of such a relation choosing $Re_c = 1350$ (which corresponds to the $Re_{\tau,c} = 95$ of Kashyap et al. (2022)). The formula

$$r(Re) = r_c(Re_c)\left(\frac{Re - s}{Re_c - s}\right)^b, \tag{6.15}$$

with $Re_c = 1350$, $r_c(Re_c) = 0.1991$, $s = 420$ and $b = 0.38$, gives the black curve traced in figure 6.7. From low to high Re, this curve crosses first the r_{sn} curve at $Re \approx 700$ and then the r_c curve at $Re = 1350$. Therefore, if this relation is used, the model will undergo a saddle-node bifurcation, generating the turbulent fixed point at $Re_{sn} \approx 700$ and this fixed point would be linearly unstable until $Re_c = 1350$. In conclusion, the model has a qualitative behaviour coherent with the linear instability reported by Kashyap et al. (2022) and can be tuned to match their critical Re, k_x and k_z (in principle, it can also match any other reference).

These encouraging LSA results lead us to the analysis of the nonlinear saturation of the instability. For simplicity, we fix $Re = 1000$ and use r as a parameter. If the behaviour with r is qualitatively good, a satisfactory relation between r and Re can be found *a posteriori*. Figure 6.8 and 6.9 show the saturation of the instability for $r = 0.17$. The nonlinear simulation is initialised with the turbulent fixed point plus the unstable eigenmode obtained with $k_x = 0.18$ and $k_z = 0.42$ and scaled to an

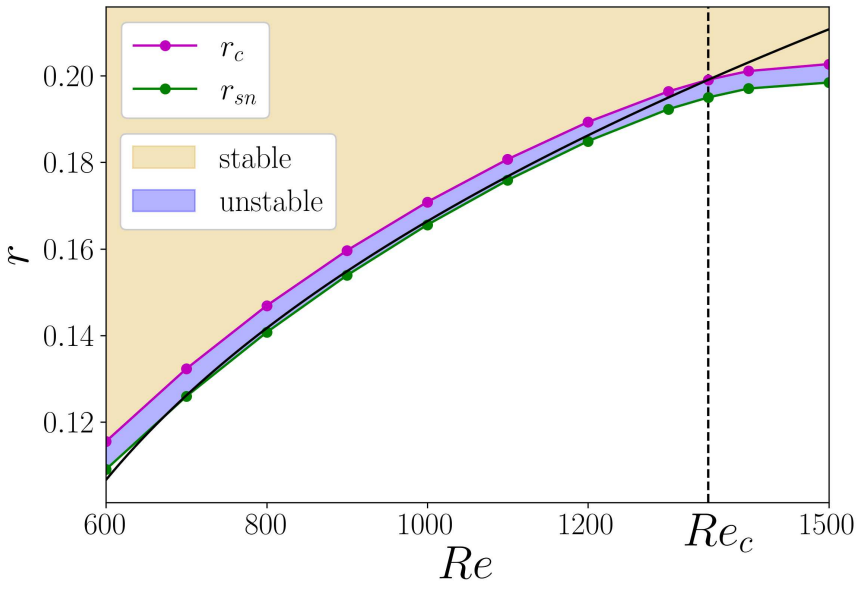

Figure 6.7: Diagram of r_{sn} and r_c as a function of Re for $\alpha = 0.1$ and $D = 1$. $Re_c = 1350$ corresponds to the critical Re of Kashyap et al. (2022). The black line is the relation (6.15). In the yellow region the turbulent fixed point is linearly stable, in the blue region it is linearly unstable and in the white region it does not exist.

amplitude of 10^{-5}. The size of the computational domain for this simulation is such that only one wavelength of the instability is simulated. Moreover, for these simulations, the number of collocation points is the same as used for DNS, namely $N_x \times N_y \times N_z = 180 \times 65 \times 180$ (before dealiasing in x and z).

The perturbation grows exponentially in time with the growth rate predicted by LSA. Above some amplitude, nonlinear effects come into play, distort the eigenmode and saturate the amplitude of the modulation. Figure 6.8 shows the distortion-saturation phase in the physical space. The figure shows the wall-normal integrated streamwise-spanwise velocity field relative to the bulk velocity, along with the contours of the q variable (which is natively two-dimensional). The q field shows that nonlinear effects lead to the formation of steep fronts between the laminarising region and the turbulent region. Laminar flow is eventually reached (dark blue regions) and progressively consumes the turbulent region until an equilibrium turbulent fraction is reached. The velocity field is also slightly distorted between $t = 14500$ and $t = 16000$ and then reaches an equilibrium. After the initial transient, the solution becomes a travelling wave. This growth, distortion, saturation and equilibrium sequence of events can also be analysed in the $\breve{u} - q$ phase plane. Since $\breve{u}$ and q are both two-dimensional fields, a point can be marked in the plane for each $x - z$ position. Figure 6.9 shows that, initially, all the points are located at the turbulent fixed point. Then, the points start to move away as the eigenmode grows. At $t = 14500$, the $q = 0$ line is reached, meaning that a laminar region has formed. The differences between $t = 14500$ and $t = 16000$ are linked to the distortion of the velocity field. Finally, between $t = 16000$ and $t = 22000$, the plot does not change, signalling the onset of an equilibrium.

This nonlinear simulations was performed with $\{\widetilde{u}, \widetilde{w}\} = \{1, 0\}$. Another simulation was performed

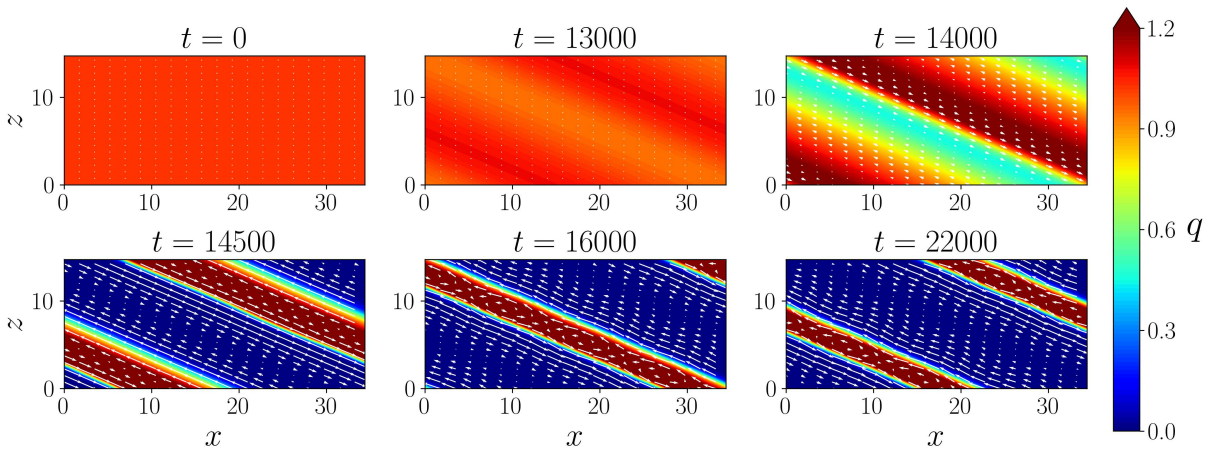

Figure 6.8: Nonlinear evolution of the instability in physical space for the same parameters of figure 6.5 and $\{\widetilde{u}, \widetilde{w}\} = \{1, 0\}$. The panels show the contours of q and the wall-normal integrated streamwise and spanwise velocity components (arrows). Here, the simulation is initialised with the unstable mode obtained from linear stability analysis of the turbulent fixed point.

using local wall-normal averages, namely

$$\widetilde{u}(x,z,t) = \frac{1}{2}\int_0^2 u(x,y,z,t)\,dy \quad \text{and} \quad \widetilde{w}(x,z,t) = \frac{1}{2}\int_0^2 w(x,y,z,t)\,dy. \tag{6.16}$$

This choice does not modify the LSA system (6.11), but introduces an additional feedback of the velocity field on q during the nonlinear simulations. This feedback leads to an instability that breaks down the pattern shortly after the saturation. The long-time behaviour of the model in this case is chaotic in time and disorganised in space. Since it looks unphysical in the frame of the comparison with DNS and experiments, we do not present it here. Therefore, only the results with $\{\widetilde{u}, \widetilde{w}\} = \{1, 0\}$ are presented in this subsection.

The extension of the laminar (blue) regions in figure 6.8 suggests that a low turbulent fraction characterises the pattern at equilibrium. Since near the critical point the instability should saturate to modulations rather than laminar-turbulent patterns (Kashyap et al., 2022, 2025), we investigate the behaviour of the turbulent fraction with r. The turbulent fraction can be defined using the q field:

$$F_t(t) = \frac{1}{QL_xL_z}\int_0^{L_x}\int_0^{L_z} q(x,z,t)\,dxdz, \tag{6.17}$$

where Q is the value of q on the turbulent fixed point. This definition implies $F_t = 1$ for the turbulent fixed point. When the travelling wave equilibrium is reached, F_t has a value constant in time and included between 0 and 1.
Since we look at the destabilisation of the turbulent flow (top-down approach), it is more interesting to look at the equilibrium laminar fraction $\chi = 1 - F_t(t_\infty)$, where t_∞ is a time at which the equilibrium is settled. This quantity is plotted in figure 6.10 as a function of r, at $Re = 1000$. We recall that the turbulent fixed point exists for $r > r_{sn}$ and is linearly stable for $r > r_c$ (yellow region in the

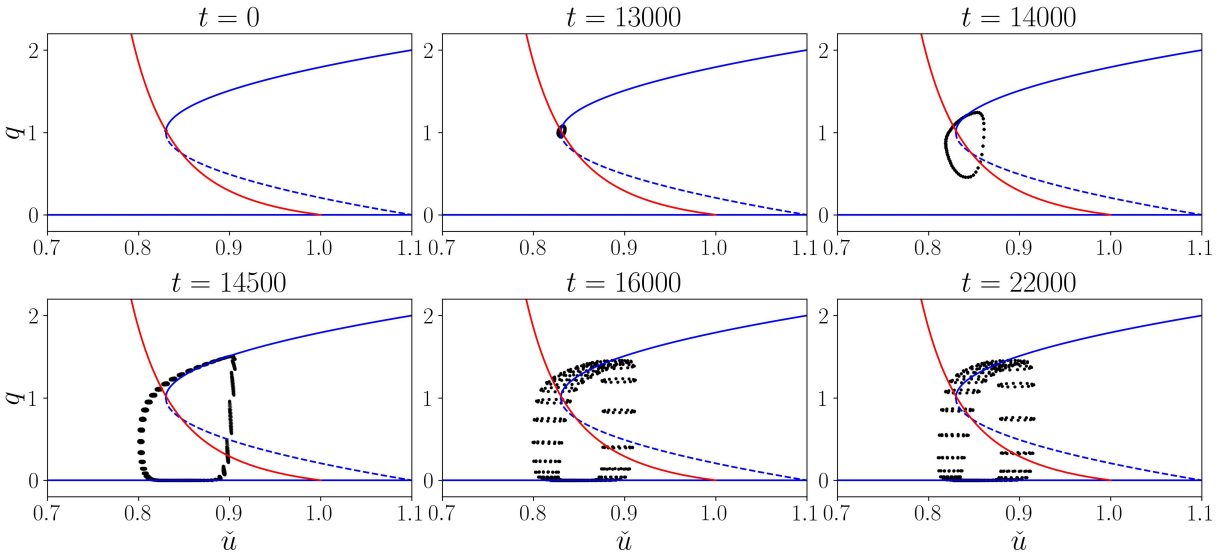

Figure 6.9: Nonlinear evolution of the instability on the $\breve{u} - q$ phase-plane for the same parameters of figure 6.8.

figure), whereas it is linearly unstable for $r_{sn} < r < r_c$ (blue region). Consistent with figure 6.7, the region of linear instability of the fixed point is rather small. The first from left red point on the plot is the simulation presented in figures 6.8 and 6.9. The other points are computed by initialising the simulation with the equilibrium obtained at the previous r and waiting for the new equilibrium to settle. The resulting bifurcation diagram shows that a stable pattern exists even when the turbulent fixed point is linearly stable. Beyond a certain r, the pattern is not observed anymore. This diagram is compatible with a subcritical bifurcation of the turbulent fixed point. In contrast, the bifurcation scenario described by Kashyap et al. (2022) is a supercritical bifurcation in which the saturation amplitude of the modulation continuously increases from zero at the critical point. Therefore, the bifurcation scenario of the current model is not consistent with DNS observations. We note that the model proposed by Kashyap et al. (2025) also displays a subcritical character that has not been analysed in detail.

6.3.3 Filter on the q field and influence of the domain size

In Section 6.3.1, we have introduced a filter used on the velocity field to prevent transition to turbulence in regions of $q = 0$. Now, we use the same filter (equation (6.13)) also on the field q. Moreover, we boost the action of the filter by increasing the cutoff values, setting the parameters to $k_{x,c} = 0.2$, $\Delta k_x = 0.1$, $k_{z,c} = 0.5$ and $\Delta k_z = 0.2$ (these values are chosen after inspection of DNS spectra). This improved filtering alleviates some of the issues presented in the previous sections. For example, we can use the advection velocities given by 6.16 without incurring the instability of the pattern mentioned in the previous subsection. The improved filter also allows us to reduce the numerical cost of the simulations. Indeed, we reduce the number of points in the streamwise and spanwise directions from the DNS resolution $N_x/L_x = 36/7$ and $N_z/L_z = 12$ (before dealiasing) to a

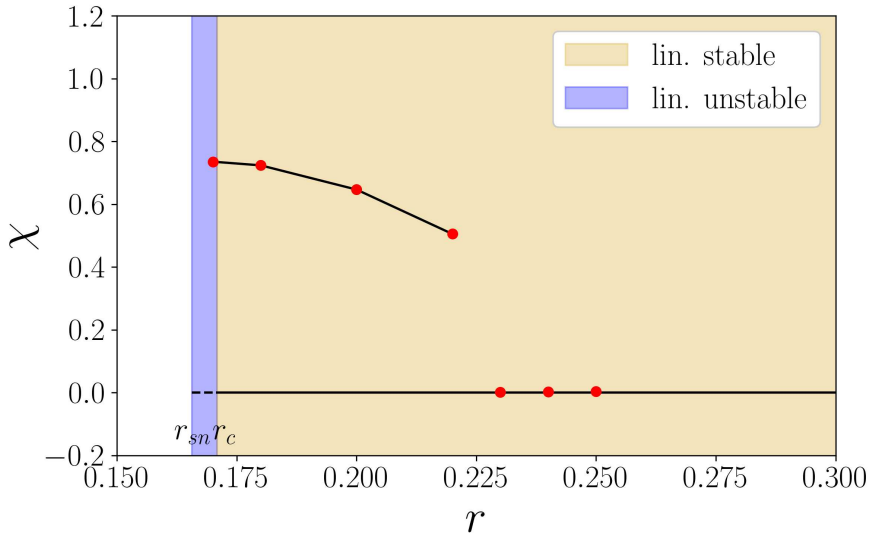

Figure 6.10: Bifurcation diagram of the pattern at $Re = 1000$ for the model with the Barkley (2011a) reaction function with $\alpha = 0.1$ and $D = 1$. The red points have been computed with nonlinear simulations. The background colour scheme is the same of figure 6.7.

lighter resolution of $N_x/L_x = 9/7$ and $N_z/L_z = 3$ (before dealiasing). Namely, the total number of points is reduced by a factor of 16 with respect to DNS.

Figure 6.11 (a) shows a nonlinear simulation of the model performed with the new filter for a parameter set similar to figure 6.8 and in the same domain. This simulation, however, is initialised with random noise added to the turbulent fixed point to observe the spontaneous appearance of the most unstable mode (among those allowed in the domain). It can be seen that the instability again saturates to an oblique travelling wave similar to that of figure 6.8. With respect to that solution, however, the new travelling wave is characterised by smoother laminar-turbulent interfaces and more balanced laminar/turbulent fractions.

The behaviour of the model is further explored by increasing the simulation domain size. Figure 6.11 (b) shows the same numerical experiment of panel (a) in a domain that is two times bigger in the streamwise and spanwise directions. An oblique pattern appears around $t = 2000$, but it is disrupted shortly after. At $t = 4000$ and $t = 7800$, the turbulent regions are arranged in spots rather than in bands. However, a turbulent band is formed again at $t = 9000$. It must be noted that the travelling wave observed in figure 6.11 (a) is still an invariant solution in the larger domain. However, in the larger domain, it loses its stability and an intermittent alternance of imperfect bands and obliquely arranged spots is observed instead. We note that this phenomenology is not incompatible with DNS observations of the flow at the same Re in comparable domains.

In figure 6.11 (c), the model is simulated starting, again, from the turbulent fixed point plus noise in a large domain of size $L_x \times L_z = 560 \times 240$. At $t = 1000$, we see how the pattern emerges from the noise with different orientations and well-defined wavelengths. This pattern seems to saturate at $t = 2000$. The snapshot at $t = 2000$ is intriguing, since it resembles the filtered DNS field shown in

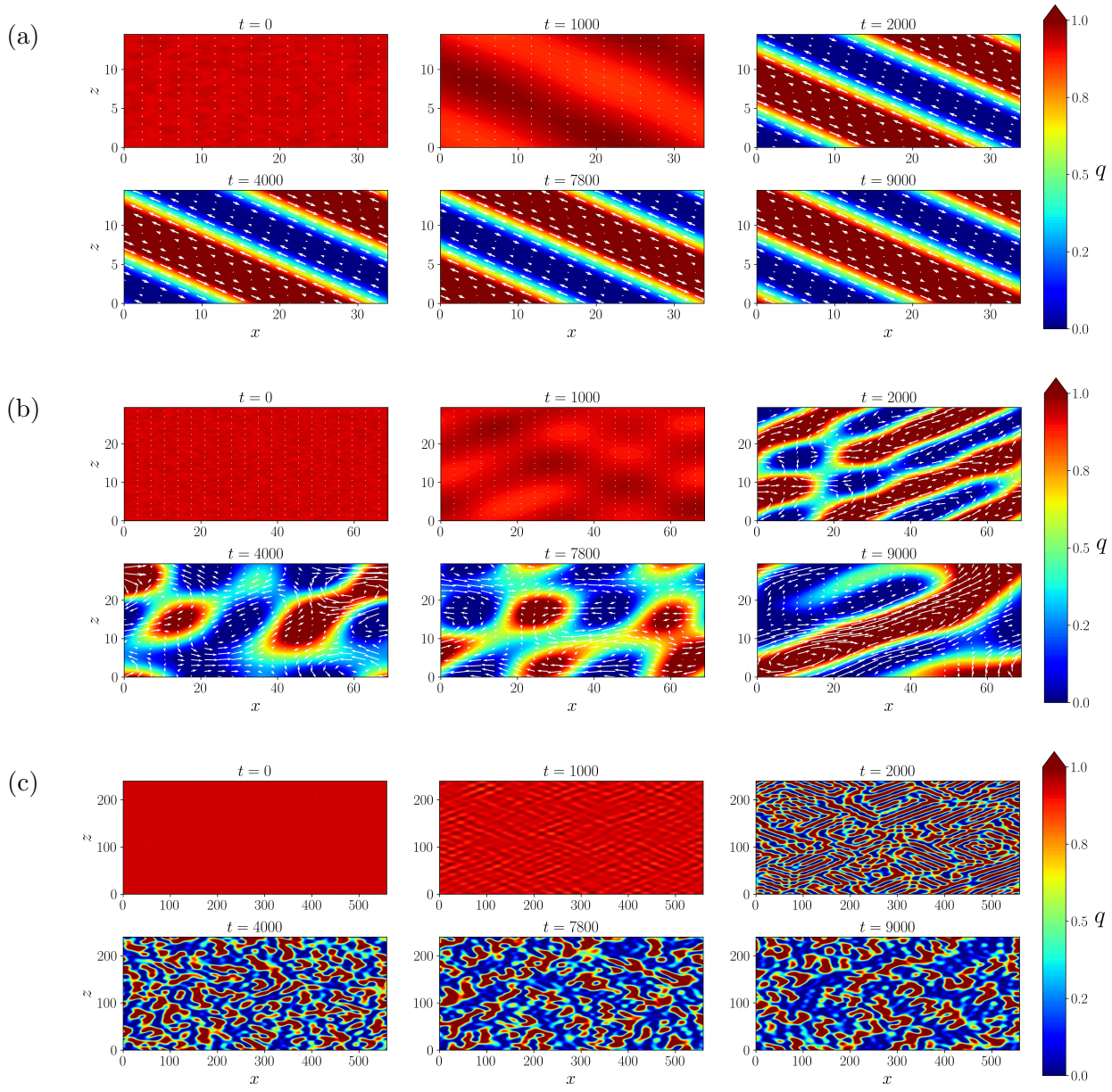

Figure 6.11: Nonlinear evolution of the instability in physical space at $Re = 1000$ and $r = 0.166$ with $\alpha = 0.1$, $D = 1$, nonlinear advection and the filter both on $\boldsymbol{u}$ and q. The panels show the contours of q and the wall-normal integrated streamwise and spanwise velocity components (arrows in panels (a) and (b)). Increasing domain from top to bottom: $L_x \times L_z =$ (a) 35×15, (b) 70×30 and (c) 560×240 (in units of channel half-gap). Here, the simulations are initialised with random noise.

figure 6.1 (b). However, this pattern is unstable again, and it is broken down around $t = 4000$. In the long run, the turbulent regions are rearranged in an oblique fashion and at $t = 9000$, a new oblique pattern consisting of broken turbulent segments can be discerned on a larger length scale.

The analysis of this first model stops at this point. We have seen that this model is capable of retrieving the desired linear instability and that in the nonlinear simulations, interesting laminar-turbulent patterns are observed. However, in large domains, these patterns are unstable, and the model shows an undesired complex behaviour. These instabilities could be due to the form of the reaction term in the q equation, which was assumed without any *a priori* comparison to DNS data. In the next section, we present two attempts to retrieve the reaction function from DNS data. The results presented in this section will be further discussed in Section 6.5.

6.4 Data-driven model

In the last section, the choice of the reaction function was motivated by its simplicity and desired properties. In this section, we search for a reaction function which can be more easily connected to the NS equations. To do so, q and $R(\breve{u}, q)$ need to be identified with quantities that are measurable in DNS. The function $R(\breve{u}, q)$ represents the local dynamics of the turbulent flow, which in a DNS context can be interpreted as the flow devoid of large scales. Such a flow can be simulated in a minimal flow unit (Jiménez and Moin, 1991), since it excludes large scales by construction. Therefore, we perform long-time simulations in a computational domain of size $L_x^+ \times L_z^+ = 400 \times 140$ at several Re between 1000 and 1500 (Re_τ between 71 and 106). Note that the size of the domain in units of channel half-gap depends on Re. Turbulence spontaneously decays in these minimal domains after a certain time. To collect more data at each Re, more than one realisation has been performed in some cases. We use these data to formulate a closure for the nonlinear model, as explained in the following subsections. Throughout this section, an overbar over the flow variables denotes a time-dependent average of the quantity over the streamwise and spanwise directions. For example:

$$\overline{u}_i(y,t) = \frac{1}{L_x L_z} \int_0^{L_x} \int_0^{L_z} u_i(x,y,z,t)\, dxdz. \tag{6.18}$$

6.4.1 Formulation with Reynolds shear stress

Since we are introducing an explicit averaging operator, we can drop the Cess (1958) formula and compute directly the relevant Reynolds stresses from data. We focus specifically on the Reynolds shear stress $-\overline{u'v'}(y,t)$ since it is the one that determines the turbulent mean profile. Figure 6.12 (a) shows this quantity obtained from the minimal flow unit DNS at $Re = 1000$. The turbulent flow in the minimal flow unit is characterised by temporal intermittency (Jiménez and Moin, 1991; Xi and Graham, 2010, 2012). For example, the figure shows that between $t = 2000$ and $t = 2250$ the Reynolds stress falls to a low amplitude and then recovers (hibernation). We encode this temporal behaviour in the scalar function q, using the following formula:

$$-\overline{u'v'}(y,t) \approx q(t)g(y), \tag{6.19}$$

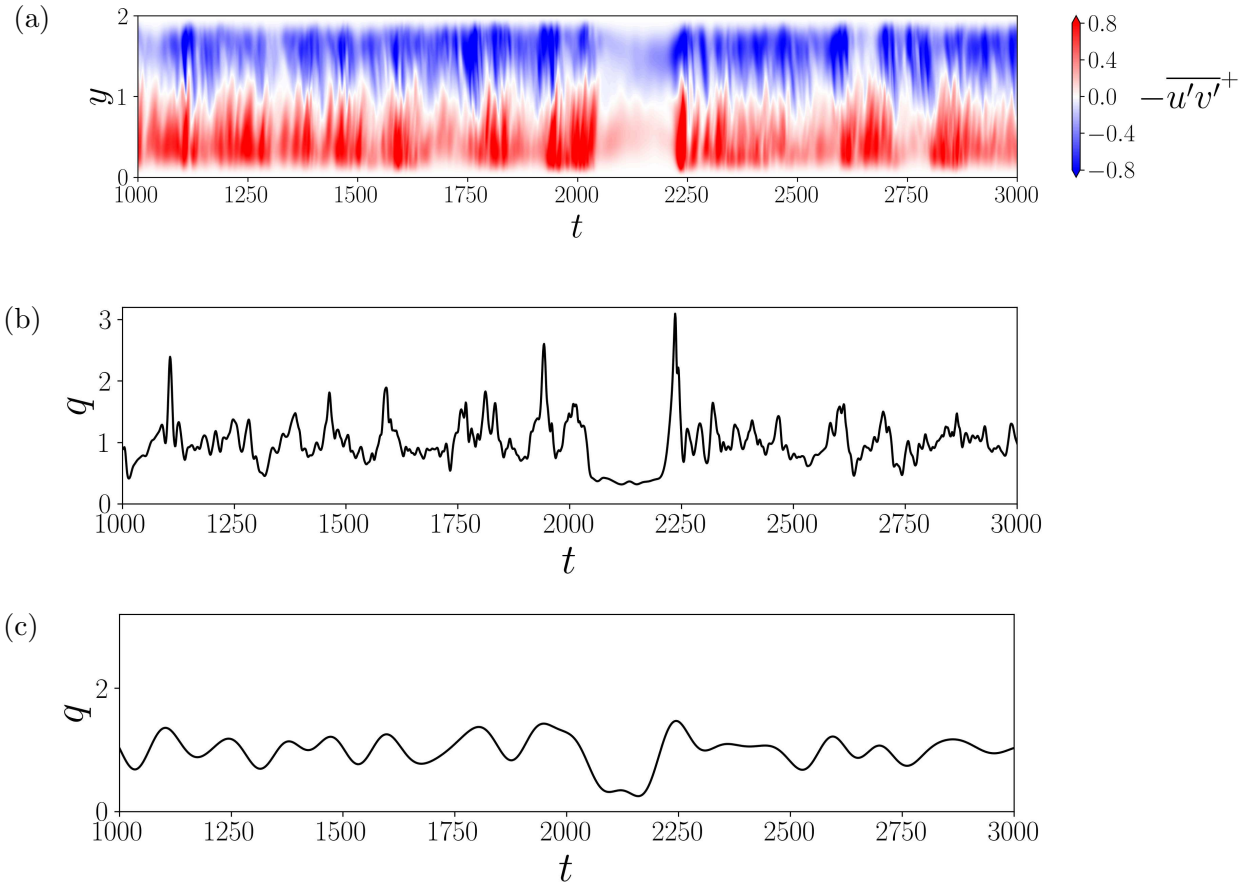

Figure 6.12: (a) Temporal behaviour at $Re = 1000$ of the Reynolds shear stress averaged over the wall-parallel directions of the minimal flow unit. (b) Temporal dynamics of $q(t)$ computed with (6.21). (c) Filtered version of (b).

where $g(y)$ is the long time average of $-\overline{u'v'}$:

$$g(y) = \lim_{T\to\infty} \frac{1}{T} \int_0^T -\overline{u'v'}(y,t)\, dt. \tag{6.20}$$

The formula (6.19) is an approximation because the dynamics of the Reynolds stress also depend on the wall-normal direction. This approximation, however, reflects our assumption of separation of variables (6.2). The time series $-\overline{u'v'}(y,t)$ and its long-time average can be directly computed from DNS data. The time series of q must be computed from these quantities, but they depend on y while q does not. However, the functional scalar product of $g(y)$ with the two sides of (6.19) can be taken and rearranged to:

$$q(t) = \frac{\int_0^2 -\overline{u'v'}(y,t)g(y)\, dy}{\int_0^2 g(y)g(y)\, dy}. \tag{6.21}$$

This formula implies that the long-time average of $q(t)$ is 1. Panel (b) in figure 6.12 shows the time series of q corresponding to panel (a) of the same figure. The comparison of the two panels

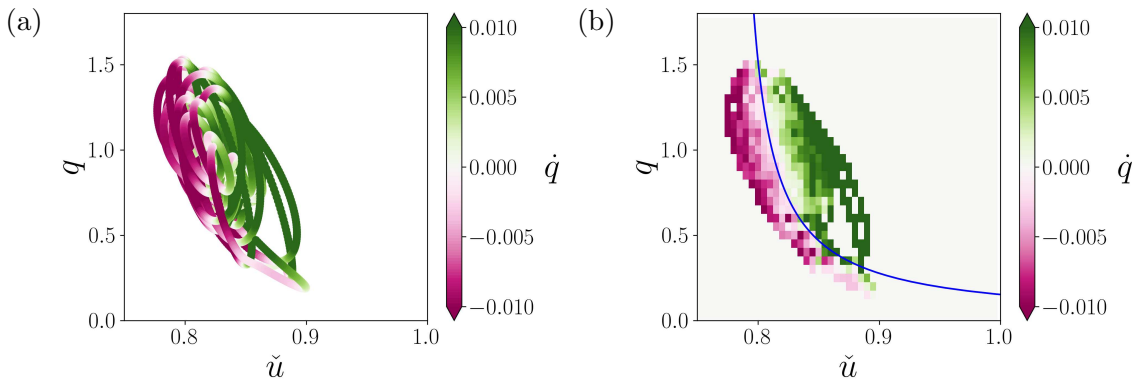

Figure 6.13: (a) Visualisation at $Re = 1000$ of the temporal dynamics of $q(t)$ in the $\breve{u} - q$ phase-plane for the Reynolds stress data-driven model. The points are coloured with the temporal derivative of $q(t)$, $\dot{q}$. (b) Coarse-grained version of (a), see the text for the method. The blue curve is the nullcline obtained after fitting (6.22) to the data.

demonstrates that q mimics correctly the amplitude of the Reynolds shear stress. This kind of time series will be used to extract information about the reaction function $R(q, \breve{u})$ using the principle that $\dot{q} = R(q, \breve{u})$[1] in a local dynamics context. Since we are interested in large-scale dynamics, the time series is smoothed with a Gaussian filter in order to remove what can be assimilated with small-scale fluctuations, including small-scale intermittency. The cutoff of the filter was fixed empirically to $f_{cf} = 1/100$[2]. In figure 6.12, the filtered time series corresponding to panel (b) is shown in panel (c).

From DNS data, the time series $\breve{u}(t)$ is extracted by rescaling the centreline value of $\overline{u}(y, t)$. This time series is also filtered with the same filter and parameters used for $q(t)$. With $q(t)$ and $\breve{u}(t)$, the trajectory of the system in the $\breve{u} - q$ phase plane can be visualised. This trajectory is shown in figure 6.13 (a) at $Re = 1000$. The points are coloured by the corresponding value of $\dot{q}$ (equal to the reaction function according to our hypothesis). Since this is a low-dimensional visualisation of a high-dimensional dynamical system, the trajectory overlaps with itself several times. However, two regions associated with different signs of $\dot{q}$ are discernible. This suggests that a single-valued reaction function can indeed be defined approximately. The approximation is performed with the following method. The $\breve{u} - q$ plane is divided into a grid of 50×36 small rectangles of size 0.005×0.05 to discretise the portion of the $\breve{u} - q$ plane $[0.75, 1.0] \times [0, 1.8]$. Each of these squares may include more than one data point. The values of $\dot{q}$ are averaged on each square. In this way, a grid with a single value of $\dot{q}$ for each $\breve{u} - q$ coordinate is obtained. The resulting coarse-grained plot is shown in figure 6.13(b) for the data shown in panel (a). Each value is also associated with the number of original points contained in that square. This number will play the role of a weight in the regression that we describe now.

The reaction function is found by fitting the data to the following expression:

$$R(q, \breve{u}) = \zeta_0 q((\breve{u} - \zeta_2)q - \zeta_1), \tag{6.22}$$

[1]The dot denotes the temporal derivative.
[2]The frequency scale is U_b^*/h^*

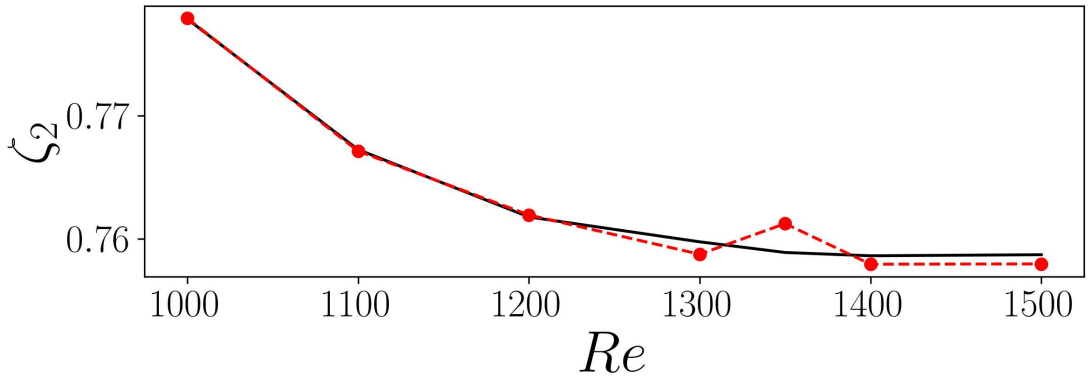

Figure 6.14: Regression coefficient ζ_2 as a function of Re. The red points are computed by individual regressions at seven different Re. The black line is (6.23). Reynolds stress data-driven model.

where ζ_0, ζ_1 and ζ_2 are the three regression parameters. This form of the reaction function is based on some empirical considerations: (i) the reaction function must be zero for laminar flow ($q = 0$) because laminar flow is an absorbing state (turbulence is not spontaneously triggered from laminar flow); (ii) the other nullcline should separate the pink and the green regions in figure 6.13 and seems to behave like a hyperbola. A general form of hyperbola is $q = \zeta_1/(\breve{u} - \zeta_2)$, which gives the term in the parenthesis in (6.22). The coefficient ζ_0 premultiplies everything and plays the same role as α in the last section. However, now it will be obtained from data and will not be a free parameter anymore. The three coefficients are found by least-squares regression (Quarteroni et al., 2006) applied to the coarse-grained data described in the last paragraph. Each value of $\dot{q}$ in a given square is repeated N times in the data matrix, where N is the number of original points present in that square.

The regression is performed at seven different Re, namely $Re = 1000, 1100, 1200, 1300, 1350, 1400, 1500$. In figure 6.13 (b), the blue curve is the nullcline as computed by the regression. As expected, this curve divides well the positive and the negative values of $\dot{q}$. For each Re, different coefficients are obtained. Nevertheless, the variation of ζ_0 and ζ_1 with Re is of minor importance for our purposes. Therefore, we simply average the obtained values and use the average at every Re. We find $\zeta_0 = 0.2548$ and $\zeta_1 = 0.03307$. Conversely, the variation of ζ_2 with Re is important because ζ_2 gives the abscissa of the vertical asymptote of the nullcline. Therefore, when changing ζ_2, the position of the nullcline changes (hence ζ_2 plays a role similar to the r of the previous section). The variation of ζ_2 with Re is fitted by the following function:

$$\zeta_2 = \left(2.6846 \times 10^{-7} Re^2 - 6.7249 \times 10^{-4} Re\right)(1 - S) - 0.42594 S + 1.1830, \tag{6.23}$$

with

$$S = \frac{1}{\pi}\left[\arctan\left(\frac{Re - 1300}{50}\right) + \frac{\pi}{2}\right]. \tag{6.24}$$

This function is plotted in figure 6.14 along with the values computed by the individual $R(q, \breve{u})$ regressions. These formulas specify the reaction function.

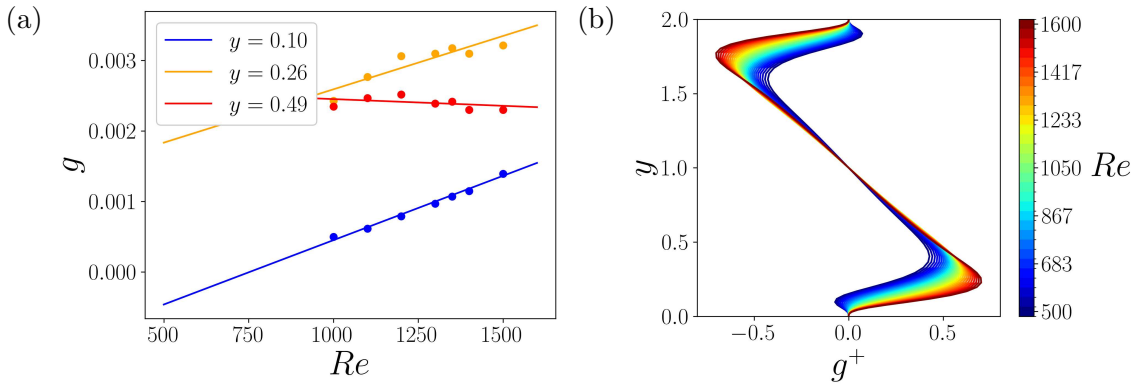

Figure 6.15: (a) Linear regression with Re of the long-time averaged Reynolds shear stress profile at different wall-normal positions. (b) Resulting Reynolds shear stress profiles at various Re.

The full model takes the form (6.6) with $\tau_{12}^R = g(y)$ and the other components equal to zero. The function $g(y)$ also depends on Re. To simplify the analysis of the model, we assume a linear dependence of $g(y)$ on Re, namely

$$g(y) = g_1(y)Re + g_0(y), \tag{6.25}$$

and we perform a least-squares fit of DNS data to find the functions $g_1(y)$ and $g_0(y)$. The result of this additional regression is shown in figure 6.15 (a) at three different wall-normal locations. The resulting Reynolds stress profiles for different Re are shown in panel (b) of the same figure. The linear fit is almost certainly inaccurate at very low Re (< 850). It was not possible to obtain data in minimal flow units at these low Re. Anyway, the very low Re range is used only to compute the saddle-node bifurcation of the turbulent fixed point, therefore it has a minor importance because the linear instability of interest here is expected at considerably higher Re.

With this closure, the fixed points of the model can be computed using the following system of equations:

$$\begin{cases} \dfrac{d^2U}{dy^2} + Q\dfrac{dg}{dy} + f_b = 0, \\ \dfrac{1}{2}\displaystyle\int_0^2 U\ dy = 1, \\ R(\breve{U}, Q) = 0. \end{cases} \tag{6.26}$$

This system is solved numerically with a bisection algorithm analogous to the one described in 6.3.1. From the first equation of (6.26), it is easy to see that the $\breve{u}-$nullclines will be straight lines. This is indeed the case, as shown in figure 6.16 (a). The $q-$nullclines for different Re are shown in panel (b) of the same figure. The intersection of the straight lines with the hyperbolas will generate two fixed points in addition to the laminar solution (see Subsection 6.4.3).

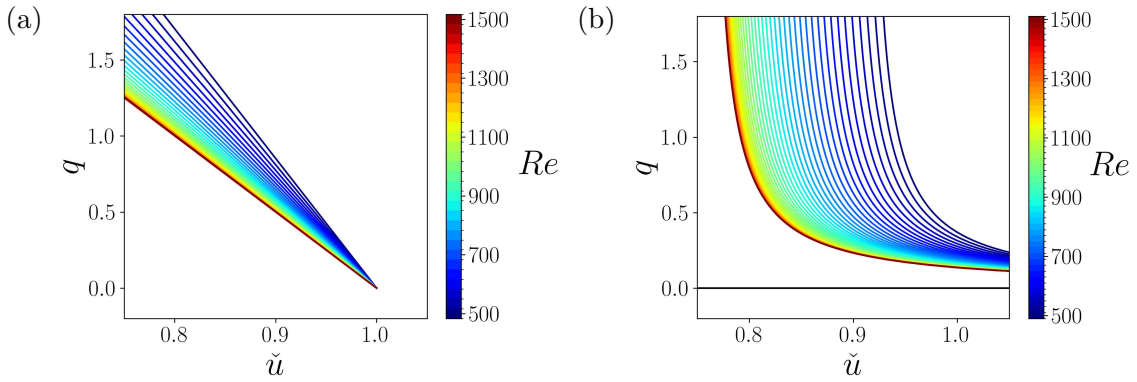

Figure 6.16: (a) $\breve{u}-$nullclines and (b) $q-$nullclines for the Reynolds stress data-driven model at various Re.

This subsection closes with the linearised stability equations for this closure. With the *ansatz*

$$\begin{bmatrix} u_i' \\ p' \\ q' \end{bmatrix} = \begin{bmatrix} \hat{u}_i(y) \\ \hat{p}(y) \\ \hat{q} \end{bmatrix} e^{\iota(k_x x + k_z z) + \sigma t}, \quad k_x, k_z \in \mathbb{R},\ \sigma \in \mathbb{C}, \tag{6.27}$$

the LSA equations are:

$$0 = \iota k_x \hat{u} + \frac{d\hat{v}}{dy} + \iota k_z \hat{w}, \tag{6.28a}$$

$$\sigma \hat{u} = -\iota k_x U \hat{u} - \frac{dU}{dy}\hat{v} - \iota k_x \hat{p} + \frac{1}{Re}\left(-k_x^2 - k_z^2 + \frac{d^2}{dy^2}\right)\hat{u} + \frac{dg}{dy}\hat{q}, \tag{6.28b}$$

$$\sigma \hat{v} = -\iota k_x U \hat{v} - \frac{d\hat{p}}{dy} + \frac{1}{Re}\left(-k_x^2 - k_z^2 + \frac{d^2}{dy^2}\right)\hat{v} + \iota k_x g \hat{q}, \tag{6.28c}$$

$$\sigma \hat{w} = -\iota k_x U \hat{w} - \iota k_z \hat{p} + \frac{1}{Re}\left(-k_x^2 - k_z^2 + \frac{d^2}{dy^2}\right)\hat{w}, \tag{6.28d}$$

$$\sigma \hat{q} = -\iota k_x \hat{q} + \zeta_0 Q^2 \mathcal{F}\hat{u} + \zeta_0\left(2\breve{U}Q - 2\zeta_2 Q - \zeta_1\right)\hat{q} - \frac{D}{Re}(k_x^2 + k_z^2)\hat{q}, \tag{6.28e}$$

with $\mathcal{F}$ defined by (6.12).

6.4.2 Formulation with eddy viscosity

The data-driven closure can be reformulated by introducing an eddy viscosity. This formulation is based on the approximation:

$$-\overline{u'v'}(y,t) \approx q(t)\nu_t(y)\frac{\partial \overline{u}}{\partial y}(y,t). \tag{6.29}$$

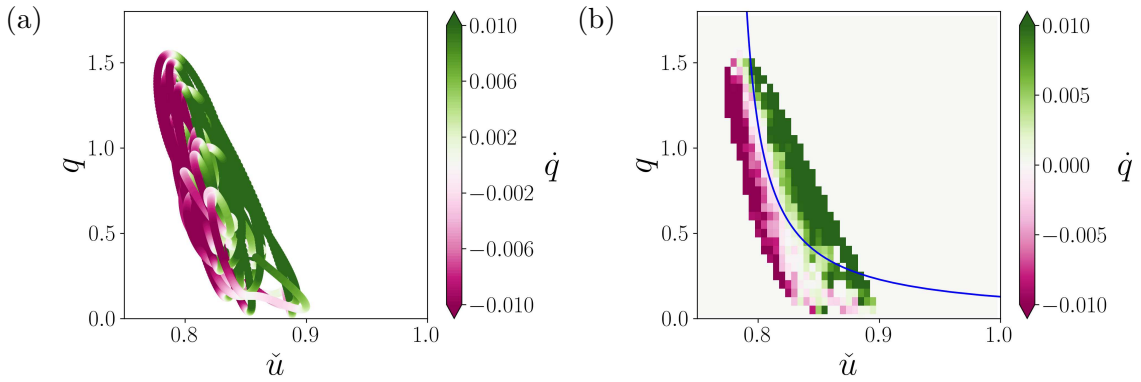

Figure 6.17: (a) Visualisation at $Re = 1000$ of the temporal dynamics of $q(t)$ in the $\breve{u} - q$ phase-plane for the eddy viscosity data-driven model. The points are coloured with the temporal derivative of $q(t)$, $\dot{q}$. (b) Coarse-grained version of (a). The blue curve is the nullcline obtained after fitting (6.22) to the data.

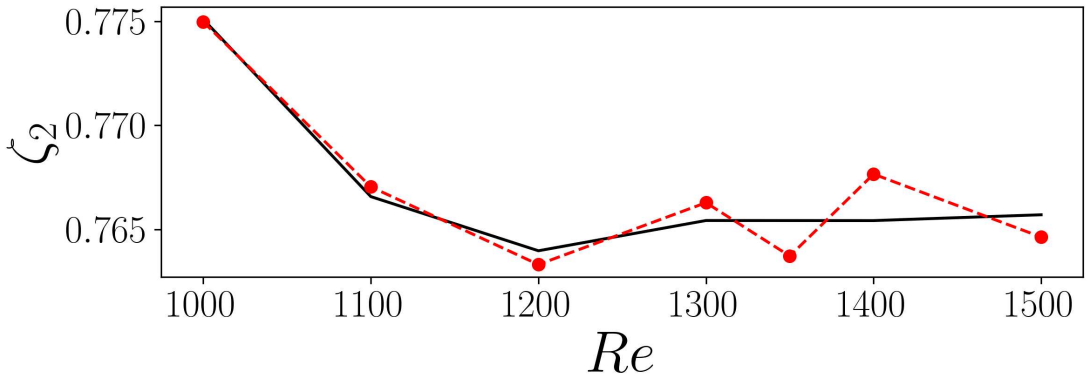

Figure 6.18: Regression coefficient ζ_2 as a function of Re. The red points are computed by individual regressions at seven different Re. The black line is (6.32). Eddy viscosity data-driven model.

The profile of ν_t is computed with DNS data using the formula[3]:

$$\nu_t(y) = \frac{\lim_{T\to\infty} \int_0^T -\overline{u'v'}(y,t)\, dt}{\lim_{T\to\infty} \int_0^T \frac{\partial \overline{u}}{\partial y}(y,t)\, dt}. \tag{6.30}$$

As before, the quantities $-\overline{u'v'}(y,t)$, $\nu_t(y)$ and $\partial_y \overline{u}(y,t)$ can be directly computed from DNS data. Denoting $s(y,t) = \nu_t(y)\partial_y \overline{u}(y,t)$, the time series of q can be computed as:

$$q(t) = \frac{\int_0^2 -\overline{u'v'}(y,t)s(y,t)\, dy}{\int_0^2 s(y,t)s(y,t)\, dy}. \tag{6.31}$$

Contrary to (6.21), this expression does not imply that the long-time average of $q(t)$ is 1. As before, the $q(t)$ time series and the corresponding $\breve{u}(t)$ time series are smoothed with a Gaussian filter with

[3]This formula is singular at the channel centre, but the singularity can be eliminated with L'Hopital's rule.

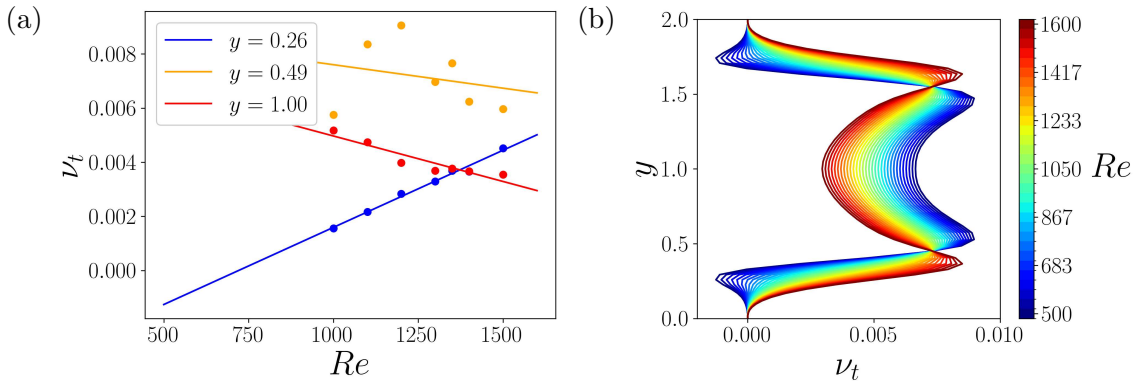

Figure 6.19: (a) Linear regression with Re of the long-time averaged eddy viscosity profile at different wall-normal positions. (b) Resulting eddy viscosity profiles at various Re.

$f_{cf} = 1/100$. The plot of these time series is very similar to figure 6.12 (b) and (c) (not shown). The trajectory of the system in the $\breve{u} - q$ phase plane is shown in figure 6.17 (a) at $Re = 1000$. Panel (b) shows the corresponding coarse-grained data obtained with the same procedure as described in Subsection 6.4.1. The reaction function takes the form (6.22) with the coefficients $\zeta_0 = 0.53767$, $\zeta_1 = 0.027116$ and

$$\zeta_2 = \left(3.0652 \times 10^{-7} Re^2 - 7.3276 \times 10^{-4} Re\right)(1 - S) - 0.43856S + 1.2020, \tag{6.32}$$

with

$$S = \frac{1}{\pi}\left[\arctan\left(\frac{Re - 1300}{50}\right) + \frac{\pi}{2}\right]. \tag{6.33}$$

The new ζ_2 function is shown in figure 6.18. These formulas specify the reaction function. The reaction function obtained with the eddy viscosity formulation is only slightly different from that obtained with the Reynolds stress formulation. Therefore, the $q-$nullcline does not change notably either. However, the $\breve{u}-$nullcline does change radically.

To compute the $\breve{u}-$nullcline at several Re, we perform a linear least-squares fit of the eddy viscosity profiles with respect to Re:

$$\nu_t(y) = \nu_t^1(y) Re + \nu_t^0(y). \tag{6.34}$$

The results of this additional regression are shown in figure 6.19. The panel (a) of the figure shows that the linear fit on the eddy viscosity is less satisfactory with respect to the one performed on the Reynolds shear stress (figure 6.15 (a)).

The full model has the form (6.4), while the fixed points are given by the system (6.9). The $\breve{u}-$nullclines are no longer straight lines. They are the curves shown in figure 6.20 (a). The $q-$nullclines are shown in panel (b) of the same figure. The curved shape of the $\breve{u}-$nullclines makes the intersections with the hyperbolas less trivial than before.

The other important change that the eddy viscosity formulation brings with respect to the Reynolds

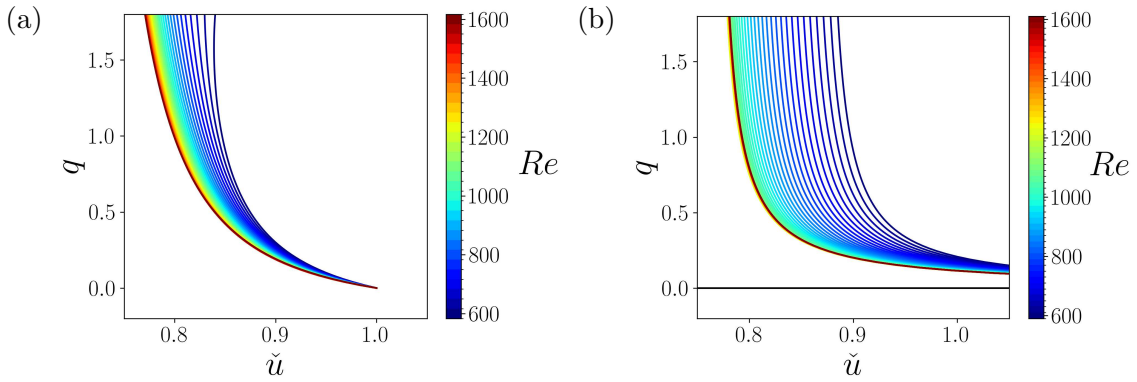

Figure 6.20: (a) $\breve{u}-$nullclines and (b) $q-$nullclines for the eddy viscosity data-driven model at various Re.

stress formulation is in the LSA equations, which read:

$$0 = \iota k_x \hat{u} + \frac{d\hat{v}}{dy} + \iota k_z \hat{w}, \tag{6.35a}$$

$$\begin{aligned}\sigma\hat{u} = &-\iota k_x U\hat{u} - \frac{dU}{dy}\hat{v} - \iota k_x\hat{p} + \left(\frac{1}{Re} + \nu_t Q\right)\left(-k_x^2 - k_z^2 + \frac{d^2}{dy^2}\right)\hat{u} \\ &+ Q\frac{d\nu_t}{dy}\left(\frac{d\hat{u}}{dy} + \iota k_x\hat{v}\right) + \frac{d}{dy}\left(\nu_t\frac{dU}{dy}\right)\hat{q},\end{aligned} \tag{6.35b}$$

$$\begin{aligned}\sigma\hat{v} = &-\iota k_x U\hat{v} - \frac{d\hat{p}}{dy} + \left(\frac{1}{Re} + \nu_t Q\right)\left(-k_x^2 - k_z^2 + \frac{d^2}{dy^2}\right)\hat{v} + 2Q\frac{d\nu_t}{dy}\frac{d\hat{v}}{dy} \\ &+ \iota k_x\nu_t\frac{dU}{dy}\hat{q},\end{aligned} \tag{6.35c}$$

$$\begin{aligned}\sigma\hat{w} = &-\iota k_x U\hat{w} - \iota k_z\hat{p} + \left(\frac{1}{Re} + \nu_t Q\right)\left(-k_x^2 - k_z^2 + \frac{d^2}{dy^2}\right)\hat{w}, \\ &+ Q\frac{d\nu_t}{dy}\left(\frac{d\hat{w}}{dy} + \iota k_z\hat{v}\right),\end{aligned} \tag{6.35d}$$

$$\sigma\hat{q} = -\iota k_x\hat{q} + \zeta_0 Q^2\mathcal{F}\hat{u} + \zeta_0\left(2\breve{U}Q - 2\zeta_2 Q - \zeta_1\right)\hat{q} - \frac{D}{Re}(k_x^2 + k_z^2)\hat{q}, \tag{6.35e}$$

using, as before, the *ansatz* (6.27) and with $\mathcal{F}$ defined by (6.12). These equations contain a velocity dissipation term proportional to $Q\nu_t$, which was present in (6.11) and absent in (6.28).

6.4.3 Results

In this subsection, the results of the two data-driven models are compared. First of all, the generation of non-laminar fixed points is analysed in figure 6.21. For both models, two fixed points are created by a saddle-node bifurcation for increasing Re. The critical Re is slightly larger for the eddy viscosity version of the model. However, the most important difference is in the curvature of the

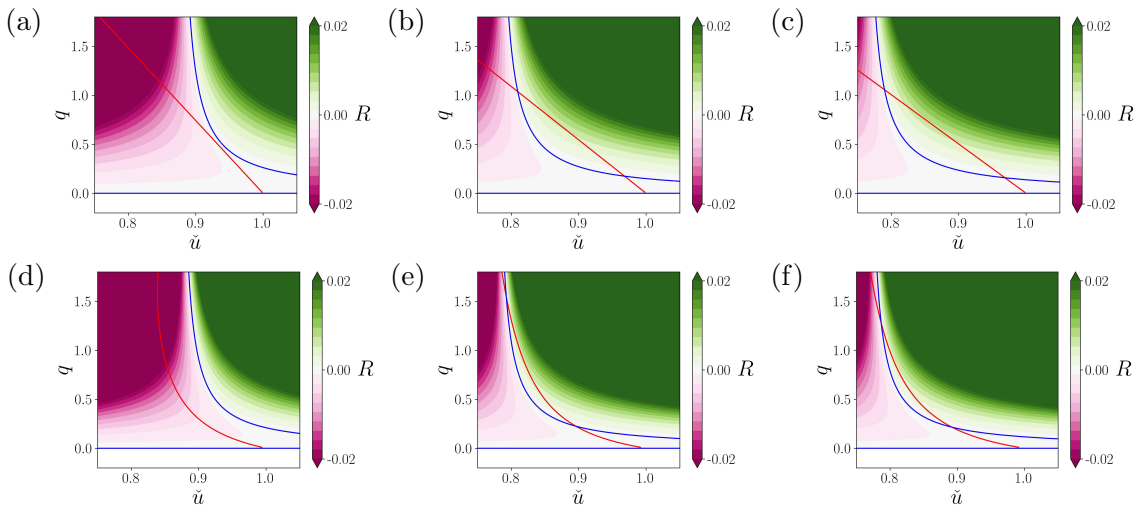

Figure 6.21: Contours of the reaction function (6.22) for (a-c) the Reynolds stress data-driven model and (d-f) the eddy viscosity data-driven model. Increasing Re from left to right: (a,d) $Re = 600$, (b,e) $Re = 1000$ and (c,f) $Re = 1500$. The blue lines are the $q-$nullclines ($R = 0$) while the red line is the $\breve{u}-$nullcline.

$\breve{u}-$nullclines (red curves). While for the Reynolds stress model the nullcline is a straight line, for the eddy viscosity model the nullcline is a curve which seems to have a vertical asymptote as a hyperbola. This fact has a consequence on the vertical position of the upper branch fixed point for varying Re. With the Reynolds stress model, this point stays near $q = 1$, whereas with the eddy viscosity model, the fixed point rises rapidly to $q \approx 1.8$ and then falls back towards 1.2. This behaviour is summarised in figure 6.22, which shows the bifurcation diagram using both Q and $\breve{U}$ (capital letters denote fixed points) as a function of Re. On one hand, the proximity of the upper-branch Q to 1 obtained with the Reynolds stress model is nicely consistent with the long-time average of q computed from the DNS data. On the other hand, the Re dependence of the upper-branch Q obtained with the eddy viscosity model is less interpretable.

For the two models, we linearise around the upper-branch fixed point (uniform turbulent solution) and study the linear stability problem varying k_x, k_z and Re. The first row of figure 6.23, panels from (a) to (c), shows the leading growth rates obtained with the Reynolds stress model for a range of k_x and k_z and three different Re. There is a large region of instability (red region) which grows with Re. At all Re, the $k_x = 0$ modes are unstable. At the largest Re considered in the figure, stability is confined to a small region and all the modes with $k_x = 0$ and/or $k_z = 0$ are unstable. The upper turbulent fixed point is unstable for all the values of Re in the range of interest. This behaviour is obviously inconsistent with observations.

The remaining two rows of figure 6.23 show the results obtained with the eddy viscosity model. The middle row, panels from (d) to (f), are obtained with $D = 1$. Even with this closure, there is a large region of instability. However, the qualitative behaviour is slightly better because the $k_x = 0$ and $k_z = 0$ tend to be stabilised and the region of instability reduces with Re. These little positive aspects motivated further computations in a parameter range in which the system is more stable. Therefore, the last row of figure 6.23, panels from (g) to (i), shows the leading growth rates obtained with the

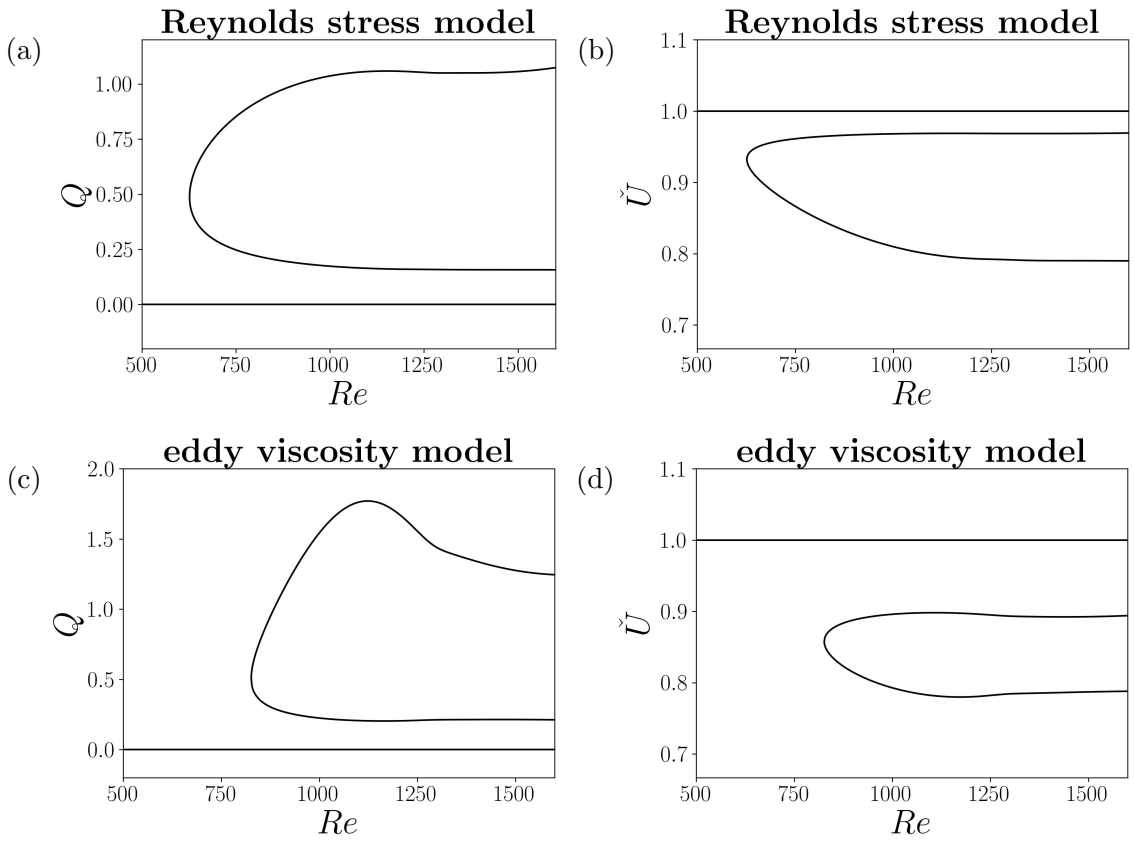

Figure 6.22: Bifurcation diagrams of the fixed points of the data-driven models as a function of Re.

eddy viscosity model and $D = 80$. The plots in this last row resemble those of figure 6.4 much more. The corresponding leading eigenmodes also resemble the one shown in figures 6.5 and 6.6. This result is consistent with the finding of Chapter 5 that the eddy viscosity term is responsible for the correct wavenumber selection. However, the turbulent fixed point is still unstable for all values of Re in the range of interest.

In summary, the LSA of the data-driven models did not yield the desired results, as the system selects neither the expected wavelengths nor a critical Re. Therefore, nonlinear simulations of these models have not been performed.

6.5 Discussion

This chapter aimed to open new perspectives on the nonlinear modelling of laminar-turbulent patterns. Some results can be considered encouraging, others are more disappointing. The present results are not conclusive, but interesting caveats can be identified.

Until now, the best model in terms of results is the one presented in Section 6.3, the most intuition-based one. It has been shown, as a proof of concept, that the various parameters involved can be

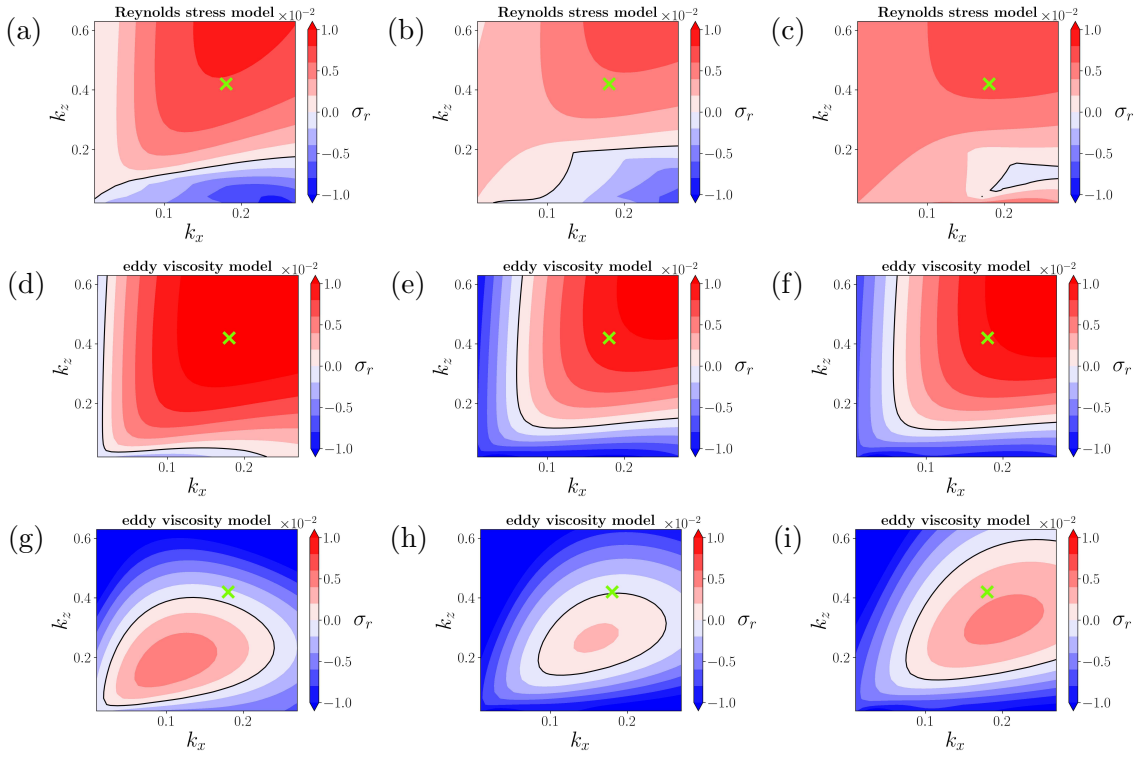

Figure 6.23: Leading growth rates from LSA of the upper branch fixed point of the data-driven models as a function of k_x and k_z. (a-c) Reynolds stress model, (d-f) eddy viscosity model with $D = 1$ and (g-i) eddy viscosity model with $D = 80$. Re incresing from left to right: (a) $Re = 800$, (d,g) $Re = 850$, (b,e,h) $Re = 1000$ and (c,f,i) $Re = 1500$. The black contour separates the stable (blue) and unstable (red) regions. The green cross denotes the critical wavenumbers of Kashyap et al. (2022), $k_x = 0.18$ and $k_z = 0.42$.

adjusted in order to make the linear instability of the turbulent fixed point critical at the desired parameter values. Moreover, a stable laminar-turbulent pattern was obtained in the nonlinear simulation of the model in a small domain. In larger domains, the model gives, at least transiently, patterns with well-defined wavelengths and several orientations, similar to those observed in DNS. However, the nonlinear behaviour of this model can be problematic in some respects. In particular, the fixed point becomes linearly unstable only very near the saddle-node bifurcation that generates it, while it shows a prominent subcritical character in the nonlinear simulations. Moreover, in the large domains, the system seems unable to keep a stable nonlinear solution characterised by the linearly unstable wavelengths. In short, the model has a more complex behaviour than desired.

We must remark that not every parameter was thoroughly tested in the nonlinear simulations. For example, the nonlinear bifurcation diagram was computed keeping $Re = 1000$ and changing r. But the bifurcation diagram shown in figure 6.10 could be different at another Re. Also, the influence of the computational domain size on the subcritical character of the instability was not assessed. Further numerical investigation is therefore possible with this model.

In the second part of the chapter, an effort was made to relate more directly the reaction term of the q equation (6.3) to Navier-Stokes turbulence. To have a manageable model, data has been

encapsulated in regression formulas. Nevertheless, the LSA results revealed that this approach does not necessarily improve the model. There can be several possible explanations for this failure of data-driven closures. For example, a crude dimensionality reduction was implied in the extraction of the reaction function from the coarse-grained data on the plane $\breve{u} - q$. Indeed, the choice of a single scalar quantity $\breve{u}$ to implement in the reaction function is a crude assumption. In principle, the whole velocity field could influence the q reaction. There is another, more trivial, reason which could explain why the data-driven models performed worse than the model based on the Barkley (2011a) reaction function. In the data-driven models, most of the coefficients have been tuned *a priori*, while in the other model we have left more free parameters (α, r, etc...) that could be tuned *a posteriori*. Clearly, tuning *a posteriori* more parameters increases the *leeway* of the model, but makes its analysis more demanding (more parameters imply more computations).

In conclusion, we believe that this chapter contains interesting efforts. Hopefully, the caveats exposed in this work will lead to better models in the future.

Chapter 7

Conclusions and Perspectives

7.1 Overall conclusions

In this thesis, we have investigated the dynamics of coherent structures in the turbulent channel flow. It has been known for a long time that structures like velocity streaks undergo instabilities. Here, we have analysed these instabilities under a new light. A light focusing on multiscale interactions.

Throughout the chapters of this thesis, various phenomenologies have been explored with an innovative combination of numerical techniques.

In Chapter 3, nonlinear optimal perturbations were computed with respect to a fully turbulent snapshot. When the optimal perturbation was injected in the flow, the pre-existing coherent structures underwent a sudden breakdown, generating an intense, transient energy cascade. We analysed, in particular, the increased production of extreme dissipation events, and we have shown with the CST-POD algorithm that the extreme events generated by the optimal perturbations have the same structure as those naturally occurring in the turbulent flow. Therefore, we argue that the destabilising mechanism revealed by the nonlinear optimal perturbation is a possible source of extreme dissipation in the turbulent channel flow.

In Chapter 4, the instability of coherent structures was addressed more directly by linearising around a base flow made of periodic streaks. Unlike previous studies, we have considered sub-harmonic or detuned instabilities characterised by wavelengths much larger than the streak wavelength. If the considered streaks are inclined with respect to the streamwise direction, an instability is found by increasing the Reynolds number Re. The wavelengths as well as the wall-normal structure of the unstable eigenmodes are comparable to those of Large Scale Motions (LSMs). The sub-harmonic or detuned instabilities of near-wall structures are, therefore, a viable mechanism to generate LSM in the turbulent channel flow. This finding may explain the transfer of energy from small to large scales observed in the recent studies of Doohan et al. (2021, 2022).

In Chapter 5, the methodology of Chapter 4 is revisited and applied at lower Re. With this revised approach, we model the linear instability of the turbulent channel flow recently reported by Kashyap et al. (2022). While a linear model based on the mean flow predicts stability at all Re (Kashyap et al.,

2024), including the streaks in the base flow, we found unstable eigenmodes reminiscent of the patterns and corresponding large-scale flow observed in DNS (Duguet and Schlatter, 2013). We computed a critical $Re - A_s$ curve, with A_s the amplitude of the streaks, and a critical wavevector which is not far from the one of Kashyap et al. (2022) (the inclination angle of the pattern is well matched too). Importantly, we have analysed the linear stability results by means of an energy budget equation, and we have found that both the streaks and the eddy viscosity play an important role in the model that allows the selection of relevant wavelengths. This fact can be seen as a modelling insight, but it also suggests that, physically, the small-scale fluctuations have an important role in the emergence of this instability.

The application of linear stability analysis to turbulent flows poses certain challenges. First of all, it is not straightforward to understand *what* becomes unstable. While in the context of transition to turbulence, it is clear that the base flow is the laminar flow or another relevant invariant solution, for turbulent flows, the choice of the base flow is part of the modelling. In addition to the base flow, an appropriate strategy must be devised to model incoherent fluctuations. This double closure problem (choice of the base flow and of the model equations) is the main source of difficulty involved in the linear stability analyses presented in this thesis. Because of these difficulties, it has not been straightforward to find the instabilities exposed in this work, and it may not be straightforward to reproduce them in the future.

In this thesis, we have done our best to base our modelling decisions on rational arguments. For this reason, the approaches have evolved throughout the chapters, as we have tried to improve both sides of the closure problem (base flow and equations). The work presented in Chapter 6 is our last effort in this sense. In this chapter, we have abandoned the stability analysis of the streaks to search for a model that provides all the ingredients directly from the equations, without the need for ad-hoc base flows and forcings. This goal has been achieved, although only partially.

Finally, notwithstanding all the necessary assumptions, this work has pointed out interesting physical processes. In particular, the idea that small-scale structures can interact with large-scale perturbations and generate large-scale coherent structures deserves further investigation. Some ideas are discussed below.

7.2 Perspectives

In Chapter 4, the instability of near-wall streaks leading to LSMs has been presented using as base flow streaks the POD modes computed from DNS data of minimal flow unit simulations. However, there are numerous alternatives to model these coherent structures. For example, in Chapter 5, a similar stability analysis was performed using the streaks computed with the resolvent analysis of the mean profile. It was argued that the resolvent streaks have several advantages with respect to POD modes: easier to compute (do not need precursor DNS), higher degree of symmetry and, also, their wavelength and inclination can be freely chosen. Moreover, since they do not need a precursor DNS, resolvent streaks could facilitate the analysis of actual high$-Re$ regimes ($Re_\tau \geqslant 5000$). This would be a welcome addition to the work performed in this thesis and may lead to interesting results. Lastly,

according to our experience, the resolvent does not have convergence issues, contrary to the POD modes. Therefore, the results obtained with the resolvent streaks would be more easily reproducible.

The physical mechanism of the instability at high Re can be analysed more deeply. In Chapter 4, we have focused especially on the comparison of the eigenmodes with DNS and experiments, but we have said little about the mechanism that induces the instability. The energy budget equation used in Chapter 5 could be a good starting point. Another idea would be to analyse the base flow - perturbation bilinear terms present in the stability equations to investigate how the large-scale component of the eigenmode is created.

Furthermore, we have said in Section 1.2 that large-scale structures can also survive without smaller-scale structures. The bottom-up instability is not necessary to maintain LSMs. Therefore, a DNS study should be performed in the channel flow in order to clarify what is the net contribution of large-scale instabilities to the total production of LSMs. Similar studies of interscale interactions have already been performed (see Section 1.2.1.3), but a more direct comparison with the modal instability presented in this thesis could still be interesting.

Concerning the modulations and laminar-turbulent patterns at low Re, the work on the nonlinear model (Chapter 6) is itself a perspective work. Encouraging results have already been obtained, since an instability that saturates to a laminar-turbulent pattern has been found. However, the nonlinear behaviour of the model can be improved, especially concerning its marked subcritical character and its behaviour in large domains. Probably, the idea of a direct link with DNS data should be abandoned until the effect of an explicit coarse-graining operator (like a low-pass filter) on the flow dynamics is better understood. In the meantime, it could be instructive to find a model that mimics the correct phenomenology without necessarily searching to relate the model variables to DNS data. Our *preliminary* model based on the Barkley (2011a) reaction function seems promising in this respect.

Moreover, it would be interesting to investigate whether a model that captures well the turbulent flow instability is also able to capture the patter/solitary stripe transition and the critical scaling at onset (*i.e.* for turbulent fraction approaching zero). Such a model would be useful to investigate scaling laws that are usually not accessible by DNS and experiments due to the huge domains required to avoid finite-size effects.

Another important question about turbulence modulations that must be addressed in the near future is their characterisation in other flows. Both Kashyap (2021) thesis and this thesis have analysed the modulations in the channel flow. It is important to assess whether the modulations that precede the patterns in the top-down point of view are observed in other wall-bounded flows as well (Couette flow, Taylor-Couette flow, etc...). The work of Duguet et al. (2010a) as well as the recent works of Gomé et al. (2023b) and Manneville and Shimizu (2025) suggest that modulations are not observed in Couette flow, but a direct comparison in this respect between channel and Couette flow is lacking in the literature. Modulations seem to be present in Taylor-Couette flow, as already suggested by the early works of Prigent et al. (2002, 2003) and confirmed more recently by the DNS of Berghout et al. (2020). Moreover, the ongoing PhD thesis of Arthur Viallefont at the Laboratoire Ondes et Milieux Complexes of Le Havre University suggests that the turbulent Taylor-Couette flow undergoes a pattern-forming linear instability, similar to the channel flow. In summary, further comparative

studies on different flow configurations would be welcome in the literature. In this respect, we remark that in the formulation of Chapter 6 we have not made any assumptions inherent to the channel flow, except the Cess (1958) eddy viscosity formula. Therefore, our ideas can be easily extended and tested on other shear flows.

Lastly, we have seen in figure 5.37 that the velocity Fourier spectrum in the patterned regime is characterised by two separated bulges of energy. The one at large wavelengths (small wavenumbers in the figure) is the large-scale flow. The other bulge is the ensemble of turbulent scales. The nonlinear model, ideally, aims at separating these two bulges, *i.e.*, solving for the large-scale part without solving the small-scale part. However, different approaches based directly on the Navier-Stokes equations could be used towards this aim. For example, the Generalised Quasilinear approximation (GQL) mentioned in Section 1.2.3 could be an interesting approach. This would be a more conservative modelling approach in which small scales are progressively cut off from the resolved spectrum until the phenomenology is disrupted. This investigation could also reveal interesting facts about scale interactions at these low Re regimes.

One day, some of these ideas could be transformed into results.

Bibliography

[1] H. Abe, H. Kawamura, and H. Choi. Very large-scale structures and their effects on the wall shear-stress fluctuations in a turbulent channel flow up to re τ= 640. *J. Fluids Eng.*, 126(5): 835–843, 2004.

[2] S. Abootorabi and A. Zare. Model-based spectral coherence analysis. *Journal of Fluid Mechanics*, 958:A16, 2023.

[3] R. J. Adrian. Hairpin vortex organization in wall turbulence. *Physics of fluids*, 19(4), 2007.

[4] R. J. Adrian, C. D. Meinhart, and C. D. Tomkins. Vortex organization in the outer region of the turbulent boundary layer. *Journal of fluid Mechanics*, 422:1–54, 2000.

[5] S. Albensoeder, H. C. Kuhlmann, and H. J. Rath. Three-dimensional centrifugal-flow instabilities in the lid-driven-cavity problem. *Physics of fluids*, 13(1):121–135, 2001.

[6] G. Alfonsi and L. Primavera. The structure of turbulent boundary layers in the wall region of plane channel flow. *Proceedings of the Royal Society A: Mathematical, Physical and Engineering Sciences*, 463(2078):593–612, 2007.

[7] F. Alizard. Linear stability of optimal streaks in the log-layer of turbulent channel flows. *Physics of Fluids*, 27(10), 2015.

[8] F. Alizard, S. Cherubini, and J.-C. Robinet. Sensitivity and optimal forcing response in separated boundary layer flows. *Physics of Fluids*, 21(6), 2009.

[9] C. D. Andereck, S. S. Liu, and H. L. Swinney. Flow regimes in a circular couette system with independently rotating cylinders. *Journal of fluid mechanics*, 164:155–183, 1986.

[10] P. Andersson, L. Brandt, A. Bottaro, and D. S. Henningson. On the breakdown of boundary layer streaks. *Journal of Fluid Mechanics*, 428:29–60, 2001.

[11] A. Andreolli, D. Gatti, R. Vinuesa, R. Örlü, and P. Schlatter. Separating large-scale superposition and modulation in turbulent channels. *Journal of Fluid Mechanics*, 958:A37, 2023.

[12] K. Avila, D. Moxey, A. De Lozar, M. Avila, D. Barkley, and B. Hof. The onset of turbulence in pipe flow. *Science*, 333(6039):192–196, 2011.

[13] M. Avila, A. P. Willis, and B. Hof. On the transient nature of localized pipe flow turbulence. *Journal of Fluid Mechanics*, 646:127–136, 2010.

[14] M. Avila, D. Barkley, and B. Hof. Transition to turbulence in pipe flow. *Annual Review of Fluid Mechanics*, 55(1):575–602, 2023.

[15] R. Ayats, L. Klotz, and B. Hof. From directed percolation to patterned turbulence. *arXiv preprint arXiv:2501.08014*, 2025.

[16] B. J. Balakumar and R. J. Adrian. Large-and very-large-scale motions in channel and boundary-layer flows. *Philosophical Transactions of the Royal Society A: Mathematical, Physical and Engineering Sciences*, 365(1852):665–681, 2007.

[17] J. R. Baltzer, R. J. Adrian, and X. Wu. Structural organization of large and very large scales in turbulent pipe flow simulation. *Journal of Fluid Mechanics*, 720:236–279, 2013.

[18] P. R. Bandyopadhyay. Aspects of the equilibrium puff in transitional pipe flow. *Journal of Fluid Mechanics*, 163:439–458, 1986.

[19] J. R. Barber. *Elasticity*. Springer, 2004.

[20] D. Barkley. A model for fast computer simulation of waves in excitable media. *Physica D: Nonlinear Phenomena*, 49(1-2):61–70, 1991.

[21] D. Barkley. Linear analysis of the cylinder wake mean flow. *Europhysics Letters*, 75(5):750, 2006.

[22] D. Barkley. Simplifying the complexity of pipe flow. *Physical Review E*, 84(1):016309, 2011a.

[23] D. Barkley. Modeling the transition to turbulence in shear flows. In *Journal of Physics: Conference Series*, volume 318, page 032001. IOP Publishing, 2011b.

[24] D. Barkley. Theoretical perspective on the route to turbulence in a pipe. *Journal of Fluid Mechanics*, 803:P1, 2016.

[25] D. Barkley and L. S. Tuckerman. Computational study of turbulent laminar patterns in couette flow. *Physical Review Letters*, 94(1):014502, 2005.

[26] D. Barkley and L. S. Tuckerman. Mean flow of turbulent–laminar patterns in plane couette flow. *Journal of Fluid Mechanics*, 576:109–137, 2007.

[27] D. Barkley, B. Song, V. Mukund, G. Lemoult, M. Avila, and B. Hof. The rise of fully turbulent flow. *Nature*, 526(7574):550–553, 2015.

[28] S. J. Benavides and D. Barkley. Model for transitional turbulence in a planar shear flow. *Proceedings of the Royal Society A*, 481(2323):20250391, 2025.

[29] P. Berghout, R. J. Dingemans, X. Zhu, R. Verzicco, R. J. A. M. Stevens, W. Van Saarloos, and D. Lohse. Direct numerical simulations of spiral taylor–couette turbulence. *Journal of Fluid Mechanics*, 887:A18, 2020.

[30] G. Berkooz, P. Holmes, and J. L. Lumley. The proper orthogonal decomposition in the analysis of turbulent flows. *Annual Review of Fluid Mechanics*, 25(1):539–575, 1993.

[31] P. J. Blonigan, M. Farazmand, and T. P. Sapsis. Are extreme dissipation events predictable in turbulent fluid flows? *Physical Review Fluids*, 4(4):044606, 2019.

[32] G. Boffetta, P. Giuliani, G. Paladin, and A. Vulpiani. An extension of the lyapunov analysis for the predictability problem. *Journal of the Atmospheric Sciences*, 55(23):3409–3416, 1998.

[33] S. Bottin and H. Chaté. Statistical analysis of the transition to turbulence in plane couette flow. *The European Physical Journal B-Condensed Matter and Complex Systems*, 6:143–155, 1998.

[34] S. Bottin, O. Dauchot, and F. Daviaud. Intermittency in a locally forced plane couette flow. *Physical Review Letters*, 79(22):4377, 1997.

[35] S. Bottin, F. Daviaud, P. Manneville, and O. Dauchot. Discontinuous transition to spatiotemporal intermittency in plane couette flow. *Europhysics Letters*, 43(2):171, 1998.

[36] E. Brand and J. F. Gibson. A doubly localized equilibrium solution of plane couette flow. *Journal of Fluid Mechanics*, 750:R3, 2014.

[37] L. Brandt. The lift-up effect: the linear mechanism behind transition and turbulence in shear flows. *European Journal of Mechanics-B/Fluids*, 47:80–96, 2014.

[38] J. U. Bretheim, C. Meneveau, and D. F. Gayme. Standard logarithmic mean velocity distribution in a band-limited restricted nonlinear model of turbulent flow in a half-channel. *Physics of Fluids*, 27(1), 2015.

[39] G. Brethouwer, Y. Duguet, and P. Schlatter. Turbulent–laminar coexistence in wall flows with coriolis, buoyancy or lorentz forces. *Journal of Fluid Mechanics*, 704:137–172, 2012.

[40] K. Butler and B. Farrell. Three-dimensional optimal perturbations in viscous shear flow. *Physics of Fluids A: Fluid Dynamics*, 4(8):1637–1650, 1992.

[41] K. M. Butler and B. F. Farrell. Optimal perturbations and streak spacing in wall-bounded turbulent shear flow. *Physics of Fluids A: Fluid Dynamics*, 5(3):774–777, 1993.

[42] C. Canuto, M. Y. Hussaini, A. Quarteroni, and T. A. Zhang. *Spectral methods in fluid turbulence*. Springer, Berlin, 1988.

[43] A. Cassinelli, M. de Giovanetti, and Y. Hwang. Streak instability in near-wall turbulence revisited. *Journal of Turbulence*, 18(5):443–464, 2017.

[44] S. Cerqueira and D. Sipp. Eigenvalue sensitivity, singular values and discrete frequency selection mechanism in noise amplifiers: the case of flow induced by radial wall injection. *Journal of fluid mechanics*, 757:770–799, 2014.

[45] R. D. Cess. A survey of the literature on heat transfer in turbulent tube flow. *Res. Rep*, pages 8–0529, 1958.

[46] M. Chantry, L. S. Tuckerman, and D. Barkley. Turbulent–laminar patterns in shear flows without walls. *Journal of Fluid Mechanics*, 791:R8, 2016.

[47] M. Chantry, L. S. Tuckerman, and D. Barkley. Universal continuous transition to turbulence in a planar shear flow. *Journal of Fluid Mechanics*, 824:R1, 2017.

[48] H. Chaté and P. Manneville. Transition to turbulence via spatio-temporal intermittency. *Physical review letters*, 58(2):112, 1987.

[49] S. Cherubini and P. De Palma. Nonlinear optimal perturbations in a couette flow: bursting and transition. *Journal of Fluid Mechanics*, 716:251–279, 2013.

[50] S. Cherubini and P. De Palma. Minimal-energy perturbations rapidly approaching the edge state in couette flow. *Journal of Fluid Mechanics*, 764:572–598, 2015.

[51] S. Cherubini, P. De Palma, J.-C. Robinet, and A. Bottaro. Rapid path to transition via nonlinear localized optimal perturbations in a boundary-layer flow. *Physical Review E*, 82(6):066302, 2010.

[52] S. Cherubini, P. De Palma, J.-C. Robinet, and A. Bottaro. The minimal seed of turbulent transition in the boundary layer. *Journal of Fluid Mechanics*, 689:221–253, 2011.

[53] S. Cherubini, P. De Palma, and J.-C. Robinet. Nonlinear optimals in the asymptotic suction boundary layer: Transition thresholds and symmetry breaking. *Physics of Fluids*, 27(3):034108, 2015.

[54] M. Cho, Y. Hwang, and H. Choi. Scale interactions and spectral energy transfer in turbulent channel flow. *Journal of Fluid Mechanics*, 854:474–504, 2018.

[55] N. Ciola, P. De Palma, J.-C. Robinet, and S. Cherubini. Nonlinear optimal perturbation of turbulent channel flow as a precursor of extreme events. *Journal of Fluid Mechanics*, 970:A6, 2023.

[56] N. Ciola, P. De Palma, J.-C. Robinet, and S. Cherubini. Large-scale coherent structures in turbulent channel flow: a detuned instability of wall streaks. *Journal of Fluid Mechanics*, 997: A18, 2024.

[57] N. Ciola, Y. Duguet, J.-C. Robinet, P. De Palma, and S. Cherubini. Large-scale streak instabilities of transitional channel flow. *arXiv preprint arXiv:2507.03132*, 2025.

[58] R. M. Clever and F. H. Busse. Three-dimensional convection in a horizontal fluid layer subjected to a constant shear. *Journal of Fluid Mechanics*, 234:511–527, 1992.

[59] R. M. Clever and F. H. Busse. Tertiary and quaternary solutions for plane couette flow. *Journal of Fluid Mechanics*, 344:137–153, 1997.

[60] D. Coles and C. Van Atta. Progress report on a digital experiment in spiral turbulence. *AIAA Journal*, 4(11):1969–1971, 1966.

[61] C. Cossu. Onset of large-scale convection in wall-bounded turbulent shear flows. *Journal of Fluid Mechanics*, 945:A33, 2022.

[62] C. Cossu and Y. Hwang. Self-sustaining processes at all scales in wall-bounded turbulent shear flows. *Philosophical Transactions of the Royal Society A: Mathematical, Physical and Engineering Sciences*, 375(2089):20160088, 2017.

[63] C. Cossu, M. Chevalier, and D. S. Henningson. Optimal secondary energy growth in a plane channel flow. *Physics of fluids*, 19(5), 2007.

[64] C. Cossu, G. Pujals, and S. Depardon. Optimal transient growth and very large–scale structures in turbulent boundary layers. *Journal of Fluid Mechanics*, 619:79–94, 2009.

[65] C. Cossu, L. Brandt, S. Bagheri, and D. S. Henningson. Secondary threshold amplitudes for sinuous streak breakdown. *Physics of fluids*, 23(7), 2011.

[66] A. G. Darbyshire and T. Mullin. Transition to turbulence in constant-mass-flux pipe flow. *Journal of Fluid Mechanics*, 289:83–114, 1995.

[67] F. Daviaud, J. Hegseth, and P. Bergé. Subcritical transition to turbulence in plane couette flow. *Physical review letters*, 69(17):2511, 1992.

[68] M. de Giovanetti, Y. Hwang, and H. Choi. Skin-friction generation by attached eddies in turbulent channel flow. *Journal of Fluid Mechanics*, 808:511–538, 2016.

[69] M. de Giovanetti, H. J. Sung, and Y. Hwang. Streak instability in turbulent channel flow: the seeding mechanism of large-scale motions. *Journal of Fluid Mechanics*, 832:483–513, 2017.

[70] J. C. Del Alamo and J. Jimenez. Linear energy amplification in turbulent channels. *Journal of Fluid Mechanics*, 559:205–213, 2006.

[71] J. C. Del Alamo, J. Jiménez, P. Zandonade, and R. D. Moser. Scaling of the energy spectra of turbulent channels. *Journal of Fluid Mechanics*, 500:135–144, 2004.

[72] D. J. C. Dennis and T. B. Nickels. Experimental measurement of large-scale three-dimensional structures in a turbulent boundary layer. part 1. vortex packets. *Journal of Fluid Mechanics*, 673:180–217, 2011.

[73] R. Deshpande, C. M. de Silva, and I. Marusic. Evidence that superstructures comprise self-similar coherent motions in high reynolds number boundary layers. *Journal of Fluid Mechanics*, 969:A10, 2023.

[74] E. Deusebio, C. P. Caulfield, and J. R. Taylor. The intermittency boundary in stratified plane couette flow. *Journal of Fluid Mechanics*, 781:298–329, 2015.

[75] J. Ding, D. Chung, and S. J. Illingworth. Mode-to-mode nonlinear energy transfer in turbulent channel flows. *Journal of Fluid Mechanics*, 1002:A42, 2025.

[76] S. Dong. Evidence for internal structures of spiral turbulence. *Physical Review E*, 80(6):067301, 2009.

[77] P. Doohan, A. P. Willis, and Y. Hwang. Shear stress-driven flow: the state space of near-wall turbulence as. *Journal of Fluid Mechanics*, 874:606–638, 2019.

[78] P. Doohan, A. P. Willis, and Y. Hwang. Minimal multi-scale dynamics of near-wall turbulence. *Journal of Fluid Mechanics*, 913:A8, 2021.

[79] P. Doohan, Y. Bengana, Q. Yang, A. P. Willis, and Y. Hwang. The state space and travelling-wave solutions in two-scale wall-bounded turbulence. *Journal of Fluid Mechanics*, 947:A41, 2022.

[80] Y. Duguet. Puffing along. *Nature Physics*, 20(8):1227–1227, 2024.

[81] Y. Duguet and P. Schlatter. Oblique laminar-turbulent interfaces in plane shear flows. *Physical review letters*, 110(3):034502, 2013.

[82] Y. Duguet, A. P. Willis, and R. R. Kerswell. Transition in pipe flow: the saddle structure on the boundary of turbulence. *Journal of Fluid Mechanics*, 613:255–274, 2008.

[83] Y. Duguet, P. Schlatter, and D. S. Henningson. Formation of turbulent patterns near the onset of transition in plane couette flow. *Journal of Fluid Mechanics*, 650:119–129, 2010a.

[84] Y. Duguet, A. P. Willis, and R. R. Kerswell. Slug genesis in cylindrical pipe flow. *Journal of Fluid Mechanics*, 663:180–208, 2010b.

[85] Y. Duguet, A. Monokrousos, L. Brandt, and D. S. Henningson. Minimal transition thresholds in plane couette flow. *Physics of Fluids*, 25(8):084103, 2013.

[86] T. S. Eaves and C. P. Caulfield. Disruption of states by a stable stratification. *Journal of Fluid Mechanics*, 784:548–564, 2015.

[87] B. Eckhardt, T. M. Schneider, B. Hof, and J. Westerweel. Turbulence transition in pipe flow. *Annu. Rev. Fluid Mech.*, 39(1):447–468, 2007.

[88] T. Ellingsen and E. Palm. Stability of linear flow. *Physics of Fluids*, 18(4):487–488, 1975.

[89] M. P. Encinar and J. Jiménez. Momentum transfer by linearised eddies in turbulent channel flows. *Journal of Fluid Mechanics*, 895:A23, 2020.

[90] H. Faisst and B. Eckhardt. Traveling waves in pipe flow. *Physical Review Letters*, 91(22):224502, 2003.

[91] H. Faisst and B. Eckhardt. Sensitive dependence on initial conditions in transition to turbulence in pipe flow. *Journal of Fluid Mechanics*, 504:343–352, 2004.

[92] M. Farano. *Using nonlinear optimization to understand coherent structures in turbulence and transition*. PhD thesis, Politecnico di Bari, 2018.

[93] M. Farano, S. Cherubini, J.-C. Robinet, and P. De Palma. Hairpin-like optimal perturbations in plane poiseuille flow. *Journal of Fluid Mechanics*, 775:R2, 2015.

[94] M. Farano, S. Cherubini, J.-C. Robinet, and P. De Palma. Subcritical transition scenarios via linear and nonlinear localized optimal perturbations in plane poiseuille flow. *Fluid Dynamics Research*, 48(6):061409, 2016.

[95] M. Farano, S. Cherubini, J.-C. Robinet, and P. De Palma. Optimal bursts in turbulent channel flow. *Journal of Fluid Mechanics*, 817:35–60, 2017.

[96] M. Farano, S. Cherubini, P. De Palma, and J.-C. Robinet. Nonlinear optimal large-scale structures in turbulent channel flow. *European Journal of Mechanics-B/Fluids*, 72:74–86, 2018.

[97] B. F. Farrell and P. J. Ioannou. Perturbation structure and spectra in turbulent channel flow. *Theoretical and computational fluid dynamics*, 11(3):237–250, 1998.

[98] B. F. Farrell and P. J. Ioannou. Dynamics of streamwise rolls and streaks in turbulent wall-bounded shear flow. *Journal of Fluid Mechanics*, 708:149–196, 2012.

[99] T. M. Fischer and U. Dallmann. Primary and secondary stability analysis of a three-dimensional boundary-layer flow. *Physics of Fluids A: Fluid Dynamics*, 3(10):2378–2391, 1991.

[100] O. Flores and J. Jiménez. Hierarchy of minimal flow units in the logarithmic layer. *Physics of Fluids*, 22(7), 2010.

[101] D. P. G. Foures, C. P. Caulfield, and P. J. Schmid. Localization of flow structures using-norm optimization. *Journal of Fluid Mechanics*, 729:672–701, 2013.

[102] M. Frigo and S. G. Johnson. The design and implementation of fftw3. *Proceedings of the IEEE*, 93(2):216–231, 2005.

[103] U. Frisch. *Turbulence: the legacy of AN Kolmogorov*. Cambridge university press, 1995.

[104] G. Gallavotti. *Foundations of fluid dynamics*. Springer Science & Business Media, 2013.

[105] D. F. Gayme, B. J. McKeon, A. Papachristodoulou, B. Bamieh, and J. C. Doyle. A streamwise constant model of turbulence in plane couette flow. *Journal of fluid mechanics*, 665:99–119, 2010.

[106] D. F. Gayme, B. J. McKeon, B. Bamieh, A. Papachristodoulou, and J. C. Doyle. Amplification and nonlinear mechanisms in plane couette flow. *Physics of Fluids*, 23(6), 2011.

[107] J. Gibson, F. Reetz, S. Azimi, A. Ferraro, T. Kreilos, H. Schrobsdorff, M. Farano, A. F. Yesil, S. S. Schütz, M. Culpo, and T. M. Schneider. Channelflow 2.0. 2021. URL https://www.channelflow.ch/.

[108] J. F. Gibson, J. Halcrow, and P. Cvitanović. Visualizing the geometry of state space in plane couette flow. *Journal of Fluid Mechanics*, 611:107–130, 2008.

[109] J. F. Gibson, J. Halcrow, and P. Cvitanović. Equilibrium and travelling-wave solutions of plane couette flow. *Journal of Fluid Mechanics*, 638:243–266, 2009.

[110] A. Goharzadeh and I. Mutabazi. Experimental characterization of intermittency regimesin the couette-taylor system. *The European Physical Journal B-Condensed Matter and Complex Systems*, 19:157–162, 2001.

[111] N. Goldenfeld, N. Guttenberg, and G. Gioia. Extreme fluctuations and the finite lifetime of the turbulent state. *Physical Review E*, 81(3):035304, 2010.

[112] S. Gomé, L. S. Tuckerman, and D. Barkley. Statistical transition to turbulence in plane channel flow. *Physical Review Fluids*, 5(8):083905, 2020.

[113] S. Gomé, L. S. Tuckerman, and D. Barkley. Patterns in transitional shear turbulence. part 1. energy transfer and mean-flow interaction. *Journal of Fluid Mechanics*, 964:A16, 2023a.

[114] S. Gomé, L. S. Tuckerman, and D. Barkley. Patterns in transitional shear turbulence. part 2. emergence and optimal wavelength. *Journal of Fluid Mechanics*, 964:A17, 2023b.

[115] S. Gomé, A. Rivière, L. S. Tuckerman, and D. Barkley. Phase transition to turbulence via moving fronts. *Physical Review Letters*, 132(26):264002, 2024.

[116] M. Guala, S. E. Hommema, and R. J. Adrian. Large-scale and very-large-scale motions in turbulent pipe flow. *Journal of Fluid Mechanics*, 554:521–542, 2006.

[117] V. Gupta, A. Madhusudanan, M. Wan, S. J. Illingworth, and M. P. Juniper. Linear-model-based estimation in wall turbulence: improved stochastic forcing and eddy viscosity terms. *Journal of Fluid Mechanics*, 925:A18, 2021.

[118] M. J. P. Hack and P. Moin. Coherent instability in wall-bounded shear. *Journal of Fluid Mechanics*, 844:917–955, 2018.

[119] M. J. P. Hack and O. T. Schmidt. Extreme events in wall turbulence. *Journal of Fluid Mechanics*, 907, 2021.

[120] M. J. P. Hack and T. A. Zaki. Streak instabilities in boundary layers beneath free-stream turbulence. *Journal of fluid mechanics*, 741:280–315, 2014.

[121] P. Hall and F. T. Smith. On strongly nonlinear vortex/wave interactions in boundary-layer transition. *Journal of fluid mechanics*, 227:641–666, 1991.

[122] J. M. Hamilton, J. Kim, and F. Waleffe. Regeneration mechanisms of near-wall turbulence structures. *Journal of Fluid Mechanics*, 287:317–348, 1995.

[123] J. J. Hegseth, C. D. Andereck, F. Hayot, and Y. Pomeau. Spiral turbulence and phase dynamics. *Physical review letters*, 62(3):257, 1989.

[124] T. Herbert. Secondary instability of boundary layers. *Annual Review of Fluid Mechanics*, 20: 487–526, 1988.

[125] C. G. Hernández, Q. Yang, and Y. Hwang. Generalised quasilinear approximations of turbulent channel flow. part 1. streamwise nonlinear energy transfer. *Journal of Fluid Mechanics*, 936: A33, 2022a.

[126] C. G. Hernández, Q. Yang, and Y. Hwang. Generalised quasilinear approximations of turbulent channel flow. part 2. spanwise triadic scale interactions. *Journal of Fluid Mechanics*, 944:A34, 2022b.

[127] J. Hoepffner, L. Brandt, and D. S. Henningson. Transient growth on boundary layer streaks. *Journal of Fluid Mechanics*, 537:91—-100, 2005.

[128] B. Hof, A. Juel, and T. Mullin. Scaling of the turbulence transition threshold in a pipe. *Physical Review Letters*, 91(24):244502, 2003.

[129] B. Hof, J. Westerweel, T. M. Schneider, and B. Eckhardt. Finite lifetime of turbulence in shear flows. *Nature*, 443(7107):59–62, 2006.

[130] B. Hof, A. De Lozar, D. J. Kuik, and J. Westerweel. Repeller or attractor? selecting the dynamical model for the onset of turbulence in pipe flow. *Physical Review Letters*, 101(21): 214501, 2008.

[131] B. Hof, A. De Lozar, M. Avila, X. Tu, and T. M. Schneider. Eliminating turbulence in spatially intermittent flows. *Science*, 327(5972):1491–1494, 2010.

[132] J. J. Holford, M. Lee, and Y. Hwang. Optimal white-noise stochastic forcing for linear models of turbulent channel flow. *Journal of Fluid Mechanics*, 961:A32, 2023.

[133] J. J. Holford, M. Lee, and Y. Hwang. A data-driven quasi-linear approximation for turbulent channel flow. *Journal of Fluid Mechanics*, 980:A12, 2024a.

[134] J. J. Holford, M. Lee, and Y. Hwang. The energetics and colour for linearised models of wall turbulence. *Journal of Fluid Mechanics*, 1000:A42, 2024b.

[135] P. Holmes, J. L. Lumley, G. Berkooz, and C. W. Rowley. *Turbulence, Coherent Structures, Dynamical Systems and Symmetry*, volume 292. Cambridge Monographs on Mechanics, 2012.

[136] M. Holzner, B. Song, M. Avila, and B. Hof. Lagrangian approach to laminar–turbulent interfaces in transitional pipe flow. *Journal of Fluid Mechanics*, 723:140–162, 2013.

[137] S. Hoyas and J. Jiménez. Scaling of the velocity fluctuations in turbulent channels up to re_τ= 2003. *Physics of fluids*, 18(1), 2006.

[138] S. Hoyas, M. Oberlack, F. Alcántara-Ávila, S. V. Kraheberger, and J. Laux. Wall turbulence at high friction reynolds numbers. *Physical Review Fluids*, 7(1):014602, 2022.

[139] N. Hutchins and I. Marusic. Evidence of very long meandering features in the logarithmic region of turbulent boundary layers. *Journal of Fluid Mechanics*, 579:1–28, 2007.

[140] N. Hutchins and I. Marusic. Large-scale influences in near-wall turbulence. *Philosophical Transactions of the Royal Society A: Mathematical, Physical and Engineering Sciences*, 365(1852): 647–664, 2007.

[141] Y. Hwang. Near-wall turbulent fluctuations in the absence of wide outer motions. *Journal of Fluid Mechanics*, 723:264–288, 2013.

[142] Y. Hwang. Statistical structure of self-sustaining attached eddies in turbulent channel flow. *Journal of Fluid Mechanics*, 767:254–289, 2015.

[143] Y. Hwang. Mesolayer of attached eddies in turbulent channel flow. *Physical Review Fluids*, 1 (6):064401, 2016.

[144] Y. Hwang and Y. Bengana. Self-sustaining process of minimal attached eddies in turbulent channel flow. *Journal of Fluid Mechanics*, 795:708–738, 2016.

[145] Y. Hwang and C. Cossu. Linear non-normal energy amplification of harmonic and stochastic forcing in the turbulent channel flow. *Journal of Fluid Mechanics*, 664:51–73, 2010a.

[146] Y. Hwang and C. Cossu. Amplification of coherent streaks in the turbulent couette flow: an input–output analysis at low reynolds number. *Journal of Fluid Mechanics*, 643:333–348, 2010b.

[147] Y. Hwang and C. Cossu. Self-sustained process at large scales in turbulent channel flow. *Physical Review Letters*, 105(4):044505, 2010c.

[148] Y. Hwang and C. Cossu. Self-sustained processes in the logarithmic layer of turbulent channel flows. *Physics of Fluids*, 23(6), 2011.

[149] Y. Hwang and B. Eckhardt. Attached eddy model revisited using a minimal quasi-linear approximation. *Journal of Fluid Mechanics*, 894:A23, 2020.

[150] Y. Hwang, A. P. Willis, and C. Cossu. Invariant solutions of minimal large-scale structures in turbulent channel flow for up to 1000. *Journal of Fluid Mechanics*, 802:R1, 2016.

[151] S. J. Illingworth, J. P. Monty, and I. Marusic. Estimating large-scale structures in wall turbulence using linear models. *Journal of Fluid Mechanics*, 842:146–162, 2018.

[152] T. Ishida, Y. Duguet, and T. Tsukahara. Transitional structures in annular poiseuille flow depending on radius ratio. *Journal of Fluid Mechanics*, 794:R2, 2016.

[153] T. Ishida, Y. Duguet, and T. Tsukahara. Turbulent bifurcations in intermittent shear flows: from puffs to oblique stripes. *Physical Review Fluids*, 2(7):073902, 2017a.

[154] T. Ishida, G. Brethouwer, Y. Duguet, and T. Tsukahara. Laminar-turbulent patterns with rough walls. *Physical Review Fluids*, 2(7):073901, 2017b.

[155] R. Jahanbakhshi and T. A. Zaki. Nonlinearly most dangerous disturbance for high-speed boundary-layer transition. *Journal of Fluid Mechanics*, 876:87–121, 2019.

[156] Y. Jiao, Y. Hwang, and S. I. Chernyshenko. Orr mechanism in transition of parallel shear flow. *Physical review fluids*, 6:023902, Feb 2021.

[157] Y. Jiao, S. I. Chernyshenko, and Y. Hwang. A driving mechanism of near-wall turbulence subject to adverse pressure gradient in a plane couette flow. *Journal of Fluid Mechanics*, 941:A37, 2022.

[158] J. Jiménez. Cascades in wall-bounded turbulence. *Annual Review of Fluid Mechanics*, 44(1): 27–45, 2012.

[159] J. Jiménez. How linear is wall-bounded turbulence? *Physics of Fluids*, 25(11):110814, 2013.

[160] J. Jiménez. Direct detection of linearized bursts in turbulence. *Physics of Fluids*, 27(6), 2015.

[161] J. Jiménez. The streaks of wall-bounded turbulence need not be long. *Journal of Fluid Mechanics*, 945:R3, 2022.

[162] J. Jiménez. A perron–frobenius analysis of wall-bounded turbulence. *Journal of Fluid Mechanics*, 968:A10, 2023.

[163] J. Jiménez and P. Moin. The minimal flow unit in near-wall turbulence. *Journal of Fluid Mechanics*, 225:213–240, 1991.

[164] J. Jiménez and A. Pinelli. The autonomous cycle of near-wall turbulence. *Journal of Fluid Mechanics*, 389:335–359, 1999.

[165] J. Jiménez and M. P. Simens. Low-dimensional dynamics of a turbulent wall flow. *Journal of Fluid Mechanics*, 435:81–91, 2001.

[166] J. Jiménez, G. Kawahara, M. P. Simens, M. Nagata, and M. Shiba. Characterization of near-wall turbulence in terms of equilibrium and "bursting" solutions. *Physics of Fluids*, 17(1), 2005.

[167] A. Jouin. *Instabilités dans les systèmes spatialement périodiques: application aux instabilités secondaires et aux surfaces complexes.* PhD thesis, HESAM Université; Politecnico di Bari, 2023.

[168] A. Jouin, N. Ciola, S. Cherubini, and J.-C. Robinet. Detuned secondary instabilities in three-dimensional boundary-layer flow. *Physical Review Fluids*, 9(4):043901, 2024.

[169] J. Jovanović, F. Durst, and T. G. Johansson. Statistical analysis of the dynamic equations for higher-order moments in turbulent wall bounded flows. *Physics of Fluids A: Fluid Dynamics*, 5 (11):2886–2900, 1993.

[170] M. R. Jovanović and B. Bamieh. Componentwise energy amplification in channel flows. *Journal of Fluid Mechanics*, 534:145–183, 2005.

[171] K. Kaneko. Spatiotemporal intermittency in coupled map lattices. *Progress of Theoretical Physics*, 74(5):1033–1044, 1985.

[172] P. Kashyap. *Subcritical transition to turbulence in wall-bounded shear flows: spots, pattern formation and low-order modelling*. PhD thesis, Université Paris-Saclay, 2021.

[173] P. V. Kashyap, Y. Duguet, and O. Dauchot. Flow statistics in the transitional regime of plane channel flow. *Entropy*, 22(9):1001, 2020.

[174] P. V. Kashyap, Y. Duguet, and O. Dauchot. Linear instability of turbulent channel flow. *Physical Review Letters*, 129(24):244501, 2022.

[175] P. V. Kashyap, Y. Duguet, and O. Dauchot. Linear stability of turbulent channel flow with one-point closure. *Physical Review Fluids*, 9(6):063906, 2024.

[176] P. V. Kashyap, J. F. Marín, Y. Duguet, and O. Dauchot. Laminar-turbulent patterns in shear flows: Evasion of tipping, saddle-loop bifurcation, and log scaling of the turbulent fraction. *Physical Review Letters*, 134(15):154001, 2025.

[177] G. Kawahara and S. Kida. Periodic motion embedded in plane couette turbulence: regeneration cycle and burst. *Journal of Fluid Mechanics*, 449:291–300, 2001.

[178] R. R. Kerswell. Nonlinear nonmodal stability theory. *Annual Review of Fluid Mechanics*, 50: 319–345, 2018.

[179] T. Khapko, P. Schlatter, Y. Duguet, and D. S. Henningson. Turbulence collapse in a suction boundary layer. *Journal of Fluid Mechanics*, 795:356–379, 2016.

[180] H. T. Kim, S. J. Kline, and W. C. Reynolds. The production of turbulence near a smooth wall in a turbulent boundary layer. *Journal of Fluid Mechanics*, 50(1):133–160, 1971.

[181] J. Kim, P. Moin, and R. D. Moser. Turbulence statistics in fully developed channel flow at low reynolds number. *Journal of Fluid Mechanics*, 177:133–166, 1987.

[182] K. C. Kim and R. J. Adrian. Very large-scale motion in the outer layer. *Physics of Fluids*, 11 (2):417–422, 1999.

[183] S. J. Kline, W. C. Reynolds, F. A. Schraub, and P. W. Runstadler. The structure of turbulent boundary layers. *Journal of Fluid Mechanics*, 30(4):741–773, 1967.

[184] L. Klotz, G. Lemoult, K. Avila, and B. Hof. Phase transition to turbulence in spatially extended shear flows. *Physical Review Letters*, 128(1):014502, 2022.

[185] M. J. Kochenderfer and T. A. Wheeler. *Algorithms for optimization*. Mit Press, 2019.

[186] K. Kohyama, M. Sano, and T. Tsukahara. Sidewall effect on turbulent band in subcritical transition of high-aspect-ratio duct flow. *Physics of Fluids*, 34(8), 2022.

[187] M. T. Landahl. A note on an algebraic instability of inviscid parallel shear flows. *Journal of Fluid Mechanics*, 98(2):243–251, 1980.

[188] L. D. Landau and E. M. Lifshitz. *Fluid Mechanics: Volume 6*, volume 6. Elsevier, 1987.

[189] J. H. Lee and H. J. Sung. Very-large-scale motions in a turbulent boundary layer. *Journal of Fluid Mechanics*, 673:80–120, 2011.

[190] J. H. Lee, H. J. Sung, and R. J. Adrian. Space–time formation of very-large-scale motions in turbulent pipe flow. *journal of fluid mechanics*, 881:1010–1047, 2019.

[191] M. Lee and R. D. Moser. Direct numerical simulation of turbulent channel flow up to. *Journal of Fluid Mechanics*, 774:395–415, 2015.

[192] M. Lee and R. D. Moser. Spectral analysis of the budget equation in turbulent channel flows at high reynolds number. *Journal of Fluid Mechanics*, 860:886–938, 2019.

[193] G. Lemoult, J.-L. Aider, and J. E. Wesfreid. Turbulent spots in a channel: large-scale flow and self-sustainability. *Journal of Fluid Mechanics*, 731:R1, 2013.

[194] G. Lemoult, K. Gumowski, J.-L. Aider, and J. E. Wesfreid. Turbulent spots in channel flow: an experimental study: large-scale flow, inner structure and low-order model. *The European Physical Journal E*, 37:1–11, 2014.

[195] G. Lemoult, L. Shi, K. Avila, S. V. Jalikop, M. Avila, and B. Hof. Directed percolation phase transition to sustained turbulence in couette flow. *Nature Physics*, 12(3):254–258, 2016.

[196] G. Lemoult, V. Mukund, H.-Y. Shih, G. Linga, J. Mathiesen, N. Goldenfeld, and B. Hof. Directed percolation and puff jamming near the transition to pipe turbulence. *Nature Physics*, pages 1–7, 2024.

[197] E. R. Lindgren. Propagation velocity of turbulent slugs and streaks in transition pipe flow. *The Physics of Fluids*, 12(2):418–425, 1969.

[198] C. Liu and D. F. Gayme. Structured input–output analysis of transitional wall-bounded flows. *Journal of Fluid Mechanics*, 927:A25, 2021.

[199] J. Liu, Y. Xiao, L. Zhang, M. Li, J. Tao, and S. Xu. Extension at the downstream end of turbulent band in channel flow. *Physics of Fluids*, 32(12), 2020.

[200] T. Liu, B. Semin, R. Godoy-Diana, and J. E. Wesfreid. Lift-up and streak waviness drive the self-sustained process in wall-bounded transition to turbulence. *Physical Review Fluids*, 9(3): 033901, 2024.

[201] A. Lozano-Durán and J. Jiménez. Effect of the computational domain on direct simulations of turbulent channels up to reτ= 4200. *Physics of Fluids*, 26(1), 2014.

[202] A. Lozano-Durán, O. Flores, and J. Jiménez. The three-dimensional structure of momentum transfer in turbulent channels. *Journal of Fluid Mechanics*, 694:100–130, 2012.

[203] A. Lozano-Durán, N. C. Constantinou, M.-A. Nikolaidis, and M. Karp. Cause-and-effect of linear mechanisms sustaining wall turbulence. *Journal of Fluid Mechanics*, 914:A8, 2021.

[204] J. Lu, J. Tao, W. Zhou, and X. Xiong. Threshold and decay properties of transient isolated turbulent band in plane couette flow. *Applied Mathematics and Mechanics*, 40(10):1449–1456, 2019.

[205] S. S. Lu and W. W. Willmarth. Measurements of the structure of the reynolds stress in a turbulent boundary layer. *Journal of Fluid mechanics*, 60(3):481–511, 1973.

[206] J. L. Lumley. The structure of inhomogeneous turbulent flows. *Atmospheric turbulence and radio wave propagation*, pages 166–178, 1967.

[207] A. Madhusudanan, S. J. Illingworth, and I. Marusic. Coherent large-scale structures from the linearized navier–stokes equations. *Journal of Fluid Mechanics*, 873:89–109, 2019.

[208] P. Manneville. On the decay of turbulence in plane couette flow. *Fluid Dynamics Research*, 43 (6):065501, 2011.

[209] P. Manneville. Turbulent patterns in wall-bounded flows: A turing instability? *Europhysics Letters*, 98(6):64001, 2012.

[210] P. Manneville and J. Rolland. On modelling transitional turbulent flows using under-resolved direct numerical simulations: the case of plane couette flow. *Theoretical and Computational Fluid Dynamics*, 25:407–420, 2011.

[211] P. Manneville and M. Shimizu. Transitional channel flow: a minimal stochastic model. *Entropy*, 22(12):1348, 2020.

[212] P. Manneville and M. Shimizu. Critical properties of laminar-turbulent pattern emergence in plane couette flow. *Europhysics Letters*, 151(3):33001, 2025.

[213] E. Marensi, G. Yalnız, and B. Hof. Dynamics and proliferation of turbulent stripes in plane-poiseuille and plane-couette flows. *Journal of Fluid Mechanics*, 974:A21, 2023.

[214] M. Marquillie, U. Ehrenstein, and J.-P. Laval. Instability of streaks in wall turbulence with adverse pressure gradient. *Journal of Fluid Mechanics*, 681:205–240, 2011.

[215] J. B. Marston, G. P. Chini, and S. M. Tobias. Generalized quasilinear approximation: application to zonal jets. *Physical review letters*, 116(21):214501, 2016.

[216] I. Marusic, D. Chandran, A. Rouhi, M. K. Fu, D. Wine, B. Holloway, D. Chung, and A. J. Smits. An energy-efficient pathway to turbulent drag reduction. *Nature Communications*, 12(1):5805, 2021.

[217] R. Mathis, N. Hutchins, and I. Marusic. Large-scale amplitude modulation of the small-scale structures in turbulent boundary layers. *Journal of Fluid Mechanics*, 628:311–337, 2009.

[218] B. J. McKeon. The engine behind (wall) turbulence: perspectives on scale interactions. *Journal of Fluid Mechanics*, 817:P1, 2017.

[219] B. J. McKeon and A. S. Sharma. A critical-layer framework for turbulent pipe flow. *Journal of Fluid Mechanics*, 658:336–382, 2010.

[220] A. Meseguer and L. N. Trefethen. Linearized pipe flow to reynolds number 10^7. *Journal of Computational Physics*, 186(1):178–197, 2003.

[221] A. Meseguer, F. Mellibovsky, M. Avila, and F. Marques. Families of subcritical spirals in highly counter-rotating taylor-couette flow. *Physical Review E*, 79(3):036309, 2009.

[222] Y. Mizuno and J. Jiménez. Wall turbulence without walls. *Journal of Fluid Mechanics*, 723: 429–455, 2013.

[223] R. Moarref, A. S. Sharma, J. A. Tropp, and B. J. McKeon. Model-based scaling of the streamwise energy density in high-reynolds-number turbulent channels. *Journal of Fluid Mechanics*, 734: 275–316, 2013.

[224] H. K. Moffatt. Fixed points of turbulent dynamical systems and suppression of nonlinearity comment 1. In *Whither Turbulence? Turbulence at the Crossroads: Proceedings of a Workshop Held at Cornell University, Ithaca, NY, March 22–24, 1989*, pages 250–257. Springer, 1989.

[225] P. Moin and R. D. Moser. Characteristic-eddy decomposition of turbulence in a channel. *Journal of Fluid Mechanics*, 200:471–509, 1989.

[226] A. Monokrousos, A. Bottaro, L. Brandt, A. Di Vita, and D. S. Henningson. Nonequilibrium thermodynamics and the optimal path to turbulence in shear flows. *Physical review letters*, 106 (13):134502, 2011.

[227] J. P. Monty, J. A. Stewart, R. C. Williams, and M. S. Chong. Large-scale features in turbulent pipe and channel flows. *Journal of Fluid Mechanics*, 589:147–156, 2007.

[228] J. P. Monty, N. Hutchins, H. C. H. Ng, I. Marusic, and M. S. Chong. A comparison of turbulent pipe, channel and boundary layer flows. *Journal of fluid mechanics*, 632:431–442, 2009.

[229] P. Morra, O. Semeraro, D. S. Henningson, and C. Cossu. On the relevance of reynolds stresses in resolvent analyses of turbulent wall-bounded flows. *Journal of Fluid Mechanics*, 867:969–984, 2019.

[230] R. D. Moser, J. Kim, and N. N. Mansour. Direct numerical simulation of turbulent channel flow up to re_τ= 590. *Physics of fluids*, 11(4):943–945, 1999.

[231] D. Moxey and D. Barkley. Distinct large-scale turbulent-laminar states in transitional pipe flow. *Proceedings of the National Academy of Sciences*, 107(18):8091–8096, 2010.

[232] V. Mukund and B. Hof. The critical point of the transition to turbulence in pipe flow. *Journal of Fluid Mechanics*, 839:76–94, 2018.

[233] V. Mukund, C. S. Paranjape, M. P. Sitte, G. Yalnız, and B. Hof. Aging and memory of transitional turbulence. *Nature Communications*, 16(1):8447, 2025.

[234] S. D. Muralidhar, B. Podvin, L. Mathelin, and Y. Fraigneau. Spatio-temporal proper orthogonal decomposition of turbulent channel flow. *Journal of Fluid Mechanics*, 864:614–639, 2019.

[235] M. Nagata. Three-dimensional finite-amplitude solutions in plane couette flow: bifurcation from infinity. *Journal of Fluid Mechanics*, 217:519–527, 1990.

[236] T. Nemoto and A. Alexakis. Method to measure efficiently rare fluctuations of turbulence intensity for turbulent-laminar transitions in pipe flows. *Physical Review E*, 97(2):022207, 2018.

[237] N. Nikitin. On the rate of spatial predictability in near-wall turbulence. *Journal of Fluid Mechanics*, 614:495–507, 2008.

[238] N. Nikitin. Characteristics of the leading lyapunov vector in a turbulent channel flow. *Journal of Fluid Mechanics*, 849:942–967, 2018.

[239] M. Nishi, B. Ünsal, F. Durst, and G. Biswas. Laminar-to-turbulent transition of pipe flows through puffs and slugs. *Journal of Fluid Mechanics*, 614:425–446, 2008.

[240] W. M. F. Orr. The stability or instability of the steady motions of a perfect liquid and of a viscous liquid. part ii: A viscous liquid. In *Proceedings of the Royal Irish Academy. Section A: Mathematical and Physical Sciences*, volume 27, pages 69–138. JSTOR, 1907.

[241] K. Osawa and J. Jiménez. Causal features in turbulent channel flow. *Journal of Fluid Mechanics*, 1000:A4, 2024.

[242] W. Oxley and R. R. Kerswell. Transient growth in streaky unbounded shear flow: A symbiosis of orr and push-over mechanisms. *arXiv preprint arXiv:2503.05611*, 2025.

[243] C. S. Paranjape, Y. Duguet, and B. Hof. Oblique stripe solutions of channel flow. *Journal of Fluid Mechanics*, 897:A7, 2020.

[244] E. Parente. *Etude de la dynamique auto-entretenue des bandes turbulentes et de la turbulence pleinement développée dans un écoulement de canal*. PhD thesis, HESAM Université; Politecnico di Bari. Dipartimento di Ingegneria Meccanica . . . , 2021.

[245] E. Parente, J.-C. Robinet, P. De Palma, and S. Cherubini. Linear and nonlinear optimal growth mechanisms for generating turbulent bands. *Journal of Fluid Mechanics*, 938:A25, 2022a.

[246] E. Parente, J.-C. Robinet, P. De Palma, and S. Cherubini. Minimal energy thresholds for sustained turbulent bands in channel flow. *Journal of Fluid Mechanics*, 942:A18, 2022b.

[247] J. Park, Y. Hwang, and C. Cossu. On the stability of large-scale streaks in turbulent couette and poiseulle flows. *Comptes Rendus Mécanique*, 339(1):1–5, 2011.

[248] M. Pausch, Q. Yang, Y. Hwang, and B. Eckhardt. Quasilinear approximation for exact coherent states in parallel shear flows. *Fluid Dynamics Research*, 51(1):011402, 2019.

[249] J. Peixinho and T. Mullin. Decay of turbulence in pipe flow. *Physical Review Letters*, 96(9): 094501, 2006.

[250] R. Peyret. *Spectral methods for incompressible viscous flow*, volume 148. Springer, 2002.

[251] J. Philip and P. Manneville. From temporal to spatiotemporal dynamics in transitional plane couette flow. *Physical Review E—Statistical, Nonlinear, and Soft Matter Physics*, 83(3):036308, 2011.

[252] Y. Pomeau. Front motion, metastability and subcritical bifurcations in hydrodynamics. *Physica D: Nonlinear Phenomena*, 23(1-3):3–11, 1986.

[253] Y. Pomeau. The long and winding road. *Nature Physics*, 12(3):198–199, 2016.

[254] S. B. Pope. A more general effective-viscosity hypothesis. *Journal of Fluid Mechanics*, 72(2): 331–340, 1975.

[255] S. B. Pope. Turbulent flows. 2000.

[256] A. Prigent, G. Grégoire, H. Chaté, O. Dauchot, and W. van Saarloos. Large-scale finite-wavelength modulation within turbulent shear flows. *Physical Review Letters*, 89(1):014501, 2002.

[257] A. Prigent, G. Grégoire, H. Chaté, and O. Dauchot. Long-wavelength modulation of turbulent shear flows. *Physica D: Nonlinear Phenomena*, 174(1-4):100–113, 2003.

[258] C. C. T. Pringle and R. R. Kerswell. Using nonlinear transient growth to construct the minimal seed for shear flow turbulence. *Physical review letters*, 105(15):154502, 2010.

[259] C. C. T. Pringle, A. P. Willis, and R. R. Kerswell. Minimal seeds for shear flow turbulence: using nonlinear transient growth to touch the edge of chaos. *Journal of Fluid Mechanics*, 702: 415–443, 2012.

[260] G. Pujals, M. García-Villalba, C. Cossu, and S. Depardon. A note on optimal transient growth in turbulent channel flows. *Physics of fluids*, 21(1), 2009.

[261] G. Pujals, C. Cossu, and S. Depardon. Forcing large-scale coherent streaks in a zero-pressure-gradient turbulent boundary layer. *Journal of Turbulence*, 11:N25, 2010.

[262] A. Quarteroni, R. Sacco, and F. Saleri. *Numerical mathematics*, volume 37. Springer Science & Business Media, 2006.

[263] S. Rawat, C. Cossu, Y. Hwang, and F. Rincon. On the self-sustained nature of large-scale motions in turbulent couette flow. *Journal of Fluid Mechanics*, 782:515–540, 2015.

[264] F. Reetz, T. Kreilos, and T. M. Schneider. Exact invariant solution reveals the origin of self-organized oblique turbulent-laminar stripes. *Nature communications*, 10(1):2277, 2019.

[265] O. Reynolds. Xxix. an experimental investigation of the circumstances which determine whether the motion of water shall be direct or sinuous, and of the law of resistance in parallel channels. *Philosophical Transactions of the Royal society of London*, (174):935–982, 1883.

[266] W. C. Reynolds and A. K. M. F. Hussain. The mechanics of an organized wave in turbulent shear flow. part 3. theoretical models and comparisons with experiments. *Journal of Fluid Mechanics*, 54(2):263–288, 1972.

[267] W. C. Reynolds and W. G. Tiederman. Stability of turbulent channel flow, with application to malkus's theory. *Journal of Fluid Mechanics*, 27(2):253–272, 1967.

[268] K. F. Riley, M. P. Hobson, and S. J. Bence. *Mathematical methods for physics and engineering: a comprehensive guide*. Cambridge university press, 2006.

[269] S. Robinson. Coherent motions in the turbulent boundary layer. *Annual review of fluid mechanics*, 23(1):601–639, 1991.

[270] J. Rolland. Extremely rare collapse and build-up of turbulence in stochastic models of transitional wall flows. *Physical Review E*, 97(2):023109, 2018.

[271] J. Rolland and P. Manneville. Ginzburg–landau description of laminar-turbulent oblique band formation in transitional plane couette flow. *The European Physical Journal B*, 80:529–544, 2011a.

[272] J. Rolland and P. Manneville. Pattern fluctuations in transitional plane couette flow. *Journal of Statistical Physics*, 142:577–591, 2011b.

[273] H. Salwen, F. W. Cotton, and C. E. Grosch. Linear stability of poiseuille flow in a circular pipe. *Journal of Fluid Mechanics*, 98(2):273–284, 1980.

[274] D. Samanta, A. De Lozar, and B. Hof. Experimental investigation of laminar turbulent intermittency in pipe flow. *Journal of fluid mechanics*, 681:193–204, 2011.

[275] M. Sano and K. Tamai. A universal transition to turbulence in channel flow. *Nature Physics*, 12(3):249–253, 2016.

[276] T. P. Sapsis. Statistics of extreme events in fluid flows and waves. *Annual Review of Fluid Mechanics*, 53:85–111, 2021.

[277] P. J. Schmid and L. Brandt. Analysis of fluid systems: stability, receptivity, sensitivity: lecture notes from the flow-nordita summer school on advanced instability methods for complex flows, stockholm, sweden, 2013. *Applied Mechanics Reviews*, 66(2):024803, 2014.

[278] P. J. Schmid and D. S. Henningson. *Stability and transition in shear flows*, volume 142. Springer Science & Business Media, 2012.

[279] P. J. Schmid, M. F. De Pando, and N. Peake. Stability analysis for n-periodic arrays of fluid systems. *Physical Review Fluids*, 2(11):113902, 2017.

[280] O. T. Schmidt and P. J. Schmid. A conditional space–time pod formalism for intermittent and rare events: example of acoustic bursts in turbulent jets. *Journal of Fluid Mechanics*, 867, 2019.

[281] F. G. Schmitt. About boussinesq's turbulent viscosity hypothesis: historical remarks and a direct evaluation of its validity. *Comptes Rendus Mécanique*, 335(9-10):617–627, 2007.

[282] T. M. Schneider, B. Eckhardt, and J. A. Yorke. Turbulence transition and the edge of chaos in pipe flow. *Physical Review Letters*, 99(3):034502, 2007.

[283] T. M. Schneider, D. Marinc, and B. Eckhardt. Localized edge states nucleate turbulence in extended plane couette cells. *Journal of Fluid Mechanics*, 646:441–451, 2010.

[284] W. Schoppa and F. Hussain. Coherent structure generation in near-wall turbulence. *Journal of Fluid Mechanics*, 453:57–108, 2002.

[285] A. S. Sharma and B. J. McKeon. On coherent structure in wall turbulence. *Journal of Fluid Mechanics*, 728:196–238, 2013.

[286] A. S. Sharma, R. Moarref, B. J. McKeon, J. S. Park, M. D. Graham, and A. P. Willis. Low-dimensional representations of exact coherent states of the navier-stokes equations from the resolvent model of wall turbulence. *Physical Review E*, 93(2):021102, 2016.

[287] L. Shi, M. Avila, and B. Hof. Scale invariance at the onset of turbulence in couette flow. *Physical Review Letters*, 110(20):204502, 2013.

[288] M. Shimizu and S. Kida. A driving mechanism of a turbulent puff in pipe flow. *Fluid dynamics research*, 41(4):045501, 2009.

[289] M. Shimizu and P. Manneville. Bifurcations to turbulence in transitional channel flow. *Physical Review Fluids*, 4(11):113903, 2019.

[290] N. Skouloudis and Y. Hwang. Scaling of turbulence intensities up to re τ= 10 6 with a resolvent-based quasilinear approximation. *Physical Review Fluids*, 6(3):034602, 2021.

[291] J. D. Skufca, J. A. Yorke, and B. Eckhardt. Edge of chaos in a parallel shear flow. *Physical Review Letters*, 96(17):174101, 2006.

[292] A. J. Smits, B. J. McKeon, and I. Marusic. High–reynolds number wall turbulence. *Annual Review of Fluid Mechanics*, 43:353–375, 2011.

[293] B. Song, D. Barkley, B. Hof, and M. Avila. Speed and structure of turbulent fronts in pipe flow. *Journal of Fluid Mechanics*, 813:1045–1059, 2017.

[294] S. Symon, K. Rosenberg, S. T. M. Dawson, and B. J. McKeon. Non-normality and classification of amplification mechanisms in stability and resolvent analysis. *Physical Review Fluids*, 3(5): 053902, 2018.

[295] S. Symon, S. J. Illingworth, and I. Marusic. Energy transfer in turbulent channel flows and implications for resolvent modelling. *Journal of Fluid Mechanics*, 911:A3, 2021.

[296] S. Symon, A. Madhusudanan, S. J. Illingworth, and I. Marusic. Use of eddy viscosity in resolvent analysis of turbulent channel flow. *Physical Review Fluids*, 8(6):064601, 2023.

[297] K. Taira, S. L. Brunton, S. T. M. Dawson, C. W. Rowley, T. Colonius, B. J. McKeon, O. T. Schmidt, S. Gordeyev, V. Theofilis, and L. S. Ukeiley. Modal analysis of fluid flows: An overview. *AIAA journal*, 55(12):4013–4041, 2017.

[298] K. Takeishi, G. Kawahara, H. Wakabayashi, M. Uhlmann, and A. Pinelli. Localized turbulence structures in transitional rectangular-duct flow. *Journal of Fluid Mechanics*, 782:368–379, 2015.

[299] J. J. Tao, B. Eckhardt, and X. M. Xiong. Extended localized structures and the onset of turbulence in channel flow. *Physical Review Fluids*, 3(1):011902, 2018.

[300] G. I. Taylor. Dispersion of soluble matter in solvent flowing slowly through a tube. *Proceedings of the Royal Society of London. Series A. Mathematical and Physical Sciences*, 219(1137):186–203, 1953.

[301] V. L. Thomas, B. K. Lieu, M. R. Jovanović, B. F. Farrell, P. J. Ioannou, and D. F. Gayme. Self-sustaining turbulence in a restricted nonlinear model of plane couette flow. *Physics of Fluids*, 26(10), 2014.

[302] S. M. Tobias and J. B. Marston. Three-dimensional rotating couette flow via the generalised quasilinear approximation. *Journal of Fluid Mechanics*, 810:412–428, 2017.

[303] S. Toh and T. Itano. A periodic-like solution in channel flow. *Journal of Fluid Mechanics*, 481: 67–76, 2003.

[304] S. Toh and T. Itano. Interaction between a large-scale structure and near-wall structures in channel flow. *Journal of Fluid Mechanics*, 524:249–262, 2005.

[305] A. Towne, A. Lozano-Durán, and X. Yang. Resolvent-based estimation of space–time flow statistics. *Journal of Fluid Mechanics*, 883:A17, 2020.

[306] A. A. R. Townsend. *The structure of turbulent shear flow*. Cambridge university press, 1976.

[307] L. N. Trefethen. *Spectral methods in MATLAB*. SIAM, 2000.

[308] T. Tsukahara, Y. Seki, H. Kawamura, and D. Tochio. Dns of turbulent channel flow at very low reynolds numbers. In *Fourth International Symposium on Turbulence and Shear Flow Phenomena*. Begel House Inc., 2005.

[309] T. Tsukahara, N. Tillmark, and P. H. Alfredsson. Flow regimes in a plane couette flow with system rotation. *Journal of Fluid Mechanics*, 648:5–33, 2010.

[310] L. S. Tuckerman and D. Barkley. Bifurcation analysis of the eckhaus instability. *Physica D: Nonlinear Phenomena*, 46(1):57–86, 1990.

[311] L. S. Tuckerman and D. Barkley. Patterns and dynamics in transitional plane couette flow. *Physics of Fluids*, 23(4), 2011.

[312] L. S. Tuckerman, D. Barkley, and O. Dauchot. Instability of uniform turbulent plane couette flow: Spectra, probability distribution functions and k–Ω closure model. In *Seventh IUTAM Symposium on Laminar-Turbulent Transition: Proceedings of the Seventh IUTAM Symposium on Laminar-Turbulent Transition, Stockholm, Sweden, 2009*, pages 59–66. Springer, 2010.

[313] L. S. Tuckerman, T. Kreilos, H. Schrobsdorff, T. M. Schneider, and J. F. Gibson. Turbulent-laminar patterns in plane poiseuille flow. *Physics of Fluids*, 26(11), 2014.

[314] L. S. Tuckerman, M. Chantry, and D. Barkley. Patterns in wall-bounded shear flows. *Annual Review of Fluid Mechanics*, 52:343–367, 2020.

[315] M. Vallikivi, B. Ganapathisubramani, and A. J. Smits. Spectral scaling in boundary layers and pipes at very high reynolds numbers. *Journal of Fluid Mechanics*, 771:303–326, 2015.

[316] C. W. H. van Doorne and J. Westerweel. The flow structure of a puff. *Philosophical Transactions of the Royal Society A: Mathematical, Physical and Engineering Sciences*, 367(1888):489–507, 2009.

[317] P. Vincenti, J. Klewicki, C. Morrill-Winter, C. M. White, and M. Wosnik. Streamwise velocity statistics in turbulent boundary layers that spatially develop to high reynolds number. *Experiments in fluids*, 54:1–13, 2013.

[318] F. Waleffe. On a self-sustaining process in shear flows. *Physics of Fluids*, 9(4):883–900, 1997.

[319] F. Waleffe. Three-dimensional coherent states in plane shear flows. *Physical Review Letters*, 81 (19):4140, 1998.

[320] F. Waleffe. Exact coherent structures in channel flow. *Journal of Fluid Mechanics*, 435:93–102, 2001.

[321] F. Waleffe. Homotopy of exact coherent structures in plane shear flows. *Physics of Fluids*, 15 (6):1517–1534, 2003.

[322] J. M. Wallace, H. Eckelmann, and R. S. Brodkey. The wall region in turbulent shear flow. *Journal of Fluid Mechanics*, 54(1):39–48, 1972.

[323] H. Wedin and R. R. Kerswell. Exact coherent structures in pipe flow: travelling wave solutions. *Journal of Fluid Mechanics*, 508:333–371, 2004.

[324] A. P. Willis and R. R. Kerswell. Critical behavior in the relaminarization of localized turbulence in pipe flow. *Physical review letters*, 98(1):014501, 2007.

[325] A. P. Willis, Y. Hwang, and C. Cossu. Optimally amplified large-scale streaks and drag reduction in turbulent pipe flow. *Physical Review E—Statistical, Nonlinear, and Soft Matter Physics*, 82 (3):036321, 2010.

[326] W. W. Willmarth and S. S. Lu. Structure of the reynolds stress near the wall. *Journal of Fluid Mechanics*, 55(1):65–92, 1972.

[327] A. T. Winfree. Varieties of spiral wave behavior: An experimentalist's approach to the theory of excitable media. *Chaos: An Interdisciplinary Journal of Nonlinear Science*, 1(3):303–334, 1991.

[328] Y. Wu and B. Song. Transient characteristics of fully localised turbulence in transitional channel flow. *Journal of Fluid Mechanics*, 1009:R2, 2025.

[329] I. J. Wygnanski and F. H. Champagne. On transition in a pipe. part 1. the origin of puffs and slugs and the flow in a turbulent slug. *Journal of Fluid Mechanics*, 59(2):281–335, 1973.

[330] I. J. Wygnanski, M. Sokolov, and D. Friedman. On transition in a pipe. part 2. the equilibrium puff. *Journal of Fluid Mechanics*, 69(2):283–304, 1975.

[331] L. Xi and M. D. Graham. Active and hibernating turbulence in minimal channel flow of newtonian and polymeric fluids. *Physical Review Letters*, 104(21):218301, 2010.

[332] L. Xi and M. D. Graham. Intermittent dynamics of turbulence hibernation in newtonian and viscoelastic minimal channel flows. *Journal of Fluid Mechanics*, 693:433–472, 2012.

[333] X. Xiao and B. Song. The growth mechanism of turbulent bands in channel flow at low reynolds numbers. *Journal of Fluid Mechanics*, 883:R1, 2020.

[334] X. Xiong, J. Tao, S. Chen, and L. Brandt. Turbulent bands in plane-poiseuille flow at moderate reynolds numbers. *Physics of Fluids*, 27(4), 2015.

[335] Q. Yang, A. P. Willis, and Y. Hwang. Exact coherent states of attached eddies in channel flow. *Journal of Fluid Mechanics*, 862:1029–1059, 2019.

[336] L. Yin, Y. Hwang, and J. C. Vassilicos. Dynamics of turbulent energy and dissipation in channel flow. *Journal of Fluid Mechanics*, 996:A12, 2024.

[337] A. Ying, Z. Li, and L. Fu. Stochastic forcing in linear analysis for turbulent channel flow: Optimization and modeling. *Physical Review Fluids*, 10(7):074601, 2025.

[338] S. Zammert and B. Eckhardt. Streamwise and doubly-localised periodic orbits in plane poiseuille flow. *Journal of Fluid Mechanics*, 761:348–359, 2014.

[339] S. Zammert and B. Eckhardt. Streamwise decay of localized states in channel flow. *Physical Review E*, 94(4):041101, 2016.

[340] A. Zare, M. R. Jovanović, and T. T. Georgiou. Colour of turbulence. *Journal of Fluid Mechanics*, 812:636–680, 2017.

[341] Z. Zhou, C.-X. Xu, and J. Jiménez. Interaction between near-wall streaks and large-scale motions in turbulent channel flows. *Journal of Fluid Mechanics*, 940:A23, 2022.

Ciola Nicola

Instabilities and emergence of coherent structures in the turbulent channel flow

Résumé: Les écoulements turbulents se caractérisent par une phénoménologie remarquable combinant chaos et ordre, fluctuations à de multiples échelles et motifs récurrents appelés *structures cohérentes*. L'objectif de cette thèse est d'élucider certains processus physiques impliquant des structures cohérentes dans l'écoulement turbulent de canal plan. Différentes techniques numériques sont mises en œuvre dans ce but, avec un fil conducteur commun : étudier comment les structures cohérentes deviennent instables et, finalement, engendrent de nouvelles structures cohérentes à d'autres échelles. Cette étude est divisée en trois parties.

Dans la première partie, la génération d'événements extrêmes de dissipation est examinée. Des perturbations optimales non linéaires sont calculées par rapport à un champ instantané pleinement turbulent, et la dynamique induite par ces perturbations est analysée et comparée à celle des événements extrêmes se produisant naturellement, établissant ainsi un lien entre les deux. Fait intéressant, la perturbation optimale non linéaire agit vers une déstabilisation des *stries* proches de la paroi, ce qui suggère qu'une instabilité de ces stries pourrait être à l'origine des événements extrêmes.

Dans la deuxième partie, l'instabilité des stries est abordée plus directement, mais sous un angle différent. Une analyse de stabilité linéaire est effectuée sur un réseau périodique de stries afin de montrer que ces structures subissent des instabilités sous-harmoniques ou désaccordées, caractérisées par des modes instables de grande longueur d'onde (plusieurs fois supérieure à celle des stries). Ces instabilités sont reliées aux mouvements de grande échelle (Large-Scale Motions, LSMs) observés dans les expériences et les simulations numériques directes d'écoulements à nombre de Reynolds élevé.

Dans la troisième partie, l'instabilité linéaire à grande échelle des stries est réexaminée à faible nombre de Reynolds afin de déterminer les longueurs d'onde et le nombre de Reynolds critique de l'instabilité menant à la formation de motifs laminaires-turbulents. La thèse se conclut par le développement d'un modèle non linéaire de formation des motifs laminaires-turbulents. Les idées, les limitations et les pistes d'amélioration de ce modèle sont testées et discutées.

Mots clés: Instabilités, structures cohérentes, formation de motifs, écoulements cisaillés par paroi

Abstract: Turbulent flows are characterised by a marvellous phenomenology combining chaos and order, fluctuations on multiple scales and recurrent patterns named *coherent structures*. This thesis aims to elucidate certain physical processes involving coherent structures in the turbulent channel flow. Different numerical techniques are implemented towards this aim, with a common ground: investigate how coherent structures become unstable and, eventually, generate new coherent structures on different scales. This investigation is divided into three parts.

In the first part, the generation of extreme dissipation events is considered. Nonlinear optimal perturbations are computed with respect to a fully turbulent snapshot, and the dynamics induced by these perturbations are analysed and compared to the dynamics of naturally occurring extreme events, establishing a connection between the two. Interestingly, the nonlinear optimal perturbation works towards a destabilisation of near-wall *streaks*, suggesting that an instability of streaks is a possible cause of extreme events.

In the second part, the instability of streaks is addressed more directly but in a different direction. A linear stability analysis is performed on an array of periodic streaks to show that these structures undergo sub-harmonic or detuned instabilities with unstable modes characterised by large wavelengths (several times larger than the streak's wavelength). These instabilities are related to the large-scale motions (LSMs) observed in experiments and direct numerical simulations of high-Reynolds number flows.

In the third part, the large-scale linear instability of streaks is revisited at low Reynolds number in order to capture the wavelengths and the critical Reynolds number of the instability leading to laminar-turbulent patterns. The thesis concludes with the development of a nonlinear model for laminar-turbulent pattern formation. Ideas, limitations and possible directions to improve this model are tested and discussed.

Keywords: Instabilities, coherent structures, pattern formation, wall-bounded turbulence